Precision Low Temperature Calorimetry and Susceptibility of Magnetic Pyrochlores

by

David Pomaranski

A thesis
presented to the University of Waterloo
in fulfillment of the
thesis requirement for the degree of
Doctor of Philosophy
in
Physics

Waterloo, Ontario, Canada, 2018

Examining Committee Membership

The following served on the Examining Committee for this thesis. The decision of the Examining Committee is by majority vote.

Supervisor: Jan B. Kycia
Professor at the University of Waterloo
in the Department of Physics and Astronomy

Internal Members: Robert W. Hill
Professor at the University of Waterloo
in the Department of Physics and Astronomy

Roger G. Melko
Professor at the University of Waterloo
in the Department of Physics and Astronomy
and Perimeter Institute for Theoretical Physics

Internal-External Member: Adam Wei Tsen
Professor at the University of Waterloo
in the Department of Chemistry
and Institute for Quantum Computing

External Examiner: Mark W. Meisel
Professor at the University of Florida
in the Department of Physics,
the National High Magnetic Field Laboratory,
and Center for Condensed Matter Sciences

I hereby declare that I am the sole author of this thesis. This is a true copy of the thesis, including any required final revisions, as accepted by my examiners.

I understand that my thesis may be made electronically available to the public.

Abstract

Spin-ice models feature the same statistical disorder as water ice, which is identified as the source of zero-point entropy. Gapped topological excitations with properties of monopoles are associated with the violation of the magnetic flux divergence condition $\nabla \cdot \boldsymbol{B} = 0$, and electric charges are constructed on the dual diamond lattice. These emergent structures have the characteristic long-range 'Coulomb' algebraic correlations, as well as a linearly dispersing photon. Quantum tunneling between states, defined on closed loops of magnetic flux give rise to persistent spin-liquid dynamics. Under the influence of geometrical frustration, electronic properties of matter often crystallize into patterns described by complex symmetry, and in some cases exhibit topological order accompanied by long range entanglement. The general features of spin-ice are manifest in a large class of materials with the chemical formula $R_2M_2O_7$, where R^{3+} is a rare earth ion from the lanthanide series, and M^{4+} is a transition metal. The versatility of this lattice gives rise to a wide range of interesting and tantalizing behaviours.

This thesis starts with a brief review of the concept of frustration in condensed matter physics, and the ice model is motivated by several common abstractions. Relevant properties of the classical Ising pyrochlore dipolar magnet, dysprosium titanate $Dy_2Ti_2O_7$ are discussed. Ytterbium titanate $Yb_2Ti_2O_7$, and terbium titanate $Tb_2Ti_2O_7$, are both classified as spin$-\frac{1}{2}$ pyrochlores with proposed spin-liquid behaviour at very low temperature. Their general properties are also introduced, and motivated for this study. The second chapter reviews some of the basic microscopic electronic interactions in the rare earth ions, which originate mainly from atomic $4f$ orbitals.

The second part of this work is dedicated to experimental methods, and instrumentation used to obtain the main results of this thesis. Chapters 3 and 4 describe specific heat and magnetic susceptibility measurements, which are tools used to analyze magnetic properties of matter into the millikelvin range. Essential details involved in calibrating the temperature of a helium dilution cryostat with resistance thermometry, paramagnetic susceptibility, and nuclear orientation, are the topic of Chapter 5.

In Chapter 6, specific heat measurements on $Dy_2Ti_2O_7$ between 340 mK and 1 K are presented, where it was discovered that this material reaches equilibrium on extremely long timescales. Evidence for this was observed in the unconventional thermal relaxation curves, which were used to obtain new results for the heat capacity and zero-point entropy. The onset of a transition at low temperature was identified, which has eluded previous work for more than two decades. The nature of this ordering transition is also discussed in the context of studies that have recently investigated its behaviour.

In Chapter 7, magnetic ac-susceptibility on $Dy_2Ti_2O_7$ between 0.5 K and 1 K is used to investigate the effect of oxygen vacancy lattice defects, on the evolution of the spin-ice transition. Magnetic properties of a crystal are compared, before and after high temperature annealing in oxygen. These results highlight the prominent features in susceptibility that are affected by subtle levels of oxygen deficiency. The conclusions are aimed at deducing which characteristics of magnetic susceptibility can be associated with lattice defects.

In Chapter 8, specific heat measurements on $Yb_2Ti_2O_7$ between 15 mK and 660 mK are used to search for evidence of unconventional excitations associated with spin-liquid behaviour. Specific heat below 100 mK exhibits a large anomaly attributed to nuclear hyperfine interactions, which is modeled and subtracted. This reveals an uncommon power-law in the specific heat $c(T) \propto T^4$, and several interpretations are discussed within the context of existing models.

In Chapter 9, specific heat measurements of $Tb_2Ti_2O_7$ between 15 mK and 1 K are presented, where the precise stoichiometry has been "stuffed" with an excess, or shortage of Tb^{3+} on the order of 0.1%. These small variations in stoichiometry have been proposed to alter the low energy state between electric quadrupole order and quantum spin liquid behaviour. Features in specific heat are found to be extremely sensitive to these variations, which is also reflected in the specific heat anomaly resulting from hyperfine interactions. The underlying electronic specific heat appears to drop exponentially below 0.1 K in two samples of nominally stuffed, and under-stuffed $Tb_{2+x}Ti_{2-x}O_{7+y}$.

Chapter 10 is a summary of all the results, highlighting the important conclusions and implications of the research presented in this thesis. The appendices summarize a number of additional projects that were carried out during this thesis, in addition to any measurements that were performed as part of a collaboration.

Acknowledgements

Colleagues at the University of Waterloo
⋆ Jan Kycia ⋆
Jeff Mason, Luke Yaraskavitch, Halle Revell Achkar, Shuchao Meng, Chris Mitchelitis, Shaoxiong Li, Cliff Plesha, Ian Andrews, Jen Reid, William Toews, Kevin Liu, Bohdan Kulchytskyy, Lauren Hayward Sirens, Giacomo Torlai, Anael Berrouet, Andrew Achkar, Behnam Javanparast, Jenny Warrington

Collaborators at McMaster University
Bruce Gaulin, Kate Ross, Edwin Kermarrec, Katharina Fritsch, Graeme Luke, Tim Munsie, Rob D'Ortenzio, Hanna Dabkowska

Collaborators at Royal Holloway University of London
Jon Goff, Gabriele Sala

Machining and electronics support
Hiruy Haile, Andrew Dube, Michael Lang, Jacek Szubra, Krunomir Dvorski

Administrative support in the department of physics and astronomy
Anja Drygala, Judy McDonnell

Notable lecturers in the department of physics and astronomy
Anton Burkov, Chris O'Donovan, Michel Gingras, Tan Dinh, Jeff Gardiner, John Vanderkooy, Hartwig Peemoeller

Committee members
Roger Melko, Rob Hill, Adam Wei Tsen, Richard Oakley, Mark Meisel

Financial support and academic hospitality
A. G. Bell Canada Graduate Scholarship Program,
NORDITA Nordic Institute for Theoretical Physics,
Perimeter Institute for Theoretical Physics

Friends and family
Bounmy Inthavong, Natalia Pomaranski, Sadeed Hasaan, Mina Fouad, Zrebiec Family

Dedication

❧ Małgorzata i Janusz ❧

Table of Contents

List of Tables

List of Figures

xiv

Part I

Background and Motivation

Chapter 1

Introduction

The goal of this chapter is to introduce some of the general concepts that describe many-body interactions on the pyrochlore lattice, with attention to three particular materials that are the focus of this thesis: $Dy_2Ti_2O_7$, $Yb_2Ti_2O_7$, and $Tb_2Ti_2O_7$, which obtain magnetic properties from their respective rare-earth ions Dy^{3+}, Yb^{3+}, and $Tb.^{3+}$. These rare-earth titanium-oxides are closely related by geometry, but their magnetic properties differ drastically at low temperatures. Starting from the concept of geometrical frustration, microscopic spin-ice models are discussed in relation to specific heat and ac-susceptibility measurements, which are the research tools used for this thesis. The conceptual ice model is generalized from its classical version that treats spins as Ising variables, to one that can support exotic features such as deconfined fractionalized excitations with an emergent U(1) gauge structure.

1.1   Geometrical Frustration

Frustration refers to the inability of a system to simultaneously satisfy all of its individual interactions. In the classical description of magnetism, spins are treated as vectors located at the vertices of a lattice, where the interactions are described by a Hamiltonian model

$$\mathcal{H} = -\sum_{\langle i,j \rangle} J_{ij} \boldsymbol{S}_i \cdot \boldsymbol{S}_j. \tag{1.1}$$

The conventional notation $\langle i, j \rangle$ represents a double summation on i and its nearest neighbours j, where the coupling energy J_{ij} is positive for ferromagnetic (FM), and negative for

antiferromagnetic (AFM) interactions. The dimensionality of the spin $\boldsymbol{S}_i$ for the Ising, XY, and Heisenberg cases is 1, 2, and 3 respectively. In the case of a two dimensional square lattice, the lowest energy ground state is trivial for both FM/AFM interactions, as shown in figure 1.1. It is easy to see how frustration can be induced by the particular geometry of the lattice. For example, in the case of AFM interactions on the triangular lattice, it is impossible to simultaneously satisfy all of the bonds on the lattice, indicated by the solid lines in figure 1.2. In this case, there are many distinct configurations with the same total energy.
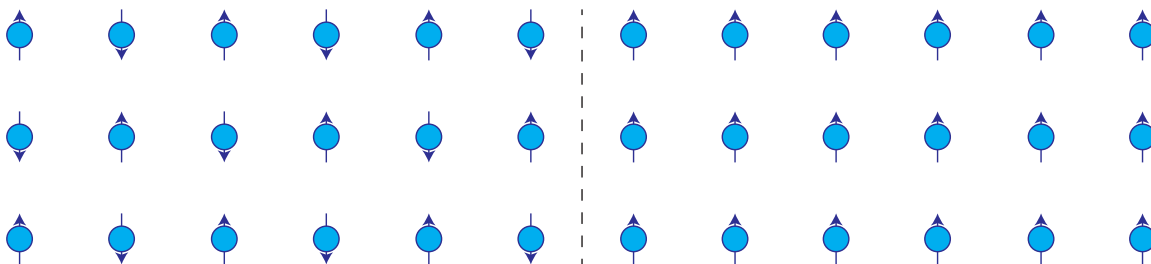
Figure 1.1: Ground state of the Ising exchange model on a square lattice with antiferromagnetic (left) and ferromagnetic exchange (right) interactions.
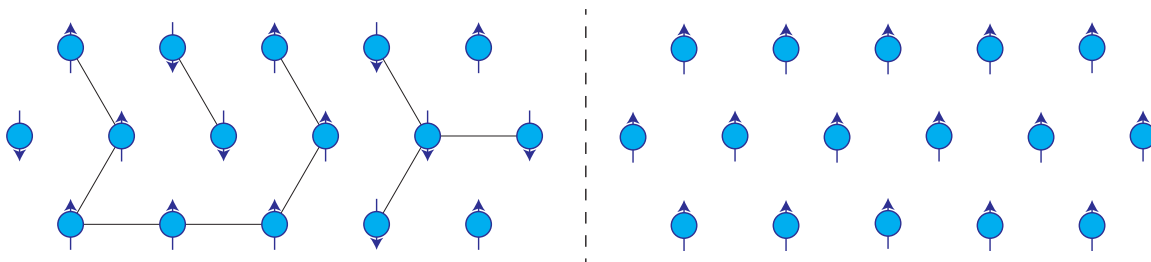
Figure 1.2: Left: The triangular lattice cannot satisfy all antiferromagnetic (AFM) interactions simultaneously. Solid lines indicate bonds that violate the AFM condition. Right: The ferromagnetic (FM) case is trivial to satisfy.

Another common type of frustration in conventional spin-glasses is induced by interactions that can vary between coupled spins. The Ruderman-Kittel-Kasuya-Yosida (RKKY) interaction is mediated by conduction electrons, and oscillates between FM and AFM depending on the distance between two spins. Another trivial example shown in figure 1.3 has FM nearest-neighbour interactions, but AFM next-nearest-neighbour interactions. In this

3

case, the square lattice is frustrated because of the mixed interactions, unlike the trivial ground state depicted in figure 1.1.
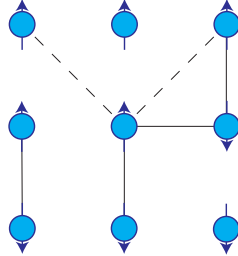
Figure 1.3: Square lattice with mixed ferromagnetic bonds between nearest neighbours, and AFM diagonal bonds. Because the system is unable to simultaneously satisfy all of the bonds indicated by a line (solid for NN-FM, and dashed for NNN-AFM), the resulting system is frustrated.

Characteristic features of magnetic ordering are often manifest as a singularity in the magnetic susceptibility or specific heat. This defines the critical temperature T_c below which magnetic ordering spontaneously arises, called the Curie temperature for a FM, or the Néel temperature (T_N) for an AFM. Susceptibility diverges as T approaches T_c according to a power law

$$\chi \propto (T - T_c)^{-\gamma}, \tag{1.2}$$

where the critical exponent $\gamma = 1$ for classical mean field (Landau) theory gives rise to the Curie-Weiss law. While this mean field approach often gives a poor description near the critical temperature, it does hold for $T \gg T_c$ in many systems. Within this approximation, the critical temperature T_c is distinguished from an elevated Curie-Weiss temperature θ, which is positive (FM) or negative (AFM) depending on the sign of J_{ij}. A convenient way to determine if a system is generally FM or AFM is by fitting the high temperature susceptibility to $\chi \propto (T - \theta)^{-1}$.
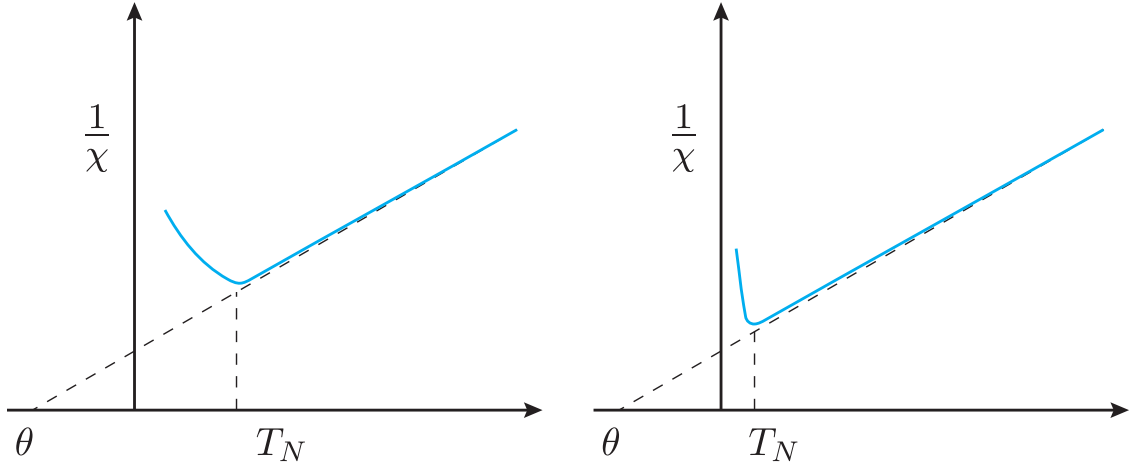
Figure 1.4: General temperature dependence of the inverse susceptibility χ^{-1} for a typical nonfrustrated antiferromagnet with $|\theta| \sim T_N$ (on the left), and for $|\theta| >> T_N$ as a criterion for frustration (on the right).

Introducing frustration to the system has the effect of suppressing magnetic ordering to lower temperatures as depicted in figure 1.4, thereby establishing the frustration criterion to determine whether a system is frustrated or not[1]

$$f = -\theta/T_c \gtrsim 10. \tag{1.3}$$

Another simple, yet powerful probe for detecting frustration in a magnetic system is through the residual entropy Δs of the magnetic specific heat c

$$\Delta s = \int_0^T \left(\frac{c}{T}\right) dT, \tag{1.4}$$

where in general for a non-frustrated magnet, the maximum entropy is $\ln(2S + 1)$ per spin for an effective spin-S system. In the presence of frustration, the ground state still contains a finite residual energy degeneracy as the system approaches zero temperature.

1.2 Ice Models

Spin-ice gets its name from an elegant analogy to water-ice, which contains a very similar type of frozen-in disorder at very low temperatures. This disorder arises because of geometrical frustration intrinsic to the crystalline structure of water-ice H_2O, which forms a tetrahedral arrangement of H-O bond directions. Analogously, magnetic moments on the pyrochlore lattice of spin-ice are constrained to point towards the center of the tetrahedral sub-structure. This analogy between water-ice and spin-ice is illustrated in figure 1.5 for a pair of adjacent tetrahedra that make up the lattice.
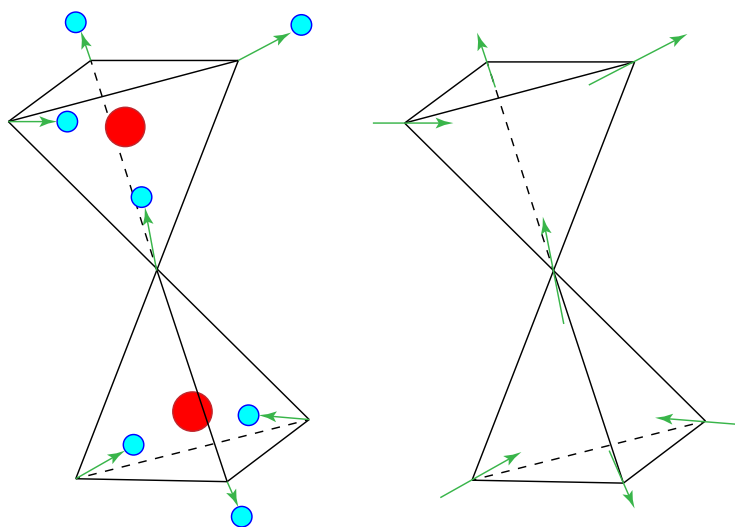
Figure 1.5: The analogy between Pauling's model of proton ordering in water ice (left) and the magnetic spin ice model (right).

It was known for some time in the early 1930's that the entropy differences between various reactions involving H_2O did not agree with the values derived from low temperature heat capacity measurements, $\int_0^T C_p d\ln T$. In 1933, Giauque and Ashley ruled out the possiblity that these discrepancies are due to inaccuracies in experimental data, and suggested that the persistent rotation of water molecules in ice below 10 K is most likely the cause.[2] Three years later Giauque and Stout did a more careful analysis of the heat capacity of water-ice from 15 to 273 K, and found that this difference in entropy is in excellent agreement with the theoretical value predicted from Pauling's model of random orientation of hydrogen bond directions in ice.[3, 4] This difference in entropy is attributed to the fact that there are multiple energetically equivalent configurations of the H-O bond directions on a single tetrahedron.

The model of spin-ice developed from studies of the compounds $Ho_2Ti_2O_7$, and $Dy_2Ti_2O_7$, where the rare-earth ions Ho^{3+} and Dy^{3+} spins have large magnetic moments ($\sim 10\mu_B$) that are constrained to point along the local $\langle 111 \rangle$ direction of the cubic unit cell, which points along the line towards the center of a tetrahedron, as shown in figure 1.5.[5, 6] The Curie-Weiss constant in both of these materials indicates the presence of ferromagnetic interactions at high temperatures, which would naïvely give rise to an ordered magnet at low temperatures. However, because of the axial anisotropy of the rare earth ion, the resulting interaction between spins is effectively antiferromagnetic, which can give rise to frustrated interactions. This point is expressed by writing a Hamiltonian for classical spin vectors $\boldsymbol{S}_i$, in terms of an effective Ising variable $S_i^z = \pm 1$ that points along the local $\langle 111 \rangle$ direction (defined here as $\hat{z}_i$)

$$\mathcal{H} = -J \sum_{\langle ij \rangle} \boldsymbol{S}_i \cdot \boldsymbol{S}_j = -J \sum_{\langle ij \rangle} \left(\hat{z}_i S_i^z \right) \cdot \left(\hat{z}_j S_j^z \right) = +\frac{J}{3} \sum_{\langle ij \rangle} S_i^z S_j^z, \tag{1.5}$$

where the product $\hat{z}_i \cdot \hat{z}_j = -1/3$ changes the sign of the exchange interaction when the spins are Ising-like.[7] When effective antiferromagnetic interactions exist between Ising variables constrained to point into or out of a single single tetrahedron, it is not possible to simultaneously satisfy the interactions between all four spins. This leads to a frustrated ground state. There exist $\binom{4}{2} = 6$ energetically degenerate spin orientations satisfying the constraint, shown in figure 1.6.
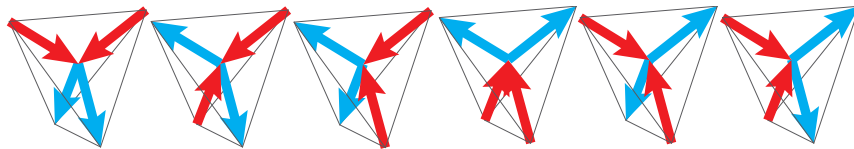
Figure 1.6: Antiferromagnetic spins on a tetrahedron constrained to point along the local $\langle 111 \rangle$ direction has 6 energetically equivalent permutations that obey this constraint.

The large-scale degeneracy of spin ice arises from the total number of equivalent microstates that satisfy the ice-rules on the pyrochlore lattice. This calculation is a common heuristic argument presented in reference [7] and takes the following approach: For a lattice with N sites, there are $N/4$ individual tetrahedra that each have 6 degenerate configurations, resulting in $6^{N/4}$ independent configurations that satisfy the ice-rules. However, because the tetrahedra are interconnected, this number is reduced by a factor proportional to the probability of a single tetrahedron satisfying the ice rules, $6/16$. Therefore, the total number of microstates on the pryochlore lattice is $\Omega \approx 6^{N/4}(6/16)^{N/4}$. It follows that the

total residual entropy per spin S/N is the natural logarithm of the number of microstates, multiplied by the Boltzmann constant k_B, yielding

$$S/N = k_B \ln \Omega = \frac{k_B}{2} \ln \left(\frac{3}{2} \right).$$

(1.6)
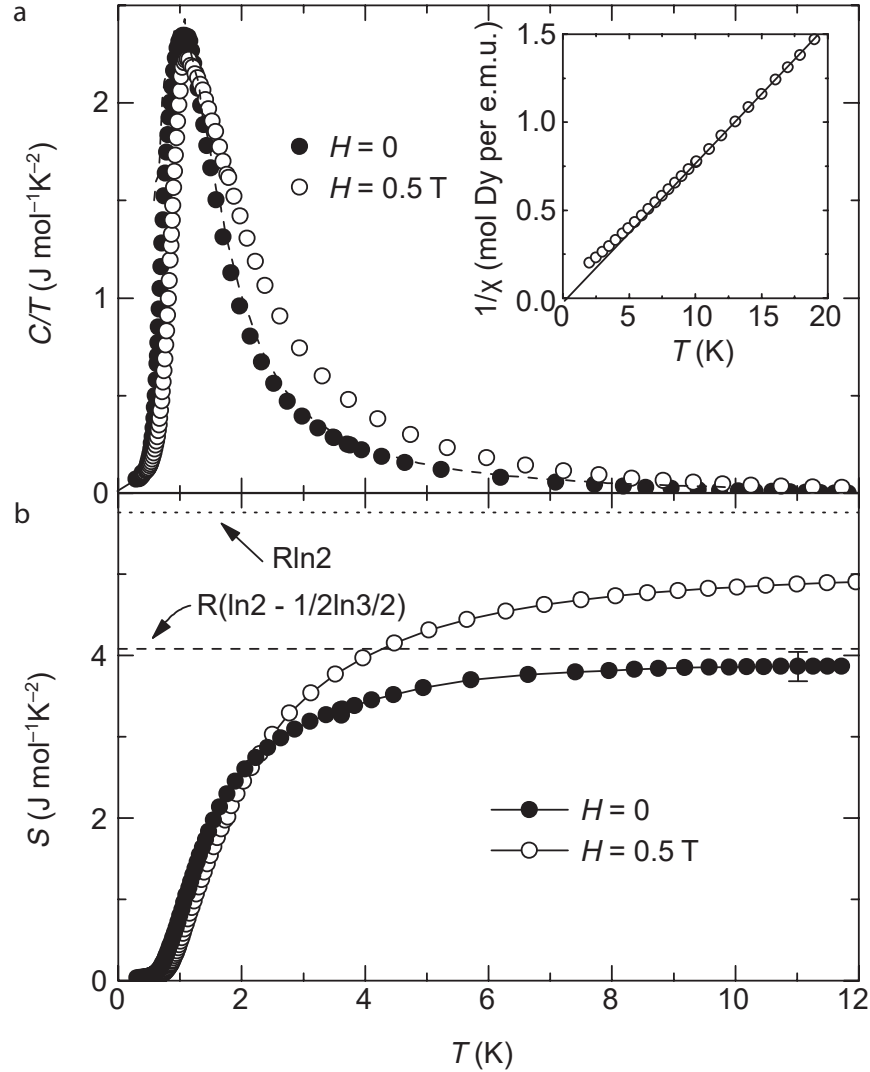
Figure 1.7: Pauling's residual entropy in $Dy_2Ti_2O_7$. The inset shows inverse susceptibility, indicating a small ferromagnetic Curie-Weiss constant $\theta \approx 1K$. Figure reproduced from reference [6] with permission.

This ground state entropy is equal to Pauling's residual entropy per proton, enforcing the analogy between water-ice and spin-ice.[3, 8] In the high temperature limit where the magnetic spins are fluctuating randomly and completely disordered, there are 2^N configurations corresponding to an entropy $k_B \ln 2$ per spin. Therefore, an experimental measurement of the entropy will capture the difference between the fully disordered, and frozen states corresponding to $\Delta S/R = \ln 2 - (1/2)\ln(3/2)$ per mole, where $R = k_B N_A$ is the gas constant and N_A is the Avogadro constant. One of the landmark experimental verifications of the spin ice model was the measurement of Pauling's residual entropy in $Dy_2Ti_2O_7$ shown in figure 1.7 where upon integrating the magnetic component of C/T from 0.2 to 14 K, one recovers the difference in entropy expected for the spin-ice ground sate.[6]

1.2.1 Long Range Dipolar Interactions

While the nearest-neighbour antiferromagnetic Ising model in equation 1.5 provides a good starting point to understand qualitative features of the classical spin-ice materials $Ho_2Ti_2O_7$ and $Dy_2Ti_2O_7$, it neglects an important contribution that arises from magnetic dipole-dipole interactions between rare-earth moments. Unlike the nearest neighbour Ising exchange interaction, the dipolar interaction is a long range interaction that decays as the inverse cube of the distance between two dipoles, r^{-3}. The classical interaction energy for two parallel neighbouring dipoles separated by a distance r_{nn} is given by

$$D = \frac{\mu_0}{4\pi}\frac{\mu^2}{r_{\mathrm{nn}}^3}, \tag{1.7}$$

which is on the order of $D \sim 1$ K in the Dy/Ho spin-ice materials. It turns out that this is the same order of magnitude as the Ising exchange interaction $J \sim 1$ K, indicating the equal importance of both interactions in the real materials. The dipolar spin-ice (DSI) model includes these interactions as well as the exchange interactions

$$\mathcal{H}_{\mathrm{DSI}} = -J\sum_{\langle ij \rangle}\boldsymbol{S}_i \cdot \boldsymbol{S}_j + Dr_{\mathrm{nn}}^3 \sum_{i>j}\left[\frac{\boldsymbol{S}_i \cdot \boldsymbol{S}_j}{|\boldsymbol{r}_{ij}|^3} - \frac{3(\boldsymbol{S}_i \cdot \boldsymbol{r}_{ij})(\boldsymbol{S}_j \cdot \boldsymbol{r}_{ij})}{|\boldsymbol{r}_{ij}|^5}\right], \tag{1.8}$$

where $\boldsymbol{S}_i$ are classical spin vectors that point along the local $\langle 111 \rangle$ axes with a local magnetic moment $\boldsymbol{\mu} = \mu\boldsymbol{S}_i$. The DSI model is often truncated to nearest neighbours (NN) only, leading to an effective exchange Hamiltonian that replaces the spins with Ising-like variables S_i

$$\mathcal{H}_{\mathrm{eff}} = J_{\mathrm{eff}}\sum_{\langle ij \rangle}S_i S_j, \tag{1.9}$$

where the effective NN exchange constant $J_{\text{eff}} = J_{\text{nn}} + D_{\text{nn}}$, accounting for the NN Ising exchange $J_{\text{nn}} = J/3$, and the effective nearest-neighbour dipole interaction, $D_{\text{nn}} = 5D/3$.[1] This simplified model successfully captures many qualitative features of the classical spin ice materials. Monte Carlo simulations of spin-ice typcially implement dipolar interactions using Ewald summation, a technique which performs sums to infinite distance rather than defining a nearest-neighbour cutoff. In order to obtain the spin-ice manifold of states, Den Hertog and Gingras concluded that the nearest neighbour exchange term in $Dy_2Ti_2O_7$ is antiferromagnetic, and spin-ice behaviour is due to long-range dipolar interactions.[9]

Because of the long-range, highly anisotropic nature of dipolar interactions, there are relatively few cases of dipolar systems that do not form long-range order. It was quite surprising when early research on spin-ice could not identify the presence of such an ordered state in these materials.[10, 9, 11] Melko *et al.*, shed some light on this conundrum with a numerical algorithm providing speedup of spin dynamics at low temperature. Their approach incorporated loop moves into the standard Metropolis Monte Carlo Algorithm, by which closed loops on the lattice such as the one shown in figure 1.8 undergo spin reversal and give rise to favourable energetic conditions. This type of excitation does not violate the 2-in, 2-out rules, and therefore has a relatively low energy cost relative to a single spin flip. The loop algorithm drastically speeds up the equilibration time in simulations, and successfully identified the true long-range ordered ground state of the dipolar spin-ice model. The simulated transition to long-range order was accompanied by a singularity in specific heat around 0.18 K, using the known exchange parameters for real spin-ice materials.[12] In much of the work that followed, it was assumed that for real materials, the spin-ice ground state is practically frozen because of extremely slow dynamics at low temperature. This point is addressed in a later chapter on experimental measurements of the spin-ice $Dy_2Ti_2O_7$.

---

[1]The sign convention is the standard one where $J > 0$ corresponds to ferromagnetic and $J < 0$ to antiferromagnetic interactions. This allows for a very simple interpretation of the ground states. For $J_{\text{eff}} > 0$, we get effective antiferromagnetic interactions, leading to the 2 in-2 out ice rules, while for $J_{\text{eff}} < 0$ (where $J < -5D$, and $D > 0$ always), there are two unique ferromagnetic ground states corresponding to 4 in and 4 out alternating tetrahedra on the two sublattices.
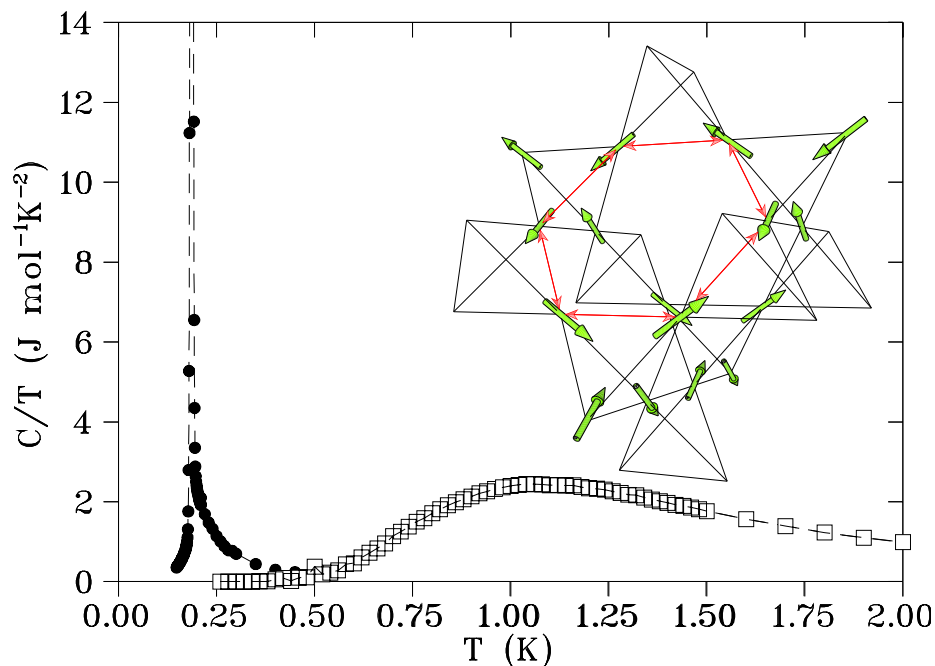
Figure 1.8: Numerical ground state configuration of the classical dipolar spin-ice model. The hexagonal loop on the lattice indicates a low-energy mode that may resonate quantum mechanically if electronic and magnetic interactions between magnetic atoms permits. The corresponding specific heat obtained with the metropolis monte carlo algorithm permits such low energy fluctuations to occur. Data reproduced from reference [12] with permission.

1.2.2 Spin Dynamics

Ac-susceptibility is the most suitable technique for characterizing the frequency response of spin-ice materials below 20 K, which respond to a broad range of magnetic signals from dc to 10^4 Hz. At higher temperatures, neutron scattering can capture the frequency range from $\sim 10^7$ to 10^{14} Hz, while muon spin relaxation can bridge the gap from $\sim 10^6$ to 10^8 Hz. It is believed that some very fast processes occurring near the resolution limit of neutrons $\sim 10^{12}$ Hz, are associated with incoherent wobble that may be attributed to hyperfine coupling, or even spin dynamics of electrons.[13, 14] Such oscillations are typically small in amplitude, and distinguished from the larger fluctuations associated with spin rotations or reversals.

Magnetic ac-susceptibility temperature scans $\chi(T)$ on $Dy_2Ti_2O_7$ shown in figure 1.9, identified peaks near 1 K and 15 K.[15, 16] This distinguishes three regions of distinct

spin relaxation behaviour: (I) a low-temperature region below 1 K, (II) an intermediate region between 1 K and 15 K, and (III) a high temperature region above 15 K. The 15 K peak is lowered in temperature with decreased driving frequency, an indication that spin dynamics slow down as the system freezes. The temperature dependence of the characteristic relaxation frequency, which is defined at the peak in $\chi'(T)$ or $\chi''(T)$ for a given temperature, is described by the common Arrhenius scaling $f = f_0 \exp[-E/T]$ with an activation energy $E \approx 200$ K.[15, 16]
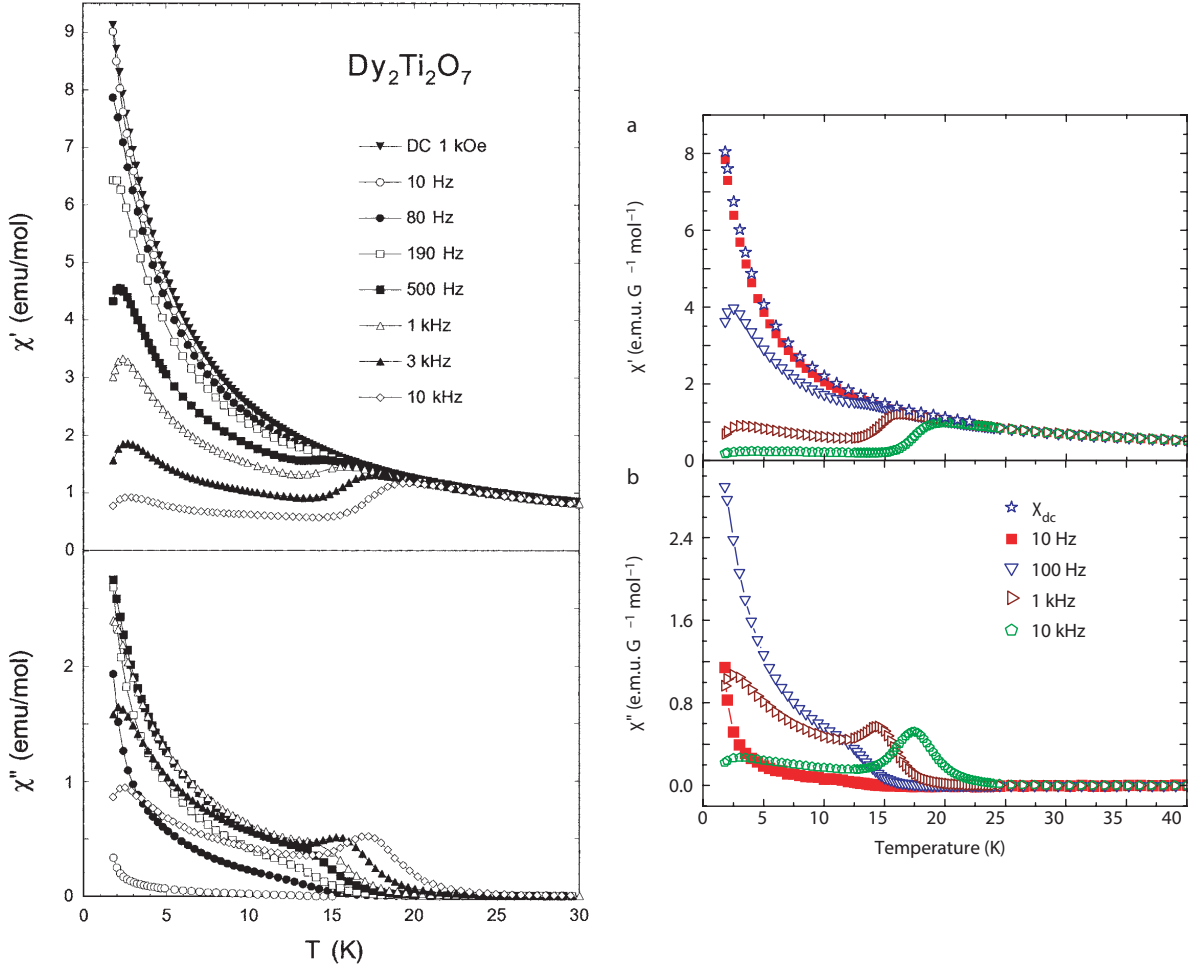
Figure 1.9: Magnetic ac-susceptibility of $Dy_2Ti_2O_7$ from 1.8 to 40 K in the audio frequency range. Figure on left reproduced from [15] with permission. Figure on right reproduced from reference [16] with permission. Both independent studies show reasonable qualitative agreement.

Similar information can be extracted from the complex frequency dependence of $\chi(\omega)$ shown in figure 1.10. The imaginary component $\chi''(\omega)$ exhibits a maximum in frequency for a given temperature, and corresponds to a spin relaxation mechanism that dissipates energy. The shape of $\chi''(\omega)$ and $\chi'(\omega)$ also contains information about the frequency distribution of relaxation modes. In the case of a single relaxation mode, the Debye distribution $\chi(\omega) = \chi_0(1 + i\omega\tau)^{-1}$ is obtained, and an Argand plot of $\chi''(\omega)$ versus $\chi'(\omega)$ has the shape

13

of a half-circle. Deviations from the Debye model are manifest as deformations in the symmetry of this half-circle. Different phenomenological models that correspond to a distribution of relaxation modes are discussed in section 4.2. For the present discussion, it is worth noting that the intermediate temperature (1 K $\lesssim T \lesssim 15$ K) modes of relaxation in $Dy_2Ti_2O_7$ are adequately captured by the generalized Davidson-Cole formalism $\chi(\omega) = \chi_0(1 + i\omega\tau)^{-\beta}$.
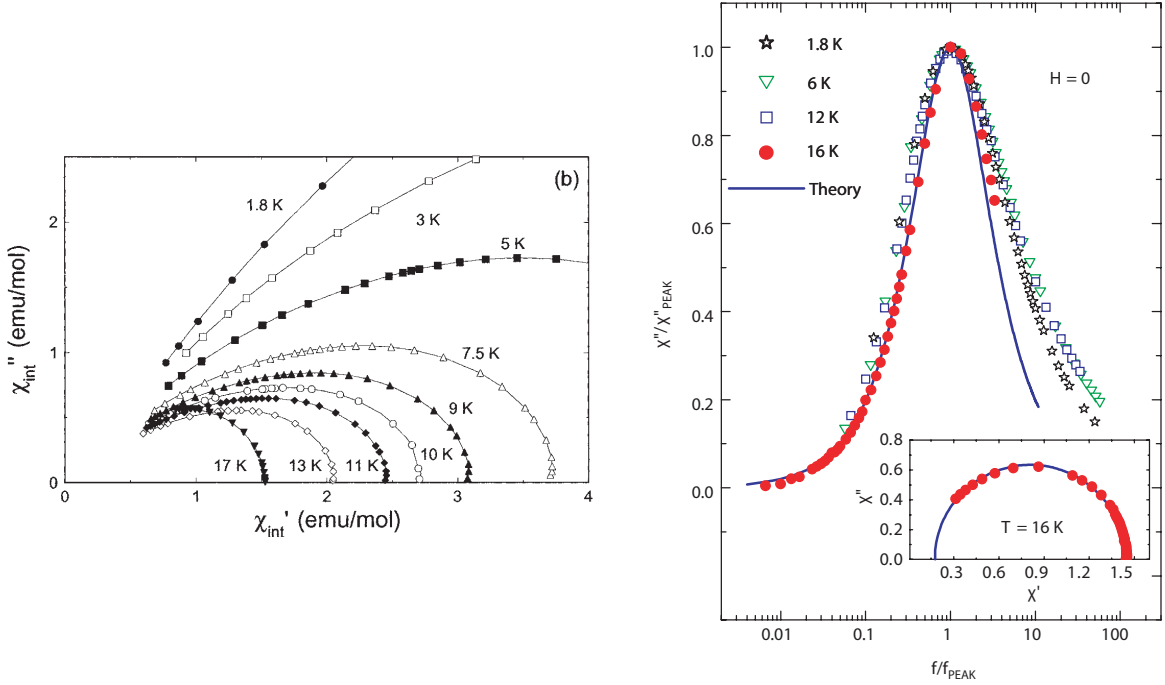
Figure 1.10: Left: Argand plots of $\chi''(\omega)$ vs. $\chi'(\omega)$, reproduced from reference [15] with permission. Right: Normalized $\chi''(\omega)$ of $Dy_2Ti_2O_7$ between 1.8 K and 17 K, reproduced from reference [16] with permission.

Neutron spin echo (NSE) is often used to obtain generalized susceptibility $\chi''(q, \omega)$, which can be compared with bulk ac-susceptibility measurements. Analogous to the spin echo from nuclear magnetic resonance, a polarized beam of neutrons undergo Larmor precession before and after interacting with the sample. The beam phase is inverted at the half-way point, allowing spins to rephase and form a "spin-echo". The change in neutron velocity imparted by the sample is detected as a loss of polarization, which is a measure of the dynamic correlation function $S(q, \omega)$. The Fourier transform of this function is then

directly proportional to the generalized susceptibility $S(q,\omega) \propto \chi(q,\omega)$. Investigations on the classical spin-ice compound $Ho_2Ti_2O_7$ distinguishes two distinct relaxation mechanisms separated near 15 K.[14] It was found that a single exponential characterizes the spin relaxation after a weak perturbation, $S(q,t)/S(q,0) = A\exp[-t/\tau(T)]$, and the activation energy exhibits thermal Arrhenius behaviour above 15 K $\tau(T) = \tau_0 \exp[-E/T]$, with $E \approx 300$ K, in agreement with the bulk ac-susceptibility measurements.[14] The process independent of neutron scattering wave-vector $\boldsymbol{q}$ indicates that the dominant relaxation mode involves only single spin reversals. This is also supported by the activation energy being close to the first set of excited crystal electric field levels near 300 K.[14, 17] In an independent study, Sutter *et al.* also measured the relaxation of $Dy_2Ti_2O_7$ down to 8 K using a less common technique of nuclear forward scattering of synchrotron radiation from the 25.65 keV resonance of ^{161}Dy nuclei, and obtained a similar value for the activation energy.[18]

Relaxation mediated through the first set of crystal field levels becomes very unlikely for $2 < T < 15$ K, due to the large activation energy. Here, the characteristic spin relaxation time $\tau(T)$ observed with ac-susceptibility, and neutron spin echo measurements, is temperature independent; characteristic of a mechanism that involves quantum spin tunneling. It is believed that tunneling between states within the ground doublet is induced by transverse couplings between the neighbouring rare-earth sites.[19] Similar processes have been suggested for Dy^{3+} systems in reference [20], and may be analogous to Mn_{12} clusters in reference [21] or the situation in $LiHoF_4$ in reference [22], where transverse fields play an important role in quantum spin tunneling.

As the spin ice ground state develops below about 1 K, the temperature independent process gradually gives way to a sharp increase in the relaxation time, corresponding to an activation of about 10 K.[23, 24, 25] These dynamics arise from the collective behaviour of correlated spins and are perhaps the least understood at this point in time. The following chapter digresses to the concept of emergent electromagnetism in spin-ice, which is a convenient description of low energy magnetic excitations that may shed some light on the origin of dynamics in this phase.

1.2.3 Fractionalization

Because magnetic moments in spin ice are constrained to point along the local $\langle 111 \rangle$ axes, its often convenient to think of each spin as contributing a net positive, or negative magnetic flux to each tetrahedron. Ising spin variables S_i, are mapped to a fictitious magnetic flux b_i, directed into, or out of each tetrahedron. Any state which obeys the 2-in, 2-out ice rule must therefore have zero net magnetic flux at its center. These flux variables are directed along the bond that joins the centers of two neighbouring tetrahedra, as shown between sites A and B in figure 1.11.
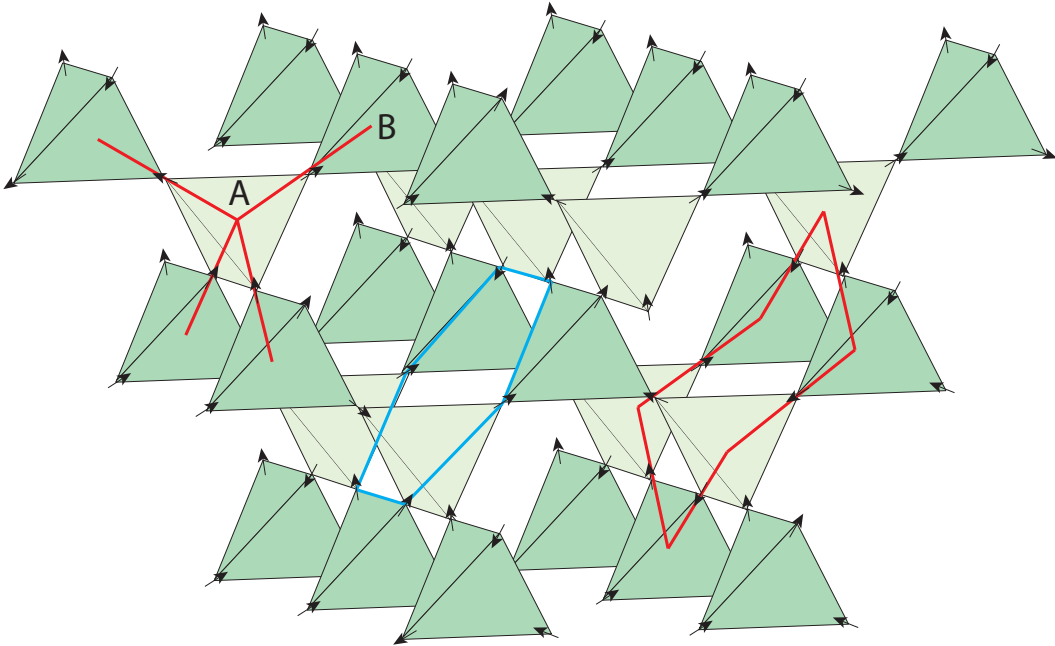
Figure 1.11: Tetrahedra on the pyrochlore lattice can be decomposed into two sublattices A/B that each define an fcc lattice. The bonds of a diamond lattice site are highlighted in the A tetrahedron. A hexagonal plaquette of the diamond lattice is highlighted in red, and in blue for the pyroclore lattice. Figure by H. M. Revell.[26]

Vertices of these bonds form a diamond lattice, and tetrahedra satisfying the spin ice rules are equivalent to a divergence-free condition

$$\sum_{i \in t} S_i^z = 0 \quad \rightarrow \quad \sum_{A \leftarrow B} b_i = \nabla \cdot \mathbf{B} = 0, \tag{1.10}$$

16

where the sum of four spins on a tetrahedron t is mapped to a sum over the directed bonds of a diamond lattice site. In the classical theory of electromagnetism, the divergence-free condition is typically associated with the absence of magnetic monopoles.[2] In the lattice-analog defined here, reversing a single spin creates a 3 in-1 out or 1 in-3 out tetrahedron, violating the divergence-free condition. At distances above the atomic length scale, this may be effectively interpreted as point magnetic source with the properties of a fictitious monopole. The adjacent tetrahedron carries a monopole of opposite charge.

The energy cost of creating a single monopole is therefore related to the cost of violating the 2 in-2 out ice condition. For the nearest neighbour spin-ice model, the energy cost of reversing a single spin is $4J_{\text{eff}}$, so the creation of a single monopole should come at a cost of approximately $2J_{\text{eff}}$. Once a pair of monopoles are created, they can move to adjacent tetrahedra via subsequent spin flips without increasing the total number of monopoles in the system. There is however, a small energy cost associated with moving these objects apart due to their mutual Coulombic interaction $-\mu_0 q_m^2 (4\pi r)^{-1}$, where q_m is the magnetic charge and μ_0 is the vacuum permeability.[27] As separation is increased, it is possible to trace the path of a "string" of dipoles aligned head to tail, with the monopole pairs at its ends. These are considered as infinitesimally thin solenoidal tubes of magnetic flux with monopole-antimonopole pairs at the ends (analogous to Dirac strings). The tension in each string is associated with the energy cost of manipulating or lengthening a string, arising from the Coulombic interaction between magnetic charges at its endpoints. At large distances, the two magnetic charges become deconfined, and can move independently with no energy cost.[27]

This description is consistent with the nearest neighbour effective exchange model, and provides a good account of the experiment from ~ 2 K to ~ 8 K where measurements observe a quasi-plateau in the magnetic relaxation time. Numerical simulations have demonstrated that the effect of this additional Coulombic interaction is to slow down diffusion through the creation of locally bound pairs, thereby increasing the relaxation timescales.[28]

---

[2]It is also possible to define this mapping in terms of an electric field ($\mathbf{E}$), which is the dual of the magnetic field ($\mathbf{B}$), but in the case of spin-ice, it is more convenient to think of these as magnetic monopoles.

1.2.4   Lattice Defects

Two common lattice defects that are known to affect the low temperature magnetic properties of spin-ice compounds are: substitutional defects known as stuffed sites, and oxygen vacancies.

Substitutional Defects

Stuffing is a type of substitutional defect on the pyrochlore lattice described by the chemical formula $R_{2+x}Ti_{2-x}O_{7-x/2}$, whereby a rare earth cation R^{3+} occupies a non-magnetic Ti^{4+} site, or vice versa. This defect is accompanied with reduced oxygen concentration in order to preserve charge balance. The effect is enhanced when ionic radii of the two cations are similar. For some lanthanide compounds with sufficiently large values of x, it leads to the formation of a completely different fluorite-type phase with the chemical formula R_2TiO_5.[29, 30]

Neutron scattering on single crystals of $Ho_{2+x}Ti_{2-x}O_{7-\delta}$ with $x \leq 0.3$ demonstrated that despite the relatively large value of x, spin-ice behaviour is preserved, and the residual entropy is consistent with the increase expected for additional paramagnetic Ho^{3+} spins on the Ti^{4+} sites.[31] One of the distinguishing features is a broadened quantum spin tunneling regime from 1 K to 40 K, which normally only covers the range from 1 K to 15 K.[32] Stuffing also has the effect of stretching the spin relaxation function $\sim \exp\left[-\left(t/\tau(T)\right)^{\beta}\right]$ where the Kohlrausch relaxation constant is $\beta \approx 0.5$ from 1.5 K to 200 K, compared with $\beta = 1$ for nominal stoichiometry. Stretched relaxation is common to a wide range of physical systems, and typically results from a distribution of relaxation times associated with glassy dynamics. For the case of stuffing in spin ice, this may be due to a random distribution of magnetic defects, or with the presence of hierarchically constrained spin dynamics where fast degrees of freedom successively constrain the slower ones.[32, 33] Qualitatively, similar effects were observed in $Dy_2Ti_2O_7$.[34] It is likely that magnetic ions on the non-magnetic sites create pathways for exchange interactions that introduce new relaxation dynamics.

Classical spin-ices $Dy_2Ti_2O_7$ and $Ho_2Ti_2O_7$ are robust to large levels of stuffing on the order $x \leq 0.3 = 15\%$.[35] These compounds have the general features of spin-ice, but this is not necessarily the case for other rare-earth compounds. For example, $Tb_2Ti_2O_7$ has shown sensitivity to very small levels of stuffing down to $x \approx \pm0.001 = \pm0.05\%$. One of the distinct features of the $x - T$ phase diagram near $x_c = -0.0025$ is the transition between a putative $U(1)$ quantum spin liquid, and quadrupolar ordered state. The latter exhibits

a sharp feature in specific heat near 0.5 K.[36, 37] Likewise, $Yb_2Ti_2O_7$ has variations in the sharpness and position of a sharp peak in specific heat near 0.2 K, that have also been correlated with very small levels of stuffing $x \gtrsim 0.01 = 0.5\%$.[38, 39] These correlations are believed to originate from the expansion or contraction of the lattice when a rare earth cation takes the place of a Ti^{4+} cation. Rietveld refinements of neutron and x-ray diffraction data are commonly used to identify the small changes in cubic lattice parameter $a(x)$ that result from small changes in the stuffing x. To give perspective, stuffing at the level of $x = \pm 0.01$ can result in deviations of lattice parameter on the order of ± 0.001 Å, from a typical value of 10 Å. Lattice parameters can be obtained at room temperature as indicators of stoichiometry before proceeding to more time consuming characterizations at low temperatures.[39, 38, 37]

There is no doubt that a great deal of variability observed between experiments is correlated with stuffing. Even small levels of stuffing (0.05%) previously thought to be negligible can affect the magnetic properties of rare earth titanates at sufficiently low temperatures. This suggests that the features of magnetic ordering are very delicate to perturbations caused by defects or impurities. In some materials this is significant, while in other cases the manifestations of disorder are negligible.

Oxygen Vacancies

The second common defect relevant to rare earth pyrochlores arises with oxygen deficient stoichiometries. Shortage of O^{2-} results in the chemical formula $R_2Ti_2O_{7-\delta}$, where charge compensation is fulfilled by the transformation of Ti^{4+} to Ti^{3+}. This reduction of Ti^{4+} causes it to acquire a magnetic moment, known as quenched orbital magnetism. Two distinct types of oxygen vacancies can be distinguished on the pyrochlore lattice: O(1) sites occupy the interior position of a rare-earth tetrahedron, while O(2) sites form a scalenohedron surrounding the magnetic ion.

Figure 1.12 depicts a portion of the pyrochlore lattice and demonstrates the effects of an O(1)-site oxygen vacancy on the magnetic properties of the rare-earth ions. There are two important consequences of an O(1) oxygen vacancy. When a negatively charged oxygen ion is removed, the surrounding positively charged Dy^{3+} ions experience an increased Coulomb repulsion, resulting in an expansion of the tetrahedral structure. This oxygen vacancy changes the symmetry of the crystal field, which changes the anisotropy of the Dy^{3+} ions from Ising like, to xy-like. The second consequence of an oxygen vacancy, is the reduction of two Ti^{4+} atoms to Ti^{4+}, which compensates for the loss of negative charge. This change in electronic structure produces a magnetic moment on the Ti site, which normally is non-magnetic.
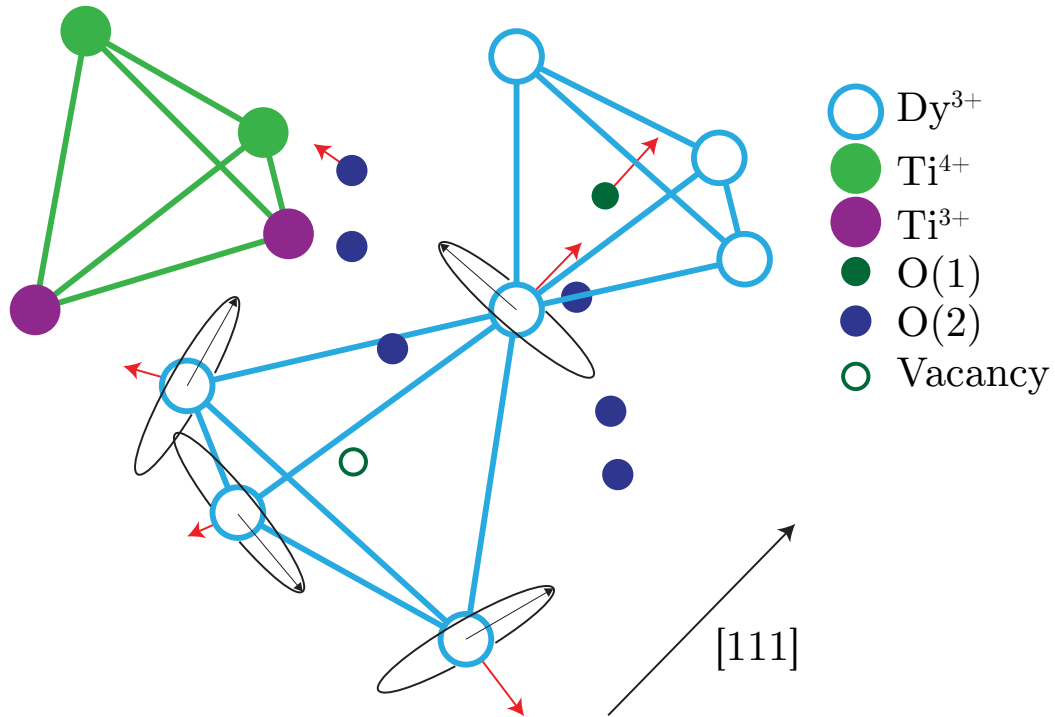
Figure 1.12: Position of two distinct oxygen sites: O(1) and O(2) in spin-ice materials ($Dy_2Ti_2O_7$ shown). An O(1)-site vacancy expands the tetrahedral structure and changes the magnetic isotropy of surrounding rare-earth ions. Two neighbouring titanium sites are reduced to compensate for charge imbalance. Figure interpreted from reference [40] with permission.

Sala *et al.* developed a model of O(1) oxygen vacancies that qualitatively reproduces the main features of diffuse neutron scattering in $Y_2Ti_2O_7$. The Y^{3+} ions are non-magnetic, making this compound a good candidate to study the magnetism Ti^{3+} sites in the absence of a large field contribution from the otherwise magnetic rare-earth ions. They found that the Y^{3+} ions surrounding an O(1) vacancy at the center of a rare-earth tetrahedron experience an increased Coulomb repulsion, resulting in an effective expansion of the tetrahedral cage. Meanwhile, oxygen atoms occupiying neighbouring O(2) sites are pushed towards the Ti^{4+} ions, converting two of these to Ti^{3+} in order to preserve charge balance. Crystal electric field calculations indicate that an O(1) vacancy changes the easy-axis ⟨111⟩ anisotropy of surrounding rare earth ions to easy-plane type.[40]

1.3 Quantum Ice Models

This section describes general features of a quantum spin liquid (QSL) state without mathematical rigor. This phase of matter is often associated with (I) a very large degree of quantum entanglement between spins on a lattice, that (II) do not exhibit features associated with classical magnetic ordering. Rather vaguely, (I) is defined as a long range entangled state that cannot be transformed into a direct product of local states ($|\Psi\rangle = \otimes_i |\psi\rangle_i$) with local unitary transformations. (II) is intereseting because QSL's are predicted to support the existence of non-local excitations known as spinons, which are spin excitations that behave as fractions of magnons or spin waves.[41]

For many years, the conventional method to describe ordering in matter was based on the Landau theory of phase transitions, which identifies changes in symmetry of a particular property of the system.[42] In the late 1980's it was realized that a theory based on symmetry breaking cannot explain the behaviour of spin liquids,[3] and later the notion of topological order was introduced to explain order beyond the symmetry description.[45, 46]

Resonating Valence Bonds

Conceptual origins of a QSL are attributed in part to P. W. Anderson, who proposed resonating valence bonds (RVB) as an alternate ground state to classical Néel antiferromagnet, for the spin$-\frac{1}{2}$ triangular lattice Heisenberg antiferromagnet.[47] The conceptual ingredients of a resonating state have origins in Pauling's idea of resonating valence bond theory, and is also a common approach used to describe compounds in quantum-organic chemistry (eg. valence-bonds in aromatic compounds).[48]

The basic idea is that neighbouring pairs of spins form singlet dimers $|\uparrow\downarrow - \downarrow\uparrow\rangle/\sqrt{2}$ in order to lower the ground state energy. There are a small number of exactly solvable quantum spin models. The Majumdar-Ghosh model is one that provides a simple example of the valence-bond solid (VBS) state.[49] The Hamiltonian of this model has nearest, and next-nearest neighbour interactions

$$\mathcal{H} = J \sum_i \boldsymbol{S}_i \cdot \boldsymbol{S}_{i+1} + \frac{J}{2} \sum_i \boldsymbol{S}_i \cdot \boldsymbol{S}_{i+2}, \tag{1.11}$$

where $\boldsymbol{S}_i$ is a quantum spin$-\frac{1}{2}$ operator. The ground state of this Hamiltonian has two equivalent ground states in which neighbouring pairs form singlet dimers. The Majumdar-

---

[3]In particular the chiral spin state.[43, 44]

Ghosh wavefunction is a product of singlet wavefunctions for each pair

$$|\psi\rangle = 2^{-N/2}|(\uparrow\downarrow - \downarrow\uparrow)(\uparrow\downarrow - \downarrow\uparrow)\cdots(\uparrow\downarrow - \downarrow\uparrow)\rangle, \qquad (1.12)$$

is illustrated in figure 1.13. Quantum spin liquids can arise in frustrated magnets with low spin$-S$, where strong quantum fluctuations are sufficient to destroy conventional long-range order.
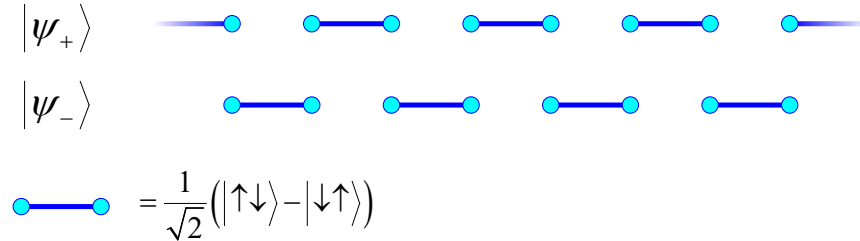
Figure 1.13: Resonating valence bond state on the Majumdar-Ghosh Heisenberg antiferromagnetic spin chain. The model has two gapped, degenerate ground states, which are dimerized states with dimers on even and odd links.

1.3.1   Quantum Liquids in Spin$-\frac{1}{2}$ Pyrochlores

The quantum spin-ice model introduces quantum fluctuations between spins on the pyrochlore lattice. These models were originally studied in the limit of strong easy-axis exchange anisotropy, where it was demonstrated that there exists a fractionalized spin liquid with an emergent $U(1)$ gauge structure.[50] The emergent spinons are analogous to gapped electric and magnetic charges, and a gapless photon. Magnetic charges are gapped with an energy $2\Delta \sim J_{zz}$, the cost of a spin flip out of the mainfold of spin-ice states. The origin of the dual electric charge is less intuitive, understood as gapped topological excitations arising from a wave packet of ice configurations with suitably chosen phases.[51] Finally, the photons responsible for Coulombic interactions between the elementary charges are gapless excitations with linear energy dispersion for small wave vector $\boldsymbol{k}$, $\omega = c|\boldsymbol{k}|$, where c is the speed of light corresponding to the fictitious photon that mediates the interaction between emergent electrons and monopoles.

Quantum effects have been observed in various spin-ice compounds including $Yb_2Ti_2O_7$, $Tb_2Ti_2O_7$, $Er_2Ti_2O_7$, $Tb_2Sn_2O_7$, $Pr_2Sn_2O_7$, $Pr_2Ir_2O_7$, and each of the rare-earth ions have unique properties that can be classified by the irreducible representations of the D_{3d} local

symmetry group.[4] The single-ion ground states correspond to the following irreducible representations of this symmetry group.[52]

Γ_4 pseudospin doublet

In the simplest case, the ground state wavefunction is a doublet state that is protected by time-reversal. Recall Kramers theorem, which states that for a Hamiltonain that obeys time reversal symmetry $[\mathcal{H}, \mathcal{T}] = 0$, where $\mathcal{T}$ is the time-reversal operator, all its eigenstates are at least twofold degenerate.

$$|\pm\rangle = \alpha|\pm\frac{1}{2}\rangle + \beta|\mp\frac{5}{2}\rangle + \ldots \tag{1.13}$$

The effective spin operators (S_x, S_y, S_z) represent magnetic dipoles, with a net magnetic moment given by

$$\boldsymbol{\mu}_i = \mu_B[g_\pm(\boldsymbol{x}_i S_i^x + \boldsymbol{y}_i S_i^y) + g_z \boldsymbol{z}_i S_i^z], \tag{1.14}$$

which transforms the same way as spin$-\frac{1}{2}$ under the symmetries of the pyrochlore lattice. Examples of this representation are the single-ion ground states of $Yb_2Ti_2O_7$, and $Er_2Ti_2O_7$.

E_g non-Kramers doublet

This state is not protected by time-reversal

$$|\pm\rangle = \alpha|\pm 4\rangle + \beta|\pm 1\rangle + \ldots \tag{1.15}$$

The S_z operator transforms as a magnetic dipole, while the S_x, S_y operators transform as electric quadrupoles. The magnetic moment is therefore produced by S_z only

$$\mu_i = \mu_B g_z S_i^z \boldsymbol{z}_i. \tag{1.16}$$

Examples are $Ho_2Ti_2O_7$, and $Tb_2Ti_2O_7$.

---

[4]This includes a C_3 axis (local z), C_2 axis (local y), and an inversion center, due to the local symmetry of the crystalline electric field at the rare-earth site.

$\Gamma_5 \oplus \Gamma_6$ dipolar-octupolar doublet

The irreducible representation $\Gamma_5 \oplus \Gamma_6$, is connected by time-reversal

$$|\pm\rangle = \alpha|\pm\frac{3}{2}\rangle + \beta|\mp\frac{9}{2}\rangle + \dots \tag{1.17}$$

This state is conceptually more complex, because the S_x and S_z operators transform like magnetic dipoles along the local $z-$axis, while S_y is invariant under all D_{3d} symmetries, and transforms like a magnetic octupole. An example is $Dy_2Ti_2O_7$.

Pseudospin$-\frac{1}{2}$ XXZ model

One starting point to study quantum spin-ice is to consider the rare-earth atoms which possess ground state doublets that can be modeled as effective spin$-\frac{1}{2}$ objects on the pyrochlore lattice. Projecting the superexchange Hamiltonian into the space of doublets, gives rise to the effective model[53, 54]

$$\mathcal{H}_{QSI} = \sum_{\langle ij \rangle} J_{zz}\mathsf{S}_i^z\mathsf{S}_j^z - J_\pm \left(\mathsf{S}_i^+\mathsf{S}_j^- + \mathsf{S}_i^-\mathsf{S}_j^+ \right) + J_{\pm\pm} \left(\gamma_{ij}\mathsf{S}_i^+\mathsf{S}_j^+ + \gamma_{ij}^*\mathsf{S}_i^-\mathsf{S}_j^- \right)$$
$$+ J_{z\pm} \left[\mathsf{S}_i^z \left(\zeta_{ij}\mathsf{S}_j^+ + \zeta_{ij}^*\mathsf{S}_j^- \right) + \left(\zeta_{ij}\mathsf{S}_i^+ + \zeta_{ij}^*\mathsf{S}_i^- \right) \mathsf{S}_j^z \right], \tag{1.18}$$

where the sum is over all nearest neighbour sites i and j on the pyrochlore lattice. The pseudospin operators S_i^z are proportional to the magnetic moment along the local $\langle 111 \rangle$ axis, and $\mathsf{S}_i^x, \mathsf{S}_i^y$, to the in-plane components of the magnetic dipole moment for the Kramers case.[5] The phase diagram of this Hamiltonian was investigated using a novel gauge theory formulated in terms of slave-rotors by Savary *et al.*, and is shown in figure 1.14.[57] They studied the problem for $J_{\pm\pm} = 0$ and $J_z > 0$, and found two exotic phases: a $U(1)$ quantum spin liquid (QSL), and a Coulomb ferromagnet (CFM), in addition to the generic ferromagnetic (FM) and antiferromagnetic (AFM) phases. The Coulomb ferromagnetic phase with fully ordered moments, is viewed as a polarized version of the $U(1)$ QSL, and also supports deconfined spinons.

In order to identify this phase with experiment, it is common to look for signatures of the spinons and photons. Inelastic neutron scattering can identify the presence of fractionalized spinons,[54, 58] or look for the linear dispersion ($\propto \omega$) in the low-energy limit, which normally diverges ($\propto \omega^{-1}$) in the case of a spin-wave.[57] This photon dispersion should also appear as $c \propto T^3$ in the low-temperature specific heat, something that was predicted for $Yb_2Ti_2O_7$, and was the focus of chapter 8.

---

[5]In the non-Kramers case, the latter are proportional to the quadrupole moment as a result of time reversal invariance.[55, 56]
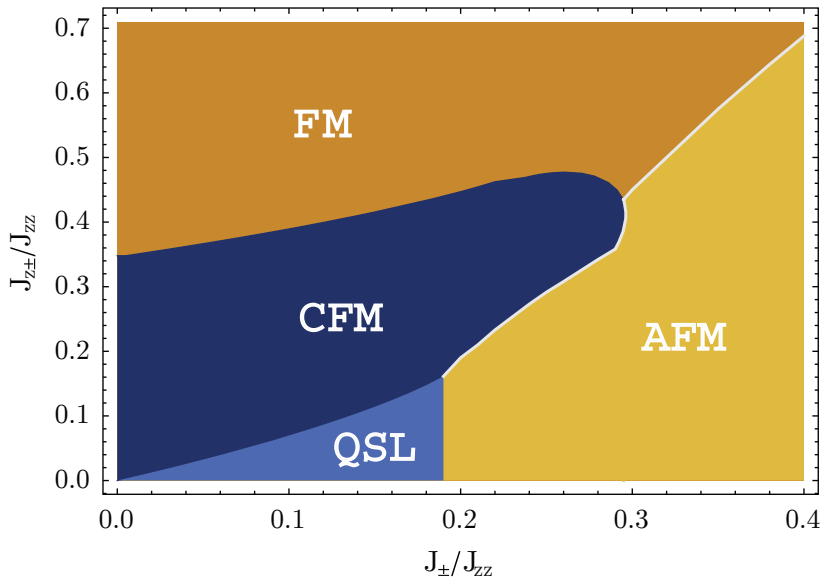
Figure 1.14: Phase diagram for the quantum spin-ice hamiltonian in equation 1.18 obtained for $J_{\pm\pm} = 0$ and $J_{zz} > 0$ using gauge mean field theory. Figure reproduced from reference [57] with permission.

1.4 Ytterbium Titanate Yb$_2$Ti$_2$O$_7$

A good starting point to discuss the magnetic properties of ytterbium titanate Yb$_2$Ti$_2$O$_7$, is to consider the electronic ground state of an isolated Yb^{3+} ion. As for all the insulating rare earth pyrochlore titanate oxides, the Yb^{3+} ion is surrounded by a scalenohedron of O^{2-} atoms that produce a crystal field with D$_{3d}$ symmetry. Under the symmetry of this crystal field, the eight-fold degenerate $^2F_{7/2}$ electronic ground state of the Yb^{3+} ion is split into four Kramers doublets. For Yb$_2$Ti$_2$O$_7$, the ground state is given by

$$|\pm\rangle = \alpha \left|\pm\frac{1}{2}\right\rangle + \beta \left|\pm\frac{5}{2}\right\rangle + \gamma \left|\pm\frac{7}{2}\right\rangle, \tag{1.19}$$

with $\alpha \approx -0.9283$, $\beta \approx \pm 0.0866$ and $\gamma \approx \pm 0.3616$.[59] This consists primarily of $m_J = \pm 1/2$, confirmed by a variety of experimental and theoretical investigations. [60, 61, 62, 59] The lowest ground doublet is separated from the first excited state by about 600 to 900 K, which can be ignored at low energies. This justifies the effective spin$-\frac{1}{2}$ description that is commonly adopted for this system. The g-tensor components $g_z \approx 2$ and $g_{||} \approx 4$ indicate a strong tendency for the magnetic moments to have planar XY anisotropy in the local $\langle 111\rangle$

basis.[60, 63, 64] Despite the highly anisotoropic $g-$tensor, the dominant exchange interaction in the material is in fact Ising-ferromagnetic, implying that the ordered Yb moment lies primarily along the local $\langle 111 \rangle$ direction with magnitude $\approx 1\mu_B$.[64, 53, 65, 66, 54, 67] It follows that the magnetic dipole interaction is significantly reduced in comparison to the classical spin ices ($Dy_2Ti_2O_7$ and $Ho_2Ti_2O_7$), which have large classical moments $\sim 10\mu_B$. Quadrupole moments do not exist in the atomic ground state doublet (eq'n 1.19).[53] The dominant interaction in $Yb_2Ti_2O_7$ results from a strong superexchange between Yb $4f$ orbitals via neighbouring O $2p$ orbitals.

Ferromagnetic Ordering and Persistent Dynamics

An abundance of experimental evidence indicates that $Yb_2Ti_2O_7$ undergoes ferromagnetic ordering below the specific heat transition ~ 270 mK. There is also significant support for residual fluctuations below this temperature, which may seem to contradict an ordered ferromagnetic state. Magnetic Bragg reflections observed with neutron scattering that are indicative of long range ferromagnetic order, have been observed by some authors,[63, 68, 69] while others have presented evidence for persistent spin dynamics below the ordering transition.[70, 71, 58] One picture of the ground state corresponding to splayed-ferromagnetic order of the type shown in figure 1.15 was obtained from a magnetic neutron diffraction pattern.[72]
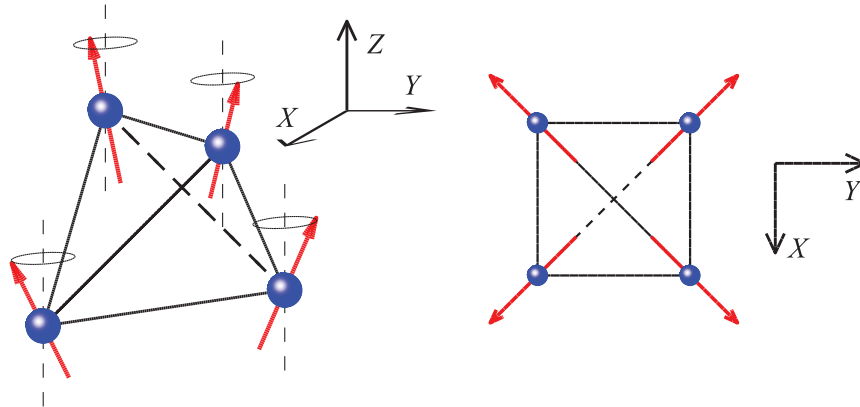
Figure 1.15: Magnetic structure of $Yb_2Ti_2O_7$ inferred from magnetic neutron diffraction. Figure reproduced from reference [72] with permission.

Muon spin resonance (μSR) measurements by various groups have also observed somewhat contradictory results regarding the presence of spin fluctuations and long-range order.

In one of the studies, there is almost no temperature dependence to the muon spin relaxation below the ordering transition, and therefore no evidence for long-range order or frozen spin dynamics.[73] In the other independent study, there is a strong indication that the magnetic moments are static below the ordering transition.[69] The $Yb_2Ti_2O_7$ samples in both of these reports exhibit nearly identical features in the low temperature specific heat, but the μSR measurements are completely different. It is difficult to attribute these differences as a sample dependence issue, since the features in specific heat are known to be excellent indicators of sample quality, and yet the μSR results could not be more different.

Suscpetibility and magnetization measurements also support the picture of a first order transition that exhibits hysteresis in the magnetization. This transition is accompanied by the development of a spontaneous ferromagnetic moment that is not fully saturated, supporting the picture that there is a fluctuating component present in the material.[74]

Specific Heat

Typically, an ordered ferromagnet which is gapped will display an exponenial drop in specific heat below the ordering transition. The existence of low energy magnetic excitation should be reflected in the specific heat. For example, according to spin wave theory, the ferromagnetic Heisenberg Hamiltonian has low temperature specific heat $\sim T^{3/4}$. The $U(1)$ quantum spin liquid model should have gapped spinons at high temperature (monopoles and electrons). At low temperatures, it should be governed by gapless photons that give rise to cubic $\sim T^3$ specific heat. Therefore, considering all of the controversy surrounding the ground state properties of $Yb_2Ti_2O_7$, it is obvious that the specific heat is an absolutely critical component to constructing a complete picture of this unique material.

Numerous experimental and numerical investigations of the low temperature specific heat of $Yb_2Ti_2O_7$ exist in the literature. Magnetic spin correlations become apparent in the specific heat below approximately 10 K, where the T^3 phonon contribution has almost vanished, and the zero-field specific heat exhibits a broad Schottky anomaly centered around 2 K. At temperatures well above the magnitude of exchange interactions ≈ 1 K, the material behaves as a paramagnet. Numerical studies of the effective spin$-\frac{1}{2}$ anisotropic exchange quantum spin-ice model [equation 1.18] quantitatively reproduce the main features of the 2 K Schottky anomaly.[67, 75, 76] These results, derived from 4th order numerical linked cluster (NLC) expansion with Euler extrapolations were limited to 700 mK due to computational complexity.[67] Classical Monte Carlo simulations fail to capture this 2 K anomaly, indicating the role of quantum effects in this feature. More recent calculations based on the finite temperature Lanczos method (FTLM) on a 32-site cluster of spins reached even lower temperatures, and reproduced qualitative features of

the ferromagnetic ordering transition observed by experiment.[76] The numerical results are compared in figure 1.16.
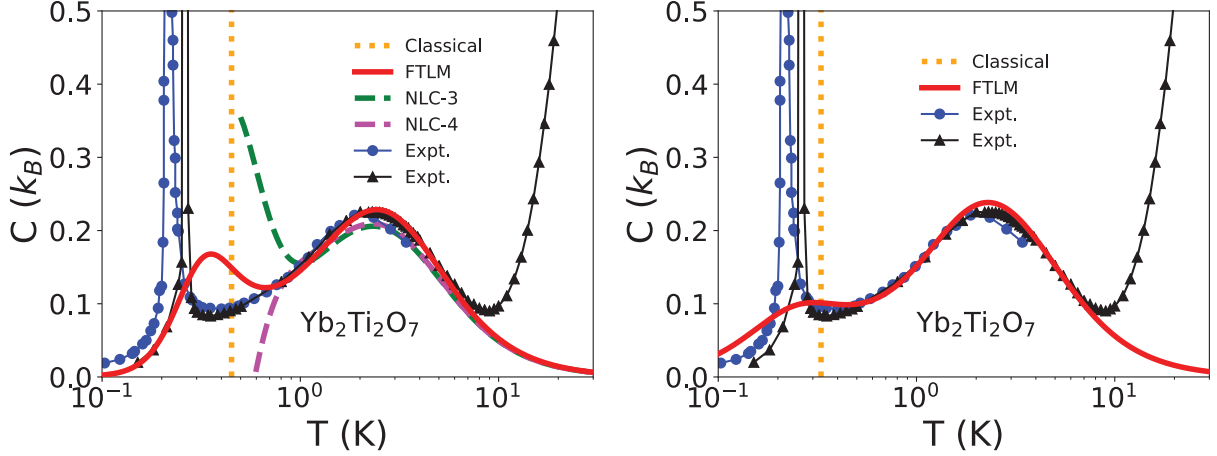
Figure 1.16: $Yb_2Ti_2O_7$: Comparison of heat capacity from numerical simulations with the finite temperature Lanczos method (FTLM)[76], the numerical linked cluster (NLC) expansion to 3rd and 4th order,[67] and experiment (blue circles,[77] and black triangles[38]). In the figure on the left, FTLM calculations were done using the exchange parameters from reference [54], while those on the right are from reference [78]. Both figures reproduced from reference [76] with permission.

Multi-Phase Competition

The low temperature ground state doublet should be well represented by a pseudospin$-\frac{1}{2}$ effective exchange model. The nearest neighbour Hamiltonian can be represented by four independent coupling constants J_i after accounting for the symmetry of the pyrochlore lattice

$$\mathcal{H} = \sum_{\langle ij \rangle} \vec{S}_i \bar{\mathcal{J}}_{ij} \vec{S}_j \qquad \bar{\mathcal{J}} = \begin{pmatrix} J_2 & J_4 & J_4 \\ -J_4 & J_1 & J_3 \\ -J_4 & J_3 & J_1 \end{pmatrix} \tag{1.20}$$

where $\bar{\mathcal{J}}_{ij}$ are related by cubic rotations. These exchange parameters can be identified with XY (J_1), Ising (J_2), symmetric off-diagonal (J_3) and Dzyaloshinskii-Moriya (J_4) like interactions.[54, 79, 80] The relevant parameters in the case of $Yb_2Ti_2O_7$ (as well as $Er_2Ti_2O_7$ and $Er_2Sn_2O_7$) are $J_3 < 0$, $J_4 = 0$, which results in a competition between

four different type types of order: Palmer-Chalker (Ψ_4), noncollinear ferromagnet (FM), coplanar antiferromagnet (Ψ_3), and noncoplanar antiferromagnet (Ψ_2).[80] The phase diagrams corresponding to the Hamiltonian in equation 1.20 were obtained for classical, and quantum linear spin wave theory, shown in figure 1.17.[80] The finite temperature phase diagram, outlined by the white circle, was obtained using classical Monte Carlo simulations. These illustrations indicate, using the parameters of reference [54], that $Yb_2Ti_2O_7$ has a low temperature ground state with noncollinear splayed ferromagnetic order, which is consistent with several neutron scattering results.[69, 81, 82, 83] However, an outstanding puzzle that has not been resolved is the observation of a gapless continuum in contrast to the expectation of a finite gap associated with coherent spin waves. Given the proximity of $Yb_2Ti_2O_7$ to the phase boundary between the FM and Ψ_3 phases, it has been proposed that the presence of competing phases may explain its behaviour at low temperatures.[79] It has been proposed that this may also explain the rod-like features observed with neturon scattering, indicative of dimensional reduction and anisotropic exchange interactions.[80, 84, 58, 54, 66, 85]
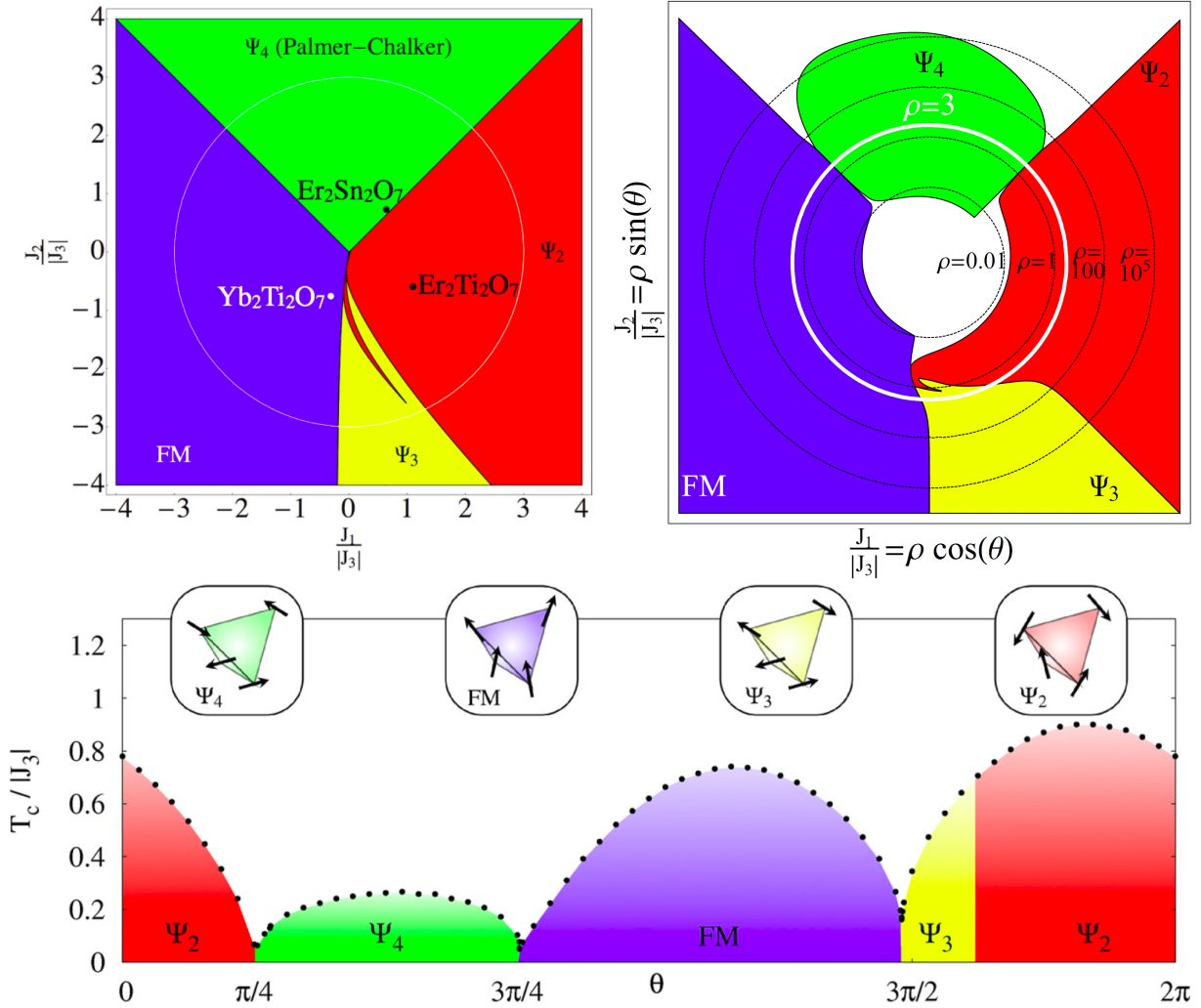
Figure 1.17: Top Left: Classical ground state phase diagram [equation 1.20] for nearest neighbour interactions, symmetric off-diagonal exchange $J_3 < 0$ and no Dzyaloshinskii-Moriya interaction $J_4 = 0$. Top Right: Quantum fluctuations suppress the classical order. White regions indicate where linear spin wave theory predicts suppression of conventional LRO. The axes are plotted on a log-polar scale with $0 < \rho \lesssim 10^6$. The lower figure shows the trace indicated by the white circle in the upper figure. All three figures were reproduced from reference [80] with permission. Estimates published for $Yb_2Ti_2O_7$,[54] $Er_2Ti_2O_7$,[86] and $Er_2Sn_2O_7$[87].

1.5 Terbium Titanate $Tb_2Ti_2O_7$

An intriguing feature of the Tb pyrochlore $Tb_2Ti_2O_7$ is the absence of detectable conventional long-range ordering as low as 50 mK, despite a negative Curie temperature ($\theta_p \sim -19$) indicating antiferromagnetic exchange interactions.[88, 89]

If one neglects the axial distortion of oxygen surrounding the Tb^{3+} ion and assumes cubic symmetry, then crystal field theory within the point charge approximation predicts that the lowest energy levels for Tb^{3+} consist of a Γ_3 singlet, a nonmagnetic Γ_2 doublet and a $\Gamma_5^{(2)}$ triplet. Adding trigonal distortion as a perturbation only splits the $\Gamma_5^{(2)}$ triplet into a singlet and a doublet.[90] Neutron spectroscopic studies of the crystal field excitations in $Tb_2Ti_2O_7$ confirm that the Γ_3 ground doublet is dominated by $|m_J = \pm 4\rangle$ components, with $|m_J = \pm 5\rangle$ in the first excited state.[91] This suggests significant Ising anisotropy along the local $\langle 111 \rangle$ direction. There is evidence of mixing with other states because the first excited doublet is separated from the ground doublet by about 18 K. This is relatively low in comparison to the classical Ising systems (Dy, Ho) that are on the order of 300 K.[92]

An effective quantum pseudospin$-\frac{1}{2}$ model provides a good account of the behaviour of local magnetic doublets in the pyrochlore oxides in zero field: [55]

$$\begin{aligned}
\mathcal{H} =& J_{nn} \sum_{\langle \boldsymbol{r}, \boldsymbol{r}' \rangle} \left[\sigma_{\boldsymbol{r}}^z \sigma_{\boldsymbol{r}'}^z + 2\delta(\sigma_{\boldsymbol{r}}^+ \sigma_{\boldsymbol{r}'}^- + \sigma_{\boldsymbol{r}}^- \sigma_{\boldsymbol{r}'}^+) + 2q(e^{2i\phi_{\boldsymbol{r},\boldsymbol{r}'}} \sigma_{\boldsymbol{r}}^+ \sigma_{\boldsymbol{r}'}^+ + \text{h.c.}) \right] \\
&+ D r_{nn}^3 \sum \left[\frac{\boldsymbol{e}_{\boldsymbol{r}}^z \cdot \boldsymbol{e}_{\boldsymbol{r}'}^z}{|\boldsymbol{r} - \boldsymbol{r}'|^3} - \frac{3[\boldsymbol{e}_{\boldsymbol{r}}^z \cdot (\boldsymbol{r} - \boldsymbol{r}')][\boldsymbol{e}_{\boldsymbol{r}'}^z \cdot (\boldsymbol{r} - \boldsymbol{r}')]}{|\boldsymbol{r} - \boldsymbol{r}'|^5} \right] \sigma_{\boldsymbol{r}}^z \sigma_{\boldsymbol{r}'}^z,
\end{aligned} \tag{1.21}$$

where the second term is the dipolar interaction. For a non-Kramers magnetic doublet, the in plane pseudospin operators σ_i^x, σ_i^y are associated with quadrupole moment $\sim \{J_i^\pm, J_i^z\}$, a result of time-reversal invariance. This is in contrast to the Kramers case (Yb^{3+}, Nd^{3+}, Er^{3+}), where the in-plane components of pseudospin are proportional to the magetic dipole moment and there is no quadrupole moment. Classical mean-field calculations have shown that there are two distinct electric quadrupole long range ordered phases, the planar antiferropseudospin (PAF), and planar ferropseudospin (PF) phases, which are in close proximity to the spin ice (SI) phase, which is replaced by a $U(1)$ quantum spin liquid phase in the presence of quantum fluctuations.[55] The corresponding phase diagram is shown in figure 1.18. Early experimental and theoretical considerations of $Tb_2Ti_2O_7$ made observations of short range correlations at very low energies down to 50 mK, [88] which was attributed with dynamical behaviour associated with quantum effects.[93] Historically, the interpretation of numerous experimental works has been problematic, due to sample dependence attributed to small levels of off-stoichiometry in the form of $Tb_{2+x}Ti_{2-x}O_{7+y}$,
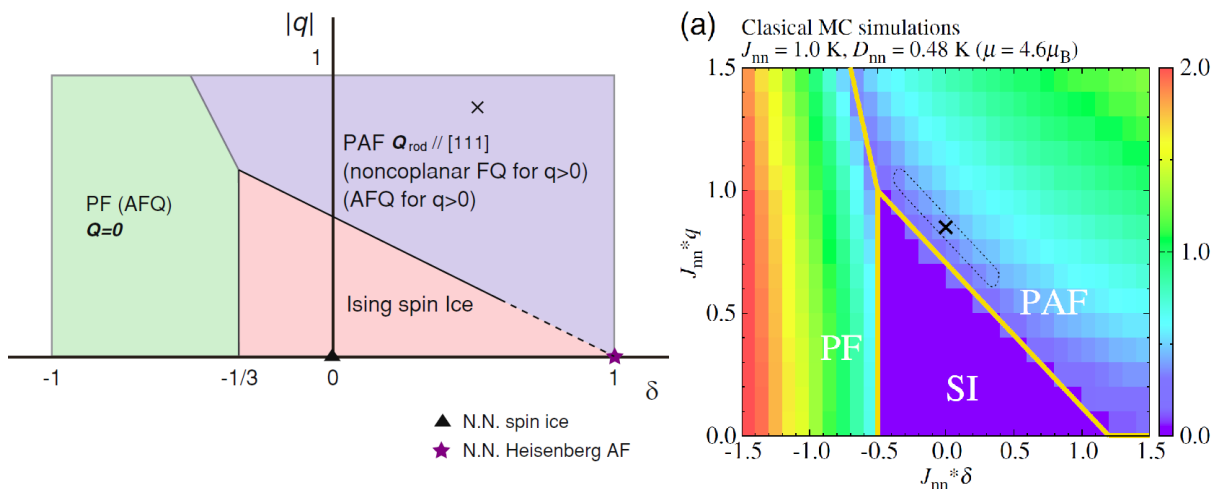
Figure 1.18: Classical mean field phase diagram of the effective quantum pseudospin $1/2$ Hamiltonian from reference [55] (left) and with specific parameters for $Tb_2Ti_2O_7$ from reference [96] (right). Both figures reproduced with copyright permission.

where $-0.01 < x < 0.01$ is even common in nominally stoichiometric samples.[94, 36] Within this range, an ordering peak is typically observed with specific heat from 0.4 to 0.5 K, where this phase transition has also been correlated with other measurements including magnetic susceptibility, inelastic neutron scattering, neutron spin echo, and muon spin resonance.[95, 72, 94, 89, 96, 36, 97]

Specific heat measurements on $Tb_2Ti_2O_7$ show significant differences among samples below 2 K. The measurements on polycrystalline samples have generally produced more consistent results, displaying a peak in the specific heat between 0.35 to 0.5 K, indicating the presence of a phase transition. Variations in the peak position were correlated with the non-stoichiometry of polycrystalline $Tb_{2+x}Ti_{2-x}O_{7+y}$, by adjusting the mass ratio of the two starting materials Tb_4O_7, and TiO_2, relative to the nominal value of $x = 0 \pm 0.002$, as illustrated in figure 1.19.[36] The investigation established that the non-stoichiometry parameter, x, is correlated to the lattice constant of $Tb_{2+x}Ti_{2-x}O_{7+y}$, as well as the position of the specific heat peak in temperature. Their hypothesis was that there is a critical value $x > x_c$ whereby the ground state of the system undergoes long range order, while for $x < x_c$, the ground state is consistent with a spin-liquid state. The specific heat and hypothetical phase diagram from this reference is shown in the inset in figure 1.19. The magnetization measurements observed a very weak anomaly in the vicinity of the temperature that the specific heat peak was observed for sample with $x = 0$ and ± 0.005. Inelastic neutron

scattering on the $x = 0.005$ $(> x_c)$ sample in that reference also showed the opening of a gap in the magnetic excitation spectrum below T_c, indicating an ordered phase.
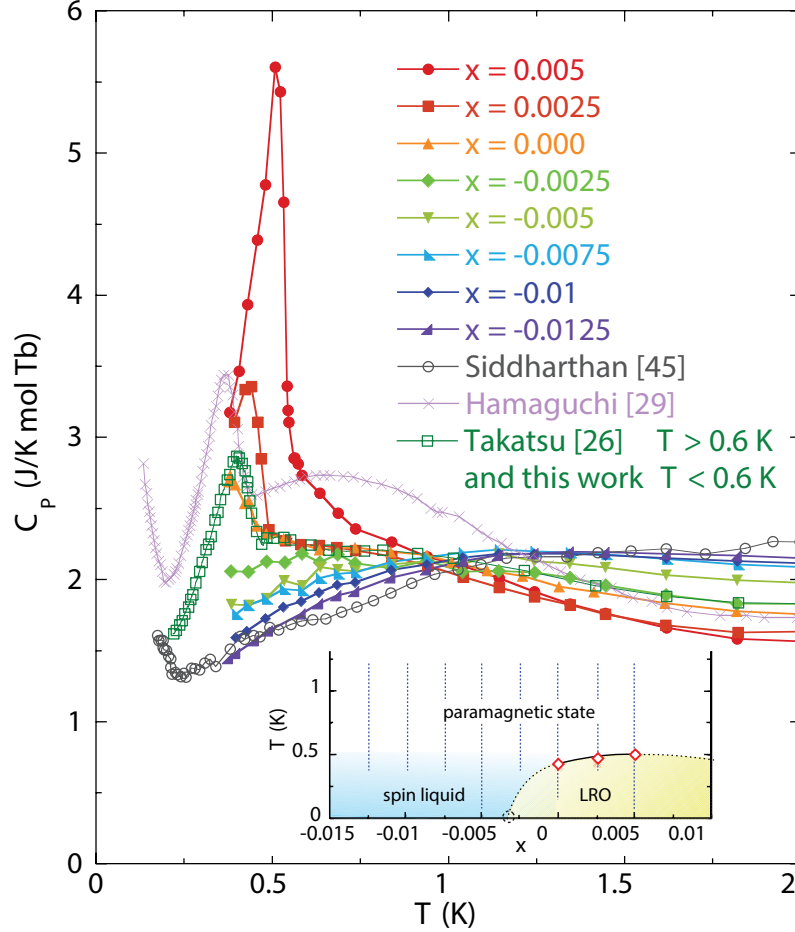
Figure 1.19: Specific heat measurements of $Tb_{2+x}Ti_{2-x}O_{7+y}$ for various nominal values of x. Figure reproduced from reference [36] with permission.

Subsequent work was done on a single crystal of $Tb_2Ti_2O_7$ grown with the floating zone method. This resulted in a gradient along the length of the rod that is correlated with the non-stoichiometry parameter, x.[37] Portions of the sample were cut at different lengths, then characterized with x-ray diffraction, and specific heat measurements. The measurements revealed that the lattice constant diverges from ideal stoichiometry, and that the peak associated quadrupolar ordering disappears abruptly below $x = x_c \simeq -0.0025$.

Chapter 2

f-Orbital Physics

Magnetism of atoms can be derived from three dominant sources: intrinsic spin of unpaired electrons, angular momentum of electrons orbiting the nucleus, and intrinsic nuclear spin of unpaired nucleons. (I) Each electron carries intrinsic spin angular momentum $\boldsymbol{s} = \frac{1}{2}$ with a magnetic moment approximately equal to one Bohr magneton $\mu_B = -9.27 \times 10^{-24}$ [J/T]. (II) The orbital angular momentum of an electron surrounding an atom is given by the cross product of its momentum and position $\boldsymbol{l} = \boldsymbol{r} \times \boldsymbol{p}$, and the corresponding dipole moment is given by $\mu_l = -g_L \mu_B \hbar^{-1} \boldsymbol{l}$, where g_L is the electron orbital $g-$factor (III) The nuclear magnetic moment is primarily due to the nucleons, which have intrinsic spin$-\frac{1}{2}$ derived from elementary quarks and gluons. The magnetic moment of a proton is $\mu_p = 2.79\mu_N$ and a neutron is $\mu_n = -1.91\mu_N$, where $\mu_N \approx 5.05 \times 10^{-27}$ [J/T] is the nuclear magneton. Note that the electrons magnetic moment is typically much larger than that of a nucleon $\mu_N/\mu_B \approx 10^3$.

The magnetism associated with $4f$ orbitals arises in the elements Ce, Pr, Nd, Pm, Sm, Eu, Gd, Tb, Dy, Ho, Er, Tm, Yb and Lu. These electrons experience a broad energy range of interactions, depicted roughly by the temperature scale

hyperfine   exchange   crystal-field   spin-orbit   coulomb

10^{-2} 10^{-1} 10^{0} 10^{1} 10^{2} 10^{3} 10^{4} 10^{5} $[^{o}K]$
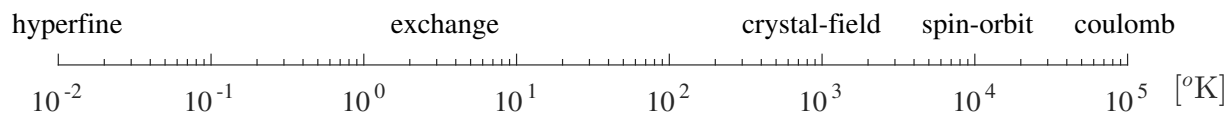
The separation of these energy scales with little overlap makes the $4f$ series highly desirable for the study of many-body exchange interactions at low temperatures. Overlapping

34

energy scales are more common among the transition metals (d−block). The phenomena concerning this thesis is relevant below ~ 1 K, where exchange and hyperfine interactions are concerned. The Hamiltonian describing an isolated $4f$ ion is commonly treated a sum of parts that are separated in energy

$$\mathcal{H} = \mathcal{H}_{\text{spin}} + \mathcal{H}_{\text{orbital}} + \mathcal{H}_{\text{nuclear}}, \tag{2.1}$$

corresponding to the orbital motion of electrons surrounding the nucleus, the electronic spin degrees of freedom, and the complete description of nuclear hyperfine structure. In the following chapters we will consider each of these contributions with more detail.[1]

2.1   Coulomb

The orbital potential is the largest term in equation 2.1, accounting for the Coulomb forces, and kinetic motion experienced by the electrons surrounding a nucleus. For an N-electron atom with nuclear charge Z, the concise form of this time-independent Hamiltonian is

$$\mathcal{H}_{\text{orbital}} = -\frac{\hbar^2}{2m_e} \sum_i^N \nabla_i^2 + \sum_i^N \sum_{j \neq i}^N \frac{e^2}{|\boldsymbol{r}_i - \boldsymbol{r}_j|} + \sum_i^N \frac{Ze^2}{|\boldsymbol{r}_i|}, \tag{2.2}$$

where the first term is the kinetic potential energy $\hat{T}_e$, the second term is the electron-electron Coulomb repulsion $\hat{V}_{ee}$, and the third term is the Coulomb attraction between electrons and the nucleus $\hat{V}_{eN}$, treated here as a point source with no internal structure. This treatment is valid as a first order approximation because the energy splitting for nuclear hyperfine interactions is small compared to the other terms considered here. Hyperfine interactions are considered with more detail in section 2.5. The remaining problem to be solved for the free atom is the time-independent Schrodinger equation

$$\left[\hat{T}_e + \hat{V}_{ee} + \hat{V}_{eN} \right] \Psi = E\Psi, \tag{2.3}$$

where $\Psi = \Psi(\boldsymbol{r}_1, \boldsymbol{r}_2, ..., \boldsymbol{r}_N)$ is the N-electron wavefunction. Due to the gross number of variables that appear in such an equation for a multi-electron atom, an exact analytic solution is not available, and a numerical solution requires a heavy amount of computation. Fortunately, there are simplifying approximations and group-theoretical arguments

---

[1]The information presented throughout this chapter has input from various sources including Refs. [98, 99],...

regarding the symmetry of the Hamiltonian and its solutions. These approximations fall under the category known as self-consistent field methods, and commonly include: (I) The Born-Oppenheimer approximation, which treats the motion of electrons as independent of a heavy stationary nucleus. This approximation was already implicit in the orbital Hamiltonian in equation 2.2, where the nucleus was treated as a point source of charge Z. The hyperfine interactions capture these effects (section 2.5). (II) Relativistic effects are neglected in the kinetic energy operator. These arise in the Dirac equation, and have an important contribution to spin-orbit coupling in the rare-earths (section 2.2). (III) If it is assumed that that the motion of each electron is independent of the rest, then the corresponding wavefunction can be written as a product of individual electronic wavefunctions, known as the Hartree product

$$\Psi(\boldsymbol{r}_1, \boldsymbol{r}_2, \ldots, \boldsymbol{r}_N) = \phi_1(\boldsymbol{r}_1)\phi_2(\boldsymbol{r}_2)\cdots\phi_N(\boldsymbol{r}_N). \tag{2.4}$$

The Pauli exclusion principle dictates that this wavefunction is anti-symmetric under exchange of any two electrons

$$\phi_i(\boldsymbol{r}_j)\phi_j(\boldsymbol{r}_i) = -\phi_i(\boldsymbol{r}_i)\phi_j(\boldsymbol{r}_j), \tag{2.5}$$

which is generalized to N electrons by the Slater determinant. With these simplifications (I-III), the variational principle is then applied to equation 2.3, which minimizes the energy of Ψ, and leads to a set of N Hartree equations

$$\left[-\frac{\hbar^2}{2m}\nabla_i^2 + V_i(\boldsymbol{r}_i)\right]\phi_i(\boldsymbol{r}_i) = E_i\phi_i(\boldsymbol{r}_i), \tag{2.6}$$

where the electrostatic potential

$$V_i(\boldsymbol{r}_i) = -\frac{Ze^2}{r_i} + e^2\sum_{j\neq i}\int d^3r_j \frac{|\phi_j(\boldsymbol{r}_j)|^2}{|\boldsymbol{r}_i - \boldsymbol{r}_j|}, \tag{2.7}$$

of electrons orbiting the nucleus requires a self-consistent solution such that each ϕ_i depends on every ϕ_j. The first term in this equation is the static electron-nuclear interaction, and the second term is the average electrostatic electron-electron repulsion. An important simplification results if $V_i(\boldsymbol{r}_i)$ is spherically symmetrical, and therefore invariant under rotations. The corresponding eigenfunctions of equation 2.6 transform according to the irreducible representation of the full rotation group, justifying the spherical harmonic representation basis. The eigenfunctions for each electronic orbital is given in spherical coordinates as

$$\phi_i(\mathbf{r}_i) = i^l R_{nl}(r)Y_l^{m_l}(\theta_i, \varphi_i), \tag{2.8}$$

where n is the principal (or radial), l the orbital (or azimuthal), and m_l the magnetic quantum numbers. These make up the particular electronic configuration of equation 2.4; commonly specified by the notation: $nx^{\#e}$, where $x = s, p, d, f, g, h, \ldots$ correspond with $l = 0, 1, 2, 3, 4, 5, \ldots$, and the superscript is used to denote the number of electrons occupying the shell. From these arguments alone, one might expect a state Ψ consisting entirely of $1s$ orbitals; however, this is prevented by the Pauli exclusion principle which does not allow electrons to share quantum numbers. For example, the first stable $4f$ electron appears for atom $Z = 58$ in Ce, where the complete configuration is given by $1s^2 2s^2 2p^6 3s^2 3p^6 3d^{10} 4s^2 4p^6 4d^{10} 5s^2 5p^6 6s^2 5d^1 \boldsymbol{4f^1}$. The number of electrons increases in the rare earth series: Pr, Nd, Pm, Sm, Eu, Gd, Tb, Dy, Ho, Er, Tm, Yb, up to Lu which has the configuration $[\text{Xe}]6s^2 5d^1 \boldsymbol{4f^{14}}$. The azimuthal variation of a $4f$ wavefunction is depicted in figure 2.1.
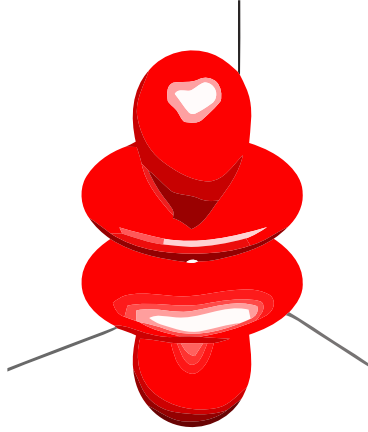
Figure 2.1: Azimuthal variation of a $4f_0$ orbital.

In order to obtain the energy levels of $\mathcal{H}_{\text{orbital}}$, it is common to solve a simpler Hamiltonian, and apply perturbation theory as a first order correction. Consider the central self-consistent field (cscf) Hamiltonian

$$\mathcal{H}_{\text{cscf}} = -\frac{\hbar^2}{2m} \sum_i \nabla_i^2 + \sum_i V_i(\boldsymbol{r}_i), \tag{2.9}$$

where $V_i(\boldsymbol{r}_i)$ is specified in equation 2.7 (and we are still assuming that it is spherically symmetrical). Notice that this Hamiltonian contains most of the information about the problem: the kinetic energy term, the static electron-nuclear interaction, and the averaged electron-electron interaction term contained in the $V_i(\boldsymbol{r}_i)$. Eigenfunctions of $\mathcal{H}_{\text{cscf}}$ depend

on n_i and l_i, and are all degenerate as a result of the invariant Hamiltonian under separate rotations of individual electron coordinates. Now consider the electrostatic (es) repulsion between electrons separately

$$\mathcal{H}_{\mathrm{es}} = \mathcal{H}_{\mathrm{orbital}} - \mathcal{H}_{\mathrm{cscf}}, \tag{2.10}$$

as a perturbation that splits the energy levels of $\mathcal{H}_{\mathrm{cscf}}$. This term couples the angular momenta of individual electrons and captures the residual behaviour not accounted for by the cscf-approximation. $\mathcal{H}_{\mathrm{cscf}}$ contains most of the inter-electronic repulsion energy, including the average spherical part (i.e., without angular dependence) so that the effect of $\mathcal{H}_{\mathrm{es}}$ is small enough to be treated as a perturbation. Before we can apply $\mathcal{H}_{\mathrm{es}}$ as a perturbation, we refer back to the total free atom Hamiltonian in equation 2.1 to note that there are other terms relative to $\mathcal{H}_{\mathrm{orbital}}$ which should also be considered as perturbations. The spin Hamiltonian $\mathcal{H}_{\mathrm{spin}}$ contains the relativistic spin-orbit (so) interaction that couples electron spin with electron oribtal angular momentum. Therefore, we must decide which perturbation to apply first: $\mathcal{H}_{\mathrm{es}}$ (LS-coupling), or $\mathcal{H}_{\mathrm{so}}$ (jj-coupling). LS-coupling is usually appropriate for light atoms, while jj-coupling is more applicable to heavy atoms where the individual coupling between electrons via the spin-orbit interaction is stronger than the electrostatic repulsion between them. This is demonstrated with more detail in section 2.2. Finally, there are a few intermediate cases where neither approximation is appropriate, and the effect of $\mathcal{H}_{\mathrm{es}} + \mathcal{H}_{so}$ has to be treated together as a perturbation. That is the subject of the next chapter.

Notice that $\mathcal{H}_{\mathrm{orbital}}$ is invariant under rotation of all $\boldsymbol{r}_i$ coordinates simultaneously, and therefore it should transform according to the group representation

$$D^{(l_1)} \times D^{(l_2)} \times \cdots \times D^{(l_N)} = \sum D^{(L)}, \tag{2.11}$$

The resulting eigenfunctions are $(2L+1)$-fold degenerate with L given by equation 2.11, and can be decomposed with coefficients specified by Wigner or Clebsch-Gordan coupling coefficients defined by

$$\sum_{m,m'} (ll'mm'|LM)\phi_m\phi_{m'}. \tag{2.12}$$

2.2 Spin-Orbit

We now consider the spin dependent part $\mathcal{H}_{\text{spin}}$ contained in the total Hamiltonain for a free atom, $\mathcal{H}$ in equation 2.1 as the next important term in the configuration of atomic energy levels. It is considered a perturbation that splits the atomic orbitals discussed in the previous section; which captures the largest energy contributions to $\mathcal{H}$. This spin Hamiltonian has several contributions. Perhaps the most intuitive is the spin-spin coupling that results from the magnetic dipole-dipole interaction between electron spins

$$\mathcal{H}_{\text{ss}} = \sum_i \sum_{j \neq i} \left[\frac{\boldsymbol{s}_i \cdot \boldsymbol{s}_j}{|\boldsymbol{r}_{ij}|^3} - \frac{3(\boldsymbol{s}_i \cdot \boldsymbol{r}_{ij})(\boldsymbol{s}_j \cdot \boldsymbol{r}_{ij})}{|\boldsymbol{r}_{ij}|^5} \right]. \tag{2.13}$$

Another term comparable in magnitude is due to magnetic interactions arising from electron currents. This does not produce many important effects, and is usually neglected. The major contribution to $\mathcal{H}_{\text{spin}}$ originates from a relativistic effect in the Dirac equation that produces an interaction between spin- and orbital-angular momentum of electrons (spin-orbit coupling). Consider a semi-classical electron moving with velocity $\boldsymbol{v} = \boldsymbol{r}/m$ in a spherically symmetric nuclear potential $V(r)$. Its motion generates an effective magnetic field

$$\boldsymbol{B} = \boldsymbol{E} \times \frac{\boldsymbol{v}}{c^2} = \left(-\frac{\boldsymbol{r}}{er} \frac{dV}{dr} \right) \times \frac{\boldsymbol{p}}{mc^2} = -\frac{1}{mec^2} \left(\frac{1}{r} \frac{dV}{dr} \right) \boldsymbol{l}, \tag{2.14}$$

resulting in an interaction between this magnetic field $\boldsymbol{B}$, and the magnetic moment of the electron spin $\boldsymbol{\mu} \approx e\boldsymbol{s}/m_e$, which has an energy

$$U_{\text{so}} = -\boldsymbol{\mu} \cdot \boldsymbol{B} = \frac{1}{m_e^2 c^2} \left(\frac{1}{r} \frac{dV}{dr} \right) \boldsymbol{l} \cdot \boldsymbol{s} = f(r) \boldsymbol{l} \cdot \boldsymbol{s}. \tag{2.15}$$

It is worth noting that if the potential generated by the nucleus is approximately Coulombic $V(r) \sim Z^* r^{-1}$, where Z^* is the effective nuclear charge seen by electrons, then the average radial dependence of U_{so} scales as $\langle f(r) \rangle \propto \frac{Z^*}{r^3} \propto \frac{(Z^*)^4}{(n^*)^6}$, implying that spin-orbit coupling is most important for heavy atoms with small diameter $Z^* >> r$. This explains why jj-coupling becomes important for heavy atoms, as mentioned in section 2.1. For multiple electrons in an atom, the spin-orbit Hamiltonian is given by

$$\mathcal{H}_{\text{so}} = \sum_i \xi(r_i) \boldsymbol{l}_i \cdot \boldsymbol{s}_i, \tag{2.16}$$

where the sum includes only the electrons outside the last closed orbital, and

$$\xi(r_i) = \frac{1}{2m^2 c^2} \frac{1}{r_i} \frac{dV}{dr_i}. \tag{2.17}$$

Neglecting the less important terms mentioned earlier, this Hamiltonian sufficiently describes splitting of atomic orbitals with perturbation theory. Terms such as $\boldsymbol{l}_i \cdot \boldsymbol{s}_i$ are no longer invariant under rotations of orbital and spin separately, but they are invariant under simultaneous rotation. Therefore, group theory dictates that the eigenfunctions of $\mathcal{H}_{\text{orbital}} + \mathcal{H}_{\text{spin}}$ must transform according to the representation

$$D^{(L)} \times D^{(S)} = \sum D^{(J)}, \tag{2.18}$$

where $J = L + S, L + S - 1, \ldots, |L - S|$. The individual sub-shell wavefunctions can be written as

$$\Psi(LSM_LM_S) = \sum_{m_l m_s} (LSM_LM_S | m_l m_s) \psi(m_l m_s). \tag{2.19}$$

Applying the Wigner-Eckhart theorem, the spin-orbit Hamiltonian can also be expressed succinctly as

$$\mathcal{H}_{\text{so}} = \zeta_{LS} \boldsymbol{L} \cdot \boldsymbol{S}, \tag{2.20}$$

where the spin-orbit coupling constant is given by

$$\zeta_{LS} = \pm \frac{\pi}{m^2 c^2 S} \int r R_{4f}^2(r) \frac{dv}{dr} dr, \tag{2.21}$$

with $+$ and $-$ corresponding to sub-shells that are less and more than half filled, respectively. The energy splitting is obtained with first order perturbation theory

$$\begin{aligned}
E_1 &= E_0 + \langle LSJm_J | \mathcal{H}_{\text{so}} | LSJm_J \rangle \\
&= E_0 + \zeta_{LS} \langle LSJm_J | \boldsymbol{S} \cdot \boldsymbol{L} | LSJm_J \rangle \\
&= E_0 + \zeta_{LS} \langle LSJm_J | \frac{1}{2} \boldsymbol{J}^2 - \boldsymbol{L}^2 - \boldsymbol{S}^2 | LSJm_J \rangle \\
&= E_0 + \frac{\zeta_{LS}}{2} \left[J(J+1) - L(L+1) - S(S+1) \right],
\end{aligned} \tag{2.22}$$

and the spacing between subsequent levels reduces to the Landé interval rule

$$\Delta E = E(J) - E(J - 1) = \zeta_{LS} J . \tag{2.23}$$

Due to orbital pairing, inner shell electrons do not produce a net magnetic moment. In many cases, the electronic ground state can be obtained through a convenient set of guidelines known as Hund's rules. According to these rules, the Pauli exclusion principle requires that two fermions (electrons) cannot share the same set of quantum numbers (n, l, m_l, m_s). Pairing of electrons in the same subshell (m_l) is unfavourable due to Coulomb repulsion; and furthermore, they experience less shielding from the nucleus in the close presence of another electron. The most favorable conditions occur when the total spin quantum number is maximized.

The Origin of Hund's Rule

Hund's rule also states that for a given electronic configuration, the one with unpaired spins is lower in energy than if the electrons are paired.

Start by considering a wavefunction which the includes spatial and spin co-ordinates of a single electron $\Psi_i = \phi_i \chi_i$, where ϕ_i is the spatial coordinate, and χ_i is the spin coordinate. A simplified model of the Hartree-Fock energy for a nucleus with N electrons

$$E = \sum_i E_i + \frac{1}{2} \sum_i \sum_j [J_{ij} - K_{ij}].$$

(2.24)

Here $E_i = \langle \chi_i | -\frac{1}{2}\nabla^2 - Zr_i^{-1} | \chi_i \rangle$ is the kinetic + electrostatic energy of an orbital designated by χ_i, the Coulomb repulsion energy between electrons in orbitals i and j is given by $J_{ij} = \langle \chi_i \chi_j | r_{ij}^{-1} | \chi_i \chi_j \rangle$, and $K_{ij} = \langle \chi_i \chi_j | r_{ij}^{-1} | \chi_j \chi_i \rangle$ is the exchange energy. The exchange energy is factorizable into spatial ψ_i, and spin $s_i = \uparrow$ or $\downarrow$, components

$$K_{ij} = \langle \Psi_i \Psi_j | r_{ij}^{-1} | \Psi_j \Psi_i \rangle = \langle \psi_i \psi_j | r_{ij}^{-1} | \psi_j \psi_i \rangle \left| \langle s_i | s_j \rangle \right|^2,$$

(2.25)

which is zero for orthogonal states (antiparralel spins) and therefore increases the total Hartree-Fock energy. This is the origin of Hund's first rule, which states that unpaired electrons arrange in parallel and maximize the total spin angular momentum. Finally, the total angular momentum, $J = |L - S|$ if the subshell is less than half full, and $J = |L + S|$ if the subshell is more than half full.

2.3 Crystal-Field

The distribution of charged ions throughout a crystalline lattice generates an internal electric field particular to the symmetry of each site. The specific anisotropy of an ion will then depend on the particular local point-group symmetry of the surrounding electric fields. In general, the electrostatic energy of a single electron at position $\boldsymbol{r}_c$, surrounded by a neighbouring charge distribution $\rho(\boldsymbol{r}_i)$ is given by

$$V_{\text{cf}}(\boldsymbol{r}_e) = -\int \frac{e\rho(\boldsymbol{r}_c)}{|\boldsymbol{r}_e - \boldsymbol{r}_c|}d\boldsymbol{r}_c, \tag{2.26}$$

In the case where the neighbouring distribution does not overlap with the charge cloud of the electron, this potential can be treated as a standard multipole series expansion in terms of spherical harmonics Y_{lm}

$$V_{\text{cf}}(\boldsymbol{r}_e) = \sum_{l,m} A_{lm} r^l Y_{lm}(\theta, \phi), \tag{2.27}$$

where multipole moments of the $4f$ electrons are $r^l Y_{lm}(\theta, \phi)$, and the associated coefficients arising from the electrostatic interaction are given by

$$A_{lm} = \frac{1}{2l+1} \int \frac{e\rho(\boldsymbol{r}_c)}{r_c^{l+1}} Y_{lm}^*(\theta, \phi)d\boldsymbol{r}_c. \tag{2.28}$$

At this point, some general considerations based on symmetry arguments can simplify the form for the potential energy. Computing the matrix elements of V_{cf} involves integrals of the type

$$\int \phi_{4f}^* r^l Y_{lm} \phi_{4f} d\tau, \tag{2.29}$$

where ϕ_{4f} are the $4f$ orbitals that transform according to the rotation group $D^{(3)}$. The product $Y_{lm}\phi_{4f}$ transforms according to $\sum D^{(j)} = D^{(l)} \times D^{(3)}$ where $|l - 3| \leq j \leq l + 3$. Therefore, the only non-vanishing integrals occur for $j \leq 3$, which restricts the allowed A_{lm} to $l \leq 6$. Another routine simplification at this stage is to restrict the values of A_{lm} based on the symmetry of the crystalline field, which may for example have 2-fold rotational symmetry that restricts the allowed values of $m = 0 \pm 2, \pm 4, \ldots$.

The conventional point-charge model regards the ionic charge distribution as a summation of i discrete point charges

$$\mathcal{H}_{\text{cf}} = \sum_i \sum_{lm} A_{lm} \alpha_l \left\langle r^l \right\rangle Y_{lm}(\boldsymbol{J}_i), \tag{2.30}$$

where α_l are the numerical Stevens factors, which depend on the distribution of the electron charge cloud, and $Y_{lm}(\boldsymbol{J}_i)$ are the spherical harmonics, where the Cartesian coordinates x, y, z, have been replaced by the respective angular momentum operators $\boldsymbol{J}_x, \boldsymbol{J}_y, \boldsymbol{J}_z$, while accounting for their anti-commutation relations (eg. $xy \to \frac{1}{2}[xy + yx]$).

Historically, the conventional representation of crystal field operators was introduced by Stevens, [100] who expressed the crystal field operators in terms of the tesseral harmonic functions Z_{lm},

$$
\begin{aligned}
Z_{l0} &= Y_{l0} \\
Z_{l,\pm|m|} &= \sqrt{\pm^1/_2} \left[Y_{l,\pm|m|} \pm (-1)^{|m|} Y_{l,|m|} \right],
\end{aligned}
\tag{2.31}
$$

where $\pm$ is for $m > 0$ or $m < 0$ respectively. These combinations of spherical harmonics are purely real functions, making them easier to work with. The standard approach is then to write the crystal field Hamiltonian in the compact form

$$
\mathcal{H}_{cf} = \sum_i \sum_{lm} B_l^m O_l^m(\boldsymbol{J}_i),
\tag{2.32}
$$

where the crystal field parameters B_l^m are typically derived from experiment unless they are easy to calculate. The operators $O_l^m(\boldsymbol{J})$ are known as the Steven's operators, which transform just like the tesseral harmonic functions. The first few Stevens operators are

$$
\begin{aligned}
O_2^0 &= 3J_z^2 - J(J+1) \\
O_2^1 &= \frac{1}{2} (J_z J_x + J_x J_z) \\
O_2^2 &= \frac{1}{2} \left(J_+^2 + J_-^2 \right) \\
O_2^{-1} &= \frac{1}{2} (J_z J_y + J_y J_z) \dots
\end{aligned}
\tag{2.33}
$$

This formalism provides a fair approximation when the crystal field splitting is small compared to the spin-orbit splitting. In this case, the separation of J states is large enough that the crystal field interaction can be treated as a perturbation that splits only the lowest J states.

2.4 Exchange

The quantum mechanical exchange interaction can be described as an effective force that exists between identical particles as a result of their indistinguishability. Its origin is purely quantum mechanical, and is attributed to the symmetry of the wavefunction upon exchanging two particles.

In the case of bosons, the symmetric nature of their wavefunction results in an effective attraction between particles often associated with Bose-Einstein condensation. In the case of fermions, the effect commonly known as Pauli repulsion arises as a result of the asymmetry of the wavefunction upon exchange. The electron exchange correlation energy arising from the Coulomb interaction was previously demonstrated in the context relevant to spin-orbit coupling, where it was found to lower the overall Hartree-Fock energy by an amount

$$K_{ij} = \langle \psi_i \psi_j | r_{ij}^{-1} | \psi_j \psi_i \rangle \left| \langle s_i | s_j \rangle \right|^2, \tag{2.34}$$

where the configuration with parallel spins s_i, minimizes the total energy. This effect justifies the rules for coupling angular momenta of atoms that were formulated in 1925 by F. Hund based on the observation of atomic spectra.

Another exchange mechanism classified as kinetic exchange is different from Coulomb exchange because it relies on electron hopping between atomic orbitals. Subject to the Pauli principle, an electron can only hop from one orbital to another if it is not occupied by another electron with the same spin. This produces an effective interaction between the atomic orbitals that is conceptualized as exchange. Kinetic exchange mechanisms are usually the dominant sources of ferromagnetic or antiferromagnetic interactions between ions. This is followed by magnetostatic interactions such as the dipole-dipole interaction, which have an effective interaction energy given by

$$\Delta E = \frac{\boldsymbol{\mu}_1 \cdot \boldsymbol{\mu}_2 - 3(\boldsymbol{r} \cdot \boldsymbol{\mu}_1)(\boldsymbol{r} \cdot \boldsymbol{\mu}_2)}{4\pi\epsilon_0 c^2 r^3}, \tag{2.35}$$

for two magnetic dipoles $\boldsymbol{\mu}_1$ and $\boldsymbol{\mu}_2$, separated by a distance $\boldsymbol{r}$.

The exchange formalism provides a good starting point to describe the behaviour of phase transitions and other correlated phenomena in real materials. The Hamiltonian representing effective magnetic exchange interaction between two ions is often reduced to a simple form

$$\sim J_{ij} S_i S_j, \tag{2.36}$$

where J_{ij} represents the effective interaction between the operators on sites i and j. We now discuss the origins of a few important exchange mechanisms that are relevant for the description of collective magnetic phenomena; namely direct exchange, and superexchange.

Direct Exchange

Direct exchange occurs due to electron transfer between neighbouring atomic orbitals that are close enough to have significant overlap. It is instructive to consider the Hubbard model to describe electron hopping

$$\mathcal{H} = -t \sum_{\langle i,j \rangle, \sigma} \left(c_{i,\sigma}^{\dagger} c_{j,\sigma} \right) + U \sum_i n_{i,\uparrow} n_{i,\downarrow} \tag{2.37}$$

where $c_{i,\sigma}^{\dagger}$ is the creation operator for a spin-σ electron at the $i-$th orbital, and $n_{i,\sigma} = c_{i,\sigma}^{\dagger} c_{i,\sigma}$ is the spin density operator. The matrix element for hopping between orbitals is given by t, and the on-site potential from electron Coulomb repulsion is given by U. For instance, consider a simple toy model of two electrons hopping between two orbitals

$$\mathcal{H} = -t \left(c_{1\uparrow}^{\dagger} c_{2\uparrow} + c_{2\uparrow}^{\dagger} c_{1\uparrow} + c_{1\downarrow}^{\dagger} c_{2\downarrow} + c_{2\downarrow}^{\dagger} c_{1\downarrow} \right) + U \left(n_{1\uparrow} n_{1\downarrow} + n_{2\uparrow} n_{2\downarrow} \right). \tag{2.38}$$

which has ground state energy, and corresponding eigenfunction given by (-)

$$\epsilon_{\pm} = \frac{U}{2} \pm \frac{\sqrt{U^2 + 16t^2}}{2} \tag{2.39}$$

$$\Psi_{\pm} = \frac{|\uparrow, \downarrow\rangle - |\downarrow, \uparrow\rangle - \frac{\epsilon_{\pm}}{2t} \left[|\uparrow\downarrow, \cdot\rangle + |\cdot, \uparrow\downarrow\rangle \right]}{\sqrt{1 + \epsilon_{\pm}^2/(2t^2)}} \tag{2.40}$$

Hence we can see that the energy of the regular states given by $|\uparrow, \downarrow\rangle, |\downarrow, \uparrow\rangle$ is lowered by the inclusion of a hopping term, t. [101]

Superexchange

Superexchange can occur between two orbitals that are too far apart to allow for direct hopping between overlapping orbitals. The hopping mechanism then proceeds through an intermediary non-magnetic anion. Depending on the conidition, the resulting coupling can be either antiferromagnetic or ferromagnetic. Superexchange is common among insulating magnetic oxides, where the dominant charge transfer process is mediated through $p-$orbitals of an intermediate oxygen anion. In most of the rare-earth elements, $4f$ electrons are screened by closed shell $5s$ and $5p$ orbitals, therefore additionally reducing the $4f - 4f$ overlap between neighbouring sites.[102] For the spin-ice compounds, superexchange is the dominant exchange mechanism that occurs between the magnetic ions. In

this case, the $p-$orbitals of non-magnetic oxygen atoms serve as intermediate hopping sites between $f-$orbitals of neighbouring rare-earth ions. This charge hopping mechanism for two rare-earth $f-$orbitals separated by an oxygen $p-$orbtial is given by

$$V = \sum_{\alpha\beta} \left[t^\dagger_{1,\alpha\beta} p^\dagger_\alpha f_{1\beta} + t_{1,\alpha\beta} f^\dagger_{1\alpha} p_\beta + t^\dagger_{2,\alpha\beta} p^\dagger_\alpha f_{2\beta} + t_{2,\alpha\beta} f^\dagger_{2\alpha} p_\beta \right], \qquad (2.41)$$

where $\alpha, \beta = (m, \sigma)$ labels the orbtial m and spin σ of the corresponding $f-$orbital of the $i-$th rare earth, or the $p-$orbital of the intermediate oxygen. The tunneling matrix element is given by $t_{i,\alpha\beta}$.[103]

2.5 Hyperfine

Hyperfine structure is a result of the interactions between the nucleus and surrounding electrons, resulting in the splitting of atomic energy levels. To completely account for the nuclear interactions, one also has to take into account the motion of the nucleus, treating it as an object with internal structure rather than a Coulombic point source. It turns out that these factors result in a small shift in energy for various isotopes, known as the isotope shift, and they can often be neglected relative to the electron-nuclear interactions. Within this approximation, we proceed with the assumption that the nucleus is a rigid object with well defined magnetic and electric moments, and these properties are not affected by the motion of external electrons.

Magnetic Hyperfine Interaction

Just as a system of interacting electrons can possess a non-zero angular momentum, the nucleus can carry a magnetic moment due to the arrangement of nucleons (protons and neutrons), which also carry intrinsic spin$-\frac{1}{2}$. The Hamiltonian describing a system of nucleons is analogous to equation 2.2

$$\mathcal{H}_{n-n} = -\frac{\hbar^2}{2} \sum_i \frac{1}{m_i} \nabla_i^2 + \frac{1}{2} \sum_{ij} U_{ij}, \tag{2.42}$$

where U_{ij} is the interaction energy between two nucleons i and j, and depends on the detailed structure of the nucleus. It can be shown that this Hamiltonian is rotationally invariant and transforms according to the rotation group $D^{(I)}$, therefore giving rise to the nuclear angular momentum I. This angular momentum is identified with nuclear spin, and possesses a magnetic moment $\boldsymbol{\mu}_N$ parallel to the nuclear angular momentum $\mathbf{I}$

$$\boldsymbol{\mu}_N = \mu_N \frac{\mathbf{I}}{\hbar I}. \tag{2.43}$$

Electrons orbiting the nucleus produce an effective magnetic field $\mathbf{H}_{\text{eff}}$, interacting with the nuclear magnetic moment in the standard way

$$\mathcal{H}_M = -\boldsymbol{\mu}_I \cdot \mathbf{H}_{\text{eff}}, \tag{2.44}$$

which can be re-written as follows, provided that the effective field of the electrons is proportional to their angular momentum $\mathbf{J}$:

$$\mathcal{H}_M = a\mathbf{I} \cdot \mathbf{J} \tag{2.45}$$

where

$$a = -\frac{\mu_N}{\hbar I} \left\langle \left| \frac{\mathbf{H}_{\text{eff}} \cdot \mathbf{J}}{\mathbf{J}^2} \right| \right\rangle \qquad (2.46)$$

It follows that $\mathcal{H}_M$ is invariant under combined rotations of electronic and nuclear coordinates, and therefore, the eigenstates of this atom can be written in terms of the combined angular momentum quantum number F and m_F, where $|I - J| \leq F \leq I + J$. Applying first order perturbation theory, the splitting of energy levels is given by

$$\begin{aligned} E(F) &= \langle IJFm_F | a\mathbf{I} \cdot \mathbf{J} | IJFm_F \rangle \\ &= \frac{1}{2} a\hbar^2 \left[F(F+1) - I(I+1) - J(J+1) \right] \end{aligned} \qquad (2.47)$$

Te effective magnetic field contributing to a in equation 2.46 can be calculated by considering separately the electrons orbiting outside and those that penetrate inside the nucleus. Qualitatively, the external contribution arises from the orbital motion of electrons,

$$a_{\text{orb}} \propto \left\langle \frac{\mathbf{L}}{r^3} \right\rangle, \qquad (2.48)$$

as well as the dipolar interaction, which yields

$$a_{\text{dip}} \propto \left\langle 3\frac{(\mathbf{S} \cdot \mathbf{r})\mathbf{r}}{r^5} - \frac{\mathbf{S}}{r^3} \right\rangle. \qquad (2.49)$$

The internal contribution known as the Fermi contact interaction, is a combined effect from $s-$electrons and the configuration of nucleons themselves,

$$a_{\text{FC}} \propto \langle \mathbf{S} \rangle \left| \Psi(0) \right|^2 \qquad (2.50)$$

where $\left| \Psi(0) \right|^2$ is the electron spin density 'inside' the nucleus. In cases where the spin-orbit coupling is weaker than the hyperfine interaction, then it is necessary to work in terms of $\mathbf{L}$ and $\mathbf{S}$ states

$$\mathcal{H} = \beta\mathbf{H}_{\text{eff}} \cdot (\mathbf{L} + g_s\mathbf{S}). \qquad (2.51)$$

Finally, if the crystal fields are stronger than even the electrostatic interactions within the atom, the full treatment is necessary in terms of individual electron states $l_i \ s_i$,

$$\mathcal{H} = \beta\mathbf{H}_{\text{eff}} \cdot \sum_i (l_i + g_s s_i). \qquad (2.52)$$

Electrostatic Hyperfine Interaction

The electrostatic hyperfine interaction is understood by expanding the electrostatic energy between the β-th electron at $\mathbf{r}_{e\beta}$ and the α-th nucleon at $\mathbf{r}_{n\alpha}$ in terms of Legendre polynomials, where $\omega_{\alpha\beta}$ is the angle between $\mathbf{r}_{n\alpha}$ and $\mathbf{r}_{e\beta}$

$$\mathcal{H}_{e-n} = -\sum_{\alpha\beta} \frac{e^2}{|\mathbf{r}_{n\alpha} - \mathbf{r}_{e\beta}|} = -e^2 \sum_{\alpha\beta} \left[\frac{1}{r_{e\beta}} + \frac{r_{n\alpha}}{r_{e\beta}^2} P_1(\cos\omega_{\alpha\beta}) + \frac{r_{n\alpha}^2}{r_{e\beta}^3} P_2(\cos\omega_{\alpha\beta}) + \cdots \right] \tag{2.53}$$

The first term ($l = 0$) in this expansion is the electrostatic potential of the nuclear charge that was already considered in the orbital Hamiltonian (equation 2.2). The second term ($l = 1$), and the odd$-l$ terms vanish because of parity invariance. This series converges rapidly because of the ratio of nuclear and electronic radius to the $l-$th power, $(r_n/r_e)^l$, and in most cases, it is sufficient to keep only the electric quadrupole interaction ($l = 2$),

$$\mathcal{H}_Q = -\frac{1}{6} \sum_{ij} Q_{ij} (\nabla\mathcal{E})_{ij} \tag{2.54}$$

$$Q_{ij} = e \sum_\alpha \left[\frac{3}{2} (r_{n\alpha i} r_{n\alpha j} + r_{n\alpha j} r_{n\alpha i}) - \delta_{ij} r_{n\alpha}^2 \right] \tag{2.55}$$

$$(\nabla\mathcal{E})_{ij} = e \sum_\beta \frac{1}{r_{e\beta}^5} \left[\frac{3}{2} (r_{e\beta i} r_{e\beta j} + r_{e\beta j} r_{e\beta i}) - \delta_{ij} r_{e\beta}^2 \right] \tag{2.56}$$

where r_i are the x, y, z components of $\mathbf{r}$. In the angular momentum representation, the $r_{n\alpha i}$ are replaced by the component I_i of the angular momentum operator $\mathbf{I}$, and the $r_{e\beta i}$ are replaced by the J_i components of $\mathbf{J}$. After some simplification, the equivalent expression in the angular momentum representation is given by

$$\mathcal{H}_Q = \frac{3e^2 q_J Q}{8I(2I-1)J(2J-1)} \left[\frac{4(\mathbf{I} \cdot \mathbf{J})^2}{\hbar^4} + \frac{2\mathbf{I} \cdot \mathbf{J}}{\hbar^2} - \frac{4\mathbf{I}^2\mathbf{J}^2}{3\hbar^4} \right] \tag{2.57}$$

The first order correction to the energy is given by

$$E_Q = \langle Fm_F|\mathcal{H}_Q|Fm_F\rangle = \frac{3e^2 q_J Q}{8I(2I-1)J(2J-1)} \left[K(K+1) - \frac{4}{3}I(I+1)J(J+1) \right] \tag{2.58}$$

where

$$\langle IJFm_F|2\mathbf{I} \cdot \mathbf{J}|IJFm_F\rangle = \hbar^2 K = \hbar^2 \left[F(F+1) - I(I+1) - J(J+1) \right] \tag{2.59}$$

Part II

Methods and Instrumentation

Chapter 3

Specific Heat

Simply put, heat capacity is the quantity of heat, Q, required to raise the temperature of a system by one degree in temperature. It can be expressed by the limit

$$C_x = \lim_{dT \to 0} \left(\frac{dQ}{dT} \right)_x = T \left(\frac{\partial S}{\partial T} \right)_x, \tag{3.1}$$

where S is entropy, and x refers to a thermodynamic quantity such as pressure, volume or magnetic field that is held constant in the limit. According to the postulates of thermodynamics, it follows that entropy and specific heat tend to vanish with the temperature of a system. This can be seen by integrating (3.1):

$$S(T) - S(0) = \int_0^T \left(\frac{C}{T} \right) dT. \tag{3.2}$$

If $\Delta S \to 0$ as $T \to 0$, then it implies $C \to 0$ as $T \to 0$. Thus, by measuring C to a very low temperature, it is possible to extract the value of $S(T)$. Depending on the nature of the excitation in a system, this may occur at several degrees Kelvin, while others may remain disordered into the μK regime or lower. In the case of a magnetic system with effective spin-S, a common way to test the validity of a theoretical model is to check that the total entropy resleased as $T \to 0$ is equal to $k_B \ln(2S + 1)$ per site.

Statistical thermodynamics is concerned with the connection between the macroscopic mechanical laws of classical thermodynamics, which encompass concepts such as temperature, entropy and heat; and the microscopic nature of nuclei, atoms and molecules. This fundamental connection is defined through the partition function

$$Z = \sum_i e^{-\epsilon_i / k_B T}, \tag{3.3}$$

which is defined such that the sum of probabilities P_i, that the system occupies microstate ϵ_i is normalized

$$\sum_i P_i = \sum_i \frac{1}{Z} e^{-\epsilon_i/k_B T} = 1. \tag{3.4}$$

The partition function relates the statistics of a microscopic ensemble, to macroscopic thermodynamic quantities such as the Helmholtz free energy F, entropy S, and specific heat C,

$$F = -k_B T \ln(Z) \tag{3.5}$$

$$S = -\left(\frac{\partial F}{\partial T}\right) \tag{3.6}$$

$$C = -T\left(\frac{\partial^2 F}{\partial T^2}\right) \tag{3.7}$$

3.1 Schottky Anomaly

The Schottky effect is a common type of specific heat anomaly that arises in a system with multiple energy levels. It is a non-cooperative effect, which means that the individual particles or modes of the system do not interact, and the total energy of the system is a sum of its components. The effect is commonly considered in the context of an ion with total angular momentum $\hbar J$, with $(2J + 1)$ degenerate energy levels. In the presence of a crystal electric field, the degeneracy is split into discrete energy levels that give rise to a Schottky anomaly.

Nuclear Specific Heat

To demonstrate its general features, we consider the situation whereby a nuclear spin I is split into $(2I + 1)$ energy levels with corresponding potential energies ϵ_i, where $i = -I, -I + 1, ..., I - 1, I$. The corresponding partition function for a single nucleus is given by

$$Z = \sum_{i=-I}^{+I} e^{-\epsilon_i/kT}. \tag{3.8}$$

The average energy of this nuclear spin is obtained from the partition function,

$$\langle \epsilon \rangle = -\frac{d(\ln Z)}{d(kT)^{-1}} = \frac{\sum_{i=-I}^{+I} \epsilon_i e^{-\epsilon_i/kT}}{\sum_{i=-I}^{+I} e^{-\epsilon_i/kT}}, \tag{3.9}$$

52

and the resulting specific heat of a system with N nuclei is simply a sum of the individual components

$$C_{\text{Sch}} = \frac{d\langle E \rangle}{dT} = \frac{d(N\langle \epsilon \rangle)}{dT} = \frac{R}{(kT)^2} \frac{\sum_{i=-I}^{+I} \sum_{j=-I}^{+I} (\epsilon_i^2 - \epsilon_i \epsilon_j) \exp\left[-(\epsilon_i + \epsilon_j)/kT\right]}{\sum_{i=-I}^{+I} \sum_{j=-I}^{+I} \exp\left[-(\epsilon_i + \epsilon_j)/kT\right]}. \quad (3.10)$$

For the common case of a two-level system with energy separation $\Delta = \epsilon_+ - \epsilon_-$, this equation reduces to the familiar form of a single Shottky anomaly shown in figure 3.1. Calculation of C_{Sch} requires knowledge of the energy levels, ϵ_i, accessible to the nuclear
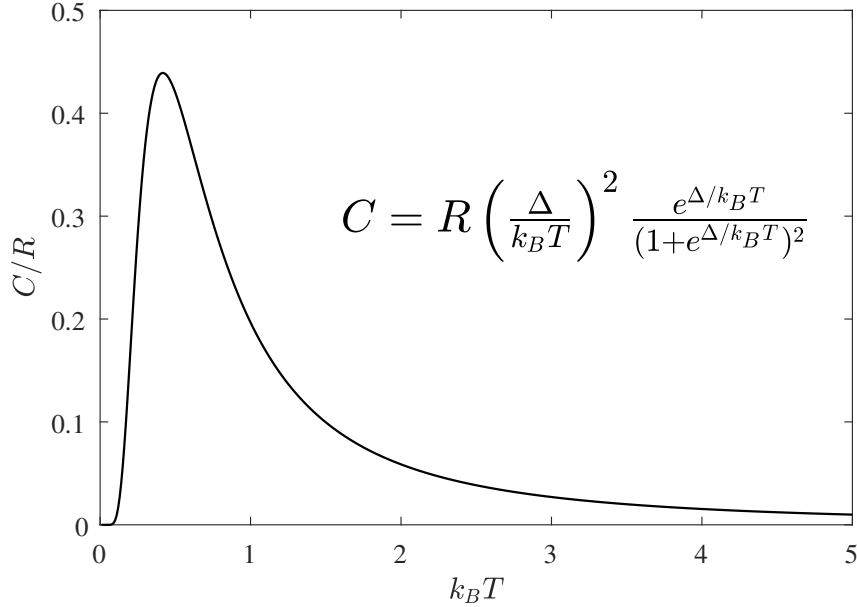
Figure 3.1: Schottky anomaly for a two-level system with energy separation $\Delta = 1$ K.

spins, which is known as the atomic hyperfine structure. An effective magnetic field, $\vec{H}_{\text{eff}}$, that is felt by the nucleus, gives rise to a magnetic interaction proportional to $\vec{\mu} \cdot \vec{H}_{\text{eff}}$. Likewise, a quadrupolar interaction between the nuclear quadrupole moment, Q, and the electric field gradient at the nucleus, q, is proportional to Qq. Collectively, these interactions lift the degeneracy and determine the distribution of energy levels ϵ_i. Without going into detail, the total Hamiltonian in the diagonal basis can be written as the sum of the magnetic and quadrupolar terms[99]

$$\mathcal{H}_D + \mathcal{H}_Q = -a'I_z + P\left[I_z^2 - \frac{1}{3}I(I+1) + \frac{\eta}{3}(I_x^2 - I_y^2)\right], \quad (3.11)$$

where $a' = \mu H_{\text{eff}}/k_N I$ and $P = 3e^2 Qq/4k_B I(2I-1)$ are the magnetic hyperfine and quadrupolar coupling parameters, respectively. The asymmetry parameters $\eta = 0$ in the common case of an axially symmetric field, and the energy levels of this system are simply

$$\epsilon_i/k_B = -a'i + P\left[i^2 - \frac{1}{3}I(I+1)\right], \tag{3.12}$$

where $i = -I, -I+1, ..., I-1, I$. The magnetic hyperfine constant is proportional to the electronic magnetization $a' \propto \langle J_z \rangle$, and the quadrupole coupling constant to the average value of the quadrupole moment $P \propto \langle J_z^2 - \frac{1}{3}J(J+1) \rangle$. Often at low temperature where magnetic systems order ferromagnetically or antiferromagnetically, these averages can be replaced by the fully saturated value $a' \propto J$ and $P \propto J(J+1)$. The microscopic origins of these interaction parameters was also touched upon in section 2.5.

In many situations, the high temperature portion of the Schottky anomaly is only accessible with experimental conditions, so it is useful to expand equation 3.10 as a power series

$$C_{\text{Sch}} = c_2 T^{-2} + c_3 T^{-3} + c_4 T^{-4} + \ldots, \tag{3.13}$$

where the coefficients are given by

$$\begin{aligned}
\frac{c_2}{R} &= \frac{1}{3}(a')^2 I(I+1) + \frac{1}{45}P^2 I(I+1)(2I-1)(2I+3), \\
\frac{c_3}{R} &= -\frac{1}{15}(a')^2 P I(I+1)(2I-1)(2I+3), \\
\frac{c_4}{R} &= -\frac{1}{30}(a')^4 I(I+1)(2I^2 + 2I + 1).
\end{aligned} \tag{3.14}$$

On the low temperature side, the expansion of equation 3.10 increases exponentially

$$C_{\text{Sch}} \sim e^{-\delta/T} \tag{3.15}$$

where δ is some average temperature which characterizes the position of the peak.

3.2 Calorimetry

An idealized calorimeter is one in which the system is adiabatically isolated from its environment and thermally linked to a convenient reference from which it is possible to apply fundamental principles of statistical physics.

The calorimeter monitors changes in temperature of a sample in response to an exchange of heat Q, between the system and its surroundings. In practice, a system is always exchanging energy due to contact with its surroundings, and this makes it difficult to realize a truly adiabatic calorimeter. Therefore, the system must be designed to restrict heat leaks to a desired level of precision. This is achieved by suspending the sample in a vacuum chamber with filaments made of poor thermal conductors such as nylon or kevlar. A thermometer and heater coupled to the sample also induce some contact with the thermal reservoir, often through a set of electrical leads that have poor thermal conductivity (i.e., superconducting filaments). These heat leaks should be minimized to a level that is negligible relative to the dominant channel of heat flow in the system.

Another complication arises in cooling down the sample, which must be thermally connected to a cold reservoir. This can be achieved with a low-pressure exchange gas, or a mechanical switch that can be opened after cooling the sample to a desired temperature. However, both of these methods have practical complications below ≈ 1 K. Exchange gases eventually solidify, or exhibit superfluidity and coat the surfaces of a cryogenic vacuum chamber. Mechanical vibrations associated with opening and closing of a heat switch often perturb the system, and their use is limited at low temperatures for this simple reason. Rather than striving for adiabatic isolation, materials with well-characterized thermal properties are used to exchange heat between a system and the thermal reservoir.

The simplified model of an idealized calorimeter is depicted in figure 3.2, which is subject to the conservation of heat energy described by the following equation

$$
\begin{array}{c}
\text{rate of change of} \\
\text{heat energy}
\end{array}
= \text{power leaving sample} + \text{power applied to sample}
$$

$$
C(T)\frac{\partial T}{\partial t} \quad = \quad \nabla \cdot (\kappa(T)\nabla T) \quad + \quad \frac{\partial Q}{\partial t}
$$

(3.16)

The first term is the rate of change of heat energy $\dot{q}$, and is related to heat capacity C

$$
\Delta q = C(T)\Delta T \quad \Rightarrow \quad \frac{\partial q}{\partial t} = C(T)\frac{\partial T}{\partial t}.
$$

(3.17)

The second term is derived from Fourier's law of heat conduction, which states that the heat flux is proportional to the thermal conductance, and the temperature gradient across
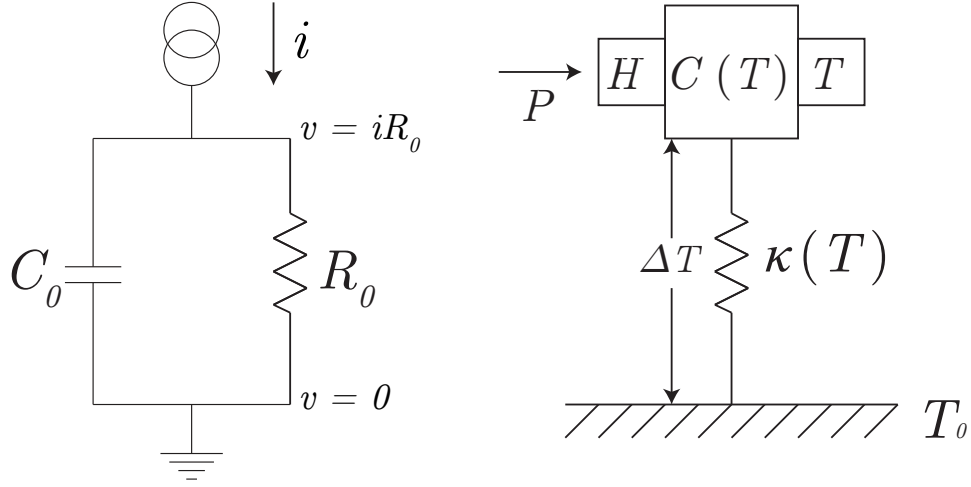
Figure 3.2: Schematic of an ideal calorimeter used to measure heat capacity $C(T)$. The sample is coupled to a thermal reservoir at T_0 by a weak link of thermal conductivity $\kappa(T)$. The heater H applies a power P to the sample, and a thermometer T measures the temperature. An equivalent electrical circuit model with capacitor C_0 and resistor R_0 is shown on the left.

the thermal link: $\vec{q} = -\kappa \nabla T$. The additional divergence of the heat flux comes from the divergence theorem. The third term $\dot{Q}$, is simply the volumetric heat flow per unit time due to applied heat. The 1-dimensional form of equation 3.16 provides a good starting point to describe the thermal evolution of the model in figure 3.2:

$$C(T)\frac{\partial T}{\partial t} - \kappa \frac{\partial^2 T}{\partial x^2} = P, \tag{3.18}$$

where the spatial derivative is taken along the direction of the weak link and $P = \dot{Q}$ is the power delivered by a heater. Integrating along the length of the wire and solving for $C(T)$

$$C(T) = \left(\frac{\partial T}{\partial t}\right)^{-1} \left(P - \int_{T_0}^{T} K(T')dT'\right), \tag{3.19}$$

where $K(T) = \frac{\kappa(T)A}{l}$ is the thermal conductance of a wire with cross-sectional area A, and length l. This universal formula for specific heat is very useful for describing the thermal relaxation of several different experimental methods.

3.3 Relaxation Method

For the idealized model in figure 3.2 described by the 1-dimensional heat equation 3.18 with a constant source of power P, we consider the case where the system has reached thermal equilibrium and suddenly the heater power is turned off. The amount of power applied is typically chosen to yield a small offset in temperature, such that $C(T)$ and $K(T)$ can be assumed to be constant over the range of ΔT. In this case, the solution to equation 3.18 is described by a single exponential

$$T(t) = (T_1 - T_0)e^{-t/\tau_1}, \tag{3.20}$$

where T_1 is the temperature of the sample before the power is switched off, and T_0 is the temperature of the thermal reservoir. Therefore, it is possible to obtain C directly after measuring τ_1 and K. Deviations from this ideal case can arise if the idealized model conditions are not met. A signature of this behaviour is often detected as a deviation from the single exponential behaviour described by equation 3.20. The appearance of an second exponential in the relaxation is commonly known as the "τ_2 effect" [104]

$$T(t) = A_1 e^{-t/\tau_1} + A_2 e^{-t/\tau_2}. \tag{3.21}$$

If $\tau_2 << \tau_1$, the initial rapid exponential drop due to τ_2 may be attributed to the internal thermal equilibration of the sample itself; or in the case where the sample is mounted to a platform, to the equilibration between the sample and a substrate. If the fast relaxation (τ_2 effect) is negligible, it follows that the heat capacity of the sample is easily extracted from the time constant and thermal conductance of the weak link

$$C = -\frac{K}{d(\ln \Delta T)/dt} = \frac{K}{\tau_1}. \tag{3.22}$$

In complex cases, more than two exponential functions may be present in the relaxation curve. If their time constants are close, then it becomes difficult, if not impossible to extract a reliable fit to a sum of exponentials. This type of effect is described by the "distributed τ" model, which is a sum of exponentials,

$$T(t) = \sum_{n=1}^{\infty} A_n e^{-t/\tau_n}. \tag{3.23}$$

This result is a solution to the Sturm-Liouville equation with the appropriate boundary conditions a realistic calorimeter that accounts for the thermal conductivity of the sample,

platform, and weak link. The coefficients, A_n, are obtained by solving transcendental equations, as demonstrated with detail in the appendix of reference [105].

Without prior knowledge of the internal distribution of thermal conductance, fitting the relaxation data to equation 3.23 with $n \geq 3$ is tricky, and in many cases unmanageable. The simplest way to address this problem is by numerically integrating the rate of heat flowing out of the calorimeter, rather than trying to extract the time constants τ_n with a fitting procedure. To our knowledge, the only explicit reference to this type of method was by Tsujii *et al.* [106] The total heat capacity of the sample and its addenda ($C(T) = C_{\text{sample}(T)} + C_{\text{addenda}}(T)$) is obtained by integrating heat flux leaving the system across the weak link of thermal conductance $K(T)$:

$$C(T) = \frac{1}{\Delta T(0)} \int_0^\infty \dot{Q}(t) dt = \frac{1}{\Delta T(0)} \int_0^\infty K(T) \Delta T(t) dt. \qquad (3.24)$$

This integral can be performed numerically using trapezoidal integration, and $K(T)$ is obtained by measuring the temperature offset for a given power, $K_{\text{avg.}} = P/\Delta T$ at various temperatures. If the relaxation step size is sufficiently small, the average value for $K(T)$ can be used. Smoothing the data may be necessary to reduce random noise, and in some cases, it may be possible to fit the tail of the data to a single exponential to reduce the increased noise as $\Delta T(t)$ approaches zero.

This model is elegant as it can be applied to any system with arbitrary thermal relaxation dynamics, as long as the appropriate conditions are met. The role of the weak link is to act as a throttle for heat, setting the rate at which the system can relax to the stage thermometer. If it is very weak (small thermal conductance), the observed thermal relaxation will be slow, and the measured $\Delta T(t)$ will have more area in the integral of equation 3.24. Alternatively, if it is very strong (large thermal conductance) relative to the internal conductance of the sample, the observed temperature decay will be fast, and the slow release of heat due to internal equilibration will not produce a large temperature gradient $\Delta T(t)$ across the link. If the time constant of the weak link is chosen appropriately, then the resulting relaxation curve has the characteristics of the distributed τ_2 effect described above, and the numerical integration procedure is appropriate. It is therefore important that a sample exhibiting the distributed τ_2 effect has a sufficient amount of time to equilibrate within its surroundings, both before and after the relaxation is measured. It may not always be clear what is a "sufficient" amount of time, in which case it is important to adiabatically cool the material from higher temperatures and look for signatures of the τ_2 effect at every step of the process. Another disadvantage worth mentioning, is that heat capacity contribution from the weak link is included in the total measured specific heat.

Bachmann *et al.,* calculated this contribution to be approximately $\frac{1}{3}C_{\mathrm{WL}}$ of the heat capacity of the weak link. [105] It is therefore desirable to choose a weak link with relatively negligible heat capacity to reduce this contribution.

3.4   Quasi-Adiabatic Heat Pulse Method

Perhaps the most intuitive method for obtaining specific heat; the quasi-adiabatic heat pulse method is accomplished by applying a fixed amount of heat Q, and measuring the resulting change in temperature ΔT. The heat capacity is expressed by the ratio $C = \frac{Q}{\Delta T}$. In practice, the step in temperature should be small enough to minimize errors arising from variations in $C(T)$. Because of the finite duration of the heat pulse, some energy will be lost through the weak link, resulting in a diminished value of ΔT. The common approach to account for this loss, is extrapolating to the half-way point in the heat pulse, as shown in figure 3.3. The data is fit before and after the heat pulse with an appropriate function that represents its behaviour. In ideal cases where the simple model of equation 3.2 can be assumed, the extrapolation is often peformed with a single exponential. In cases where the time constant of the weak link is very large, it may be appropriate to fit with a linear function $T(t) = a + bT$, which is often a good approximation.
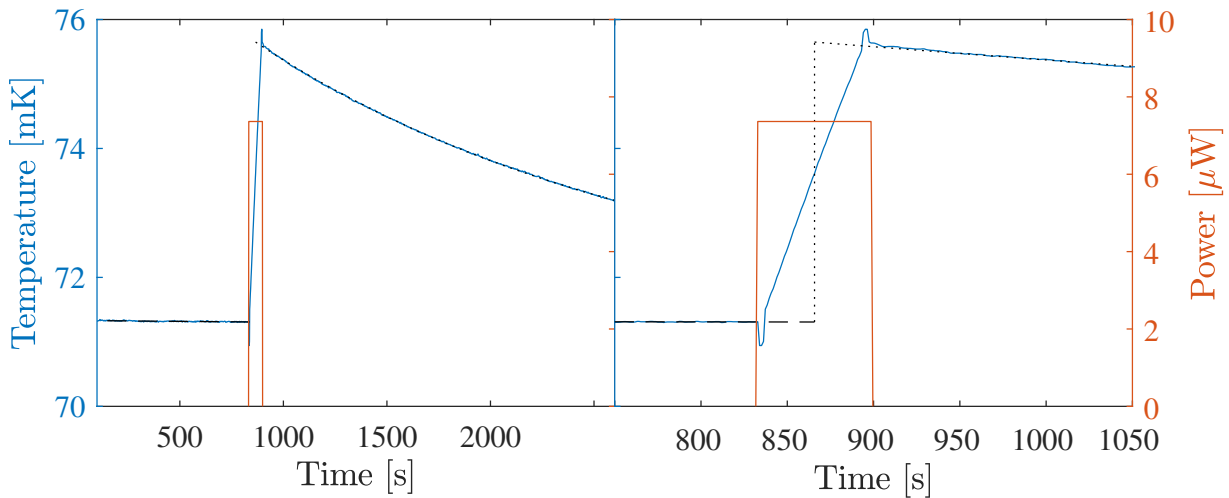
Figure 3.3: Typical heat pulse measurement below 100 mK. The relaxation after the pulse was fit to an exponential function and then extrapolated to the midpoint of the heat pulse. ΔT is extracted at midpoint of the heat pulse, indicated by the dotted line.

The utility of a heat pulse calorimeter can also become limited when the thermal conductance within the sample is comparable to the weak link. This situation is analogous to a setup where the sample is mounted onto a platform which is directly coupled to the thermometer, heater and weak link. If the sample-to-platform coupling is relatively poor, then a heat pulse will result in a characteristic overshoot in temperature of the platform, implying a lag in actual temperature of the sample. This can result in a significant overestimate of heat capacity, as shown in section 7.4.5 of the masters thesis of J. Quilliam, a previous member of the Waterloo low temperature group.[107]

3.5   Slope Method

The slope method is the most rapid, but least quantitative technique for measuring heat capacity. It is based on the notion that changes in the specific heat of a sample, will appear as a change in the cooling rate of the sample. The experimental setup is the same as for the other methods described previously. In this case, the temperature reservoir is kept at a low temperature, while the sample is heated to the highest temperature of interest. Upon reaching thermal equilibrium, the power is turned off, and the sample cools down towards the reservoir temperature, T_0, through the weak link. The corresponding cooling rate is determined by the temperature gradient across the weak link with thermal conductance $K(T)$, and the heat capacity is given by setting $P = 0$ in equation 3.19

$$C = -\left(\frac{dT}{dt}\right)^{-1} \int_{T_0}^{T} K(T')dT'. \tag{3.25}$$

Hence, the specific heat is inversely proportional to the rate of cooling $dT(t)/dt$. This result is intuitive because a transition in the specific heat that rapidly releases a large amount of energy, will result in a slowing down of the cooling rate.

As with each method, this approach has limitations. One of the major points is that the equilibration time of the sample must be very fast compared to the weak link time constant, otherwise the true temperature of the sample will lag behind the measured temperature, resulting in an offset error in the temperature axis. It can be a useful method for rapidly identifying the location and general shape of phase transitions in the specific heat, and it also produces smooth plots of the specific heat (depending on the sampling rate of the temperature $T(t)$).

3.6 Calorimeter Design
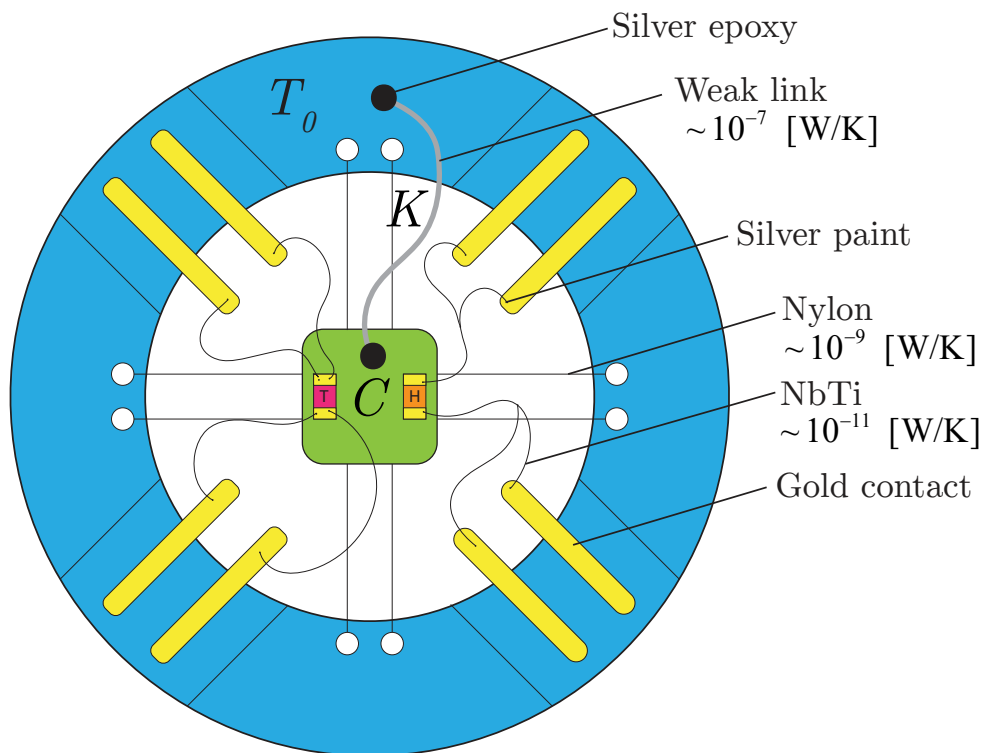
Figure 3.4: Diagram of sample calorimeter used for low temperature measurements.

The calorimeter consists of a copper ring threaded with nylon filaments used to suspend the sample, as depicted in figure 3.4. The nylon filaments are obtained by unwinding a small length of unwaxed dental floss. These nylon filaments have two desirable properties for this application: they have good mechanical strength, allowing them to be stretched and loaded with tension without breaking, and their small cross-section results in a very low thermal conductance. The heater is a 10 kΩ metal-film chip resistor, which has a typical temperature coefficient of ≈ 10 ppm/$^\circ$C, making it a very stable reference for heating the sample. The temperature of the sample is measured with a RuO$_2$ thick film chip resistor that has been laser trimmed to a nominal resistance of 1000 Ω at room temperature. Both chips are glued directly to the sample with epoxy or varnish. Superconducting electrodes to the heater and thermometer are made with $\approx 6\mu$m diameter NbTi wires that are $\approx$ 1.5 cm long. These filaments were obtained by acid etching a small piece of copper-clad,

multi-filamentary NbTi wire in concentrated nitric acid (HNO$_3$) for several minutes to dissolve the copper. The electrical contacts were made with DuPont silver paint, diluted with solvent to obtain the proper viscosity. Good contact resistance between the NbTi filament and the chip resistors can be difficult to achieve in some cases.

In some of our earlier experiments, these contacts were made with silver epoxy (Epoxy Technology Inc.), containing small particles ($\approx 20\mu$m) of conductive silver, suspended in epoxy resin to provide mechanical strength. The most ideal silver epoxy that we could find on the market had silver particles which are still larger than the diameter of our NbTi wire ($\approx 6\mu$m), making it difficult to produce reliable contacts. After switching to silver paint (Dupont Inc.), the issues with contact resistance were improved significantly. Silver paint is easier to work with because it can be easily diluted with solvent to any desired viscosity, it dries within minutes at room temperature. It is also inexpensive compared to silver epoxy, which has to be carefully prepared and cured at high temperatures.

Resistance thermometry was performed with the 4-wire ac method, eliminating contact resistance and lead resistance of the cryostat wiring. In the case of the heater, a current flowing through the contact resistance will also produce heat, so it is important to characterize this resistance if it is not negligible. The total heater resistance ($R_{\text{heater}} + R_{\text{contact}}$) is also obtained with a 4-wire measurement, however, the voltage leads are connected at the mid-point of the current leads (see figure 3.4). This measurement captures the additional contact resistance between NbTi and the heater contacts. In most cases, this additional contact resistance is negligible in comparison to the heater (< 1 part in 10^4).

Thermal links

Ideally, the thermal conductance of the nylon filaments and the NbTi electrical leads should be negligible to that of the weak link. The weak link typically consists of an impure metal wire which has its thermal conductivity dominated by electron conduction according to the Wiedemann-Franz law:

$$\kappa = \sigma L T, \tag{3.26}$$

where $L = 2.44 \times 10^{-8}$ [WΩK^{-2}] is the Lorenz number, and σ is the electrical conductivity of the metal. A good material for this application is a metal which contains impurities, or other crystallographic defects, and therefore has a residual resistance ratio $RRR = \rho_{300\text{K}}/\rho_{0\text{K}} \approx 1$. Under these conditions, σ is constant at low temperatures, and the thermal conductivity is linear in temperature according to equation 3.26. This weak link is connected between the sample and stage with a bead of conductive silver epoxy at both ends to reduce the effects of thermal contact resistance at the ends of the wire.

It turns out that this is difficult to achieve at very low temperatures ($\lesssim 100$ mK), where phonon mismatch (Kapitza resistance) often becomes significant for the geometry of our problem.

The thermal conductance of the weak link, $K = \kappa A / L$ is customized for the particular temperature range and heat capacity of the sample. This requires *a priori* estimate for the specific heat of the material, which can be calculated for the idealized model in figure 3.2, where the relaxation is governed by a single exponential $T(t) \sim e^{-t/\tau}$ with time constant

$$\tau = C(T)/K(T). \tag{3.27}$$

The ideal choice of τ depends on the particular measurement technique, temperature range, and the thermal dynamics of the sample. It can range from minutes, for the ac method, to hours, for the quasi-adiabatic heat pulse method. Longer time constants may be desirable if the internal equilibration time is slow, such as for a glassy material.

One of the practical challenges of calorimetry is the design of a heat switch for rapidly cooling the sample to the base temperature of the cryostat. This is useful when the weak link is required to have a very poor thermal conductance. Mechanical heat switches are typically practical above 1 K, but the heat produced by opening typically produces too much vibrational heating to be practical at lower temperatures. An alternative is the superconducting heat switch, which consists of a magnetic coil wrapped around a superconducting wire such as Al, that switches into a normal state when the magnetic field is beyond its critical value, H_c. Once the field is turned off, the wire superconductors and thermal conductance drops by several orders of magnitude. In practice however, this type of switch is difficult to incorporate alongside measurements of magnetic materials, where the sample needs to be in a low noise, zero-field environment. Therefore, in the case where a heat switch cannot be used, the choice of a thermal link needs to be considerate of the cooling time for a sample with large heat capacity.

Chapter 4

Magnetic Susceptibility

The kinetics of magnetism in a material are examined by measuring its response to an oscillating magnetic field. The magnetic susceptibility, χ, is defined as a dimensionless constant that is proportional to the ratio of magnetization and applied magnetic field:

$$\mathbf{M} = \chi\mathbf{H}. \tag{4.1}$$

There is an unofficial, but widely used convention for magnetic moment per unit volume M = m/V, such that volume susceptibility has the units

$$\chi_{\mathrm{v}} = \frac{\mathrm{M}}{\mathrm{H}} = \frac{\mathrm{m}}{\mathrm{VH}} \qquad \left[\frac{\mathrm{emu}}{\mathrm{cm^3 Oe}}\right]. \tag{4.2}$$

While most practices in science and engineering have already adopted the international system (SI) of units, the conversion of magnetic units has been messy and confusing. The majority of research and techincal work still uses the conventional cgs-emu system of units. This controversy is explained from various approaches in a panel discussion on units of magnetism that took place at the 1994 Joint MMM-Intermag Conference.[108] For the susceptibility measurements presented in this thesis, we adopt the conventional centimetre-gram-second (cgs) system with the electromagnetic unit (emu) in equation 4.2.

Susceptibility is not necessarily linear, but is described as a differential that depends on frequency

$$\chi(\omega) = \frac{\partial M(\omega)}{\partial H(\omega)} \tag{4.3}$$

The measured magnetic moment of a material in an alternating field with frequency ω is

$$M = \frac{\partial M}{\partial H} H \sin(\omega t) \tag{4.4}$$

For non-zero frequency, the quantity measured is the dynamic susceptibility, which can acquire a phase if the magnetization response lags behind the driving field. This gives rise to the complex representation of in phase and out of phase susceptibility, $\vec{\chi} = \chi' + i\chi''$. The imaginary component, χ'' indicates a dissipative process in the material, while the real component is the linear response that approaches the slope of the magnetization curve in the DC limit. The dynamic magnetic susceptibility can vary as a function of frequency, magnetic field bias, and amplitude; and serves as a sensitive probe that yields information about phase transitions.

The measurements described here consist of absorption and dispersion at low audio frequencies (10^{-3} to 10^3 Hz), which correspond to an average response of the material over a large population of energy levels. This is to be contrasted with a resonant measurement technique, such as electron paramagnetic resonance or nuclear magnetic resonance, where a single pair of energy levels are typically excited in a resonant manner.

4.1 Linear Response Theory

In very general terms, the goal of response theory is to characterize effects that perturbations have on a specific property of the system. Mathematically, a *non-linear* response is described by the Volterra series

$$y(t) = h_0 + \sum_{n=1}^{N} \int \cdots \int h_n(\tau_1, ..., \tau_n) \prod_{j}^{n} x(t - \tau_j)d\tau_j, \qquad (4.5)$$

where $x(t)$ is the input, and $y(t)$ the output of a continuous time-invariant system, and $h(\tau_1, ..., \tau_n)$ is a function that captures the non-linear response of the system (called the $n-$th order Volterra kernel). Similar to the common Taylor series expansion, the Volterra series also captures the time-dependent properties of the expansion variable. In this sense, the Volterra series is capable of capturing the output of a system over all times simultaneously, whereas the Taylor series correlates the input and output at one moment in time. This ability to capture time-invariant behaviour is often described as a 'Taylor series with memory', because the output is affected by past inputs.

Magnetic susceptibility χ, is a response function that describes the magnetic behaviour of a system $m(t)$, in response to an applied magnetic field $h(t)$. In the context of linear response theory, the Volterra series is truncated to the lowest order term only (omitting the constant)

$$m(t) = \int_{-\infty}^{t} \chi(t - \tau)h(\tau)d\tau + ..., \qquad (4.6)$$

where the outputs and inputs are now written specifically as magnetization, $m(t)$, and a time dependent applied field $h(\tau)$, respectively. The Volterra kernel is the linear magnetic susceptibility $\chi(t)$.

The fluctuation-dissipation theorem states that a system in thermodynamic equilibrium will produce the same response to a small applied force as it would to a spontaneous thermal fluctuation. Therefore, the linear approximation is valid when perturbing forces are small enough to keep the system in thermal equilibrium. One common manifestation of the fluctuation dissipation theorem relates to Johnson noise in electrical circuits, which has the opposite effect of resistance by exchanging thermal fluctuations with a fluctuating electrical current. Likewise, it also successfully accounts for the effects of Brownian motion and thermal radiation.

An important result of the fluctuation dissipation theorem relates the power spectrum of a sysetm $S(\omega) = \langle x(\omega)x^*(\omega)\rangle$, to the imaginary part of the Fourier transform $\tilde{\chi}(\omega)$, of the susceptibility $\chi(t)$:

$$S(\omega) = \frac{2k_BT}{\omega}\text{Im}[\tilde{\chi}(\omega)]. \tag{4.7}$$

It follows that the autocorrelation function is given by the Fourier transform of this quantity $S(\omega) = \tilde{C}(t)$, and is given explicitly in the time domain by

$$C(t) = \langle m(0)m(t)\rangle = 2k_BT \int_{-\infty}^{\infty} \frac{\chi''(\omega)}{\omega} \cos(\omega t)\mathrm{d}\omega. \tag{4.8}$$

The power dissipated due to fluctuations in $m(t)$ are directly proportional to $\chi''(\omega)$. The generality of this result demonstrates that the imaginary component of the susceptibility corresponds to the dissipative component of any linear response function.

4.2   Relaxation Models

Various relaxation models exist, and historically, they have been derived from the theory of dielectric relaxation in polar molecules. Perhaps the simplest of these theoretical models, is the Debye relaxation model, which describes the response of idealized polar molecules to an external electric field. While the models derived by Debye and others were originally for electric susceptibility measurements, they are frequently used to analyze magnetic behaviour as well.

The Debye model is based upon the notion that the temporal electric or magnetic relaxation of a system can be characterized by exponential decay, after the removal of a

static polarizing field. In the case of a magnetic system,

$$M(t) = M_0 e^{-\frac{t}{\tau}}, \tag{4.9}$$

describes the relaxation from a static polarization M_0. In frequency space, the Fourier transform takes the form of a Lorentzian function

$$M(\omega) = \int_0^\infty M_0 e^{-\frac{t}{\tau}} e^{-i\omega t} dt = \frac{M_0 \tau}{1 + i\omega\tau}. \tag{4.10}$$

This is related to magnetic susceptibility $M(\omega) = \chi(\omega)H(\omega)$, and in the case of a sinusoidal field we get

$$\chi(\omega) = \frac{M(\omega)}{H(\omega)} = \frac{M_0}{H_0} \frac{\tau}{1 + i\omega\tau} = \frac{\chi_0}{1 + i\omega\tau}, \tag{4.11}$$

where χ_0 is the static susceptibility in the limit $\omega \to 0$. The real and imaginary components of susceptibility, $\chi'(\omega)$ and $\chi''(\omega)$, take the form

$$\chi' = \frac{\chi_0}{1 + (\omega\tau)^2} \tag{4.12}$$

$$\chi'' = -\frac{\chi_0 \omega\tau}{1 + (\omega\tau)^2} \tag{4.13}$$

In the case where there is a distribution of relaxation modes corresponding to multiple time constants, the susceptibility can be generalized by a corresponding response function $f(\tau)$,

$$\chi(\omega) = \int_0^\infty \frac{f(\tau)}{1 + i\omega\tau} d\tau, \tag{4.14}$$

where the normalizing condition is $\int_0^\infty f(\tau)d\tau = 1$. In general, it can be difficult to derive $f(\tau)$ for a particular microscopic system with a general response function.

The phenomenon of Debye relaxation can be derived by various means, that generally require two major assumptions: (I) there are no interactions between dipoles, and (II) the inertia of dipoles is assumed to be negligible. Since Debye presented his original theory, a variety of solutions have also been built upon his model. [109, 110, 111, 112, 113]

Equivalent Circuit Model

Various physical phenomena are often conveniently represented by an equivalent circuit model that appropriately captures the mathematical response of the system, and the parallel $R||C$ circuit captures the essence of Debye relaxation. The total impedance of this

circuit

$$Z(\omega) = \left[j\omega C + \frac{1}{R}\right]^{-1} = \frac{R}{1 + (\omega RC)^2} - j\frac{\omega R^2 C}{1 + (\omega RC)^2}, \tag{4.15}$$

has analogous components to the susceptibility in equation 4.12 and 4.13

$$Z' = \frac{R}{1 + (\omega RC)^2} \tag{4.16}$$

$$Z'' = \frac{\omega R^2 C}{1 + (\omega RC)^2}. \tag{4.17}$$

The time constant of this circuit is $\tau = RC$, and the phase angle varies from $-\pi/2$ to 0 with decreasing frequency, reaching the critical frequency $f_c = 1/(2\pi RC)$ at $-\pi/4$. In the low frequency limit, the impedance is purely real, $Z(\omega \to 0) = R$, while in the high frequency limit, $Z(\omega \to \infty) = 0$. It is useful to keep some of these relationship in mind when analyzing the qualitative features of susceptibility. Many equivalent circuit models have no physical meaning, but are used as phenomenological tools.

Other Relaxation Models

Debye's original model was developed for an idealized liquid of non-interacting polar molecules in a non-polar solvent.[109] This model explicitly ignores dipolar inertia, as well as dipole-dipole interactions.[114] These effects are characterized as a distribution of time constants due to multiple relaxation modes. Glassy dynamics often introduce stretched exponential known as Kohlrausch relaxation behaviour, that has the functional form $f(t) = \exp\left[-(t/\tau)^\beta\right]$, where $0 < \beta \leq 1$. One of the first alternate proposals to the Debye model was introduced by brothers K. and R. Cole in 1941, who tried to explain the behaviour of glycerine, and various other polar liquids that become extremely viscous at low temperatures.[110] Their phenomenological model is expressed by

$$\chi(\omega) = \frac{\chi_0}{1 + (i\omega\tau)^\alpha}, \tag{4.18}$$

where $0 < \alpha < 1$ is a constant that reduces to the Debye model when $\alpha = 1$. As pointed out by the Cole brothers, the qualitative differences between various dispersion are most evident when plotted on an Argand diagram (or Cole-Cole plot) as $\text{Im}[\chi]$ versus $\text{Re}[\chi]$, shown in figure 4.1. The normalized Debye model produces a semi-circle which converges at the origin for $\omega \to \infty$, and intersects the real axis at finite values for $\omega \to 0$. The qualitative effect of $\alpha < 1$ is to flatten the arc, changing this angle of intersection by

euqal amounts at both high and low frequency. Two other commonly used models are also depicted in the figure. The Davidson-Cole (DC) model [112]

$$\chi(\omega) = \frac{\chi_0}{(1 + i\omega\tau)^\beta}, \tag{4.19}$$

and perhaps the most general Havriliak-Negami (HN) model [113]

$$\chi(\omega) = \frac{\chi_0}{(1 + (i\omega\tau)^\alpha)^\beta}. \tag{4.20}$$

The DC and HN functions both introduce asymmetry into the Cole-Cole plots at high and low frequency. One important distinction between these two models occurs at low frequency, where the DC model always intersects the real axis at a right angle, whereas this condition is relaxed for the HN model. While these generalized models often do not have microscopic interpretations, they are very useful for phenomenological descriptions and comparisons of a wide range of physical systems varying from dielectric liquids, to fluids, to spin liquids.

Circuit models more complex than the one described above for Debye relaxation can also be constructed to describe non-Debye models, a theme common to the field of electrochemical impedance spectroscopy (EIS). When considering the recent application of Onsager's theory of electrolytes as a method to describe the behaviour of emergent magnetic charges (monopoles) in classical spin-ice, perhaps there is a strong connection to the analytic methods already familiar to EIS.[115]
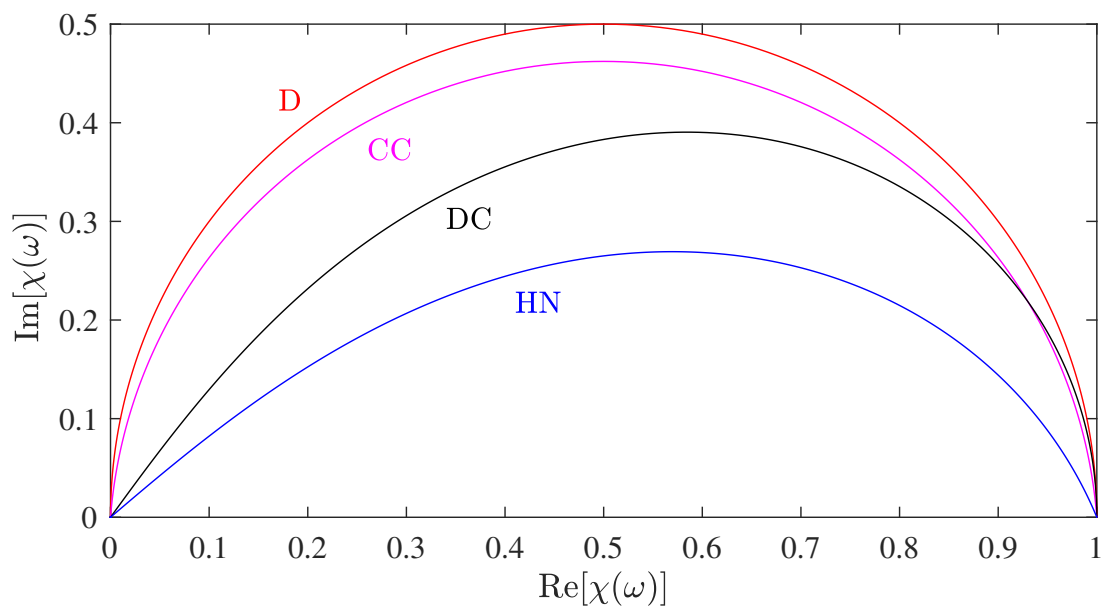
Figure 4.1: Qualitative features of three commonly encountered relaxation models are presented in the complex plane for $\omega \to 0$ to $\omega \to \infty$. [HN] The Havriliak-Negami model, which reduces to [D] the Debye model for $\alpha = \beta = 1$, [C] the Cole-Cole model for $\beta = 1$, and [DC] the Cole-Davidson model for $\alpha = 1$.

4.3 Magnetometer Design

The magnetometer is an apparatus designed to apply a magnetic field, and to measure the magnetic response of a sample that is temperature controlled on the cryostat. The magnetometer considered here was designed to isolate the sample from external fields that may perturb its magnetic state, such as earth's field. This was accomplished by enclosing the apparatus with a cylindrical superconducting shield of lead or niobium. Two different magnetometers were used in this thesis, having practically the same design but with some subtle differences. The general schematic diagram for these devices is shown in figure 4.2.
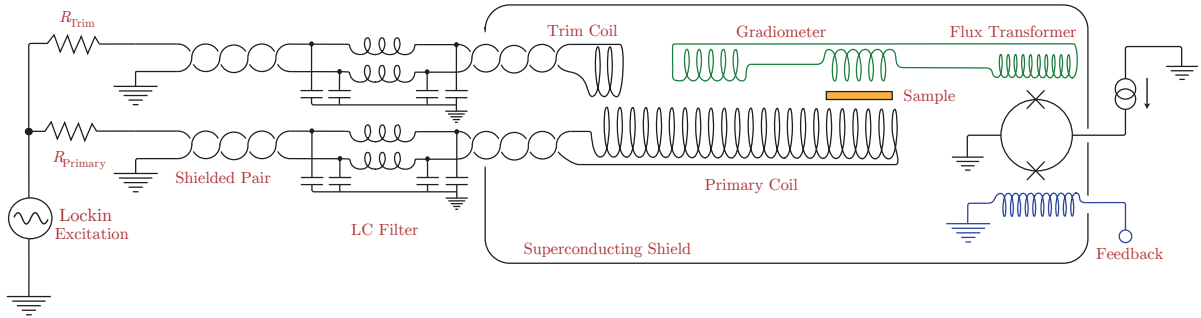
Figure 4.2: Circuit diagram for the susceptometer circuit.

Primary Coil

Inside the magnetometer is a solenoid, referred to here as the primary coil, it consists of a superconducting wire that is wrapped around non-magnetic material (with a small volume susceptibility), such as Vespel. In the limit of a solenoid that is infinitely long, the magnetic field strength inside the coil is given by

$$B = \frac{\mu I N}{L}, \tag{4.21}$$

where I is the electrical current, N is the number of turns, μ is the permeability of the material inside the coil, and $L = \mu r^2 N^2 \pi l^{-1}$ is the inductance for a length l and radius r. It is desirable to design the primary coil such that self-induced resonance does not occur in the frequency range of operation. For an RLC circuit, this resonance typically occurs at a frequency $\omega \sim (LC)^{-1/2}$. One of the important differences between the two magnetometers used in this thesis was the number and density of turns in the primary coil. One of the

devices, referred to as susceptometer I (design by Jeffrey Quilliam), had a primary coil with ~ 300 turns, which was wrapped as densely as possible with no spacing between the windings. Susceptometer II (design by Dave Vresc) had a sparse coil with ~ 100 turns, where the windings were separated by ~ 1 mm per turn. The purpose of this design was to lower the inductance; thereby raising the self-induced resonance, and allowing the device to operate at higher frequencies than susceptometer I, which was limited to ~ 1kHz for high precision results.

Gradiometer Flux Transformer

The sample is positioned inside the primary coil, where it is secured to the flat surface of a temperature controlled sapphire rod, with GE varnish or Apiezon grease. High purity sapphire is non-magnetic, which is desirable because it will not interfere with the measurement. The sample is positioned within one of the gradiometer coils, consisting of $\sim 5 - 10$ turns of Nb superconducting wire. The purpose of this loop is to inductively pick up the magnetic flux emitted from the sample. The second gradiometer coil has the same geometry as the first, but is wrapped in the opposite direction, and positioned inside the primary coil away from the sample. Both gradiometer coils detect the magnetic field of the primary; but with opposite polarity, such that the net current induced in the gradiometer loop is zero. The net current induced in the gradiometer is due to the sample, and this current is inductively coupled to the pickup coil of a dc SQUID operated in flux locked loop mode (discussed later in this chapter). The purpose of SQUID instrumentation is to convert the small signal induced in the gradiometer, into a large electrical signal that can be measured with ordinary laboratory electronics. Another coil known as the trim coil, is also inductively coupled to the empty loop in order to compensate for any imbalance present in the gradiometer. The current in the trim coil is adjusted with a current limiting resistor, R_{Trim}, that is adjusted manually to null the signal when there is no sample present in the magnetometer. In practice, the value of R_{Trim} required to balance the gradiometer with the desired precision of ~ 1 part in 10^4, has been observed to vary between subsequent cool-downs, likely due to subtle shifts in the construction of the magnetometer due to thermal expansion and contraction. To ensure optimal performance, it must be readjusted for each cool-down. In some cases, this can be accomplished at a temperature where the magnetic signal of the sample is small enough that it is not detectable by the instrument. In the case of the spin-ice compounds, the magnetic moments are effectively frozen and do not produce a magnetic signal at very low temperatures $\lesssim 300$ mK.

Lockin Amplifier Circuit

A digital lockin amplifier is used to apply a signal to the sample and measure the phase and amplitude of the response signal produced by the sample. The signal output by the lockin amplifier consists of a pure sine-wave at a single frequency that is adjustable from 1 mHz to 100 kHz. The particular magnetometer used in our experiments only has a flat frequency response in the dc to ~ 10 kHz range. At higher frequencies, parasitic effects of the circuit becomes relevant, producing a roll-off at high frequencies which would have to be characterized and subtracted. Below 1 kHz, the response of the empty susceptometer can be considered 'flat' to within a level that is not detectable by the instrumentation.

In the design of the lockin circuit, it is especially important to minimize the effects of parasitic capacitance, which affects the frequency response of the susceptometer. The primary contribution to is the capacitance of the π-filter that is used for filtering the electrical leads at the top of the cryostat. This low-pass π-filter has a capacitance of 4000 pF (API Spectrum Control Series 700 # 56-725-005) with a 3 dB point at 0.8 MHz, primarily to eliminate high frequency electromagnetic noise from the environment. The circuit diagram for the primary excitation coil is shown in figure 4.2.

Shielded twisted copper pairs are used as connections to the cryostat, in series with manganin alloy and NbTi superconducting wire throughout the cryostat. Directly at the output of the lockin amplifier is a shielded enclosure that contains a current limiting resistor for the primary and trim coils. A minimum number of resistors is used to minimize the parastitic capacitance, which is typically on the order of 0.5 pF for an axial metal film resistor. Surface mount resistors can be used to further reduce this capacitance.

Flux Locked Loop

The direct current Superconducting QUantum Interference Device (dc SQUID), consists of two identical Josephson junctions in parallel, joined by a superconducting loop. Various types of Josephson junction exist, typically consisting of two weakly coupled superconductors that are separated by a thin layer of a normal conductor (SNS), an insulator (SIS), or more generally, a weak link that breaks the coherence of the quantum mechanical wavefunction across the barrier. In essence, this device is designed as a very sensitive magnetometer that can detect changes in magnetic fields as low as 5×10^{-18} T. For a complete description of the theory and implementation of dc SQUIDs, the reader is referred to the SQUID handbook compiled by Clarke and Braginski. This handbook also contains a chapter writted by Drung and Mück that covers the essential details of SQUID electronics.[116]

When a magnetic flux threads the loop of a dc SQUID, the slope of the transfer coefficient $dV(\Phi)/d\Phi$ determines the voltage produced across the device. The $V(\Phi)$ transfer coefficient is a property that depends on the bias point intrinsic to each device. It does not remain linear for a very large range of flux. This problem is circumvented by operating the dc SQUID in an ac-flux modulated flux-locked loop mode. The modulated feedback circuit effectively counts the number of flux quanta threading the dc-SQUID loop $\Phi_0 = h/(2e)$, and its output is independent of the transfer coefficient $V(\Phi)$. For the purposes of the susceptometer circuit depicted figure 4.2, the electronic readout for the dc SQUID operated in flux locked loop mode has essential features shown in figure 4.3.
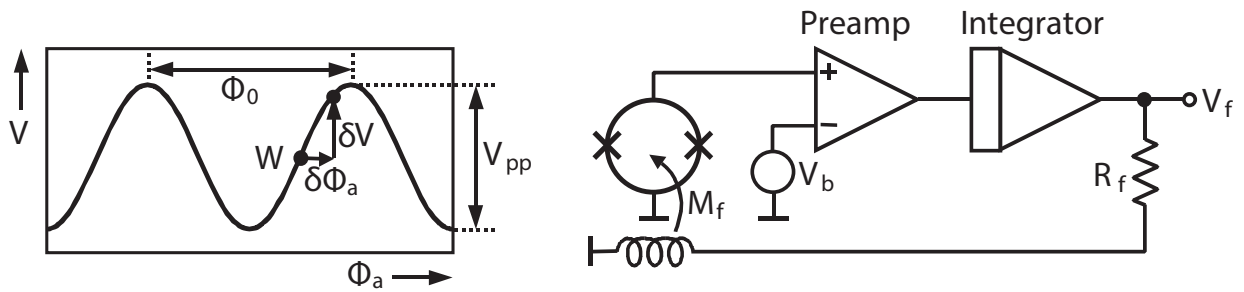

Figure 4.3: Essential features of a dc SQUID operated in flux-locked feedback mode. Figure reproduced from [116] with permission.

4.4 Demagnetization and Calibration

The magnetic field generated within a body in response to an applied field $\mathbf{H}_{\text{ext}}$ is also influenced by the magnetization $\mathbf{M}$ of the body itself. This gives rise to the magneto-static self-energy term arising from the classical interaction between dipoles, and generally depends on geometry of the body. At surfaces perpendicular to the applied field, ficti-tious magnetic poles are generated which produce a demagnetizing field $\mathbf{H}_{\text{demag}}$, effectively reducing the internal field $\mathbf{H}_{\text{int}}$

$$\mathbf{H}_{\text{int}} = \mathbf{H}_{\text{ext}} - \mathbf{H}_{\text{demag}}. \tag{4.22}$$

One can then distinguish between the true susceptibility χ and the external or apparent susceptibility χ_A, where

$$\chi = \frac{\partial \mathbf{M}}{\partial \mathbf{H}_{\text{int}}}, \quad \text{and} \quad \chi_A = \frac{\partial \mathbf{M}}{\partial \mathbf{H}_{\text{ext}}}. \tag{4.23}$$

The net effect is a reduction in the apparent susceptibility χ_A relative to the true internal susceptibility χ. This can be problematic because the demagnetizing field depends on the geometrical aspect ratio of the body. The standard method to account for this effect is to define a parameter N such that $\mathbf{H}_{\text{demag}} = N\mathbf{M}$. The demagnetizing factor $N(\chi)$ is generally a function of the susceptibility, but in the limit $N(\chi \to 0)$, it depends solely on the geometrical aspect ratio.[117] Recent work has demonstrated that in some situations, additional dependence of N from χ can arise from the microscopic spin anisotropy (Ising, XY, Heisenberg) of a particular lattice.[118] The most ideal sample geometry is one that can be wrapped with a toroidal solenoid because it effectively has no boundaries, and therefore $N = 0$. This type of geometry has only recently been implemented on the spin-ice $Dy_2Ti_2O_7$[119] and $Ho_2Ti_2O_7$,[120] whereas previous results in the literature were done with needle-shaped rectangular prisms. Fortunately, there is an analytic formula for the demagnetizing factor of a rectangular prism with dimensions a, b, and c in the direction of magnetization, when $\chi \to 0$ [121]

$$\pi N = \frac{b^2 - c^2}{2bc} \ln \left(\frac{\sqrt{a^2 + b^2 + c^2} - a}{\sqrt{a^2 + b^2 + c^2} + a} \right) + \frac{a^2 - c^2}{2ac} \ln \left(\frac{\sqrt{a^2 + b^2 + c^2} - b}{\sqrt{a^2 + b^2 + c^2} + b} \right) + ..., \tag{4.24}$$

as well as an accurate approximation method for the general case of $\chi \neq 0$.[117] For a thin needle, the demagnetization factor approaches zero as the length of the needle goes to infinity. The demagnetization factor of a perfect sphere is $1/3$.

The true susceptibility χ, is related to the external, measured susceptibility χ_A, by combining equation 4.22 and 4.23

$$\chi^{-1} = \chi_A^{-1} - 4\pi N. \tag{4.25}$$

The importance of the demagnetizing field is dependent on the ratio of χ_A^{-1}, and $4\pi N$ (cgs units), where the apparent susceptibility converges to the true susceptibility χ in the limit $N \to 0$. To illustrate the qualitative effects that the demagnetization factor N has on $\chi(\omega)$, the relationship between χ and χ_A is depicted in figure 4.4 for the Debye model (equation 4.11). For finite values of N, the amplitude of χ' and χ'' are reduced at low frequency, which effectively raises the peak of χ'' to high frequency. Note that the shape of the high, and low frequency tails in χ'' are not affected by the demagnetization factor N. Another important result concerns the scaling of $\tau\omega_p(N)$ in figure 4.4, which is the relative shift in the position of the observed χ'' peak as a function of N, as well as the susceptibility amplitude χ_0. The qualitative behaviour for these features is the same for the Havrialiak-Negami, Cole-Cole and Cole-Davidson models.
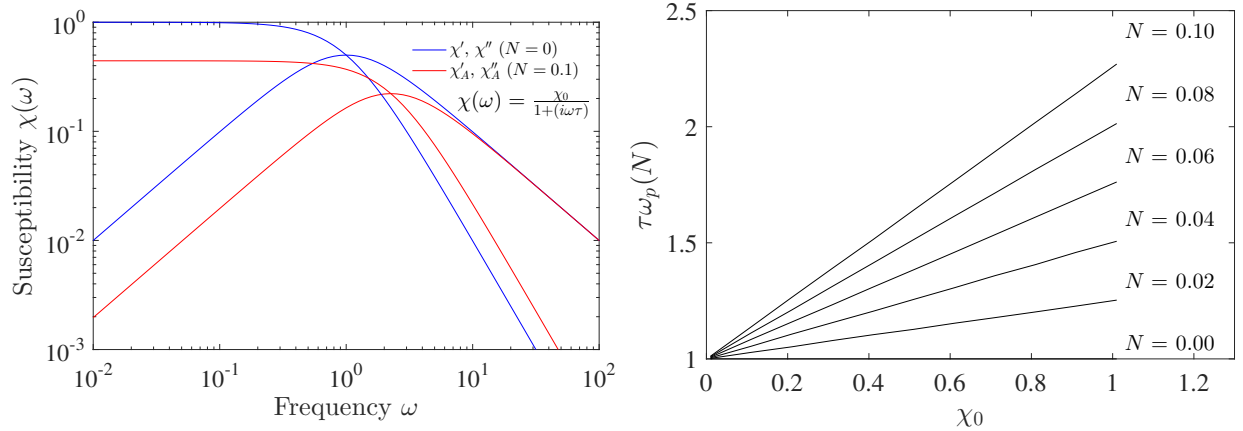
Figure 4.4: Left: Effect of a finite demagnetization factor N, on the Debye relaxation model in equation 4.11. The observed peak in χ_A'' is shifted to a higher frequency than the true χ'. The dc susceptibility $\chi_A'(\omega \to 0)$ is reduced. Right: Relative shift in the observed χ'' peak frequency, $\tau\omega_p(N)$, as a function of χ_0, and N indicating that the up-shift is amplified for large susceptibility χ_0.

4.4.1 Magnetometer flux-to-voltage calibration

Before any demagnetization correction can be applied, experimental data must first be converted to proper units of susceptibility. This is simply because the amplitude of χ_A^{-1}, relative to $4\pi N$ in equation 4.25, determines the magnitude of correction. In the circuit of figure 4.2, the measured quantity is a voltage generated by the flux-locked feedback loop, which is proportional to the magnetic flux threading the dc SQUID. The in-phase $V_x(\omega)$, and quadrature $V_y(\omega)$, signals detected by the lockin amplifier are directly proportional to the susceptibility

$$\chi_A(\omega) = a\left(V_x(\omega) + iV_y(\omega)\right), \tag{4.26}$$

where the coupling factor a depends on the mutual inductance of various elements in the magnetometer circuit [see figure 4.2], as well as the total closed-loop gain of the electronic circuitry. This factor is constant across frequency and temperature, provided that there is no flux drift of the dc SQUID, which is typically negligible. Temperature dependent dc flux drift of the SQUID may arise in some situations at low temperatures, and these factors should be assessed for relevance in each particular situation.[122, 123, 124]

One rather obvious method for obtaining the flux-to-voltage conversion of a circuit is to measure the susceptibility of a known material. A common approach is to measure a spherical lead sample, which is diamagnetic in the superconducting state with $\chi = -1$. While this method appears desirable because you only need to calibrate the instrument once, it does not account for small changes in the mutual inductance that can occur upon thermal cycling of the instrument. This is mostly due to expansion and contraction of the various circuit components.

The calibration method typically used in our laboratory; developed for the PhD thesis of J. Quilliam, requires two measurements independent measurements with unique demagnetizing factors N_1 and N_2.[125] This is simply done by reducing the geometry, and measuring the susceptibility $\chi(\omega)$ a second time in the same frequency range. There exist unique coupling factors for each sample a_1, and a_2, but have the same 'true' susceptibility according to equation 4.25. The calibration procedure is efficiently implemented as a binary search algorithm for values for a_1 and a_2, that optimize the sum of the squared residual between the two corrected data sets

$$\sum_\omega \frac{[\chi_1(\omega) - \chi_2(\omega)]^2}{\chi_1(\omega)^2 + \chi_2(\omega)^2}, \tag{4.27}$$

for two independent geometries. This calibration procedure works best when the difference between the geometrical demagnetizing factors is significant. Otherwise, the measured

susceptibility will not vary much between the two geometries. If they are too similar, then it will be impossible to obtain an accurate calibration factor from this procedure. For example, a sample of $Dy_2Ti_2O_7$ was measured for this thesis with two distinct aspect ratios corresponding to $N_1 = 0.058$, and $N_2 = 0.044$, making it was impossible to calibrate because the two data sets were too similar.

One of the outstanding questions that was observed in this thesis for low temperature (< 1 K) measurements of $Dy_2Ti_2O_7$, was the root cause of significant temperature dependence to the correction factor $a(T)$ in equation 4.26. This finding came as a surprise because the standard calibration procedure described by equation 4.27 normally produces a constant value of a, for all temperatures. Several scenarios that could introduce temperature dependence into this parameter are discussed below, and the experimental observations are presented in the appropriate section 7.3 for $Dy_2Ti_2O_7$.

4.4.2 Temperature dependent demagnetizing factor $N(T)$

The demagnetizing facactor N is independent of susceptibility $\chi(\omega)$, only in the limit of small $\chi \to 0$. But if $\chi(\omega, T)$ is large and temperature dependent, then the demagnetizing factor will certainly acquire temperature dependence through it $N(\chi(\omega, T))$. This can be computed precisely at each temperature for a rectangular prism if the dc value ($\omega \to 0$) of χ is known beforehand. For example, the dc value of $N(\chi)$ decreases from 0.058 to 0.05 for a finite value of $\chi = 1.5$.[117] For the particular case of $Dy_2Ti_2O_7$, the dc-susceptibility only varies from $\chi \approx 0.3$ at 1 K, to $\chi \approx 0.45$ at 0.5 K. This small range of values for $N(\chi)$ does not induce a large variability in the corrected susceptibility data, and it is safe to assume a constant value for N, as done previously for $Dy_2Ti_2O_7$.[126]

Another possible source of temperature dependence $N(T)$, may arise from the microscopic spin anisotropy of the lattice (Ising, XY, Heisenberg). The details of this effect were investigated in a study by Twengström *et al.,* and are summarized in figure 4.5.[118] This particular effect was relevant for large changes in susceptibility ($\chi \sim 5$) in spherical samples of $Dy_2Ti_2O_7$ at relatively high temperature ($T > 20$ K).
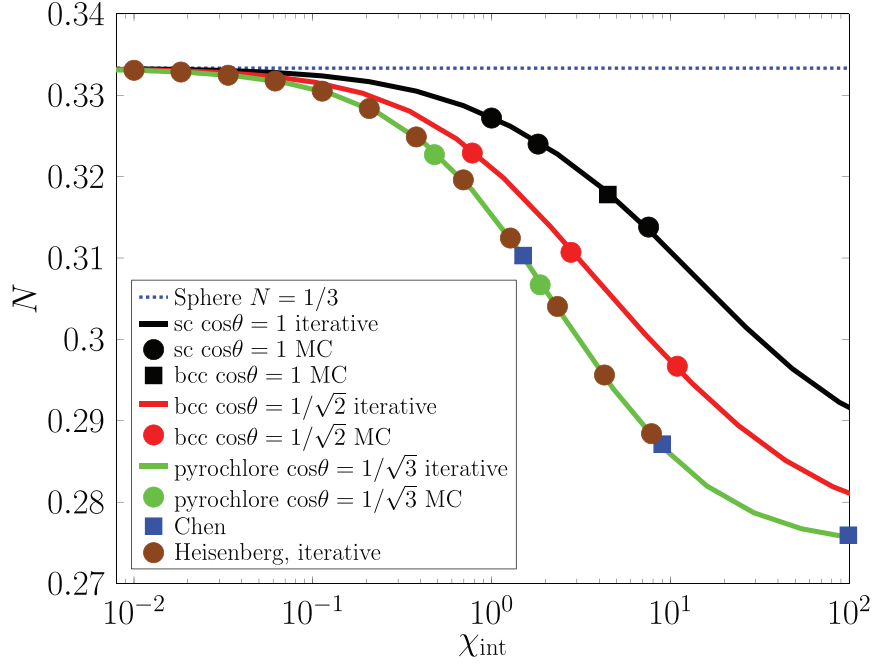
Figure 4.5: Relationship between N and true susceptibility χ_{int} for various microscopic lattice models. Blue squares are from Chen *et al.*[117] θ is the angle between the applied field and the corresponding local Ising axes. Figure reproduced from reference [118] with permission.

4.4.3   Temperature dependent dc-SQUID flux drift

The dc SQUID is operated in a flux-locked feedback loop to ensure a linear response between the measured flux, and the voltage output from the electronic circuit. Some of these details were discussed in section 4.3. Essentially, the SQUID flux to voltage transfer coefficient $V(\phi)$ is independent of the operating (bias) point, and as long as the slope of the transfer coefficient $dV/d\phi$ is large, then the feedback loop will have a constant gain. Therefore, it is typically assumed that there is no temperature dependence to the gain of a flux locked feedback loop. However, several mechanisms can been identified that have an effect on the temperature sensitivity $d\phi/dT$ of the dc SQUID output, which can impact its response, even in a flux-locked feedback loop.

Clarke *et al.,* identified two contributions.[122] The dominant external field-*dependent* effect was observed by measuring the sensitivity $d\phi/dT$ as a function of temperature by field-cooling (2.85 G) different shields made of lead, niobium, and 50/50 lead-tin solder,

where it was observed that the flux drifts are inherent to the shield material. The field-*independent* sensitivity was also investigated by cooling in nominally zero field (≤ 10 mG) where $d\phi/dT$ was found to be constant, and an order of magnitude larger than that expected for the superconducting shield. This was attributed to the asymmetry of the critical currents I_{c1} and I_{c2} of the two Josephson junctions which share the bias current passing through the dc SQUID. The temperature dependence of critical current for a Josephson junction is given by the Ambegaokar-Baratoff relation [127]

$$I_0(T) = \frac{\pi\Delta(T)}{2eR_N} \tanh\left[\frac{\Delta(T)}{2k_B T}\right].$$

(4.28)

The induced temperature dependence of the two asymmetric critical currents then generates a change in flux through the SQUID [123, 122]

$$\phi = \frac{LI_{c1}}{2} - \frac{LI_{c2}}{2} = \frac{L}{2}\Delta I_c.$$

(4.29)

Schone *et al.,* observed that the temperature dependence of the flux $d\phi/dT$ was much larger than expected from asymmetry of critical currents, or from the effects of London penetration depth $\lambda_L(T)$.[123] They concluded that $d\phi/dT \sim 0.3\Phi_0/$K was consistent with the motion of trapped vortices from large bias fields, and the movement of these vortices with temperature was found to have the largest effect on the observed temperature dependence. Far below the superconducting transition of a Nb SQUID $T << T_c \sim 9$ K, the aforementioned mechanisms are expected to be much less important. Sendelbach *et al.,* investigated the temperature dependence of flux below ~ 0.5 K, where they found evidence of a high density of unpaired surface spins in thin-film SQUIDs that gives rise to a large magnetic flux on the order of $1\Phi_0$.[124]

While most of these effects can probably be avoided with ac modulation techniques, they can certainly affect sensitive dc measurements of magnetic flux, especially when the temperature of the SQUID is changing throughout the measurement.

4.4.4 Position of the sample within the pickup coil

In order to obtain the correct demagnetizing field within a needle-shaped object, it is important to ensure proper alignment with the external field. If the sample is not aligned perpendicular to the applied field, then magnetic poles may be generated along the sides of the sample, which in turn distorts the internal demagnetizing field. This effect is difficult to characterize without performing numerical simulations.

Chapter 5

Millikelvin Thermometry

Accurate and precise thermometry presents challenges close to the base temperature of any millikelvin-range cryostat because parasitic heat flow can offset the measured temperature from its actual value. Considerable effort was invested in calibrating thermometry with a variety of methods, and optimizing heat flow throughout the cryostat in order to ensure reliability.

5.1   Resistance Thermometry

Cryogenic thermometry based on the resistance of a material is commonly used for ease of implementation. These devices are classified as secondary thermometers, but they can be attuned to a reference with a high degree of accuracy and repeatability. The sensitivity of a resistive thermometer Ω/K, is typically used as a figure of merit to determine the best temperature range for its application. The most common sensors for millikelvin thermometry are doped germanium semiconductor (GRT) from 10 mK to 100 K, ruthenium oxide (RuO_2) thick film from 10 mK to 100 K, and Zirconium Oxy-Nitride (Cernox) thin film from 100 mK to 500 K.

Temperature dependent resistivity $\rho(T)$, is a very common occurrence in materials. In the case of a pure metal, scattering of conduction electrons by lattice phonon modes results in a linear temperature dependence $\rho(T) \propto T$. In principle a very pure metal can be used for thermometry, though the application is limited to high temperatures because of their low resistance. As lattice temperature is reduced, impurities and other defects become the dominant causes for scattering, and resistivity approaches a constant defined by the

residual resistivity ratio (RRR) $\equiv \rho(T = 300 \text{ K})/\rho(T \to 0\text{K})$. In the case of a very "dirty" metal, (RRR) ≈ 1.

Conductivity in semiconductors occurs because the chemical potential (Fermi level E_{F}) is in close proximity to the conduction E_c (for p-type), or valence E_v (for n-type) band edges. Fermi-Dirac statistics dictate the distribution of electrons which can be thermally excited into conduction

$$f(E) = \frac{1}{\exp\left[\frac{E - E_{\mathrm{F}}}{k_B T}\right] + 1}. \tag{5.1}$$

A notable result is that an *intrinsic* (un-doped) semiconductor generally exhibits an exponential drop in charge carriers as temperature is lowered, and that is reflected in the resistivity

$$\rho(T) \approx \rho_0 \exp\left(\Delta E / 2 k_B T\right), \tag{5.2}$$

where ΔE is the energy gap between valence and conduction bands. This steep temperature dependence makes semiconductors great for sensitive thermometry, which can also be tuned for a particular range with appropriate doping. The temperature dependence of *extrinsic* (doped) semiconductors is slightly different. They can have intermediate ranges where reduced mobility of charge carriers inverts the polarity of the temperature coefficient. This situation is described by Mott variable range hopping, a model based on tunneling of electrons between localized charge carrier states in disordered systems. At sufficiently low temperatures, the theoretical resistivity in this model converges to a simple result when the density of states is constant

$$\rho(T) = \rho_0 \exp\left(T_0/T\right)^{\frac{1}{d+1}}, \tag{5.3}$$

where d is the dimension of the material, $T_0 \propto (g a_0)^{-3}$ where g is the density of states, and a_0 is the radius of localized states.[128] At lower temperatures there is often a gap in the density of states due to the Coulomb interaction, and the resistance increases even more rapidly with exponent $1/2$

$$\rho(T) = \rho_0 \exp\left(T_0/T\right)^{\frac{1}{2}}. \tag{5.4}$$

This simple relationship between resistance and temperature is useful as a first order approximation, but deviations from this idealized behaviour commonly arise for various reasons such as non-uniform doping in the substance. In many cases, a high-order polynomial fit can pick up the subtle deviations.

Doped Germanium

Germanium is typically doped with Arsenic (n-type) or Gallium (p-type) atoms to achieve optimal sensitivity anywhere in the range of 10 mK to 100 K. The sensors used with dilution cryostats are most often calibrated from 50 mK to 5 K with a high-order Chebychev polynomial that captures the deviations from equation 5.4. At these temperatures Ge has a poor thermal conductance and must be carefully thermalized to avoid self heating from the resistance measurement. Like most semiconductors, they are sensitive to electrostatic discharge, and must always be measured with small electrical currents to avoid re-distribution of dopant through electro-migration, which would change the calibration.
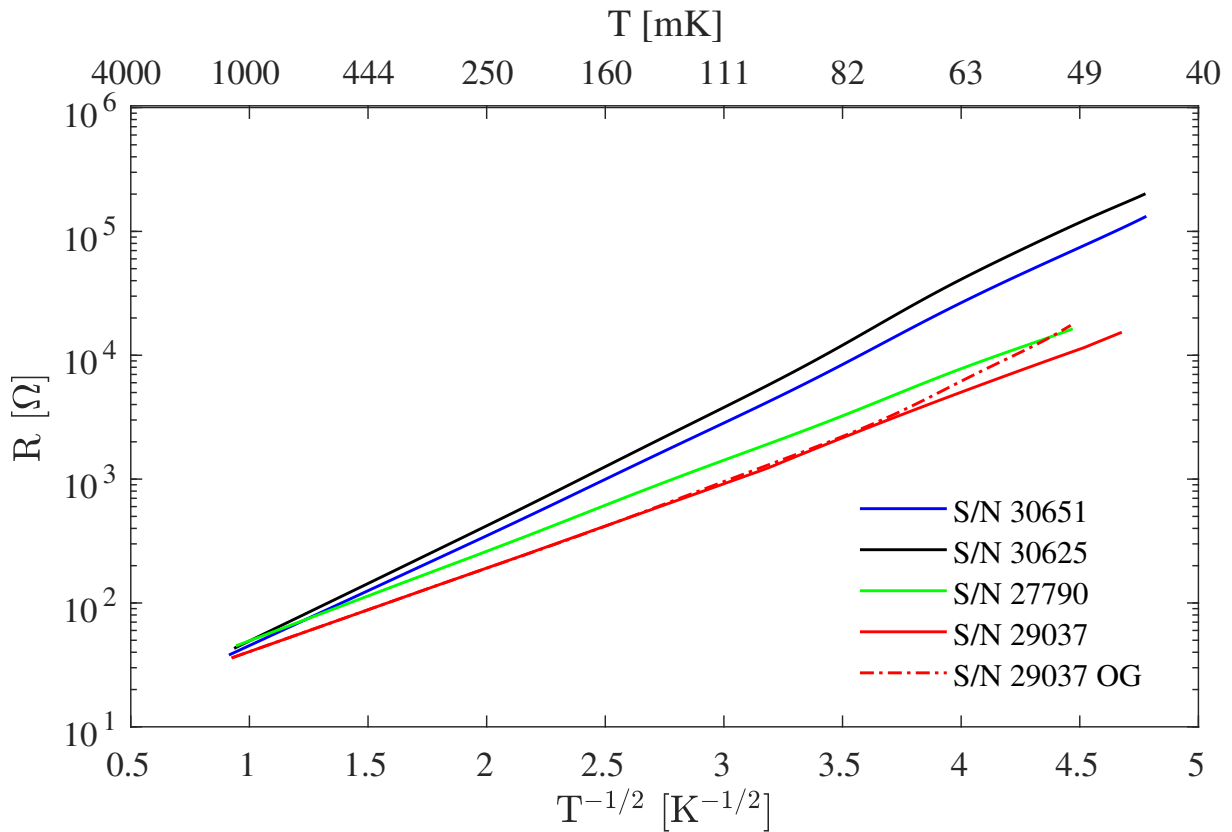

Figure 5.1: Comparison of several doped Ge temperature sensors found in the lab. Calibrations between 50 mK and 1 K were performed by LakeShore Cryotronics Inc. The original (OG) calibration for S/N 29037 was found to have errors below 100 mK.

83

The calibrations for several doped Ge sensors available in the laboratory are displayed in figure 5.1 as R versus $T^{-1/2}$. The high temperature region of these curves exhibits the theoretical behaviour [equation 5.4], with a subtle deviation at very low temperatures $T \lesssim 0.3$ K. One of the sensors purchased from Lakeshore (S/N 29037) was found to have a significant error in the calibration curve below 100 mK, despite a certificate of calibration down to 50 mK. This was confirmed by comparing the faulty sensor with three different references; a newer doped Ge sensor, ^{60}Co nuclear orientation thermometry, and paramagnetic susceptibility of cerium magnesium nitrate (CMN).

RuO$_2$ Oxide Thick Film

Thick film ruthenium oxide resistors consist of conductive RuO$_2$ powder embedded in lead-silicate glassy matrix (eg. PbO-B$_2$O$_3$-SiO$_2$) that is then deposited onto an Al$_2$O$_3$ substrate. Temperature dependence of the resistivity will depend on the ratio of metal oxide to glass, and is typically tuned for a room temperature resistance on the order of 10^2 Ω to 10^3 Ω. The mechanism of electron conduction is also described by Mott variable range hopping, where the general temperature dependence is of the form

$$\rho = \rho_0 \exp\left(T_0/T\right)^{\alpha}, \tag{5.5}$$

where ρ_0 is determined at high temperatures, $T_0 \propto N_F a^3$ where N_F is the density of states at the Fermi level, and a is the localization radius of states near the Fermi level.[129] Several theoretical models have been proposed to predict the scaling of α with temperature, which typically varies from $\alpha = 1/4$ to $\alpha = 1/2$. [130, 131, 132, 133, 134] One detailed experimental study of thick-film RuO$_2$ resistors consistently reported $\alpha = 0.345$ with accuracy <0.5% down to 6 mK.[129]

All of the RuO$_2$ thermometers used here were obtained from a single batch of Dale RC-550-20, 1 kΩ bare chip resistors. This is a commonly used brand of resistor for cryogenic thermometry because it has excellent sensitivity, reproducibility, and well desireable magnetoresistance in high magnetic fields (up to 8 T at 30 mK in Meisel *et al.*[135]). The films are deposited on a Al$_2$O$_3$ substrate and laser trimmed by the manufacturer to a nominal resistance of 1000 Ω at room temperature, with variations on the order of ~ 1 Ω. The temperature dependence of the resistance is also very similar below 1 K, showing variations on the order of only a few percent between different senso.Data points above 50 mK were obtained with a commercially calibrated doped Ge thermometer, and below 50 mK with an in-house paramagnetic cerium magnesium nitrate (CMN) susceptometer. The subtle differences between RuO$_2$ sensors are evident when they are normalized, showing $\approx$25 mK variations at the lowest temperatures investigated, as shown in figure 5.2.
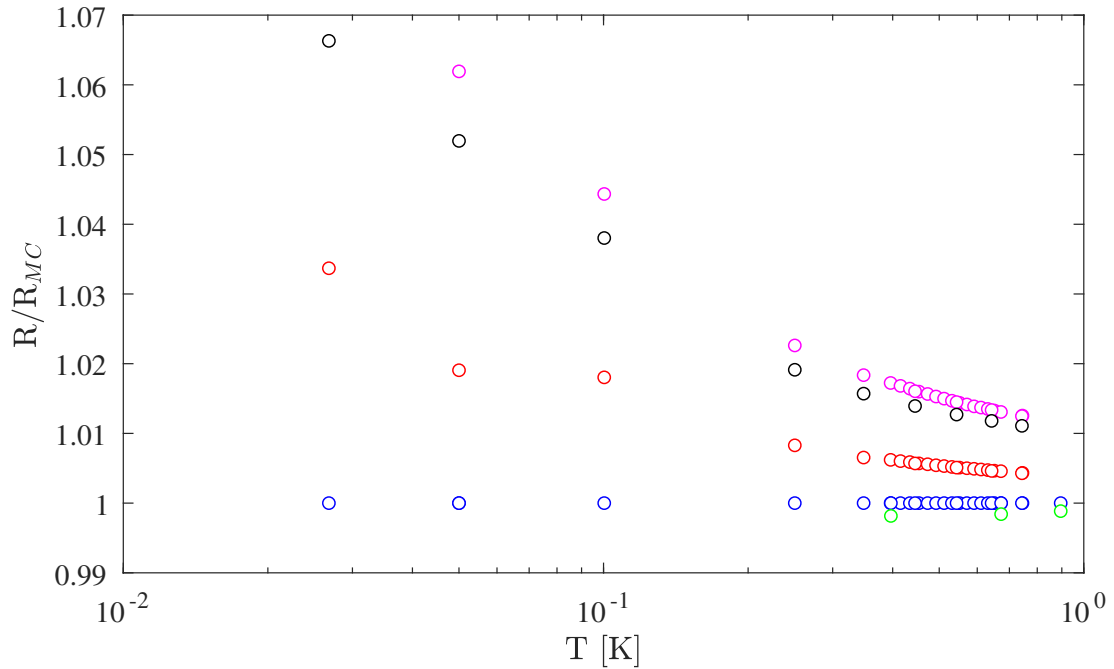
Figure 5.2: Temperature dependence of several RuO$_2$ thermometers below 1 K, normalized to a single device R$_{MC}$, to enhance the subtle differences.

The choice of a suitable function to represent the calibration can be a difficult task because a typical RuO$_2$ thermometer does not always follow the theoretical form in equation 5.5 at very low temperatures. While that model provides a sufficient representation of the data for a limited temperature range, or in the extreme limits of high and low resistance, the common approach is based on an empirical equation

$$\ln R = \sum_{n=0}^{N} a_n (\ln T)^n, \tag{5.6}$$

where a minimum number of coefficients N is chosen to give an adequate representation of the data.[135, 136] Most of the RuO$_2$ chips from our batch of 1 kΩ resistors can be accurately represented by this function with $N = 4$ or 5 parameters, as shown for a typical calibration in figure 5.3.
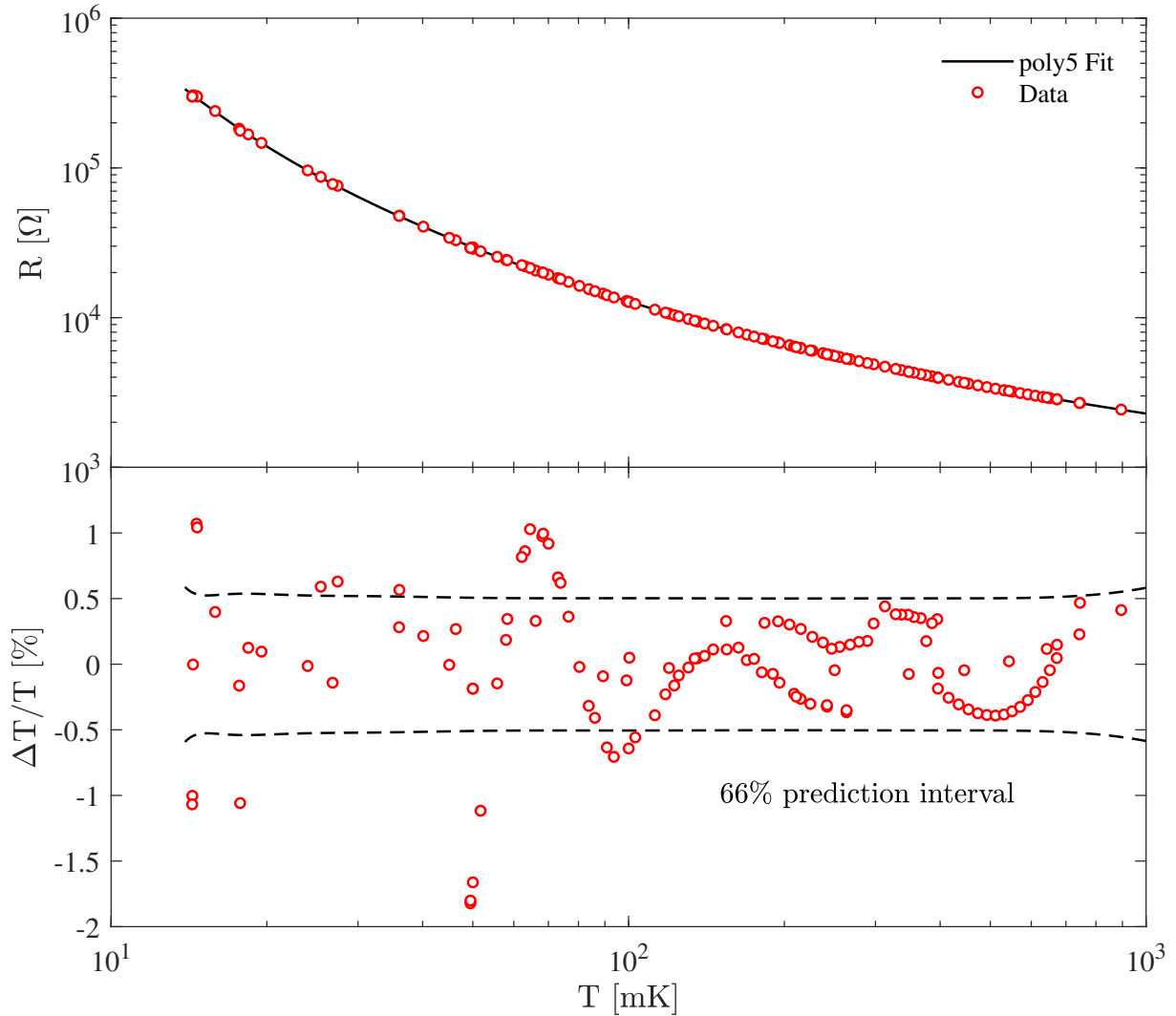
Figure 5.3: Top: Resistance vs. temperature for a tyipcal RuO$_2$ (Dale RC-550-20) 1 kΩ resistor below 1 K. The data was fit to equation 5.6 with $N = 5$ free parameters. Bottom: The fit residual, and 1σ prediction bounds.

This type of calibration procedure was carried out for each of the specific heat measurements presented in this thesis, were a new RuO$_2$ thermometer was fixed directly onto each sample. In order to ensure the accuracy of each thermometer at very low temperatures ($\lesssim 100$ mK), these samples were cooled down a second time after performing specific heat measurements with a strong thermal link (silver wire) to reduce offsets due to self heating.

Thermal noise can become an issue for very large resistances. If possible, it can be beneficial to use multiple resistors in parallel to reduce the thermal Johnson-Nyquist noise $v_T = \sqrt{4k_B T R}$ by a factor of $\sqrt{N}$ for N resistors. This was implemented for the main stage thermometer, where 4 RuO_2 thermometers (1 kΩ) were combined in parallel to reduce the electronic noise by a factor of 2. For example, a 10 kΩ resistor at 4 K has an intrinsic noise of 1.46 nV/$\sqrt{Hz}$, which surpasses the noise floor of a quality voltage amplifier.

Additional useful points for minimizing systematic errors with resistance thermometers:

- Check self-heating periodically when changing temperatures by adjusting the excitation power of the resistance bridge and look for signs of heating or cooling.

- Calibrate thermometers near important temperatures, such as features in specific heat, to reduce systematic errors.

5.2 Paramagnetic Thermometry

The magnetization of a paramagnet can provide a temperature scale for calibration. Curie's law indicates that susceptibility is inversely proportional to temperature for low levels of magnetization

$$\chi = \frac{\mu_0 M}{B} = \frac{C}{T},$$
(5.7)

where M is the resulting magnetization from an applied field B, and C is the material-specific Curie constant. In practice, deviations from this behavior occur due to factors that affect the local magnetic field, such as magnetic long-range ordering. Cerium magnesium nitrate (CMN) $Mg[Ce(NO_3)_6 \cdot 8H_2O]$ is an insulator with nearly ideal properties of a Curie paramagnet above ≈ 10 mK and an ordering temperature $T_c \approx 2$ mK that generally depends on the quality of material. The Curie constant is obtained by fitting the high temperature susceptibility to a calibrated reference. Limitations of its performance due to low thermal conductivity are avoided by tightly pressing CMN powder with silver or copper to improve the response time below 100 mK, which can approach $\gtrsim 1000$ seconds.

Two different preparations of CMN were used to calibrate the temperature of our dilution cryostat from 14 mK to 100 mK. Each of these were measured with one of the two SQUID magnetometers described in section 4.3 at a very low frequency ~ 1 to 3 Hz, and then calibrated to a commercial GRT thermometer (S/N 30651 and S/N 29037 in figure 5.1). One of the samples was prepared by compressing CMN with a roughly equal volume of silver powder. The other sample of CMN was mixed with silver epoxy in the form of a cylindrical puck. The susceptometer circuit in figure 4.2 was used to measure each of the samples, where a large current limiting resistor $R_{\mathrm{Primary}} = 100$ kΩ was necessary to provide the small excitation required to avoid self-heating of the sample. For a standard metal film resistor with temperature coefficient ± 100 ppmK^{-1}, this results in ± 10 ΩK^{-1} (where the polarity varies randomly from one resistor to another). Drifts in the electrical current by 1 part in 10^{-4} with room temperature fluctuations of the laboratory were found to have noticeable effects on the measured response when the signal-to-noise ratio of the measured susceptibility is low. These resistors were subsequently enclosed in a PID temperature controlled aluminum shield ~ 10 K above room temperature to reduce drifts observed in the amplitude of the SQUID output voltage. Some typical data before and this improvement is shown in figure 5.4.
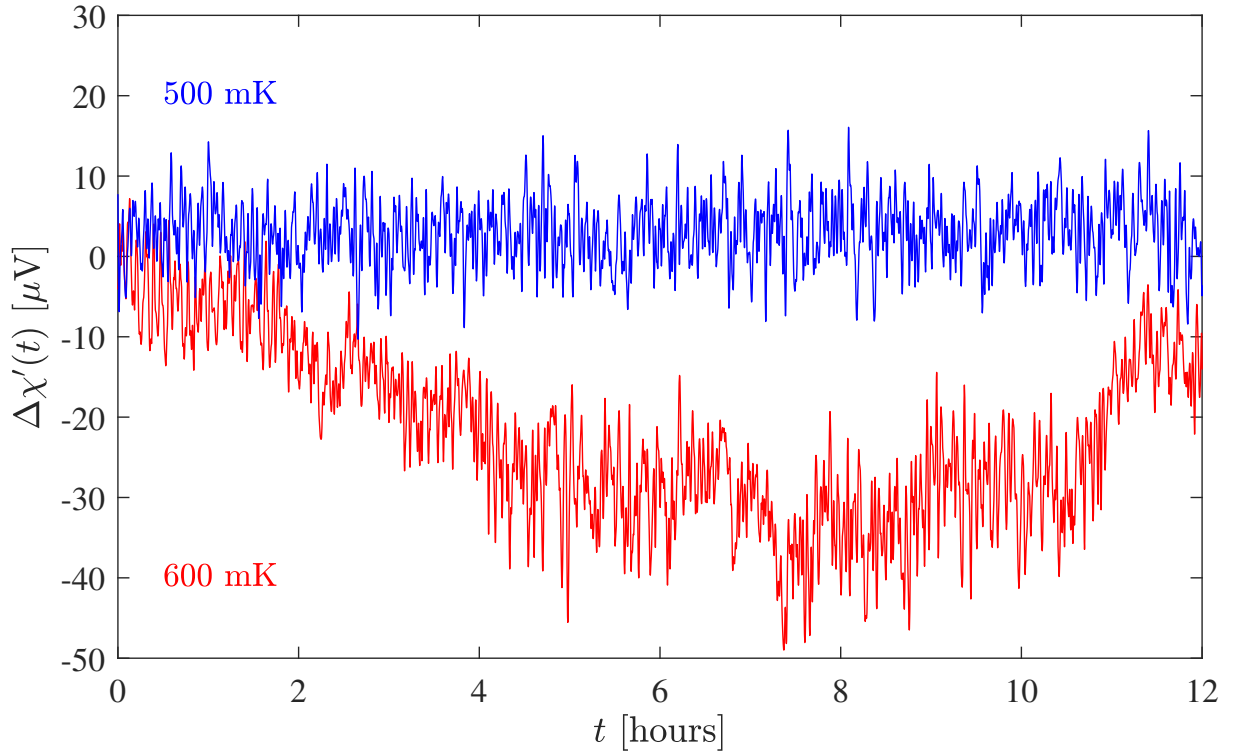
Figure 5.4: Measured susceptibility of CMN thermometer before and after improving the stability of the current source. The cryostat was held at a constant temperature throughout the duration of the experiment. Fluctuations in the CMN signal due to drifts in the temperature of the laboratory were reduced significantly when the current source was PID temperature controlled to 10°C above room temperature.

The calibration procedure for each CMN sample to a commercial GRT sensor is shown in figure 5.5 where the measured voltage is proportional to the magnetic flux produced by the sample. A linear fit to $\chi(V)$ vs T^{-1} above $\sim$75 mK was extrapolated to lower temperatures according to equation 5.7. Both samples exhibit $\propto T^{-1}$ behaviour that is expected for an ideal paramagnetic salt, confirming that both SQUID susceptometers, and CMN samples are well behaved in this temperature range.
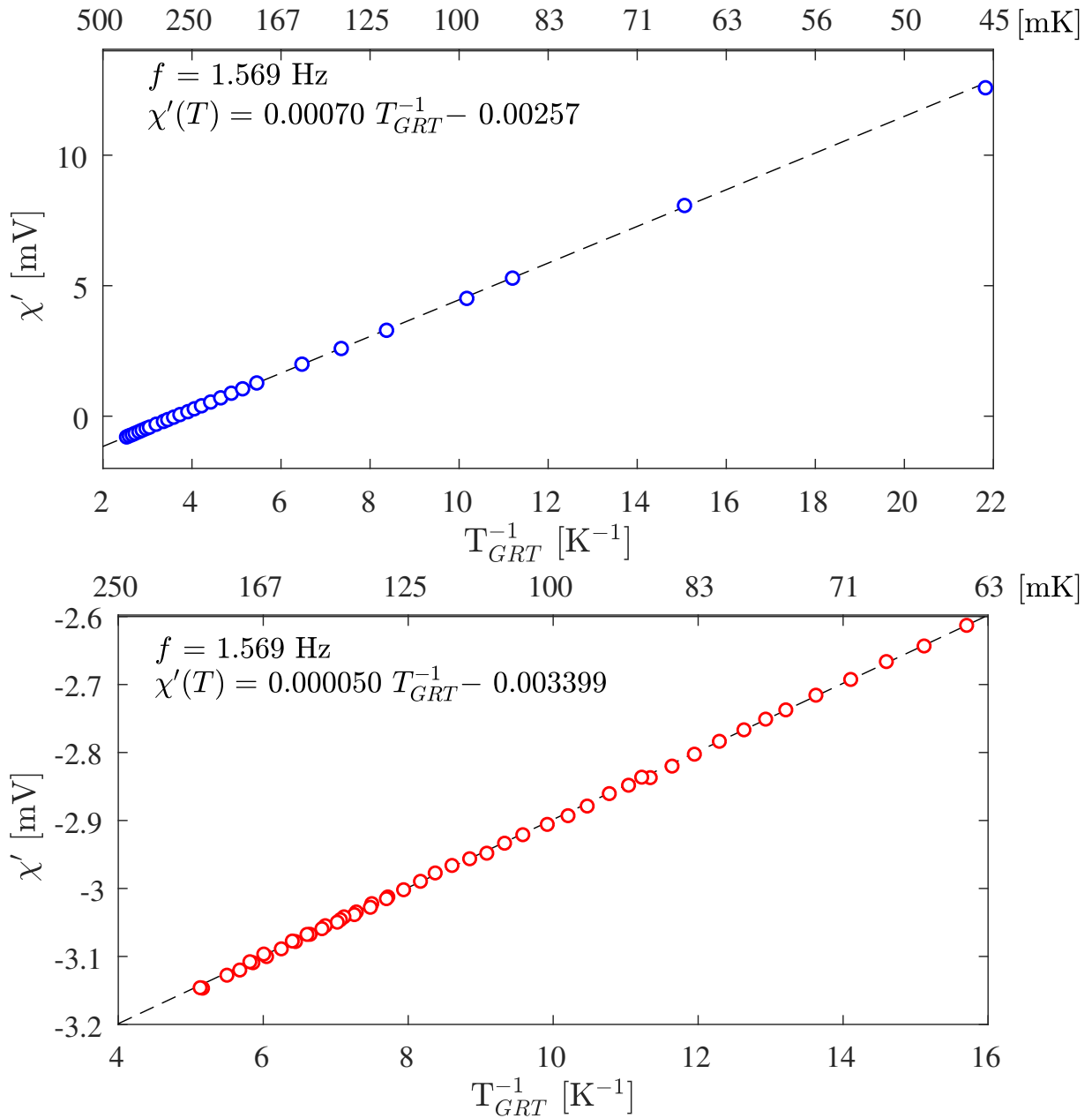
Figure 5.5: Measured susceptibility χ' (in volts) for two different samples of cerium magnesium nitrate (CMN) in the calibrated region of a commercial doped germanium sensor (GRT). Both samples follow Curies law in the measured temperature range. Error bars corresponding to the standard error of the mean $\mathrm{SE} = \sigma/\sqrt{N}$ are much smaller than the markers. Weighted least square regression was used with weights given by $(\mathrm{SE})^{-2}$.

5.3 Nuclear Orientation Thermometry

The angular distribution, or angular correlation, of γ-rays emitted from a solid can provide a method to investigate various properties of nuclear states related to their magnetic spin moment. For an ensemble of nuclear spins with no preferred direction in space, the angular distribution of emitted radiation will be isotropic, but the energy of γ-rays can be perturbed by the surrounding nuclear environment. This interaction of a nuclear spin with the surrounding hyperfine fields, or an externally applied field, can lead to an emission that is anisotropic.

Electromagnetic radiation produced by a γ-ray transition between two nuclear states with spin I_1 and I_2 with corresponding parity Π_1 and Π_2, is subject to the conservation of angular momentum. The resulting multipolar field carries angular momentum $\hbar L$ according to the selection rule

$$|I_1 - I_2| \leq L \leq |I_1 + I_2|. \tag{5.8}$$

The emitted of radiation (electric or magnetic) is determined by the change in parity, where $\Delta \Pi = (-1)^L$ for EL radiation, and $\Delta \Pi = (-1)^{L-1}$ for ML radiation.[99] Multipolar radiation is familiar from the theory of electrodynamics, where radiation fields are described by vector spherical harmonics $\mathbf{X}_{lm}(\theta, \phi)$. In the case of a pure multipole with quantum numbers l and m, the time averaged power radiated per unit solid angle Ω has the form

$$\frac{dP(l,m)}{d\Omega} = \frac{Z_0}{2k^2}|a_{lm}|^2|\mathbf{X}_{lm}|^2, \tag{5.9}$$

where the first few angular distributions $|\mathbf{X}_{lm}|^2$ are given by: [137]

l	$m = 0$	$m = \pm 1$	$m = \pm 2$
1 (dipole)	$\frac{3}{8\pi}\sin^2\theta$	$\frac{3}{16\pi}\left(1 + \cos^2\theta\right)$	
2 (quadrupole)	$\frac{15}{8\pi}\left(\sin^2\theta\cos^2\theta\right)$	$\frac{5}{16\pi}\left(1 - 3\cos^2\theta + 4\cos^4\theta\right)$	$\frac{5}{16\pi}\left(1 - \cos^4\theta\right)$
$\vdots$			

The distribution of a pure multipole with the form in equation 5.9 is isotropic because of the property

$$\sum_{m=-l}^{l}|\mathbf{X}_{lm}(\theta,\phi)|^2 = \frac{2l+1}{4\pi}. \tag{5.10}$$

In classical electrodynamics, the a_{lm} in equation 5.9 are electric and magnetic multipole coefficients, which can be determined by solving Maxwell's equations for the particular source. When the dimensions of the source are small compared to the emitted wavelength ($kr_{\text{nuc}} << 1$) as often assumed for nuclei, the electronic multipole coefficient scales as [137]

$$a_{lm}^E \propto Q_{lm} + Q'_{lm}, \tag{5.11}$$

where the electronic multipole moments generated by an electric charge distribution ρ are given by

$$Q_{lm} = \int r^l Y_{lm}^* \rho d^3x \tag{5.12}$$

$$Q'_{lm} = -i\frac{k}{(l+1)c} \int r^l Y_{lm}^* \boldsymbol{\nabla} \cdot (\boldsymbol{r} \times \boldsymbol{M}) d^3x \tag{5.13}$$

where Q'_{lm} indicates the induced electric multipole moment due to the magnetization density $\boldsymbol{M}$. Similarly, the magnetic multipole coefficient scales as

$$a_{lm}^M \propto M_{lm} + M'_{lm}, \tag{5.14}$$

where the magnetic multipole moments are determined by the magnetization densities $(\boldsymbol{r} \times \boldsymbol{J})/2$ and $\boldsymbol{M}$

$$M_{lm} = -\frac{1}{l+1} \int r^l Y_{lm}^* \boldsymbol{\nabla} \cdot (\boldsymbol{r} \times \boldsymbol{J}) d^3x \tag{5.15}$$

$$M'_{lm} = -\int r^l Y_{lm}^* \boldsymbol{\nabla} \cdot \boldsymbol{M} d^3x. \tag{5.16}$$

This is a good starting point to introduce the angular correlation function $W(\theta)$ at temperature T, which describes the angular distribution of measured γ-radiation, expanded in the set of orthogonal Legendre polynomials $P_\lambda(\cos\theta)$

$$W(\theta) = \sum_{\lambda=0}^{\lambda_{\text{max}}} \left[B_\lambda(I,T) U_\lambda A_\lambda Q_\lambda \right] P_\lambda(\cos\theta). \tag{5.17}$$

Coefficients in equation 5.17 U_λ are angular momentum reorientation coefficients which take into account the effect of unobserved intermediate transitions, A_λ are the angular correction coefficients that account for mixing of multipolar radiation fields, and Q_λ are solid angle correction factors that take into account the complex interactions within the finite size detector crystal. These values are described in sufficient detail for experimental

92

nuclear orientation theromometry by H. Marshak.[138] Particular details regarding the initial orientation of nuclear spins is captured by the statistical tensors

$$B_\lambda(I,T) = \sqrt{(2I+1)(2\lambda+1)} \sum_{m=-I}^{+I} (-1)^{I-m} \begin{pmatrix} I & I & \lambda \\ m & -m & 0 \end{pmatrix} a_m(T), \qquad (5.18)$$

where the array () is evaluated as a Wigner $3j$ symbol, and the relative population of each nuclear spin sub-state m is determined by the Boltzmann distribution

$$a_m(T) = \frac{e^{-E_m/kT}}{\sum_m e^{-E_m/kT}}. \qquad (5.19)$$

At relatively high temperatures $T >> E_m/k_B$, the nuclear sub-states are equally occupied, while at low temperatures the shift in population is towards low energy states E_m. In the presence of a magnetic field, the particular distribution of E_m is also influenced by the splitting of the nuclear spin state I. The source of this splitting can be hyperfine fields surrounding the nucleus, or Zeeman splitting by an external field. For the particular case of cobalt nuclear orientation thermometry, a small concentration of the radioactive isotope ^{60}Co is randomly distributed in a host crystal made from the stable isotope ^{59}Co. The effective hyperfine interaction Hamiltonian for the nuclear magnetic moment $\boldsymbol{\mu}$ in an effective hyperfine field $\boldsymbol{H}_{\text{eff}}$ produced by ^{59}Co is given by

$$\mathcal{H}_{\text{eff}} = -\boldsymbol{\mu} \cdot \boldsymbol{H}_{\text{eff}} + P\left[I_z^2 - \frac{1}{3}I(I+1)\right] \qquad (5.20)$$

where the quadrupole coupling constant is

$$P = \frac{3e^2qQ}{4I(2I-1)}. \qquad (5.21)$$

In a suitable orthogonal basis, the energy levels of this Hamiltonian are given by

$$E_m = -\frac{\mu m}{I}H_{\text{eff}} + P\left[m^2 - \frac{1}{3}I(I+1)\right]. \qquad (5.22)$$

In practice, these hyperfine parameters can be determined with high precision from another measurement such as specific heat or nuclear magnetic resonance (NMR). Because the effective field at the nucleus is also affected by demagnetization effects, the geometry of the sample is prepared as a long needle to reduce this effect. In the case of ^{60}CoCo(hcp) γ-ray thermometery, measured hyperfine splitting is $\Delta_{\text{hf}} = \frac{\mu H_{\text{eff}}}{kI} = -6.0725(24)$ mK, and

the quadrupole constant is given by $P/k = -2.2(4)$ μK. [138] This quadrupolar constant is relatively small, resulting in a nearly even energy spacing that is determined primarily by the hyperfine field.
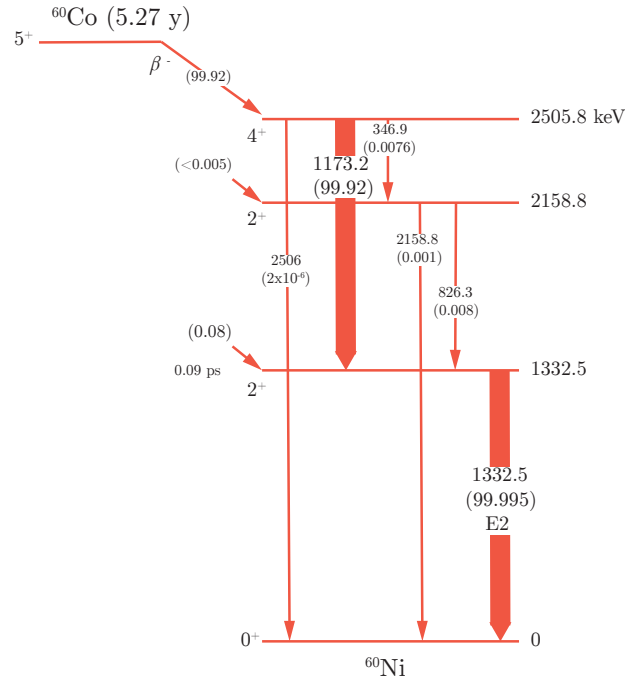
Figure 5.6: Nuclear decay scheme for ^{60}Co. Figure adapted from reference [138].

The nuclear decay scheme for ^{60}Co is shown in figure 5.6 where the isotope has a half life of 5.27 y, and decays by $\beta-$ particle emission with a branching of 99.92% to the 4^+ level of ^{60}Ni. Two dominant γ-ray emissions occur from the 4^+ to 2^+ decay (1173.2 keV), followed by 2^+ to 0^+ (1332.5 eV). Both of these transitions have pure E2 character (electric dipole), but the former has a small admixture with M3 character (magnetic quadrupole), $\delta(M3/E2) \approx -0.0008(11)$, corresponding to an error in temperature $< 0.28\%$ when neglected.[138]

For most cases of γ radiation, only the first two terms B_2 and B_4 are required because higher order B_λ terms decrease rapidly with large λ. These statistical tensors are calculated from the 'moments of orientation', as introduced by Tolhoek and Cox (1953) [139], and

have the generalized expression

$$f_\lambda(I) = \binom{2\lambda}{\lambda}^{-1} I^{-\lambda} \sum_{m=-I}^{I} \sum_{n=0}^{\lambda} (-1)^n \frac{(I-m)!(I+m)!}{(I-m-n)!(I+m-\lambda+n)!} \binom{\lambda}{n}^2 a_m. \qquad (5.23)$$

Explicit evaluation of the first two parameters yields

$$f_2 = I^{-2} \left[\sum_{m=-I}^{I} m^2 a_m - \frac{1}{3} I(I+1) \right]$$

$$f_4 = I^{-4} \left[\sum_{m=-I}^{I} m^4 a_m - \frac{1}{7} \left(6I^2 + 6I - 5 \right) \sum_{m=-I}^{I} m^2 a_m + \frac{3}{35} I(I-1)(I+1)(I+2) \right] \qquad (5.24)$$

where an additional factor is required to obtain the B_λ coefficients, which can now be computed straightforwardly from

$$B_\lambda(I) = \binom{2\lambda}{\lambda} I^\lambda \sqrt{\frac{(2\lambda+1)(2I+1)(2I-\lambda)}{(2I+\lambda+1)!}} f_\lambda(I). \qquad (5.25)$$

Additional constants that are required to compute the angular distribution $W(\theta, T)$ in equation 5.17 particular to ^{60}CoCo(hcp) are [138]

$\Delta_{\rm hf}$ (mK)	P/k (mK)	U_2	U_4	A_2	A_4
-6.0725(24)	-0.0022(4)	0.703731	0.227128	-0.597614	-1.069046

The solid angle correction factors Q_λ are integrals that depend on geometry of the detector, its distance from the source, and the linear absorption coefficient τ for the particular crystal used in the detector (NaI used here, but Ge(Li) are also very common). To be precise, the linear absorption coefficients depend on energy of the $\gamma-$rays $\tau(E_\gamma)$ and require Monte Carlo simulation, but the error introduced by assuming a constant value is negligible for the narrow range of energies considered for ^{60}CoCo nuclear orientation. The solid-angle correction factors for scintiallation detectors with cylindrical geometry are available in reference [140].

The angular distribution function below 100 mK is highly anisotropic, as shown in the polar plot in figure 5.7. Orienting the scintillation detector along the crystal field axis ($\theta = 0$) provides the greatest variation in $\gamma-$ray intensity with temperature, which peaks in sensitivity around 7 mK. The normalized angular distribution function is then compared
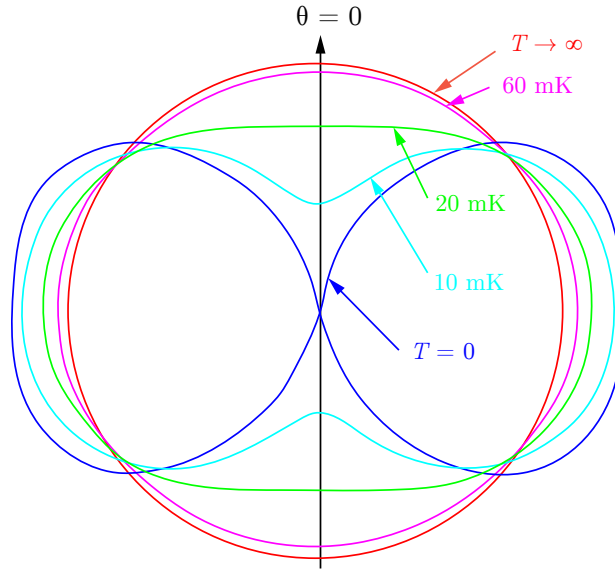
Figure 5.7: Symmetry of the angular distribution function $W(\theta, T)$ for several low temperature values. Figure adapted from reference [138].

with experimental data by comparing the 'cold' anisotrpic count rate at a low temperature C_C to the 'warm' isotropic count rate C_W at a high temperature with the ratio

$$W(0, T) = \frac{C_C}{C_W}. \tag{5.26}$$

^{60}CoCo Results

^{60}CoCo(hcp) gamma ray spectroscopy was performed on a metallic crystal purchased from Oxford Instruments about 10 years ago, at which time it had an activity of 175 kBq. This sample was estimated to have a remaining activity of $\sim$40 kBq assuming a half-life of 5.26 years for ^{60}Co, and thus required longer count times with the detector. The metallic crystal was soldered with minimal heat to a copper block with Wood's metal (too much heat can re-orient the crystal) and mounted to the same copper stage of the cryostat as the calibrated thermometers. The scintillation detector from Alpha Spectra Inc., contained a cylindrical sodium iodide (NaI) crystal of radius 1.5" and length 3" located approximately $\sim$ 24 inches from the radioactive source, and was aligned co-axially with the long direction of the oriented needle-shaped ^{60}CoCo (hcp) crystal.
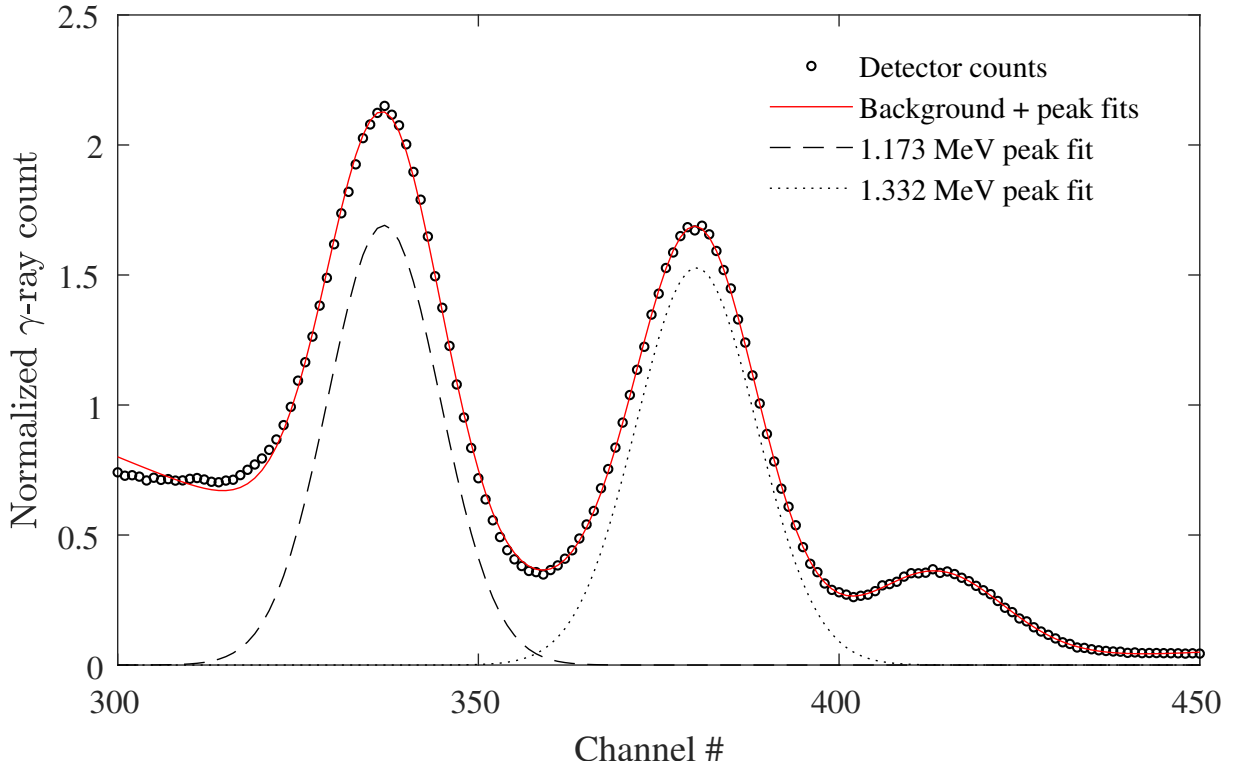
Figure 5.8: Gamma ray spectrum obtained using the NaI detector multi-channel analyzer for ^{60}CoCo for a period of 9 hours at 14 mK. The number of counts per channel are normalized by the time of the acquisition period.

The typical $\gamma-$ray spectrum obtained at the base temperature of the cryostat is shown in figure 5.8, where three distinct peaks are visible in the region. From left to right, the first two peaks are the 1.173 MeV γ-ray emission from the 4^+ to 2^+ level and the 1.3325 MeV transition from the 2^+ to 0^+ level. The third peak is a temperature-independent background peak that was subtracted from each spectrum. All three peaks were numerically fit to three independent gaussians with a quadratic polynomial background. The functional form used is given by

$$f(x) = a_1 e^{-\frac{1}{2}\left(\frac{x-b_1}{c_1}\right)^2} + a_2 e^{-\frac{1}{2}\left(\frac{x-b_2}{c_2}\right)^2} + a_3 e^{-\frac{1}{2}\left(\frac{x-b_3}{c_3}\right)^2} + d_1 + d_2 x + d_3 x^2 \qquad (5.27)$$

The background signal of any particular scintillation detector is strongly dependent on the nearby environment surrounding the detector. This is because scattering of x-rays, and other events produce signals within the detector that are difficult to control. It is common

97

practice is to measure the total photopeak area by fitting each peak to a gaussian function with the expression

$$f(x) = f_0 e^{-\frac{1}{2}\left(\frac{x-b}{c}\right)^2} \left(1 + \alpha_1(x - x_0)^n + \alpha_2(x - x_0)^m\right), \tag{5.28}$$

which is often able to capture the asymmetry in the low energy side of a gaussian peak caused by scattering internal to the detector. [141] However, for this particular experiment, the functional form in equation 5.27 provides a better fit to the observed gamma ray spectrum. The total photopeak area was summed at each temperature to obtain the total normalized counts shown in figure 5.9. The temperature scale in this figure, which was obtained with paramagnetic CMN shows excellent agreement with ^{60}CoCo nuclear orientation thermometry.
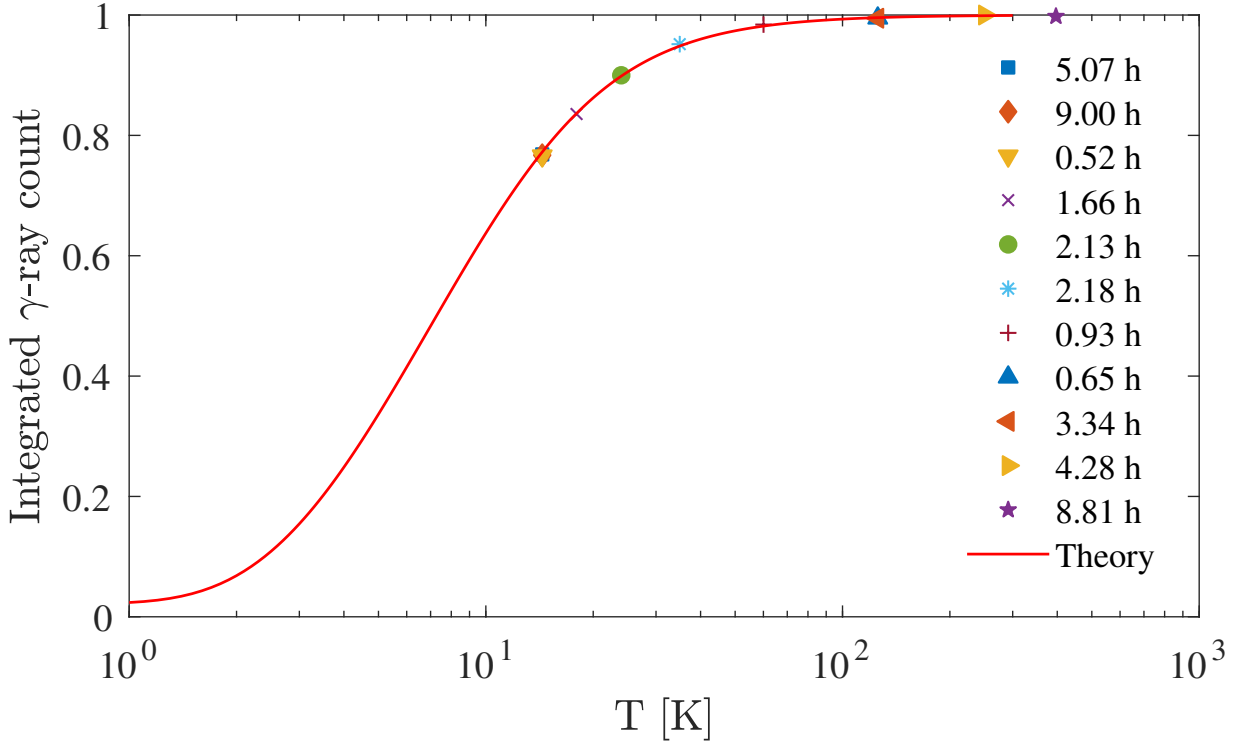

Figure 5.9: Temperature dependence of theoretical and measured photopeak area emitted by ^{60}CoCo on the dilution cryostat. The temperature scale obtained with paramagnetic CMN thermometry shows excellent agreement with the theoretical curve down to 14 mK.

Part III

Magnetic Pyrochlores

Chapter 6

Specific Heat of Dysprosium Titanate $Dy_2Ti_2O_7$

6.1   Background

Magnetic susceptibility measurements on $Dy_2Ti_2O_7$ below 1 K provide compelling evidence for very slow dynamics in the frozen spin-ice state, with characteristic frequencies near 1 mHz below 0.5 K. This relaxation is exponentially activated with an energy barrier on the order of 10 K.[23, 126, 26] This observation suggests that if a magnetic ordering mechanism is active at these temperatures, then the equilibrium properties of the material should evolve on similar timescales. The original hypothesis for this work was that changes in the lattice temperature are reflected in the magnetic spins through the mechanism of spin-phonon coupling on timescales determined by the characteristic magnetic relaxation. In order to ensure adequate thermal equilibration, and to avoid quenching the system, heating and cooling procedures should be performed on timescales that match the relaxation of the magnetic system. This provided motivation to re-measure the low temperature specific heat in this temperature range, paying particular attention to thermal equilibrium on similar timescales.

In a common quasi-adiabatic heat pulse calorimeter, power is delivered to the sample within a short duration of time, and the resulting temperature change is measured. For an idealized system where the thermal conductance of the weak link K is much less than the internal thermal conductance of the sample, the relaxation following a heat pulse can be modeled as a single time-constant exponential, given by $\tau = C/K$, where C is the total specific heat. If the ideal conditions are not met, then the thermal relaxation may

consist of multiple τ. The adiabatic heat pulse method is not a desirable technique for systems with very slow internal relaxation because the sample cannot equilibrate rapidly within the duration of a short heat pulse. In order to avoid the complications involved with multiple time-constants, a calorimetric method involving numerical integration of the total heat flowing across the thermal link was employed. This method of analysis, discussed in section 3.3, accounts for the "distributed τ effect" in relaxation calorimetry.[105] It is also insensitive to the internal configuration of the sample and the calorimeter, because it is based on the simple concept of energy conservation.[106] The total specific heat of the sample and calorimeter is given by

$$C(T) = \frac{1}{\Delta T(0)} \int_0^\infty \dot{Q}(t)dt \tag{6.1}$$

where $\dot{Q}(t) = K(T)\Delta T(t)$ is the rate of heat flowing out of the sample across the weak link of thermal conductivity K, and $\Delta T(t) = T(0) - T_B$ is the temperature difference between the sample and temperature controlled stage T_B. Simply put, the specific heat is the heat flow rate integrated over time at a given temperature. The distributed τ effect becomes noticeable in $Dy_2Ti_2O_7$ below about 600 mK where magnetic excitations out of the spin ice manifold are less favorable, and the entropy of the system is very close to Pauling's residual value $(R/2)\ln(3/2)$.

6.2 Methods

Specific heat measurements were performed in nominally zero field ($< 10^{-3}$ G) on a magnetically shielded dilution refrigerator. The crystal sample of $Dy_2Ti_2O_7$ was prepared at McMaster University using the floating zone technique was also characterized with magnetic susceptibility measurements by Revell *et al.,* and Yaraskavitch *et al.* [126, 25]. This crystal sample had a mass of 16.6 mg, and rectangular dimensions $2 \times 1 \times 1$ mm. Another 49.3 mg polycrystalline powder sample, left over from the growth rod of this crystal, was cold-pressed with an equal volume of silver powder to improve its thermal conductance. Platinum tungsten $Pt_{91}W_9$ wire was used as a weak link to connect each sample to the cryostat, with thermal conductance $K/T \approx 2.8 \times 10^{-8}$ WK^{-2} and 1.2×10^{-7} WK^{-2}, respectively, for the single crystal and powder. The measured temperature dependence for these weak links are shown in figure 6.1, where each data point was obtained by measuring the temperature change ΔT for a given power P delivered to the sample heater $K = P/\Delta T$, at each temperature step in the relaxation method. Deviations from the linear Wiedemann-Franz law $K \propto T$ expected for the metallic weak link are likely contributions due to thermal

contact resistance (Kapitza boundary resistance). These contributions do not affect the results because they are characterized by an empirical fit to $K(T)$, which is then used in equation 6.1 to compute the specific heat.
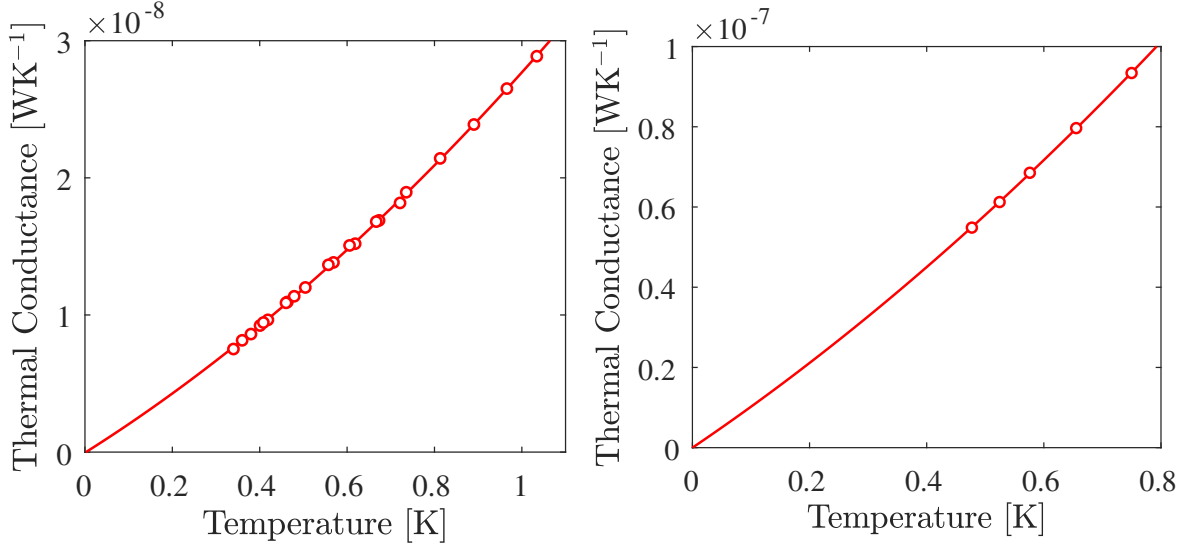
Figure 6.1: Thermal conductance of weak link vs. temperature obtained from $Dy_2Ti_2O_7$ relaxation measurements for the single crystal (left), and the polycrystalline powder (right). The solid line represents a second order polynomial fit that captures the behaviour.

The thermal relaxation technique was implemented by applying a constant power with the sample heater, thereby raising its temperature by about ~ 5 to 10% above the thermal reservoir. This power was held constant for at least the same amount of time that the thermal relaxation was measured. As mentioned previously, this step was crucial to ensure that the slow magnetic system had adequate time to thermally equilibrate with the lattice. After the heater was switched off, the thermal relaxation was recorded until changes in temperature were no longer detectable within the resolution of the instrumentation. This time required was found to increase exponentially from ~ 100 seconds at 1 K to > 100 hours at 0.34 K, where measurements become restricted by the long timescales.

The temperature of the single crystal throughout the entire duration of the measurement (approximately 2 months) is shown in figure 6.2 to illustrate the cooling protocol that was implemented. This may be used as a guide to estimate the cooling rate required to keep the material in adequate thermal equilibrium for a similar measurement.
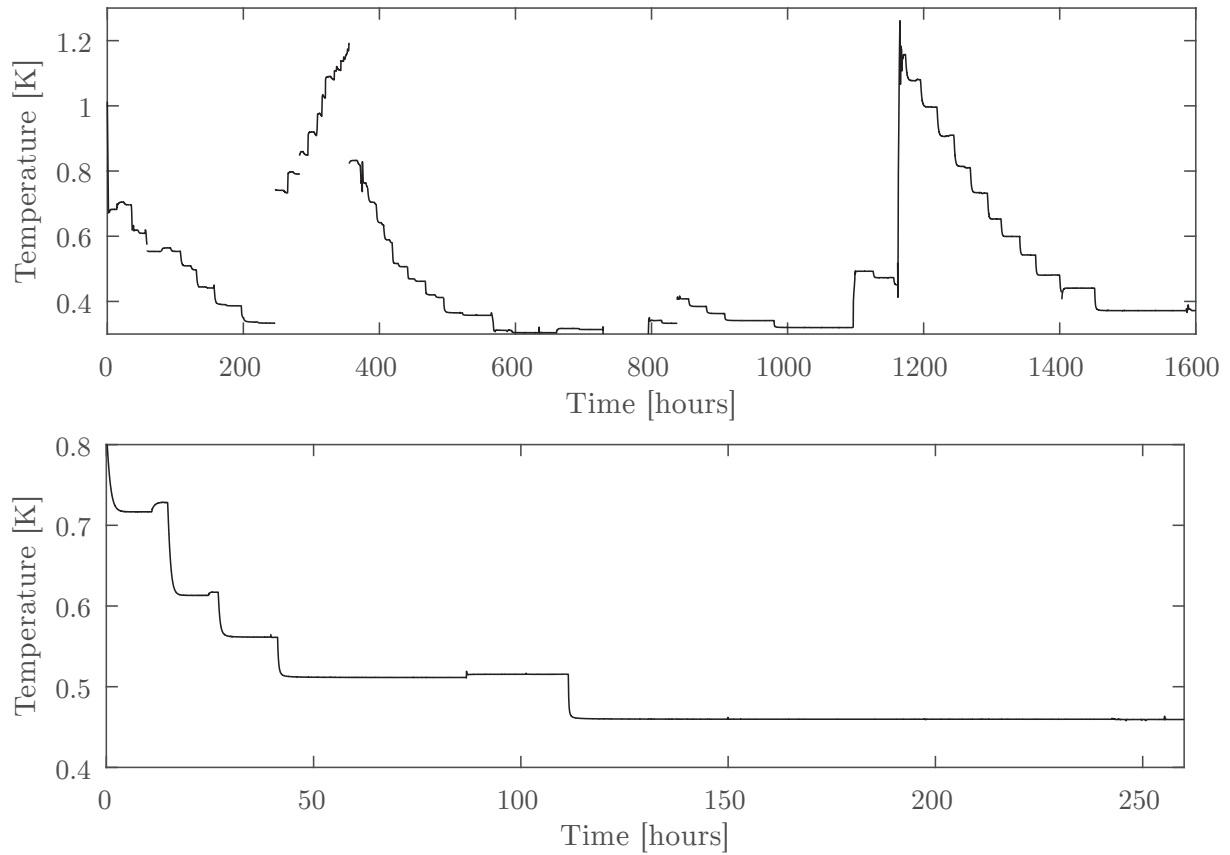
Figure 6.2: Cooling history of the $Dy_2Ti_2O_7$ crystal (top) and polycrystalline powder (bottom) throughout the entire thermal relaxation measurements.

6.3   Results

The results presented in this chapter were also published in reference [142]. Thermal relaxation curves for the single crystal sample between 0.34 K and 1.034 K are shown in figure 6.3, where the change in temperature ΔT is normalized at the start of each curve. These plots indicate that relaxation above 0.6 K is well characterized by a single exponential, which appears as a straight line on the log-linear plot. Below this temperature, a bend in the curves becomes apparent, which is characteristic of the distributed $\tau-$effect described earlier. Based on a phenomenological model of relaxation, it is possible to fit these curves to a sum of exponential functions and extract the specific heat.

Figure 6.3: Normalized thermal relaxation of $Dy_2Ti_2O_7$ at various temperatures. Typical thermal relaxation measurements acquire data for $\leq$600 s (dashed vertical line), while the quasiadiabatic heat pulse method is typically limited to a time window of $\sim$15 s (dotted vertical line near $t = 0$). ΔT values are 5 to 10% of the nominal cryostat temperature.

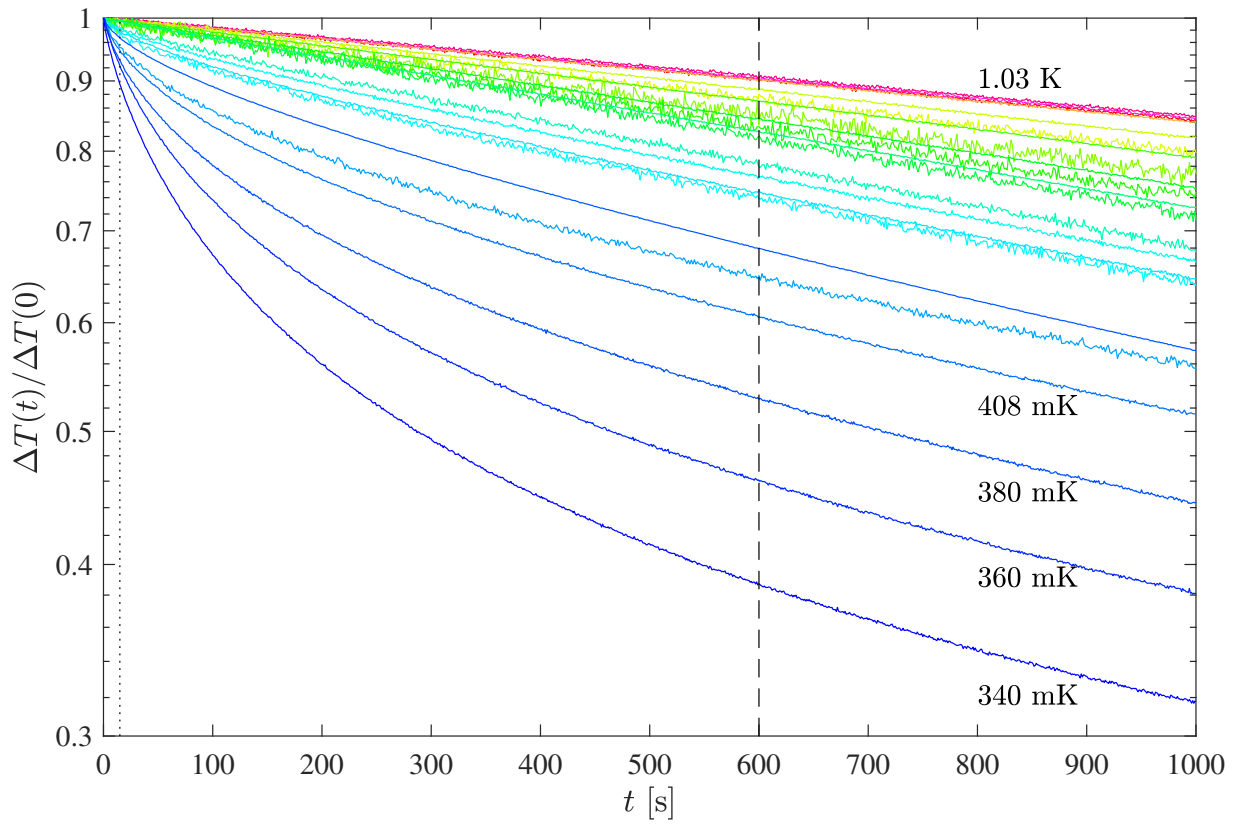The vertical line at 15 s corresponds to the typical relaxation timescale that was used to measure similar compounds using the quasi-adiabaitc heat pulse method,[1] and the line at 600 s indicates the maximum cutoff that was previously reported for relaxation measurements on $Dy_2Ti_2O_7$.[143] These timescales are adequate for $T > 600$ mK where the relaxation is captured by a single exponential, but an extrapolation beyond these timescales would not describe the true shape of the relaxation curve at lower temperatures.

The distributed $\tau-$effect becomes even more noticeable when the time axis is extended to longer timescales, as shown in figure 6.4. In particular, the relaxation can no longer be represented as a finite sum of exponential functions below 600 mK. The data can be integrated numerically using equation 6.1 to obtain the specific heat.
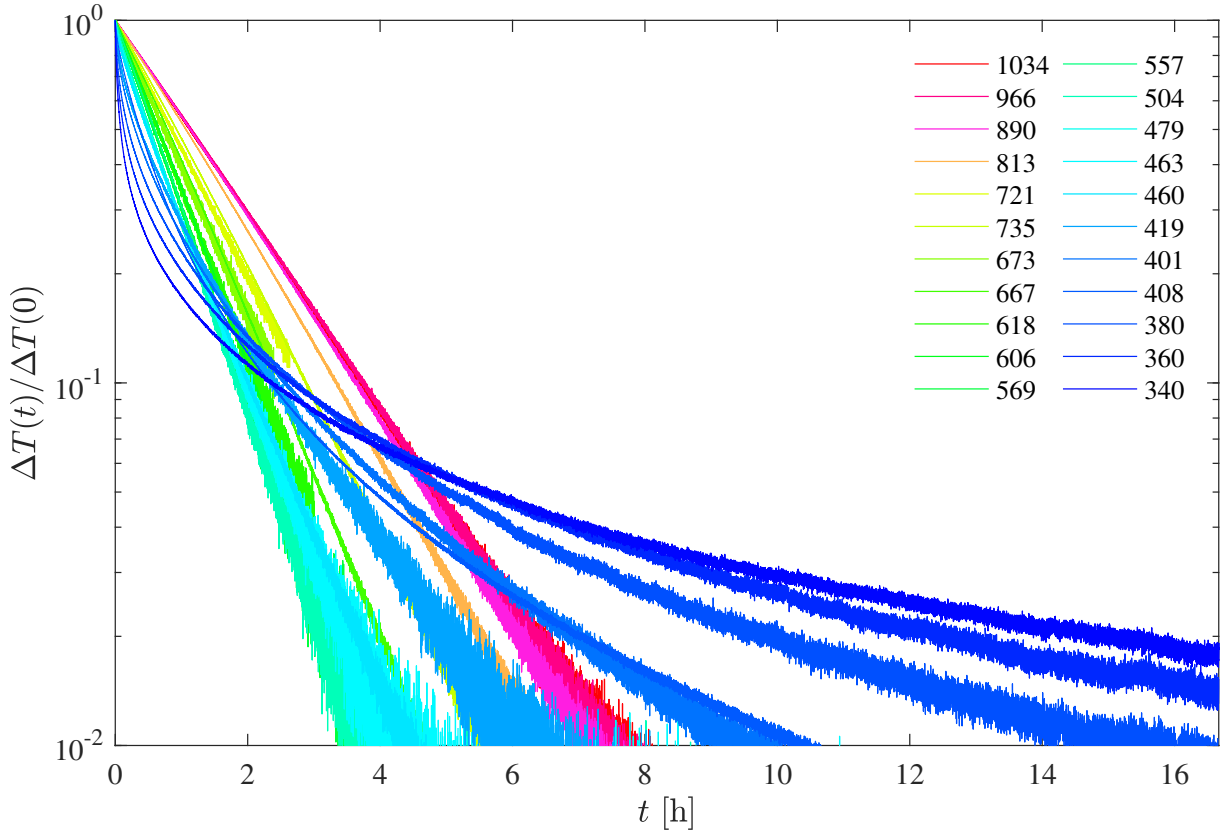
Figure 6.4: The same relaxation curves as in figure 6.3, with the time axis extended beyond 1000 s. Inset: Thermal relaxation time constants obtained by fitting the tail of the decay curve measured below 0.5 K agree with the Arrhenius-like behaviour of the magnetic relaxation time observed with susceptibility measurements.

Fitting the tail end of the data to an exponential function also provides an estimate of the average thermal relaxation time intrinsic to the material, shown in the inset of figure 6.4. It appears that the characteristic timescale of thermal relaxation in $Dy_2Ti_2O_7$ below 0.5 K behaves Arrhenius-like $\tau = \tau_0 \exp(-E_A/T)$ with an energy barrier on the order of $E_A \approx 10$ K, consistent with characteristic magnetic relaxation obtained from ac- and dc-susceptibility measurements $E_A = 9.79$ K.[126, 23] This connection indicates that slow thermal relaxation may originate from magnetic ordering, as originally hypothesized.

A natural way to present the relaxation data, is to plot the rate of heat leaving the sample as a function of time $\dot{Q}(t) = K(T)\Delta T(t)$, which is integrated to obtain the total specific heat (equation 6.1). The rate of heat-flow for the single crystal at 340 mK is shown in figure 6.5.
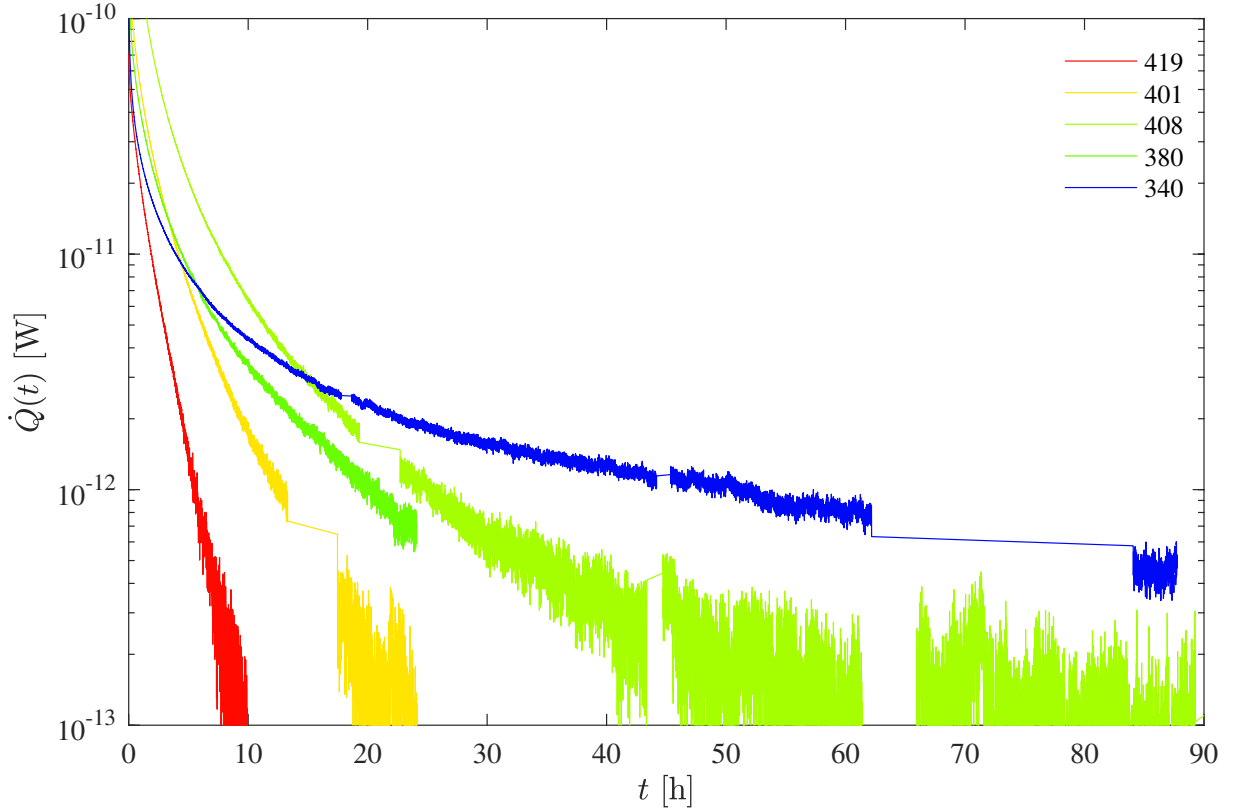
Figure 6.5: Heat flow rate versus time for the single crystal sample of $Dy_2Ti_2O_7$ at low temperature revealing the slow release of heat at the pW level.

The observed behaviour can be interpreted in the context of a very general circuit model, that describes thermal coupling between the lattice and other degrees of freedom such as magnetic spins, nuclear, or electronic degrees of freedom.
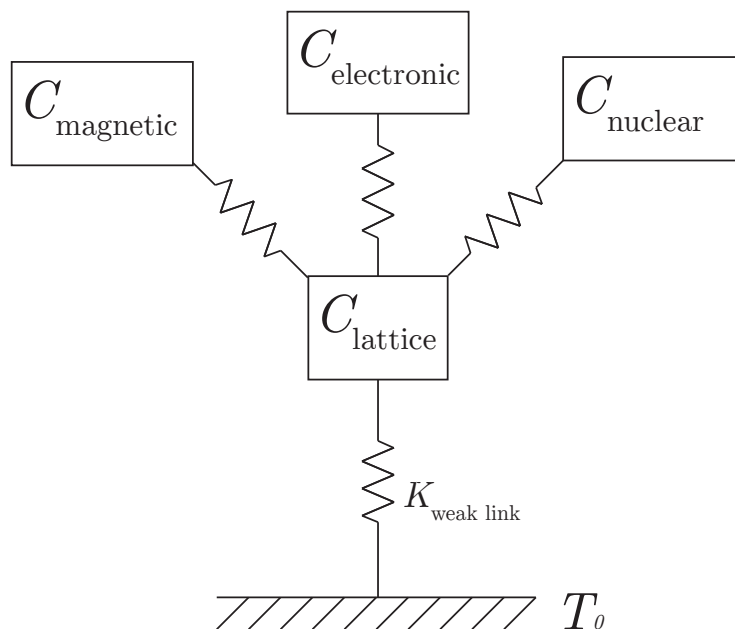
Figure 6.6: Simplified model of heat flow between the lattice and other degrees of freedom.

After integrating the heat flow for each relaxation curve, the resulting specific heat shown in figure 6.7 shows significant differences from previous measurements reported in the literature. An upturn in c/T below 0.6 K is evident, which is not captured by conventional specific heat methods. The polycrystal powder, which is typically expected to be less prone to material defects than a single crystal, also exhibits the onset of an upturn. Specific heat of the single crystal was also analyzed by restricting the relaxation time window to 600 seconds, which qualitatively reproduces the results reported in the literature. While this is not a strict comparison because those samples were not in equilibrium, it illustrates qualitative features that are associated with non-equilibrium behaviour. Disparities in the collection of measurements from the literature are likely due to variations in the cooling procedures used.
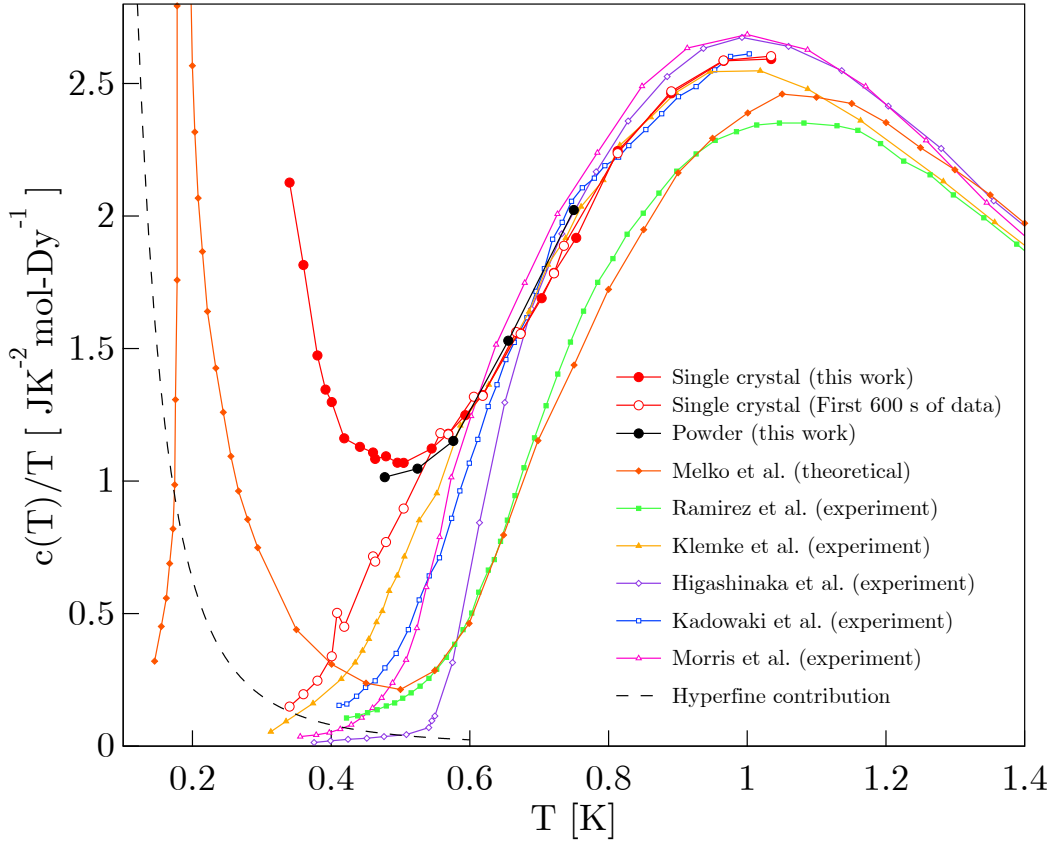
Figure 6.7: Specific heat versus temperature of $Dy_2Ti_2O_7$ in zero field.

The entropy obtained by integrating c/T from high to low temperature is shown in figure 6.8. Data above 1 K was not measured for the particular samples studied here because the variation among samples published in the literature was negligible in this temperature range, and those values could be used for the integral. The result does not exhibit a plateau at Pauling's residual entropy value once equilibrium is established in the material.
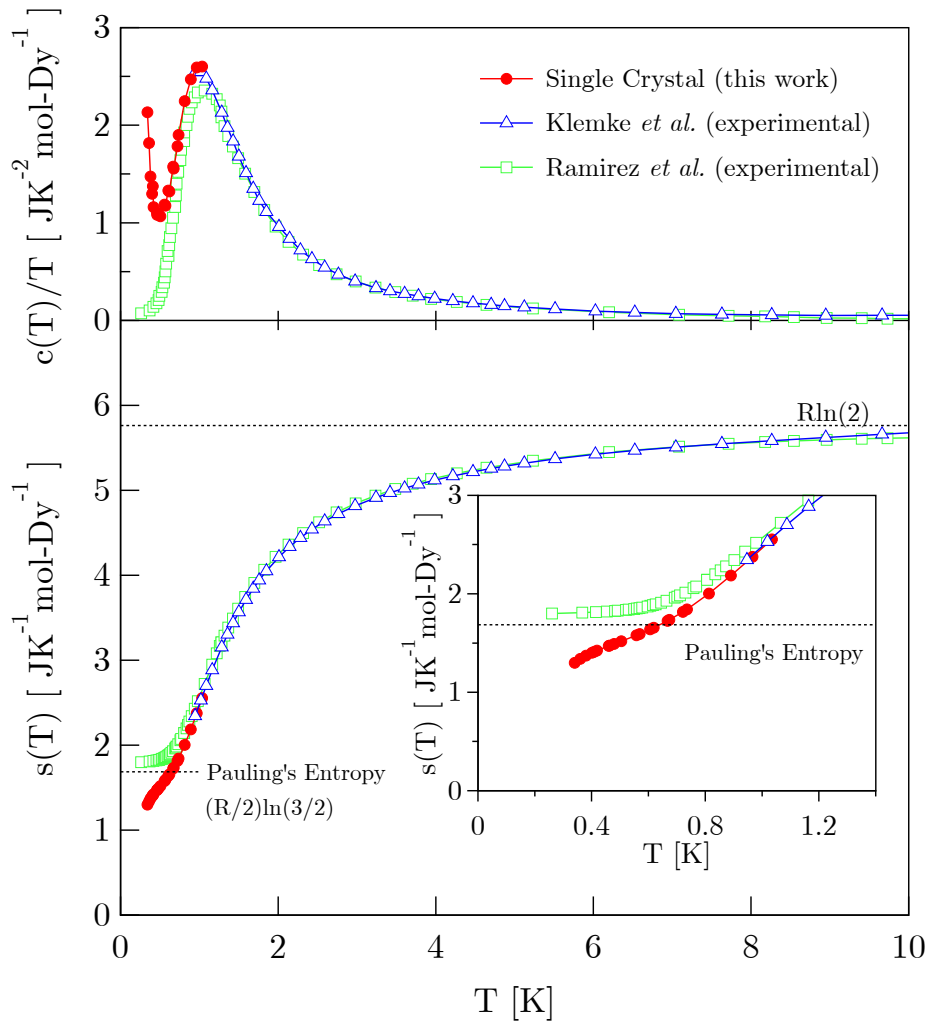
Figure 6.8: (a) Specific heat divided by temperature $c(T)/T$, was integrated from 0.34 K to 12 K, where data from reference [143] was used above 1 K. (b) The resulting entropy does not plateau at Pauling's residual value.

6.4 Discussion

These specific heat measurements suggest that the understanding of $Dy_2Ti_2O_7$ below 0.5 K incomplete. The findings suggest that when experiments are performed on sufficiently long timescales, the ground state might not have the full Pauling entropy of an ice manifold. One might expect that the long range nature of dipolar interactions should lift the degeneracy of nearest neighbour interactions, and indeed, the existence of such an ordered state was demonstrated numerically by Melko, Den Hertog, and Gingras for the dipolar spin-ice (DSI) model in 2001.[12] While their loop algorithm might not represent a realistic model for spin dynamics, it does speed up the ordering, and predicts the existence of a singularity near 0.18 K that has *qualitative* agreement with the specific heat presented in figure 6.7. While this comparison is compelling, *quantitative* fits to the experimental data within the framework of the DSI model have been unsuccessful.

The results presented here call into question whether or not a transition to long-range order occurs in $Dy_2Ti_2O_7$, and have prompted other researchers to scrutinize the DSI model. Mc Clarty *et al.,* investigated the effect of quantum fluctuations on the ground state of the DSI model.[144] Tunneling between spin-ice configurations was implemented with the following type of Hamiltonian

$$\mathcal{H}_{\text{tunneling}} = -\sum_{\hexagon} |\circlearrowleft\rangle\langle\circlearrowright| + |\circlearrowright\rangle\langle\circlearrowleft|, \tag{6.2}$$

where the sum upon $\hexagon$ runs over hexagonal plaquettes, or closed loops on the pyrchlore lattice. Using a variety of numerical and analytic techniques to explore the ground states of a classical DSI model, they demonstrated that dipolar interactions are minimized through the formation of ferromagnetically ordered spin chains that are exponentially screened from one another. Spin chains running in parallel are coupled to one another through short-range exchange that can be mapped to an effective 2-dimensional Ising model on the triangular lattice.[144]. This mapping gives rise to three distinct ordered chain states: cubic antiferromagnetic (CAF), tetragonal double-Q (TQD), and ferromagnetic (FM) order. Adding the quantum tunneling [equation 6.2] stabilizes a fourth phase, orthorhombic zigzag (OZZ), and if the tunneling term g is at least ~ 70 mK, then it can drive a quantum spin-liquid ground state. They were also able to qualitatively reproduce an upturn in c/T with a singularity at $T \approx 100$ mK, corresponding to the cubic antiferromagetic (CAF) state. Due to the proximity of multiple competing phases, small uncertainties in the interaction parameters make it difficult to conclusively determine the equilibrium ground state of $Dy_2Ti_2O_7$.

Around the same time that the aforementioned work was performed by McClarty *et al.*, another study of refrustration and competing orders was presented by Henelius *et al.*[145] This concept of refrustration refers to a competition between small effective spin-spin interactions and the magnetostatic dipolar interactions. Applying various analytic and computational methods to a generalized version of the dipolar spin-ice model (gDSM), they consider several candidates for the cause of an upturn in specific heat: an exchange-induced transition to long-range order, quantum non-Ising (transverse) terms in the effective spin Hamiltonian, nuclear hyperfine interactions, and random disorder. The experimental specific heat data could not be explained by an impending ordering transition using the parameters for $Dy_2Ti_2O_7$ in the literature. Their estimate for the quantum tunneling in $Dy_2Ti_2O_7$ is on the order of $g \sim 0.05$ mK, much smaller than the $g \sim 70$ mK required to stabilize the quantum phase predicted by McClarty *et al.* The more likely explanation for the upturn was attributed to the presence of random disorder (primarily oxygen deficiency, and stuffing), which gives rise to a Schottky-type response below 0.5 K. This would require a stuffing level on the order of 1%, with a energy scale of 1 K between impurities on the lattice. Previous magnetic studies on the same parent crystal studied here observed a longtime tail in the relaxation. Using a model of randomly distributed Ising spins on the pyrochlore lattice, this longtime tail can be explained by 0.1% stuffing.[25] The stoichiometry of Dy and Ti atoms can be measured by comparing relative intensities of Bragg peaks using x-ray diffraction. It is estimated that the precision of this method allows the stuffing to be measured down to 1%.[146] The presence of 1% random disorder cannot easily be ruled out from the list of potential explanations for the upturn in specific heat.

Rau and Gingras recently investigated the magnitude of quantum effects in rare-earth oxides, starting from a microscopic picture of electron tunneling.[103] When the electronic hopping Hamiltonian is projected into the free-ion basis ($J-$manifold, Steven's operator representation), mutual interactions arise between multipolar moments. The moment rank goes up to $2J$, where odd-rank multipoles carry magnetic, and even-rank carry electric moments. The most significant at low energy is the magnetic dipole-dipole, followed by electric quadrupole-quadrupole interactions. Super-exchange mediated through oxygen atoms also needs to be considered, in addition to many more interactions, such as those generated by direct exchange, via higher orbitals ($5d$, $6s$), via inter-shell interactions, magneto-elastic coupling, and virtual crystal field interactions; to name a few. An important conclusion from this study, is that the multipolar inter-ionic couplings that arise from superexchange are strongly suppressed beyond rank seven. This is because the process of hopping an electron from one $f-$orbital to another, involves the transfer of 3 units of angular orbital momentum L, and $\frac{1}{2}$ unit of spin angular momentum S per hop. Thus, the round trip of an electron can transfer at most 7 units of angular momentum (at most rank-7). This

explains why the behaviour of large J ions such as in the case of $Dy_2Ti_2O_7$, is strongly classical; because the ground state doublet $|\pm\frac{15}{2}\rangle$ would require a spin-flip operator of rank-15.[52] Applying this formal approach to the classical spin ice materials, they found that the generation of these high-rank multipolar interactions are strongly suppressed in $Dy_2Ti_2O_7$ and $Ho_2Ti_2O_7$. In the case of $Dy_2Ti_2O_7$, they concluded that the strength of tunneling g, appears at third order in the transverse coupling, and these effects could be relevant below 150 mK.

Another relevant study appeared during the time of writing this thesis, aimed at performing neutron scattering with timescales derived from our measurements.[147] After performing a slow cooling protocol on the sample, they could not detect any significant difference in the scattering structure factor within the resolution of their instrumentation. They also measured the specific heat of three isotopic variations of $Dy_2Ti_2O_7$: one contained natural abundances of Dy isotopes, one with only spin$-\frac{5}{2}$ ^{163}Dy, and one with only spin-0 ^{162}Dy. All three samples were measured between 1 and 0.5 K with the relaxation technique, allowing for relaxation times up to 89×10^4 s at the lowest temperature, as indicated by our work. After subtracting the appropriate nuclear hyperfine contributions, they observe that the sample with purely spin$-\frac{5}{2}$ ^{163}Dy has the largest residual upturn of the three samples. Based on this observation, they propose that hyperfine interactions provide additional pathways for electronic spin relaxation, which in turn give rise to the observed upturn in specific heat.

We corresponded with the authors of this paper to get technical details regarding their specific heat measurements. They indicated that the thermal conducitivity of weak link used for the measurements was ≈ 10 times larger ($K = 10^{-7}$ WK^{-1} at 0.5 K), and the mass of the samples were $\lesssim 2$ times smaller (≈ 2 to 8 mg) than those used for our measurements. As discussed in chapter 3.3, the thermal link converts heat flow to the measured temperature gradient, which determines the sensitivity to the slow-relaxation component. The intrinsic relaxation of the sample observed with our measurements has a very slow release of energy, and this will convert to a very small temperature difference across the weak link if its thermal conductance is large. Therefore, the smallest rate of heat that can be observed is ultimately limited by the intrinsic noise of the sample thermometer. For a heat flow rate of $\dot{Q} = 1$ pW, the temperature gradient across a weak link of thermal conductance $K = 10^{-7}$ W/K is $\Delta T(t) = \dot{Q}(t)/K(T) = 10$ μK. This resolution in thermometry can be very difficult to achieve with an ac-resistance bridge.[1]

---

[1]Consider this "back of the envelope" estimate for the *ideal* intrinsic noise in the thermometry of an 10 kΩ RuO$_2$ resistance measurement at 500 mK. The noise floor of any ac-resistance measurement is ultimately limited by the input noise of the voltage pre-amplifier. Assume that a total voltage input noise of 1 nV/$\sqrt{\text{Hz}}$ can be achieved. The Lake Shore model 3708 has 2 nV/$\sqrt{\text{Hz}}$ (see appendix F for a better

Increasing the weak link $K(T)$ corresponds to a proportional decrease in the measured $\Delta T(t)$ signal. This effect is illustrated in figure 6.9, where $\Delta T(t)$ and $\dot{Q}(t)$ are simulated using the values of K and sample mass m used in reference [147]. Given the very small heat flow rate observed in our measurements ($\lesssim$ pW), this means that a large fraction of the signal is lost when $K(T)$ is increased. Further careful studies are certainly required to conclusively explain the behaviour of the thermal relaxation.
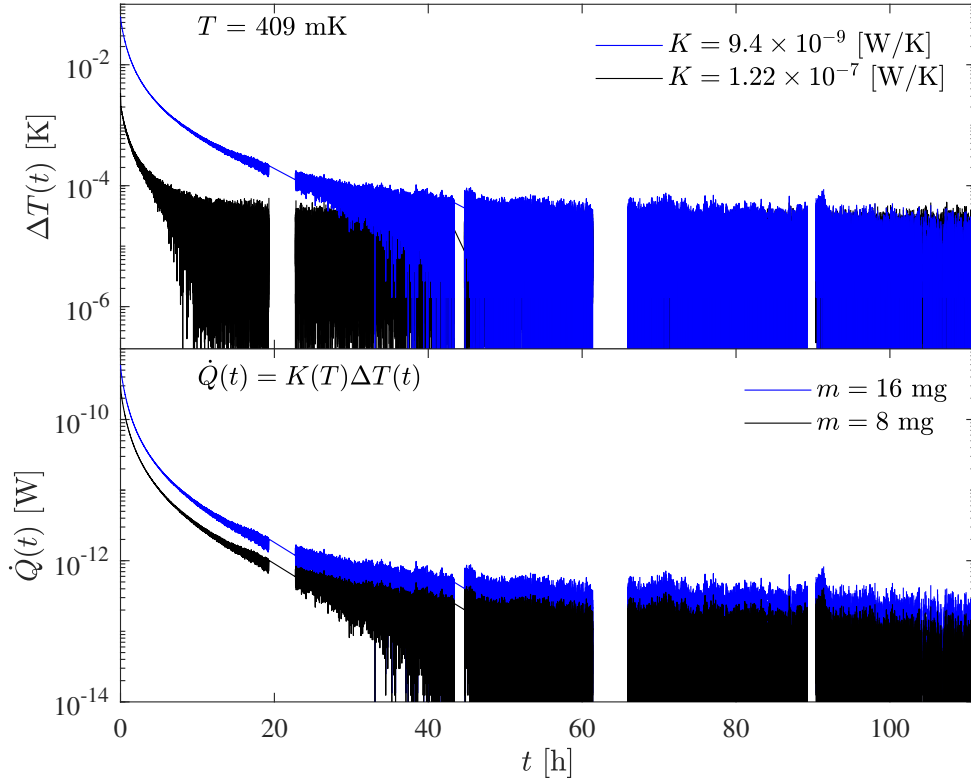
Figure 6.9: Effect of various experimental conditions on thermal relaxation of $Dy_2Ti_2O_7$ at 409 mK. Increasing the thermal conductance of the weak link K reduces the observed $\Delta T(t)$ at long timescales, while the intrinsic noise floor of the thermometry is the same. Lowering the mass of the sample reduces the internal heat release $\dot{Q}(t)$.

---

design with 0.6 nV/$\sqrt{\text{Hz}}$). Cryostat lead resistance will further increase the total noise. Using a generous excitation voltage for the ac-resistance bridge of 1 mV$_{\text{RMS}}$ would result in self-heating of the sample by ≈ 1 mK (assuming $K = 10^{-7}$ WK^{-1}). The sensitivity dR/dT of a typical RuO$_2$ between 0.5 K and 1 K ranges from 10^3 Ω/K to 10^4 Ω/K. It follows that the intrinsic temperature noise of a 10 kΩ RuO$_2$ has RMS amplitude betwen 0.1 μK to 1 μK. In practice, this noise is often about 50$\times$ higher.

Chapter 7

Magnetic susceptibility of Dysprosium Titanate $Dy_2Ti_2O_7$

High temperature magnetic relaxation in spin-ice ($T \gtrsim 15$ K) is a classical single-ion process dominated thermal fluctuations. This is distinguished from a nearly temperature-independent (2 K $\lesssim T \lesssim 15$ K) region that is mediated by quantum tunneling, described by Arrhenius scaling $f(T) = f_0 \exp(-ET^{-1})$ with $E \approx 2J_{\text{eff}}$, instead of the expected value for single spin flips within the effective nearest neighbour spin-ice (NNSI) model, $4J_{\text{eff}}$.[14] The observed energy barrier is half the expected value for a single spin flip within the effective nearest-neighbour spin-ice model (NNSI), and is equivalent to the energetic cost of a single topological defect (i.e., a single monopole).

Below 2 K, the NNSI model no longer provides an accurate description of magnetic relaxation in $Dy_2Ti_2O_7$. Long-range dipolar interactions are no longer effectively screened, and cannot be neglected. Coulomb forces $\propto r^{-1}$ are manifest between the topological defects, increasing the energy barrier to relaxation, and rapidly slowing the spin dynamics. Qualitative features of this were modelled by Jaubert and Holdsworth, who found that the inclusion of Dirac strings interconecting the monopoles improves the agreement with characteristic timescales of experiment; when compared with the evolution of monopoles themselves. While the simulations were successful at reproducing the rapid increase in characteristic timescale in the crossover region, the timescales still fall short of the experimentally observed timescales for $Dy_2Ti_2O_7$ at lower temperatures $\lesssim 1$ K. [126] The reason for this is not completely understood within the current theoretical framework of spin-ice materials.

7.1 Background

The measurements presented in this chapter are linked to a larger collaboration that investigated the effect of vacancy defects and monopole dynamics in oxygen-deficient pyrochlores.[40]. Crystals of $Dy_2Ti_2O_7$ grown by D. Prabhakaran, were provided by J. P. Goff and G. Sala. Our contribution was to characterize the magnetic relaxation below 1 K with ac-susceptibility measurements, for two samples with different levels of oxygen vacancy. As described in section 1.2.4, the most common type of oxygen vacancy occurs at O(1) sites, because these atoms are not bound as strongly as they are at O(2) sites. The presence of an O(1) vacancy at the center of a rare-earth tetrahedron modifies the electrostatic crystal field, and changes the anisotropy of these four ions from local easy-axis, to XY-like easy-plane. This gives rise to a large 16-spin cluster that has a tendency to strongly attract or repel monopoles that come into contact with the cluster.[1]

Another important type of defect encountered in spin-ice materials is stuffing due to substitutional defects; this has similar effects on spin dynamics as an O(1) vacancy. In a study by Revell *et al.,* it was demonstrated that static stuffed moments are not only capable of trapping monopoles, but also to serve as a nucleation site for these fractionalized quasiparticles, thereby raising their density in thermal equilibrium. Within that study, it was demonstrated that a characteristic signature of such a defect is a longtime tail in the decay of the magnetization. These effects are relevant for very low levels of stuffing. Monte Carlo simulations demonstrated that a very low level (0.30%) of stuffed static spins can account for particular characteristics observed in the magnetic susceptibility of $Dy_2Ti_2O_7$ below 1 K.[2]

Both studies by Sala *et al.,* and Revell *et al.,* demonstrate the importance of defects on magnetic relaxation dynamics in spin-ice below 1 K. Remarkably, the role of O(1) oxygen vacancies, and the effects of stuffing, have qualitatively similar effects on the magnetic relaxation. Both are believed to manifest a longtime tail in the relaxation, and have a tendency to increase the density of monopoles near the defective site. The purpose of this chapter is to characterize and compare the differences in magnetic relaxation between a typical "as-grown" crystal of $Dy_2Ti_2O_7$, before and after it is "annealed" with oxygen.

---

[1]As demonstrated by elegant energy computations with microscopic assumptions described in the supplementary information of reference [40].

[2]Those simulations were performed on a system with 0.30% stuffed spins (3,456 + 10 stuffed spins), by randomly placing Ising spins with magnitude $10\mu_B$ on the Ti tetrahedral sites.[25]

7.2 Methods

Ac susceptibility measurements were performed on a crystal of $Dy_2Ti_2O_7$ that was prepared with the floating zone method described in reference [148]. Depending on growth conditions, the sample can vary in colour, ranging from almost opaque and brown, to transluscent and yellow. Annealing an as-grown brown sample in oxygen at a flow rate of 50 ml min^{-1} and a temperature of 1200 °C for 2 days produces material that is transluscent and yellow; implying that the brown material may have been oxygen deficient. This is consistent with the evaporation of oxygen from the molten zone of the crystal growth. The phase diagram for the Dy_2O_3-TiO_2 system shown in figure 7.1 demonstrates the variety of neighbouring phases that occur in the crystal growth process. The melting point of $Dy_2Ti_2O_7$ occurs at 1850°C, which is the minimum temperature required for the formation of a single pyrochlore phase. Annealing in oxygen is performed at a relatively low temperature of 1200°C to avoid the separation of phases that occurs at higher temperatures in the phase diagram.
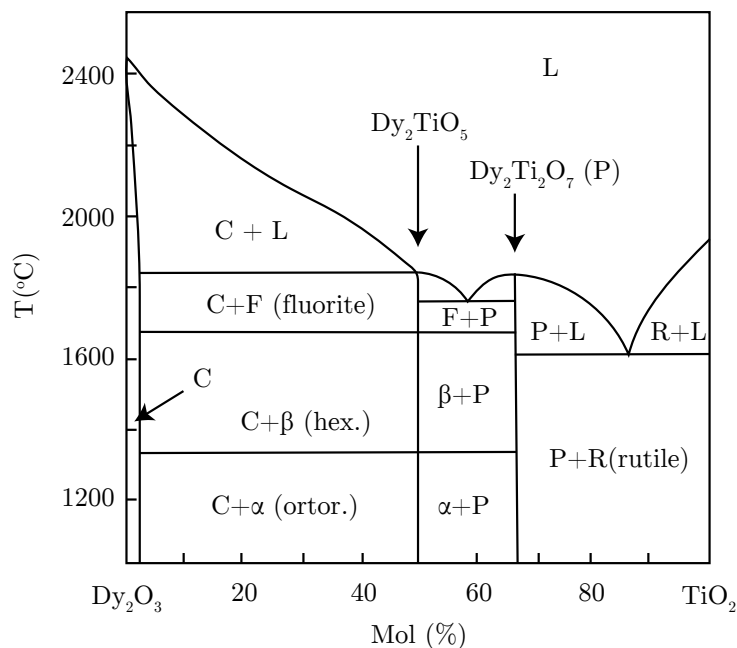
Figure 7.1: Phase diagram of the Dy_2O_3-TiO_2 system. α corresponds to the orthorhombic phase, β is the hexagonal phase, F is a cubic solid solution with the fluorite phase, P is the pyrochlore phase, and R corresponds to the rutile phase. Figure adapted from reference [149] with permission.

Additional details for the preparation of two samples 'as-grown', and 'annealed' are described in reference [148]. Both pieces were cut into needle-shaped rectangular prisms with the long axis aligned with the field of the magnetic susceptometer. In-phase and quadrature components of the susceptibility were measured with the device described in section 4.3 between 0.5 K and 1 K, with a frequency bandwidth spanning 10^{-3} to 10^3 Hz.

Thermal gravimetric analysis (TGA) presented by Sala *et al.,* indicated that the as-grown sample was slightly deficient in oxygen, corresponding to $Dy_2Ti_2O_{7-\delta}$ with $\delta \approx 0.02$.[40] This characterization was not performed on the annealed sample, and unfortunately there is no independent measure of its oxygen concentration. They also measured the magnetization of both samples, and found a smaller saturated magnetic moment in the as-grown material. Crystal electric field (CEF) calculations supporting this conclusion are consistent with a reduced moment from 10 μ_B to 5.7 μ_B at the defective Dy^{3+} sites surrounding an oxygen vacancy. Representative lattice parameters calculated from powder x-ray diffraction data on annealed and as-grown materials are 10.112 Å and 10.093 Å, respectively.[148]

7.3 Results

As-Grown Dy$_2$Ti$_2$O$_7$
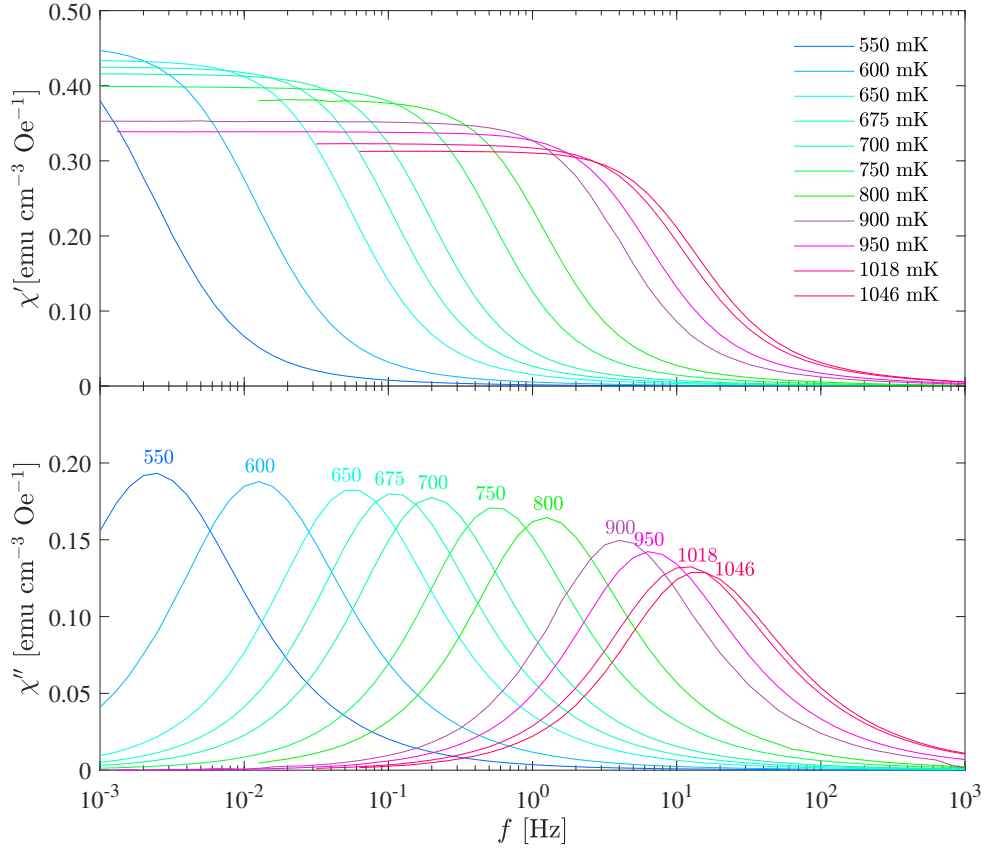
Figure 7.2: The in-phase $\chi'(\omega)$ and quadrature $\chi(\omega)''$ components of ac-susceptibility for as-grown Dy$_2$Ti$_2$O$_7$.

This crystal had dimensions $1.00 \times 1.00 \times 4.00$ mm^3, with corresponding magnetometric demagnetization factor $N = 0.108$ (using equation 4.24). Each data point was scaled by the voltage-to-flux conversion constant, before applying the demag correction in equation 4.25. The geometrical calibration procedure discussed in section 4.4 requires two measurements of the susceptibility with distinct geometry. This type of analysis was attempted for two different geometries. The results could not be reconciled due to complications caused by an ohmic contact on the superconducting flux transformer. Those data were rejected, and

instead the voltage-to-flux conversion was obtained by scaling the suscpetibility in the dc limit $\chi'(\omega \to 0)$ at 950 mK, with the value reported in reference [126]. It will be argued later that this assumption does not introduce significant errors that change the properties of interest.

Oxygen Annealed $Dy_2Ti_2O_7$
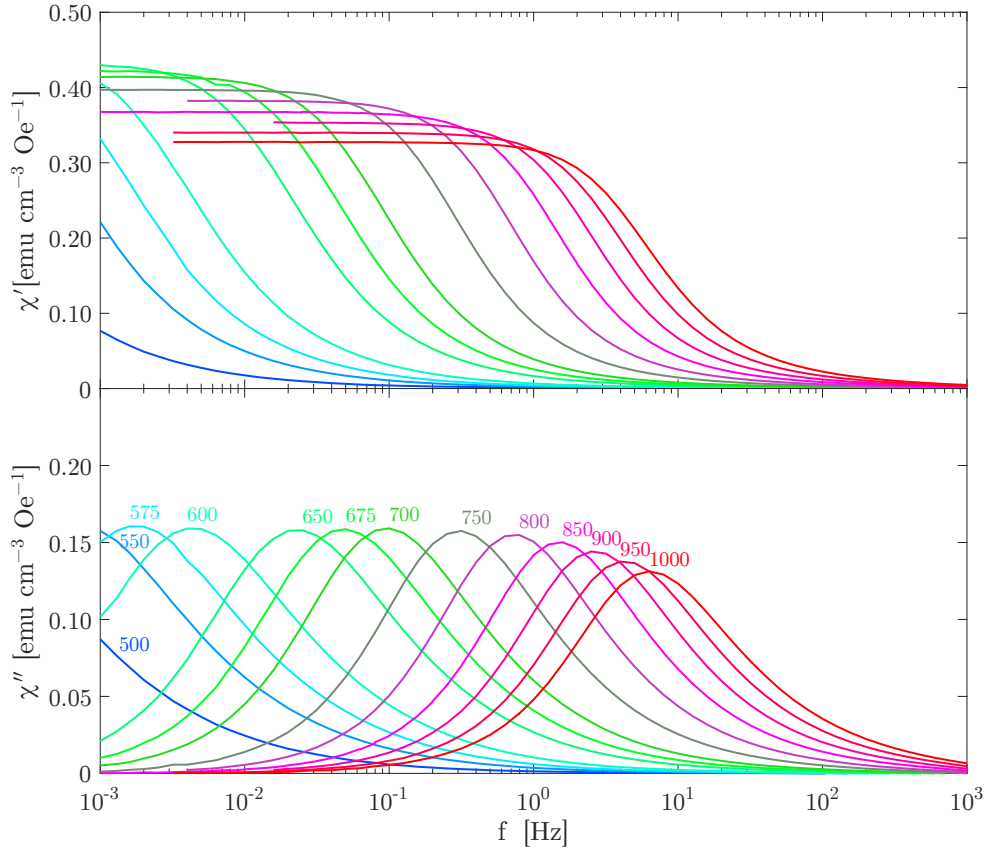
Figure 7.3: The in-phase $\chi'(\omega)$ and quadrature $\chi(\omega)''$ components of ac-susceptibility for annealed $Dy_2Ti_2O_7$.

The annealed crystal was cut to dimensions $1.00 \times 0.32 \times 4.03$ mm^3, with a corresponding magnetometric demagnetization factor $N = 0.058$. A second measurement was performed after reducing the size of this sample to $0.46 \times 0.33 \times 4.03$ mm^3, with corresponding demag factor $N = 0.044$. These two measurements had very similar demag factors, making it

impossible to obtain a reliable voltage-to-flux calibration using the method in section 4.4. The same alternate calibration procedure implemented for the as-grown sample in the preceding section, was also used here, where data was scaled to the dc susceptibility at 1 K reported in reference [126].

Calibration and Demagnetization

The greatest sources of uncertainty in these results are likely a result of the voltage-to-flux calibration constant. Its value was obtained by assuming that the dc-susceptibility for both as-grown, and annealed samples is very similar to the values reported in the literature. There are several reasons why this assumption should not introduce significant error.

1. The absolute value of dc-susceptibility for a variety of samples in the literature have nearly identical values, suggesting there is little sample dependence in this parameter.[23, 126, 150, 25] After calibration, the temperature dependence of the dc-susceptibility has excellent agreement with published data, suggesting that this trend is not strongly affected by the calibration.

2. It was demonstrated in section 4.4, that the slope of tails in $\chi''(\omega)$ are not affected by the demagnetization correction when χ does not vary much with temperature. Therefore will not alter the fitting parameters for the Debye, Cole-Cole, Davidson-Cole, or Havriliak-Negami models.

3. It was also demonstrated in section 4.4 that the effect of the demagnetizing field is to raise frequency of the peak in $\chi''(\omega_p)$, by a constant in $\log \omega$. This was illustrated for the single Debye model in figure 4.4, where $\tau \omega_p(N)$ is independent of the 'true' peak position $\tau = \omega_p(0)^{-1}$ for a constant value of χ_0. Notice that this statement is exact only when χ_0, the dc susceptibility is constant, and while it is not constant for the case of $Dy_2Ti_2O_7$, the variation is very small in the temperature range of interest $0.3 \lesssim \chi_0 \lesssim 0.5$. Therefore, the shift in frequency for both samples in figures 7.2 and 7.3, corresponds very closely to a constant shift in $\log \omega$. The raw experimental data can be analyzed to extract the slope of the relaxation frequency $d\omega/dT$, and determine the spin relaxation energy barrier with reasonable accuracy.

120

Temperature dependent voltage-to-flux calibration factor $a(T)$

An unresolved puzzle with the ac-susceptibility measurements was the observation of a temperature dependent voltage-to-flux calibration factor for a particular sample with ultra-fine needle with geometry $(0.0001 \times 0.0005 \times 0.0036 \text{ mm}^3)$. This observation was surprising because the calibration factor (a in equation 4.26) is generally independent of temperature for $Dy_2Ti_2O_7$, as demonstrated by earlier measurements.[24] The measured temperature dependence of $a(T)$ in figure 7.4 demonstrates the effect for two geometries of the annealed sample.
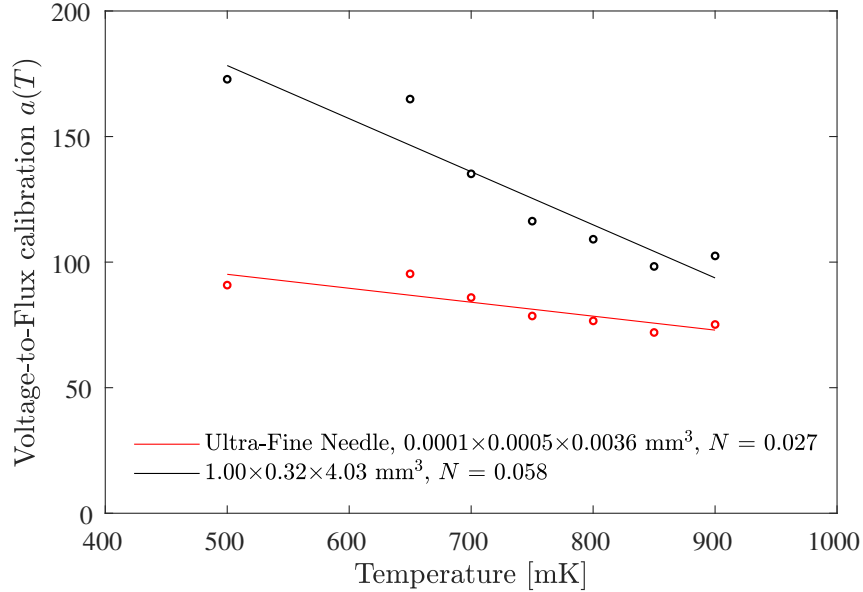
Figure 7.4: Unresolved temperature dependence of the voltage-to-flux calibration factor for two different geometries of annealed $Dy_2Ti_2O_7$. One possible explanation is that narrow geometry of the ultra-fine needle could result in a demagnetizing factor N that is extremely sensitive to the precise alignment of the crystal with the applied magnetic field.

Several potential explanations were considered in section 4.4 as the source of $a(T)$ observed here. The demagnetization factor does acquire temperature dependence $N(T)$ for finite values of susceptibility $\chi(T)$, but this variation is very small below 1 K for $Dy_2Ti_2O_7$ ($\chi \approx 0.3$ at 1 K to $\chi \approx 0.45$ at 0.5 K). Similar effects arising from the microscopic spin anisotropy of the lattice (Ising, XY, Heisenberg) are also only relevant at high temperature ($T > 20$ K) where susceptibility is large ($\chi \gtrsim 5$). Several sources of temperature

dependence due to dc-SQUID flux drift were also considered, but these factors are likely too small to have significant effects for the range of frequency and temperature considered here.

The width of the ultra-fine needle was significantly smaller than any sample previously measured with this susceptometer. It is suspected that this narrow geometry could make the demagnetizing factor N extremely sensitive to the precise alignment of the crystal with the applied magnetic field. The demagnetization factor for a rectangular prism in a tilted field would likely require detailed numerical calculations similar to those performed in reference [117]. This data set exhibited another unusual property whereas the peaks in apparent susceptibility $\chi''_A(\omega)$ shifted to lower frequencies relative to the geometry with larger N. This is opposite to what is expected theoretically. All of these factors indicate that the problem likely originated from the geometry of the ultra-fine needle sample. An alternate proposition is that the observed dependence of $a(T)$ is a characteristic of the material when constrained to a certain geometry. More evidence is required in order to pursue this as a legitimate source of the variation. It was concluded that the data for the ultra-fine needle sample with dimension $0.0001 \times 0.0005 \times 0.0036$ mm^3 was unreliable, and it was rejected from the analysis. As discussed in the previous section, the conclusions drawn from the results are not affected by the alternate voltage-to-flux calibration procedure used.

7.4 Discussion

Annealing $Dy_2 Ti_2 O_7$ in oxygen has remarkable effects on the low temperature magnetic relaxation. Several different approaches are used to characterize the variety of effects arising at low temperatures $0.5 < T < 1$ K resulting from oxygen deficiency.

Relaxation Time $\tau(T)$

Due to the broad distribution of frequencies in $\chi''(\omega)$, it is common to define the characteristic relaxation time at the peak, as $\tau = \omega_{\mathrm{peak}}^{-1} = (2\pi f_{\mathrm{peak}})^{-1}$. The scaling of this characteristic time with temperature is often presented as $\log \tau$ vs. inverse temperature, as shown in figure 7.5.
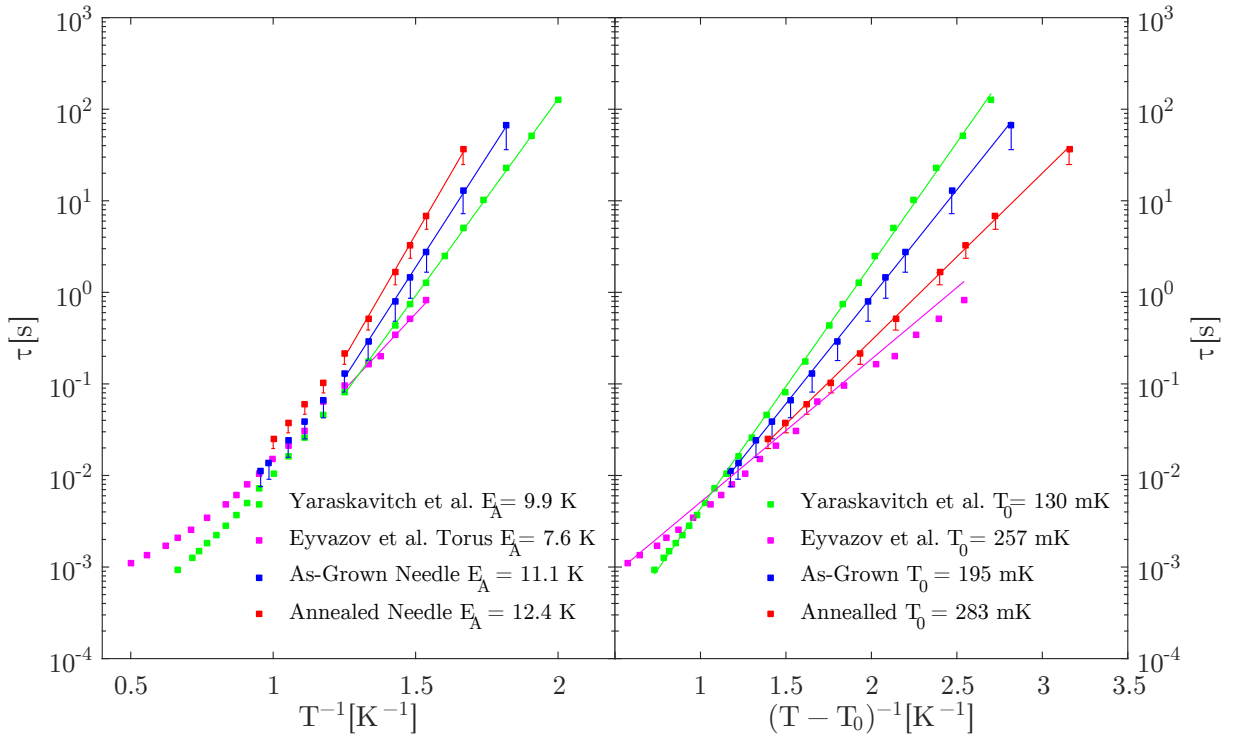

Figure 7.5: Characteristic relaxation time for $Dy_2Ti_2O_7$ presented as an Arrhenius plot on the left, and Vogel-Fulcher plot on the right. Fits to the data are indicated by solid lines. Results are presented for another needle with similar geometry from Yaraskavitch *et al.*, and for a torus-shaped sample from Eyvazov *et al.*[120, 126]

123

To show the effect of the demagnetizing factor on the slope of $\tau(T)$, error bars in figure 7.5 correspond to the characteristic time extracted from raw data prior to the corrections. The plot of $\log \tau$ versus T^{-1} produces a straight line for the commonly encountered thermally activated Arrhenius-type behaviour $\tau = \tau_0 \exp[E_A/T]$, where the barrier to relaxation E_A is determined from the slope of the low temperature tail. On the right is a plot of $\log \tau$ versus $(T - T_0)^{-1}$, where T_0 is a transition temperature obtained by fitting the entire dataset to the Vogel-Fulcher (VF) equation $\tau = \tau_0^{\mathrm{VF}} \exp[DT_0/(T - T_0)]$. The VF model is often used to describe the slowing down of relaxation processes associated with a glass transition where T_0 corresponds to the glass ordering temperature. It was recently proposed that $Dy_2Ti_2O_7$ may have characteristics of a supercooled glass-forming dipolar fluid.[119, 120] Nussinov *et al.*, also present an argument for VF behaviour in pyrochlores based on the existence of an exponentially large number of metastable states.[151] While it is tempting to use VF scaling to extrapolate the observed behaviour of $Dy_2Ti_2O_7$ and imply the existence of a supercooled spin liquid, it is difficult to make conclusive arguments when the glass (melting) temperature is not accessible to experiment. Nonetheless, the VF function does provide an improvement over the Arrhenius model for the samples presented in figure 7.5, and the fit parameters for both models are summarized in table 7.1. The slowing down of the dynamics under cooling is more sudden in fragile liquids than in strong ones, characterized by the magnitude of the fragility parameter D. It appears that oxygen deficiency increases the fragility parameter, and lowers the glass transition temperature T_0. Materials with higher fragility typically have narrow glass transitions compared to those with low fragility. This observation suggests that the presence of oxygen vacancies increases the dynamical heterogeneity, associated with an increased variation of dynamics in the material.

Table 7.1: Fit parameters for several samples of $Dy_2Ti_2O_7$, fit to the Vogel-Fulcher equation $\tau(T) = \tau_0^{\mathrm{VF}} \exp[DT_0/(T - T_0)]$, and Arrhenius scaling $\tau = \tau_0^A \exp[E_A/T]$.

	Geometry	T_0 [mK]	τ_0^{VF} [s]	D	E_A[K]	τ_0^A[s]
As-grown	Rectangular Prism	195	19μ	28	11.1	105n
Annealed	Rectangular Prism	283	66μ	15	12.4	36n
Yaraskavitch *et al.* [126]	Rectangular Prism	130	10μ	47	9.79	406n
Eyvazov *et al.* [120]	Torus	257	140μ	14	7.6	6.2μ

Another interesting feature of the comparison in table 7.1 is that the torus shaped sample has a larger characteristic attempt rate than the rectangular prisms. This might result from an effect induced by the periodic boundary conditions of the toroidal geometry.

Normalized Features of $\chi''(\omega)$

General features of $\chi''(\omega)$ with temperature are revealed by normalizing the amplitude and frequency of each of the peaks $\chi''(\omega_p)$ in figure 7.6. The full-width at half-maximum (FWHM) of both samples shows an increase below ~ 800 mK, where spin-ice correlations develop. This feature was also observed in other samples of $Dy_2Ti_2O_7$, and is consistent with an increase in the spread of relaxation timescales.[24, 152] Therefore, it appears that oxygen deficiency reduces the spread of relaxation modes. Both samples exhibit similar qualitative broadening features in the half-width at half-maximum to the left (HWHM-) and right (HWHM+) of the peak that are common to most samples of $Dy_2Ti_2O_7$.
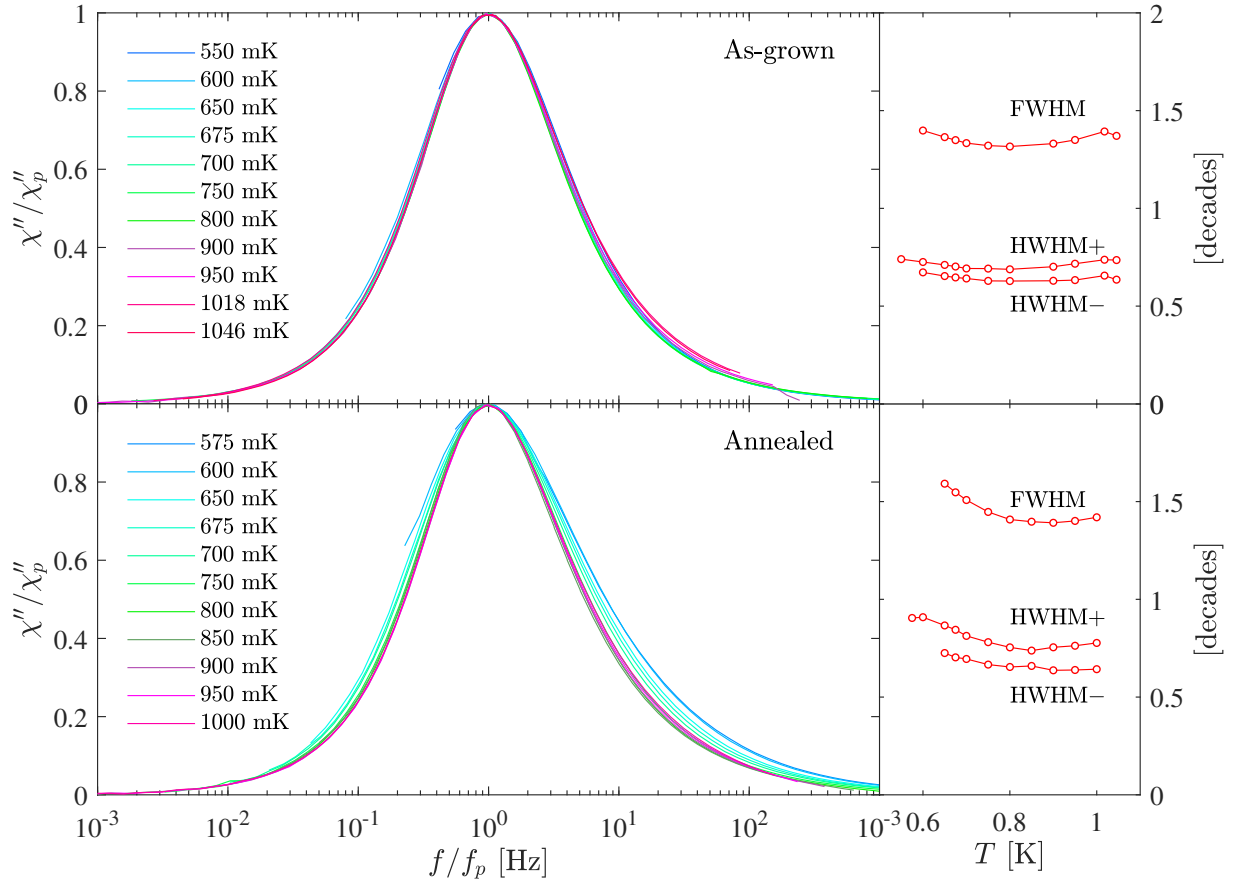

Figure 7.6: Normalized out-of-phase susceptibility for as-grown and annealed $Dy_2Ti_2O_7$. Oxygen vacancies reduce the enhancement of the full-width at half-maximum (FWHM) below $\sim$800 mK, consistent with a smaller distribution of relaxation timescales.

Susceptibility Fitting

An analytic function that accurately describes the susceptibility $\chi(\omega)$ allows for a convenient evaluation of the dynamic spin correlation function

$$C(t) = \langle M(0)M(t) \rangle = 2k_B T \int_{-\infty}^{\infty} \frac{\chi''(\omega)}{\omega} \cos(\omega t) d\omega, \qquad (7.1)$$

which is simply the Fourier cosine transformation of the complex susceptibility $\chi''(\omega)$. This relationship is a result of the fluctuation-dissipation theorem, which states that the linear response of a system to an external perturbation is expressed in terms of fluctuations of the system in thermal equilibrium.[153] This transformation of $\chi''(\omega)$ can be performed accurately with an analytic expression, and therefore it helps to fit the data to an empirical model that captures its features. Common models are often variations of the Debye equation, such as the Cole-Cole, Cole-Davidson, and Havriliak-Negami (HN) functions compared in section 4.2. The most accurate representations for the low temperature (< 1 K) behaviour of $Dy_2Ti_2O_7$ are typically given by the HN model

$$\chi''(\omega) = \mathrm{Im}\left[\frac{\chi_0}{(1 + (i\omega\tau)^{\alpha})^{\beta}} \right], \qquad (7.2)$$

or a more generalized model that was introduced in reference [25]

$$\chi''(\omega) = \frac{1}{\left[(\tau\omega)^{\alpha_1 \cdot n} + (\tau\omega)^{-\alpha_2 \cdot n} \right]^{1/n}}, \qquad (7.3)$$

where the position and sharpness of the maximum are respectively given by τ and n, and the tails of χ'' vanish with exponents α_1 and α_2. The general nature of this function captures the asymmetry of the tails in the spectrum that are not accounted for by the HN model. Differences between fits to the HN model, and the generalized model in equation 7.3 presented in figure 7.7, show very subtle improvements for the annealed sample at low frequency. An analytic model for the real component of $\chi'(\omega)$, for the generalized model could not be obtained easily using the Kramers-Kronig relation

$$\chi'(\omega) = \frac{2}{\pi} \mathcal{P} \int_0^{\infty} \frac{\omega'\chi''(\omega')}{\omega'^2 - \omega^2} d\omega', \qquad (7.4)$$

but this integral can be obtained numerically. It shows excellent agreement with the experimental $\chi'(\omega)$ data in figure 7.7. Compliance of the data with the Kramers-Kronig relation also validates the relationship between $\chi'(\omega)$ and $\chi''(\omega)$.
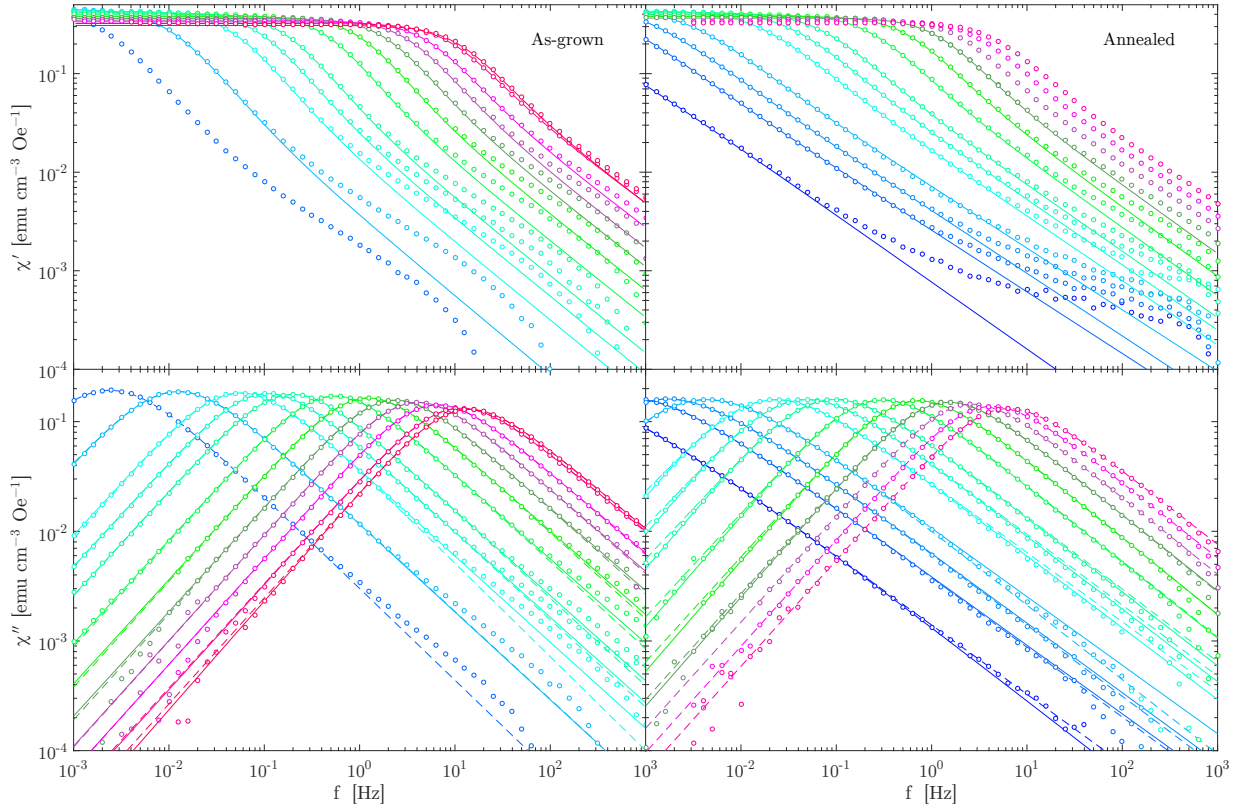
Figure 7.7: Log-log plot of $\chi''(\omega)$ comparing fits for the as-grown and annealed samples. Fits to the generalized model in equation 7.3 are solid lines, and dashed lines are fits for the Havriliak-Negami model in equation 7.2. A few of the fits are missing from the plot. The unusual behaviour at high frequencies is likely roll-off due to capacitance in the electrical network in figure 4.2.

The dynamic spin correlation function $C(t)$ (equation 7.1) was computed numerically at each temperature after fitting to the generalized χ'' model (equation 7.3). These results are shown in figure 7.8, where a characteristic difference between samples is apparent in the longtime tails of $C(t)$, often referred to as an "algebraic tail", indicating a crossover from exponential to power-law (algebraic) behaviour. In previous work on $Dy_2Ti_2O_7$, this algebraic tail was emulated with Monte Carlo simulations by randomly distributing subsitutional defects (stuffing) within the dipolar spin-ice model. Stuffing was simulated by placing static Ising 10 μ_B moments on 0.3% of the nonmagnetic Ti sites.[25] Despite these successes, the dipolar spin ice model still does not explain the rapid slowing down of dynamics below $\approx$ 2 K, or the stretched exponential observed in materials.[28] The

results presented here only indicate that annealing the material in oxygen eliminates the algebraic late time tail, suggesting that the defects produced by oxygen deficiency may have similarities to those caused by stuffing. In the lower panels of figure 7.8, the correlation function is scaled as $\ln\left[-\ln C(t)\right]$. The slope of this line is equal to the stretching factor β when $C(t) = \exp\left[-(t/\tau)^{\beta}\right]$, indicated as a dashed line in the plots. The stretching factor of the as-grown sample varies from 0.75 to 0.80, while the annealed sample is in the range 0.65 to 0.75.

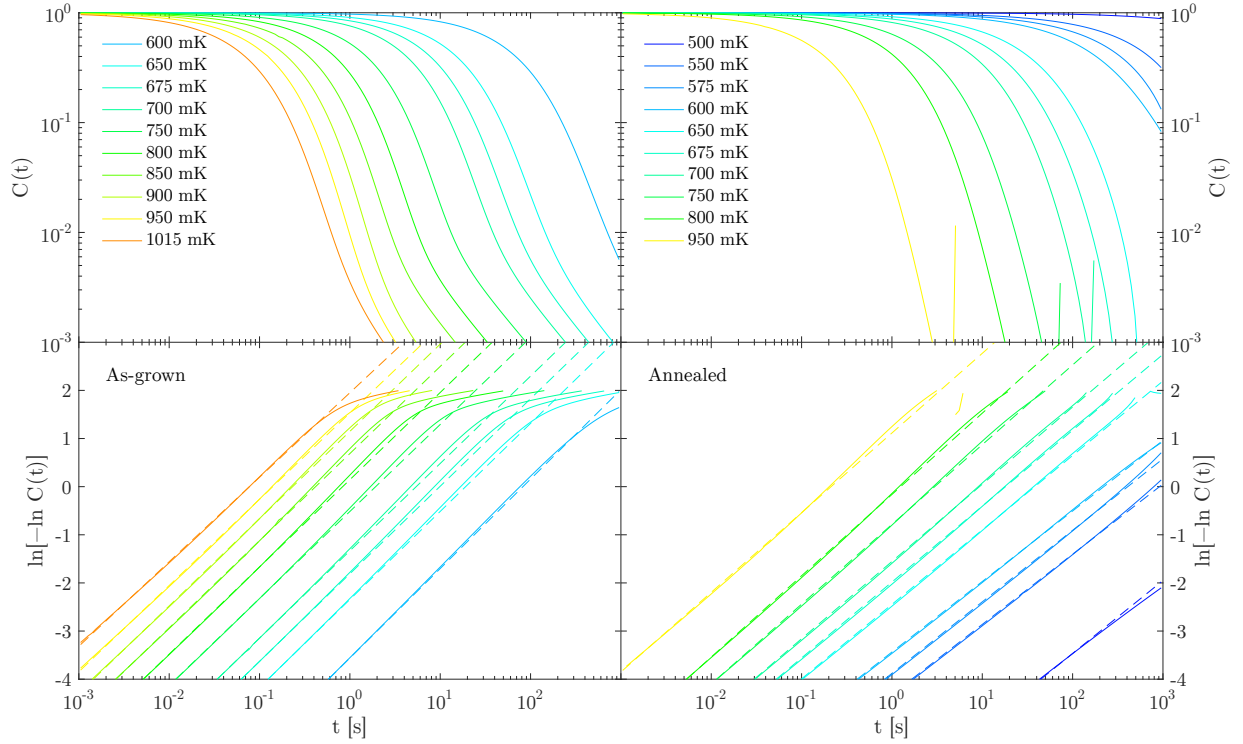Figure 7.8: Dynamic spin correlation function $C(t)$ for $Dy_2Ti_2O_7$. The algebraic longtime tails are eliminated after annealing in oxygen when the data is fit to equation 7.3. The slope of $\ln[-\ln C(t)]$ in the lower panels measures the exponential stretching factor β, indicated by dashed lines.

Argand Diagrams

Significant qualitative changes due to annealing are evident when χ'' is plotted against χ' in the form of an Argand diagram as shown in figure 7.9. The most striking difference is the temperature evolution of the slope near the origin. As demonstrated in section 4.2, the slope of this feature is captured by the Davidson-Cole (DC) parameter in equation 4.19. This parameter β, decreases with temperature for the annealed sample, while the as-grown material exhibits the opposite behaviour. At the other end of the axis, the dc susceptibility can be extracted from the intercept of the $\chi'(\omega)$ axis, and is nearly identical for both samples.
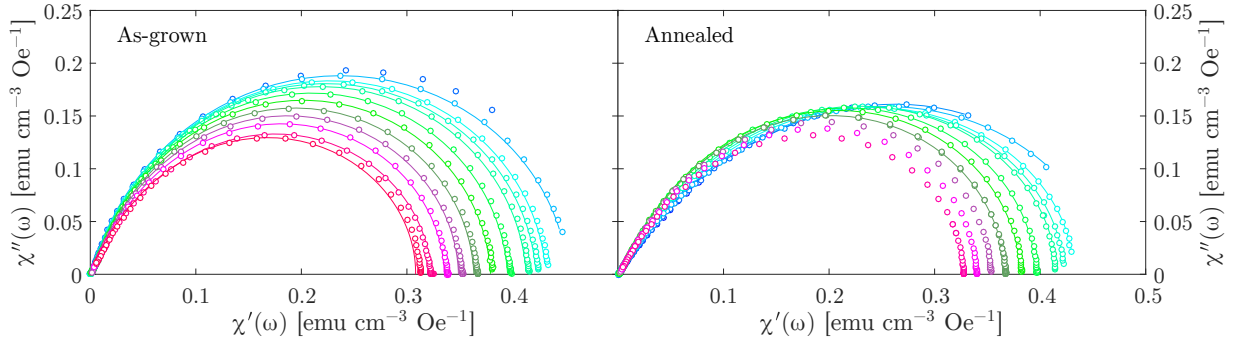
Figure 7.9: Argand plots for as-grown and annealed $Dy_2Ti_2O_7$ (Double Rainbow).

This discussion concludes with one proposal for a physical interpretation of Davidson-Cole parameter β. Calderwood suggested that temporal and spatial fluctuations of a system exhibiting this type of parameter are subject to severe turbulence, suggesting that "some dipoles will be more able than others to vibrate under the influence of an applied sinusoidal field, and execute oscillations of greater magnitude".[114, 154] Similar to the original assumption of Debye's model, this crude model of relaxation ignores dipolar inertia. Accepting this proposal would that suggest magnetic dipoles in the annealed material are subject to more fluctuations at low temperature and high frequency; whereas both samples converge to the same behaviour in the dc limit. The temperature evolution of $\beta(T)$ and $\alpha(T)$ (Cole-Cole parameter) is demonstrated in figure 7.10. These parameters were obtained from fits to the Havriliak-Negami model in figure 7.7.
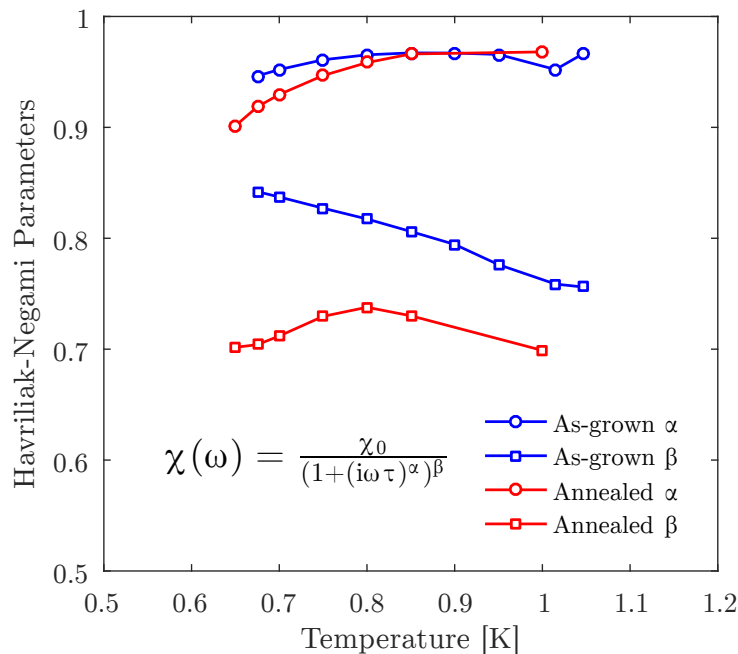
Figure 7.10: Temperature evolution of Havriliak-Negami fit parameters for as-grown and annealed $Dy_2Ti_2O_7$.

The temperature dependence of DC susceptibility extracted in the limit $\chi''(\omega \to 0)$ is shown in figure 7.11, where the temperature dependence of both samples agrees with those of Yaraskavitch *et al.,*[24, 126] and indicates that the DC susceptibility is not strongly affected by the annealing procedure implemented on these samples. This comparison also suggests that the demagnetization correction implemented in this section, which has the most prominent effects at low frequency, is indeed valid.

The approaches used to analyze the magnetic susceptibility data of $Dy_2Ti_2O_7$ below 1 K are based on phenomenological models that classify prominent features of the observed data. Results presented in this chapter have highlighted a variety of prominent features in magnetic susceptibility that are affected by oxygen annealing. The complementary work by Sala *et al.,*[40] on these samples suggests that these features arise from subtle levels of oxygen deficiency, but further work should be done to characterize the precise differences in stoichiometry to rule out the possibility that stuffing is also a culprit for the observed variation. The present work supports a conclusion that defects, stuffing, and other subtle impurities can have significant effects on the dynamics of magnetic spins, but further work is required to investigate the full effects of disorder on the energetic ground state.
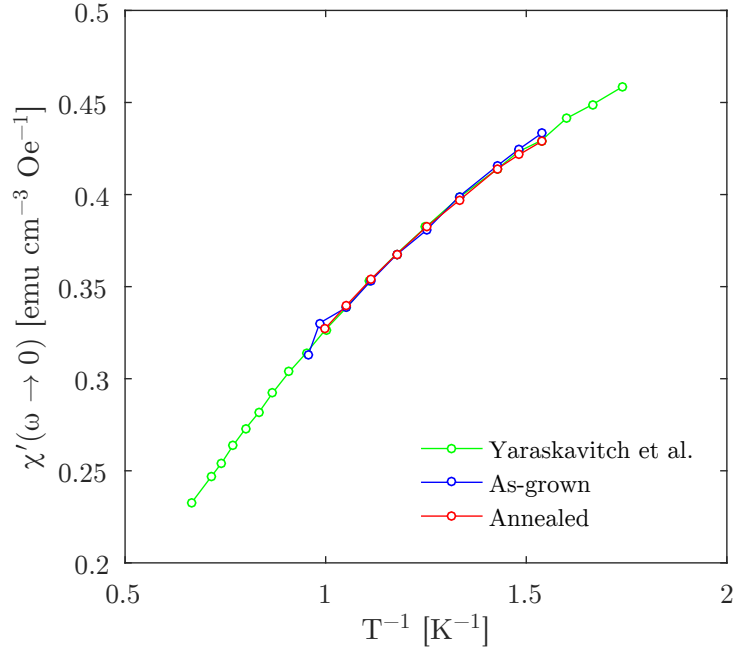
Figure 7.11: DC susceptibility $\chi''(T)$ vs. inverse temperature for $Dy_2Ti_2O_7$ below 1 K. Yaraskavitch *et al.*, is from reference [24]. $Dy_2Ti_2O_7$ also does not exhibit Curie-Weiss behavior at low temperatures.

Much of the current work on spin-ice materials is based around static properties of the ground state rather than the dynamical features of their magnetism, which makes these kinetic properties difficult to interpret. Apart from a small handful of theoretical simulations that model the dynamics of spin-ice below 1 K, there is a significant gap in the relationship between microscopic models and experiential observations that is calling for more detailed investigations from both fronts.

Chapter 8

Specific Heat of Ytterbium Titanate $Yb_2Ti_2O_7$

8.1 Methods

Specific heat of two polycrystalline $Yb_2Ti_2O_7$ samples was measured between 15 mK and 660 mK, in order to capture the ferromagnetic ordering transition, and a large portion of the nucler hyperfine specific heat. One of the samples, containing naturally occurring abundances of Yb and Ti was taken from the same batch of material studied in reference [155]. Another sample was prepared from enriched $^{174}Yb_2O_3$ and $^{48}TiO_2$ by collaborators at the Brockhouse Institute for Materials Research, at McMaster University. The enriched oxides were purchased from Trace Sciences International Corp. Isotopic abundances of the natural and enriched isotopes of Yb and Ti are presented in table 8.1 and 8.2, respectively. Both samples were prepared as polycrystalline $Yb_2Ti_2O_7$ by mixing 2 parts TiO_2 with 1 part Yb_2O_3, and then heated to 1200ºC for 24 hours with a warming and cooling rate of 100ºCh^{-1}. The natural sample had a mass of 312 mg and was pressed with 405 mg of Ag powder, while the enriched isotopic sample had a mass of 139 mg and was pressed with 206 mg of Ag powder.

Both samples were suspended in vacuum with ≈1 cm long, 6 μm nylon threads, and the 4-wire resistance measurements were made with ≈1.5 cm long, 6 μm NbTi filaments. The addenda and silver powder were measured independently, and found to contribute $< 0.8\%$ to the measured total specific heat of the enriched sample at 50 mK (and less for the natural sample). Thermal links of $Pt_{92}W_8$ wire were used as the primary thermal connection between the sample and a temperature controlled stage. This thermal link was chosen

to have a time constant from 0.5 to several hours below the ordering transition, in order ensure thermal equilibrium of the sample. Several thermal relaxation measurements of the specific heat were also performed at several temperatures, motivated by our earlier work on the frustrated magnetic compound $Dy_2Ti_2O_7$. We found that extremely long equilibration relaxation times (up to $\approx 10^5$s) were required to capture the equilibrium behaviour of that compound.[142] No evidence of unusually long equilibration was identified for this compound or any other specimen of $Yb_2Ti_2O_7$, verifying that the heat pulse method is sufficient for the present characterization.
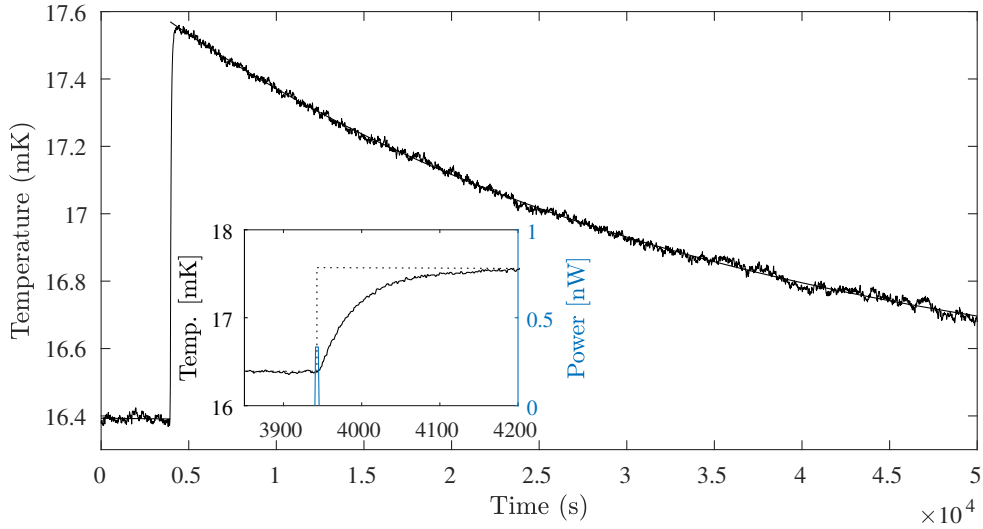
Figure 8.1: Heat pulse for a single datum in specific heat near 17 mK. The change in temperature ΔT is obtained by fitting the relaxation to an exponential, and then extrapolating to the half-time of the heat pulse. The inset shows a close up view of the extrapolation procedure.

The specific heat measurements presented here were obtained in zero field ($< 10^{-3}$ G) with the quasi-adiabatic heat-pulse method described in section 3.4, where a 1 kΩ RuO_2 thermometer (Dale RC-550-20) and 10 kΩ metal-film resistor were attached directly to the sample with silver epoxy as described in section 3.6. A typical low temperature heat-pulse response is shown in figure 8.1 demonstrating sluggish behaviour on the order of 10^2 seconds, likely arising from the sample-to-silver thermal boundary resistance. The duration of each heat pulse was typically on the order of 1 to 10 seconds. Vertical error bars presented in the specific heat plots are derived from the non-simultaneous functional prediction intervals at the midpoint of the heat pulse, with confidence interval of 1σ.

133

Extensive care was taken to ensure accurate thermometry. Resistance to temperature calibration curves for the RuO_2 sensors are shown in figure 8.2 and 8.3 for the natural and enriched materials, respectively. These were obtained on an independent cool down where the thermal weak link was shorted by a silver wire to avoid offsets in temperature due to self-heating. Calibration was performed directly to the paramagnetic susceptibility of cerium magnesium nitrate (CMN), and ^{60}Co nuclear orientation thermometry described in chapter 5. Typical residuals for the calibration fit are $< 1\%$ (1σ) over the entire temperature range.
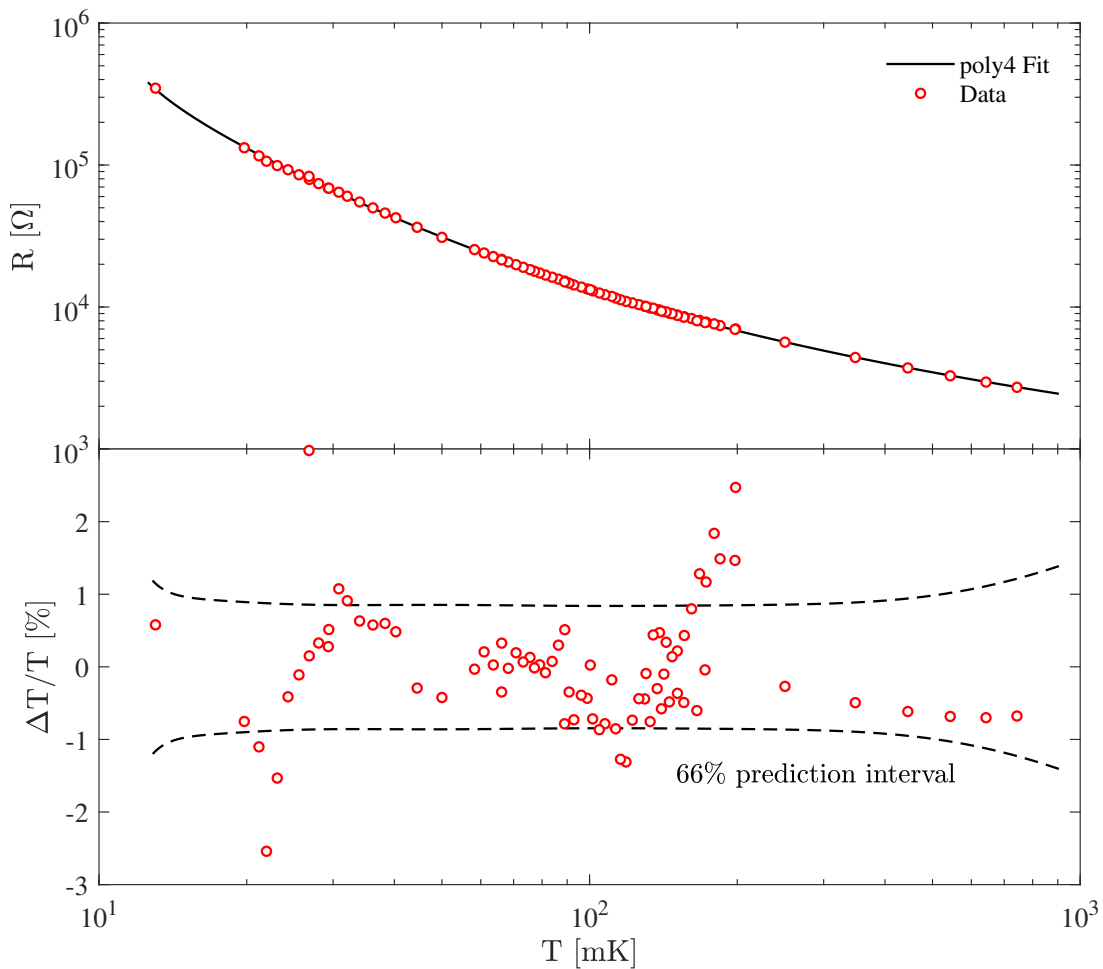
Figure 8.2: Natural $Yb_2Ti_2O_7$: Resistance vs. temperature for the RuO_2 (Dale RC-550-20) 1 kΩ resistor. The data was fit to equation 5.6 with $N = 4$ free parameters. The fit residual, and 1σ prediction bounds are shown in the lower plot.

Figure 8.3: Enriched $Yb_2Ti_2O_7$: Resistance vs. temperature for the RuO_2 (Dale RC-550-20) 1 kΩ resistor. The data was fit to equation 5.6 with $N = 4$ free parameters. The fit residual, and 1σ prediction bounds are shown in the lower plot.
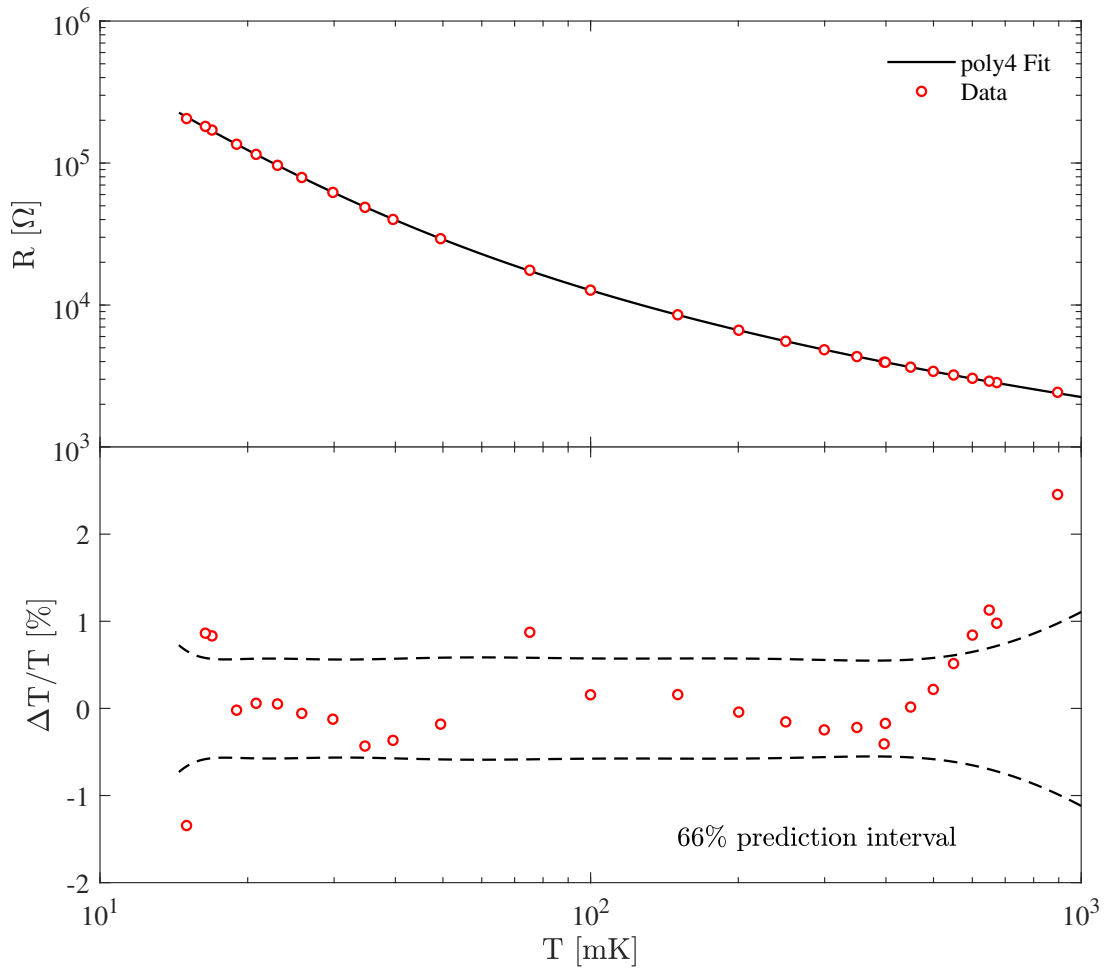
8.1.1 Hyperfine Interactions in $Yb_2Ti_2O_7$

The purpose of this section is to describe the general nature of hyperfine interactions in rare-earth oxides. Steps involved in calculating and fitting nuclear specific are demonstrated for the case of $Yb_2Ti_2O_7$.

In many rare-earth compounds, hyperfine interactions give rise to nuclear specific heat [section 2.5], and $Yb_2Ti_2O_7$ is no exception below 100 mK. Proper subtraction of this term can be challenging because it often requires accurate data, or prior knowledge of the interaction parameters. If this information is not available from complementary techniques such as Mössbauer spectroscopy, electron spin resonance, or nuclear magnetic resonance, then they can be tricky to predict on simple theoretical grounds. The most effective way to suppress hyperfine interactions in any material is to prepare the sample with nuclear isotopes free of intrinsic spin, and quadrupole moments. For the case of Yb, only two out of the seven naturally occurring isotopes listed in table 8.1 have finite nuclear spin, or quadrupole moment. The properties of Ti isotopes are also listed in table 8.2.

Table 8.1: Nuclear spin, dipole moment, quadrupole moment, and natural abundance of stable Yb isotopes. Enrichment abundances have an uncertainty of 0.1%.

	^{168}Yb	^{170}Yb	^{171}Yb	^{172}Yb	^{173}Yb	^{174}Yb	^{176}Yb
Nuclear spin I	0	0	1/2	0	5/2	0	0
Dipole moment $\mu(\mu_N)$	0	0	+0.49367	0	-0.648	0	0
Quadrupole moment Q(b)	0	0	0	0	+2.80	0	0
Natural abundance (%)	0.13	3.04	14.29	21.83	16.13	31.83	12.76
Enrichment (%)	<0.01	0.02	0.08	0.19	0.51	98.6(1)	0.57

Table 8.2: Nuclear spin, dipole moment, quadrupole moment, and natural abundance of stable Ti isotopes. Enrichment abundances have an uncertainty of 0.1%.

	^{46}Ti	^{47}Ti	^{48}Ti	^{49}Ti	^{50}Ti
Nuclear spin$-I$	0	5/2	0	7/2	0
Dipole (μ_N)	0	-0.78848	0	-1.10417	0
Quadrupole moment Q(b)	0	+0.30	0	+0.24	0
Natural (%)	8.25	7.44	73.72	5.41	5.18
Enrichment (%)	0.21	0.47	98.9(1)	0.29	0.16

There are two primary interactions that contribute to the hyperfine Hamiltonian. First is the magnetic dipole-dipole coupling between the nuclear magnetic moment $\vec{\mu}$ and the effective magnetic field $\vec{H}_{\text{eff}}$ produced by electrons orbiting the nucleus with the following effective Hamiltonian

$$\mathcal{H}_{\text{D}} = -\vec{\mu} \cdot \vec{H}_{\text{eff}} = -\frac{\mu H_{\text{eff}}}{I} I_z, \tag{8.1}$$

where the nuclear magnetic moment is given by $\vec{\mu} = g_I \mu_N \vec{I}$, g_I is the nuclear $g-$factor, and μ_N is the nuclear dipole moment. The main contribution to H_{eff} in the rare earth elements arises from unquenched orbital angular momentum the $4f$ electrons, however, there are additional contributions that should be considered for a complete picture. This includes the dipolar contribution to H_{eff}, which is typically about one tenth of the orbital interaction, while the polarization of core $s-$electrons (and conduction electrons if they are present) induced by $4f$ electrons contribute even less. Because of the electronic structure of rare-earth ions ($4f^n, 5s^2, 5p^6, 6s^2, 5d^1$), the electrons producing magnetism are typically buried deep in the atomic $4f$ shell and are not affected strongly by their surroundings. As a consequence, rare earth atoms retain their free-ion character in many compounds. This is not necessarily true for other elements such as transition metals with exposed $3d$ electrons.[99]

The second primary contribution to the hyperfine Hamiltonian results arises from the electric field gradient $\nabla V(\vec{r})$ generated by an electrostatic potential $V(\vec{r})$ at the nucleus, which interacts with the intrinsic quadrupole moment of the nucleus. The general form of this interaction is typically

$$\mathcal{H}_{\text{Q}} = \frac{3e^2 Qq}{4I(2I-1)} \left[I_z^2 - \frac{1}{3}I(I+1) + \frac{\eta}{3}(I_x^2 - I_y^2) \right], \tag{8.2}$$

where Q is the quadrupole moment of the nucleus, $eq = V_{zz}$ is the electric field gradient along the $z-$axis, and η is the asymmetry parameter.[99]. In the case of axial symmetry ($\eta = 0$), the total hamiltonian $\mathcal{H}_{\text{D}} + \mathcal{H}_{\text{Q}}$ is already in diagonal form with eigenvalues

$$\epsilon_i = -a'i + P \left[i^2 - \frac{1}{3}I(I+1) \right], \tag{8.3}$$

for $i = -I, -I+1, ..., I-1, I$, where $a' = \frac{\mu H_{\text{eff}}}{I}$ is the magnetic hyperfine constant, and $P = \frac{3e^2 Qq}{4I(2I-1)}$ is the electric quadrupole coupling constant. Recall from section 3.1, that the specific heat of a simple two-level system exhibits a Schottky anomaly defined by a single parameter Δ, equal to the difference in energy between the two levels

$$C_{\text{Schottky}} = R \left(\frac{\Delta}{T} \right)^2 \frac{e^{\Delta/T}}{\left(1 + e^{\Delta/T}\right)^2}. \tag{8.4}$$

When there are more than two energy levels, the specific heat is effectively a sum of Schottky anomalies, varying in position and amplitude. When a nuclear spin$-I$ is split into $2I+1$ energy levels, ϵ_i, where $i = -I, -I+1, ..., I-1, I$, then the total nuclear specific heat derived from the partition function has the following form

$$C_N = \frac{R}{(kT)^2} \frac{\sum_{i=-I}^{+I} \sum_{j=-I}^{+I} (\epsilon_i^2 - \epsilon_i \epsilon_j) \exp\left[-(\epsilon_i + \epsilon_j)/kT\right]}{\sum_{i=-I}^{+I} \sum_{j=-I}^{+I} \exp\left[-(\epsilon_i + \epsilon_j)/kT\right]}. \tag{8.5}$$

This function has the same high and low-temperature behaviour as a two-level Schottky anomaly. It is suppressed exponentially $\sim e^{-\delta/T}$ for $T << T_{\max}$ and exhibits $\sim T^{-2}$ behaviour for $T >> T_{\max}$, where $T_{\max} \approx (\epsilon_{i+1} - \epsilon_i)/kI$ corresponds to the average peak position of equation 8.5.[99]

Different isotopes of the same element will have magnetic hyperfine interactions related by their nuclear gyromagnetic factors μ/I through the ratio

$$\frac{a_i'}{a_j'} = \frac{\mu_i/I_i}{\mu_j/I_j}, \tag{8.6}$$

and the ratio of quadrupolar constants is

$$\frac{P_i}{P_j} = \frac{Q_i I_j (2I_j - 1)}{Q_j I_i (2I_i - 1)}. \tag{8.7}$$

These constraints are valid when the effective magnetic field H_{eff} is constant over the nuclear volume, and is likely a safe assumption for the case of $4f$ electrons which have zero density at the center of the nucleus.[99] In the case of Yb, using the nuclear moments in table 8.1 results in the constraint

$$a'(^{173}\text{Yb}) = -0.275 \times a'(^{171}\text{Yb}). \tag{8.8}$$

Theoretical values for Yb^{3+} are $aJ(^{171}\text{Yb}) = 3100$ MHz $= 148.8$ mK , $aJ(^{173}\text{Yb}) = $ -850 MHz $= $ -40.8 mK, where $J = 7/2$ for the saturated magnetic moment of the free ion.[156] These values are often compared as a single variable corresponding to the effective magnetic field at the nucleus

$$H_{\text{eff}} = \frac{a' I}{\mu}. \tag{8.9}$$

The theoretical value estimate of Bleaney gives $H_{\text{eff}} = 421$ T for a fully ordered moment ($J = \frac{7}{2}$), while another value obtained from Mössbauer spectroscopy specifically for ^{170}Yb, was 115 T.[70, 157] This large difference is due to the size of the ordered moment, which

attains its maximum value $J = \frac{7}{2}$ for the free-ion calculation. It is significantly smaller in the Mössbauer study, $\sim 1.15\mu_B$.

The isotope ^{171}Yb has nuclear spin$-\frac{1}{2}$, and therefore does not have a quadrupole moment because it is forbidden by the Wigner-Eckart theorem.[1] As mentioned earlier, the magnetic hyperfine interaction parameters in rare-earths are mainly due to orbital angular momentum of the $4f$ electrons, and are independent of the environment in a particular material. However, this is not true for the quadrupolar interaction, which depends strongly on the crystal field environment. The electric field gradient (EFG) can be computed from the crystal electric field energies, or it can be measured with a complementary technique such as Mössbauer spectroscopy. Both of these methods have been performed in the literature for $Yb_2Ti_2O_7$, yielding the same value for the EFG at the Yb^{3+} nucleus in the low temperature limit of $V_{zz} = 25$ VÅ^{-2} (it is temperature independent below 4.2 K).[60, 61] In the case of ^{173}Yb, using $Q = 3.0$b[158], $I = \frac{5}{2}$, this corresponds to a coupling constant

$$P = \frac{3eQV_{zz}}{4I(2I-1)}k_B = 0.65 \text{ mK}. \tag{8.10}$$

While Ti^{3+} ions do not carry a magnetic moment in $Yb_2Ti_2O_7$, they do have a quadrupole moment. There are no explicit estimates for the electric field gradient at the Ti^{3+} site available in the literature, but it turns out that this contribution is negligible in the analysis that follows.

---

[1]The quadrupole operator Q is a rank-2 tensor and according to the Wigner-Eckhart theorem, it couples with spin$-\frac{1}{2}$ to produce either $j = \frac{3}{2}$ or $\frac{5}{2}$, and therefore $\langle\frac{1}{2}|Q|\frac{1}{2}\rangle = 0$.

8.2 Results

The measured specific heat for both samples in figure 8.4 exhibits an offset, some differences in the shape of the ferromagnetic peak, and of course the hyperfine contribution is reduced for the enriched sample. The qualitative offset observed here for the enriched sample is likely associated with levels of excess Yb^{3+} below 1%. Variations in the position, amplitude, and width of the peak have also been attributed to very small off-stoichiometry.[38, 39]
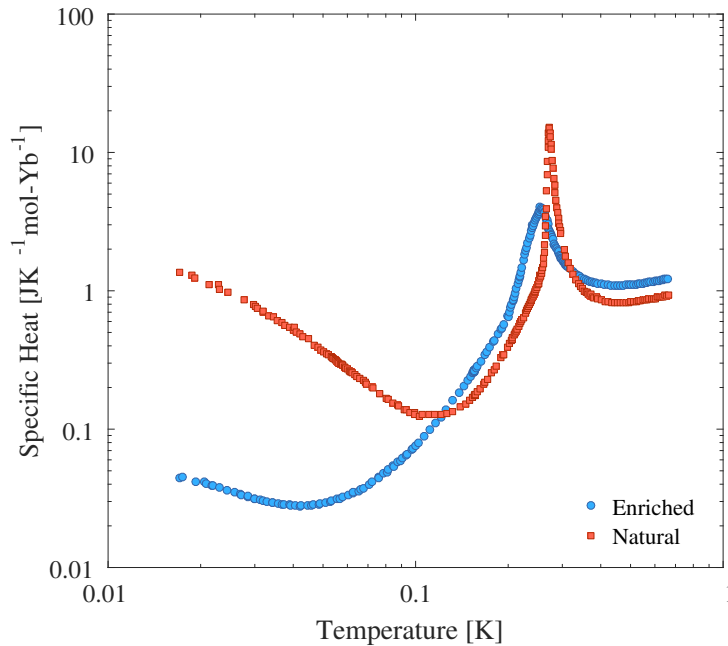
Figure 8.4: Total specific heat of natural and enriched $Yb_2Ti_2O_7$ from 15 mK to 660 mK. The sample with with natural abundance of Yb isotopes exhibits a sharp transition at 270 mK, and a large upturn below 100 mK due to nuclear hyperfine interactions. The enriched sample also exhibits a sharp transition at 260 mK and a reduced nuclear term.

The enriched material has a significant, but reduced nuclear contribution below 100 mK. The primary contribution to this anomaly is the magnetic interaction a', and to a lesser extent the electric quadrupole interaction P. Specific heat of the natural sample was fitted to equation 8.5 with energy levels given by equation 8.3. The fit was performed below 70 mK, where the nuclear specific heat of the natural sample is about an order of magnitude greater than the enriched material. The numerical fitting procedure was performed by calculating the energy level splitting for various hyperfine parameters, a', and P, consistent

with the constraints mentioned in the previous section. The best hyperfine parameters were found to be $a'(^{171}\text{Yb}) = 43.2$ mK, and $a'(^{173}\text{Yb}) = -11.9$ mK, corresponding to an effective hyperfine field $H_{\text{eff}} = 120$ T, in close agreement with $^{170}\text{Yb}_2\text{Ti}_2\text{O}_7$ Mössbauer spectroscopy which obtained $H_{\text{eff}} = 115$ T.[70] Assuming the theoretical values calculated for the fully ordered $J = \frac{7}{2}$, Yb^{3+} free-ion in reference [156], this would suggest that the saturated Yb moment is $\langle J_z \rangle = a/a' = 0.98\mu_B$. This is close to the value inferred from neutron scattering, $0.90(9)\mu_B$,[81] and from Mössbauer spectroscopy $1.15\mu_B$.[70] The quadrupole constant is particular to the chemical environment, and was found to be $P = 0.9$ mK from the fitting procedure. These numbers can be compared directly with Mössbauer spectroscopy measurements, which reported an electric field gradient $V_{zz} = eq = 25$ VÅ^{-2} for nuclear spin $I = 2$, ^{170}Yb.[60] Using the quadrupole moment $Q(^{173}\text{Yb}) = +3.0\text{b}$,[158] the quadrupolar coupling constant is then given by $P = 3e^2Qq(4I(2I-1))^{-1} = 0.7$ mK. The residual specific heat in figure 8.5 exhibits T^4 behaviour below the 270 mK ordering transition down to 60 mK.
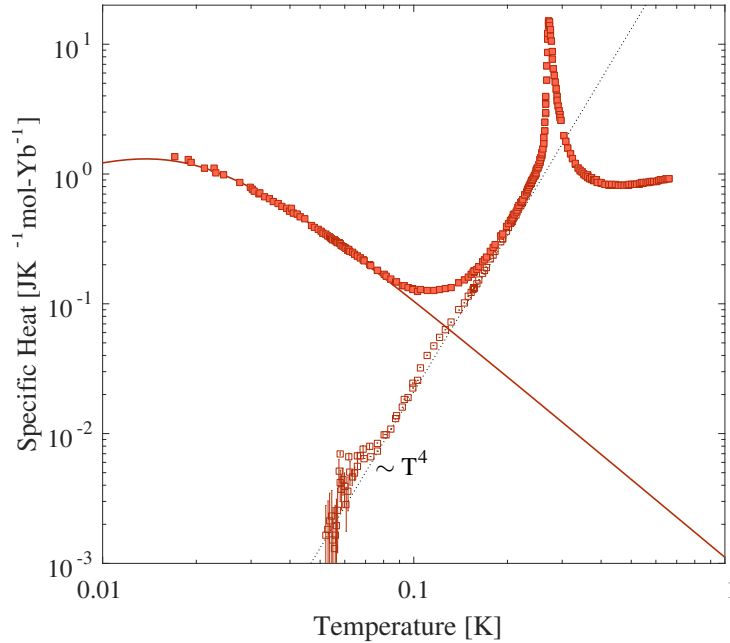
Figure 8.5: Specific heat of natural $\text{Yb}_2\text{Ti}_2\text{O}_7$ exhibiting a large nuclear anomaly below 0.1 K. Numerical fits to the anomaly were subtracted, yielding a polynomial behaviour $\sim T^4$ below the sharp transition at 0.27 K. The subtraction becomes unreliable below this temperature because it is limited by the precision of the measurement. Lattice phonon contributions on the order of 10^{-5} [JK^{-1}mol-Yb^{-1}] are insignificant below 100 mK.[159]

Hyperfine interactions are short ranged, and therefore the nuclear specific heat of the enriched sample should simply scale with the ratio of Yb isotopes with non-zero nuclear spin. The chemical assay of enriched Yb_2O_3 shown in table 8.1 provides "typical" values of 0.08% ^{171}Yb, and 0.51% ^{173}Yb quoted by the manufacturer, but the certainty of these figures was not guaranteed. The measured specific heat suggests that the total level of these isotopes should be $\sim 45\%$ higher than indicated by the manufacturers assay, in order to obtain the correct amplitude of the nuclear term at the lowest temperatures. It was therefore assumed for the remainder of the analysis that the enriched sample contained 0.12% ^{171}Yb, and 0.74% ^{173}Yb isotopes. The effective hyperfine field $H_{\mathrm{eff}} = 120$ T, and the quadrupolar constant $P = 0.9$ mK obtained from fits to the natural sample were assumed to be the same in the enriched sample. The validity of this assumption relies mainly on the fact that H_{eff} (or a') is the same for both samples, which is directly proportional to the ordered magnetic moment. It was found that varying the effective field by $\pm 10\%$ does not have a significant effect on the resulting nuclear specific heat, and therefore it is likely a safe assumption. This is also a valid assumption for the quadrupolar constant, which is independent of magnetic ordering.

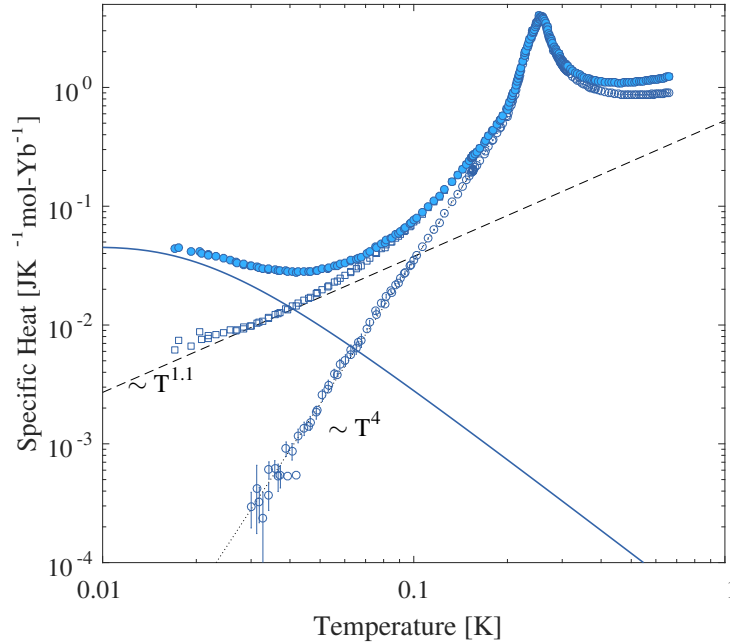Figure 8.6: Specific heat of enriched $Yb_2Ti_2O_7$ with 98.9% 174-Yb nuclear spin-0 isotopes. Hyperfine interaction parameters obtained from the natural sample were used to compute nuclear contribution, leaving residual contributions $\sim T^{1.1}$ and $\sim T^4$.

After subtracting the nuclear contribution from the enriched sample in figure 8.6, the residual specific heat contains an additional term that was not present in the natural sample. This additional term is represented well by a power-law $\sim T^{\gamma}$, with $\gamma = 1.1 \pm 0.1$ below 50 mK. Subtracting this power-law leaves behind a T^4 characteristic that matches the natural sample at low temperatures, and also improves an offset at higher temperatures. One important point, is that the empirical function $\alpha T^{1.1} + \beta T^4$ captures the behaviour very accurately, while any polynomial other than T^4 does not fit the data. The origin of this additional $T^{1.1}$ term is not entirely understood, but is believed to originate from impurities (Fe, Cu, Si, Sn) at the level of $0.6 \pm 0.12\%$ in the $^{48}TiO_2$ crystal growth material (compare to $<0.01\%$ trace metals for the natural sample). The chemical assay of impurities provided by the manufacturer is presented in table 8.3. The presence of impurities would certainly imply that $x > 0$ in $Yb_{2+x}Ti_{2-x}O_{7-\delta}$, consistent with the reduced ferromagnetic transition temperature observed.[38] The chemical formula of impurities in the material are difficult to predict because they depend on chemical reactions that take place at high temperatures during the crystal growth process. One might speculate that the Fe impurities undergo oxidation and form iron-oxide compounds. Alternate possibilities for the enhanced specific heat were also considered, such as the calorimeter addendum contribution, but this would have to be $50\times$ larger to account for the discrepancy. Another consideration is the minute levels of Ti nuclei, but that would have T^{-2} behaviour characteristic of a nuclear term. Based on this observation, it is likely that the additional $T^{1.1}$ term is a non-interacting addendum that can be subtracted from the total specific heat of the enriched sample.

Table 8.3: Assay of impurities present in the isotopically enriched Ti oxide used to prepare the enriched sample. Impurities present in the Yb oxide are insignificant in comparison to the Ti oxide. Data provided by the manufacturer, Trace Sciences International Corp.

(ppm)	Bi	Cd	Cr	Cu	Fe	Mg	Si	Sn
$^{48}TiO_2$	60	20	200	2000	6000	600	2000	2000

8.3   Discussion

The residual specific heat is compared in figure 8.7, where both samples exhibit very similar behaviour below their ferromagnetic ordering transitions. The assumptions regarding impurities in the enriched material present uncertainty in the analysis, and this should be kept in mind when making any conclusions from that sample. Conversely, the nuclear specific heat of the natural sample has excellent agreement with theoretical and experimental investigations of Yb nuclear magnetism. Both materials exhibit very clean T^4 behaviour, perhaps the only documented example of such behaviour in a magnetic system at these temperatures. Several possible scenarios are now considered for the interpretation of such behaviour.
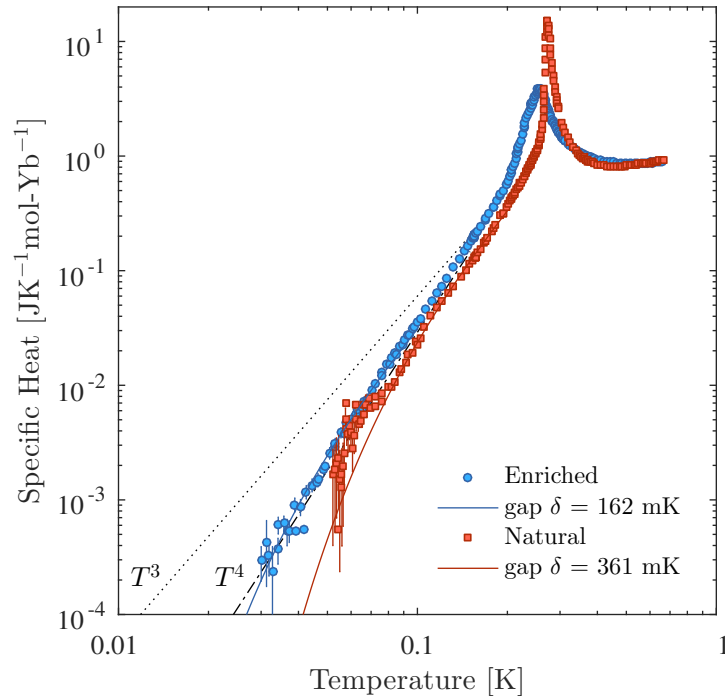

Figure 8.7: Specific heat of both samples after subtracting nuclear and impurity contributions as described in the text. The observed unconventional T^4 power-law deviates from the T^3 behaviour of gapless photons expected for a U(1) quantum spin liquid on the pyrochlore lattice. Fits to a gapped type-I pseudo-Goldstone mode are shown.

$U(1)$ **QSL and Fractional Dispersion**

It has been proposed that the existence of a quantum spin liquid phase would allow for the existence of an emergent $U(1)$ gauge field. The analogous photon would behave like the conventional photon in electrodynamics, with a linear energy dispersion relation $\omega \propto k$. Such excitations would produce energy dispersion $u \propto T^4$, and cubic specific heat $c \propto T^3$. Thus we have ruled out the possibility that these particular samples have characteristic $U(1)$ quantum spin liquid behaviour. In general, the specific heat is related to the energy dispersion through the internal energy density

$$u = \int \epsilon f(\epsilon) g(\epsilon) d\epsilon, \tag{8.11}$$

where $f(\epsilon) = (e^{\epsilon/T} - 1)^{-1}$ is the Bose-Einstein distribution, $g(\epsilon) = d\Omega/d\epsilon$ is the density of energy states where $\Omega = \frac{4\pi}{3} k^3$ is the $k-$space volume in 3-dimensions. In general, the gapless energy-wavevector relation is given by the power-law relation $\epsilon(k) = ck^n$, where n, and c are constants. This provides the link between energy and wavevector

$$g(\epsilon) = \frac{d\Omega}{d\epsilon} = \frac{4\pi n}{9} \left(\frac{1}{c}\right)^{3/n} \epsilon^{\frac{3}{n}-1}. \tag{8.12}$$

And the internal energy, where $x = \epsilon/T$, scales as

$$u(T) \propto \int \frac{\epsilon^{\frac{3}{n}}}{e^{\epsilon/T} - 1} d\epsilon = T^{1+\frac{3}{n}} \int_0^\infty \frac{x^{\frac{3}{n}}}{e^x - 1} dx. \tag{8.13}$$

For photons with linear dispersion ($n = 1$), we get $u \propto T^4$. In the present case, the measured quartic specific heat would imply that the internal energy scales as $u \propto T^5$, implying that the excitations giving rise to this energy relation have dispersion $\omega = \epsilon \propto k^{3/4}$. While rather uncommon, there do exist theoretical examples of fractional dispersion relations, such as $\omega \propto k^{3/2}$, the so-called ripplon in a superfluid-superfluid interface.[160]

Pseudo-Goldstone Modes

The observed quartic behaviour may resemble the order-by-quantum-disorder scenario in $Er_2Ti_2O_7$, where quantum zero point fluctuations, and low energy thermal fluctuations play a role in ground state selection among competing phases. This mechanism for ground state selection is inhereted from the phase boundary of neighbouring phases, and is analogous to the mechanism that selects Ψ_3 states for parameters near the ferromagnetic phase of

the anisotropic exchange model.[80] In that model, fluctuations induce a small gap in the spin-wave spectrum with dispersion, known as a type I pseudo-Goldstone mode

$$\omega_{\bm{k}} = \sqrt{v|\bm{k}|^2 + \Delta^2}.$$

(8.14)

Pseudo-Goldstone modes that appear in linear spin-wave theory are often classified as type I or type II, which correspond to having non-conserved or conserved order parameters, respectively.[161, 162, 163] Computing the energy of the system with Bose-Einstein statistics, the resulting specific heat takes the form of an integral equation [86]

$$C_\Delta = \alpha \left(\int_0^\infty dx \frac{x^2(x^2 + \delta^2)}{\sinh^2 \frac{\sqrt{x^2+\delta^2}}{2}} \right) T^3,$$

(8.15)

where α depends on various constants, $x = k\beta$ and $\delta = \beta\Delta$ are dimensionless constants. The integral depends on the gap Δ and the temperature $T = \beta^{-1}$, and it can modify the $\sim T^3$ behaviour and resemble $\sim T^4$ within a limited temperature range. The residual specific heat of each sample was fit to $C_\Delta T^{-2}$ vs. T with the least squares method, to data below 200 mK where the ferromagnetic transition peak should be negligible. The resulting fits and gap temperatures Δ are shown in figure 8.7. These fits provide reasonable agreement with the observed behaviour below 200 mK for the natural sample, indicating an upper bound for such a phenomenological gap of ~ 0.36 K. Assuming that the analysis for the isotopic sample is correct, a rough estimate for the upper bound on the pseudo-Goldstone gap is ~ 0.16 K.

The question arises: what is the nature of low energy spin excitations near the phase boundary of the FM, Ψ_2, and Ψ_3 phases that define the behaviour of $Yb_2Ti_2O_7$? We cannot rule out the observation of gapped excitations below the temperature range of our measurements, but the quartic temperature dependence of specific heat is indicative of low energy behaviour that may be associated with either magnetic, or even higher order gapless multipolar excitations.

Chapter 9

Specific Heat of Terbium Titanate $Tb_2Ti_2O_7$

Various explanations have been proposed to explain the mechanism of non-magnetic "hidden order" observed in specific heat measurements of $Tb_2Ti_2O_7$ at $T_c \approx 0.5$ K. Some proposed that magnetoelastic coupling leads to a cooperative Jahn-Teller transition, splitting the ground state doublet into two singlets. [164, 165, 166, 167] Recently, compelling evidence has surfaced that the hidden order is likely associated with electric quadrupole moments of the non-Kramers Tb^{3+} ions, or perhaps even higher order multipole moments.[168, 169, 96, 37, 170] These low-lying crystal field states do not couple directly to neutrons, making them elusive to scattering measurements. The esimated pseudospin$-\frac{1}{2}$ Hamiltonian parameters for $Tb_2Ti_2O_7$ have placed it close to a phase boundary between electric quadrupole order, and a U(1) quantum spin liquid state; suggesting that the vanishing of T_c for $Tb_{2+x}Ti_{2-x}O_{7+y}$ with $x < -0.0025$ corresponds to a transition into the putative U(1) quantum spin liquid phase.[55] In this chapter, nuclear specific heat measurements are presented for two samples that belong to either side of this transition.

9.1 Methods

Off-stoichiometric $Tb_{2+x}Ti_{2-x}O_{7+y}$ samples with a range of x were provided by collaborator H. Kadowaki from Tokyo Metropolitan University. Eight samples with nominal values of x ranging from -0.0125 to $+0.0050$ were prepared by mixing different ratios of the starting materials Tb_4O_7, and TiO_2 relative to a nominally $x = 0$ batch. The specific heat of these samples between 400 mK and 2 K in figure 1.19, was previously reported by Taniguchi *et al.*[36] The results indicated the presence of a sharp feature in the specific heat around 0.5 K that is gradually suppressed and disappears completely below the nominal critical value $x_c = -0.0025$. Powder neutron diffraction measurements performed on the $x = +0.0050$ sample above, and below this transition temperature did not exhibit any clear changes due to a structural transition. Inelastic neutron scattering was also measured above and below T_c, indicating the presence of a $\left(\frac{1}{2}\frac{1}{2}\frac{1}{2}\right)$ Bragg peak for the $x = +0.005$ sample, with an estimated upper limit on the antiferromagnetic ordered moment of about $0.1\mu_B$. This peak was absent in the $x = -0.005$ sample. The corresponding $0.08\mu_B$ ordered moment was much smaller than expected for the $\sim 5\mu_B$ ground doublets, an indication that that residual spin fluctuations might persist at these temperatures.

In this work, two polycrystalline samples of $Tb_{2+x}Ti_{2-x}O_{7+y}$ with nominal values of $x = +0.0050$ and $x = -0.0075$, were selected for specific heat measurements between 14 mK and 1 K. These samples are respectively referred to as 'stuffed' and 'under-stuffed', to indicate an excess and shortage of Tb. The study in reference [36] suggested that the stuffed compound exhibits order below 0.5 K associated with a planar antiferropseudospin (PAF) phase, while the understuffed material is believed to have be a paramagnetic quantum spin liquid. Specific heat measurements were performed in zero field ($< 10^{-3}$ G) with the quasi-adiabaitc heat pulse technique described in section 3.4, and the calorimeter design described in section 3.6. The stuffed and under-stuffed samples both had $Pt_{92}W_8$ thermal links with conductance 1.0×10^{-6} WK^{-1} and 6.6×10^{-6} WK^{-1}, respectively at 0.5 K. Both samples were mixed with approximately equal volumes of silver powder to improve the low temperature thermal conductance, which is known to be very poor at these temperatures in $Tb_2Ti_2O_7$.[171]

9.2 Results

Specific heat measurements for two polycrystalline samples of stuffed ($x = 0.005$) and under-stuffed ($x = -0.0075$) $Tb_{2+x}Ti_{2-x}O_{7+y}$ between 14 mK and 1 K are shown in figure 9.1. It was hypothesized that the stuffed sample should exhibit low-temperature quadur-polar order associated with the sharp peak at $T_c = 0.5$ K. The under-stuffed sample did not exhibit any similar features, suggesting the presence of a paramagnetic spin liquid ground state. Below ~ 200 mK, a large anomaly associated with the nuclear hyperfine interaction dominates the specific heat of both samples.
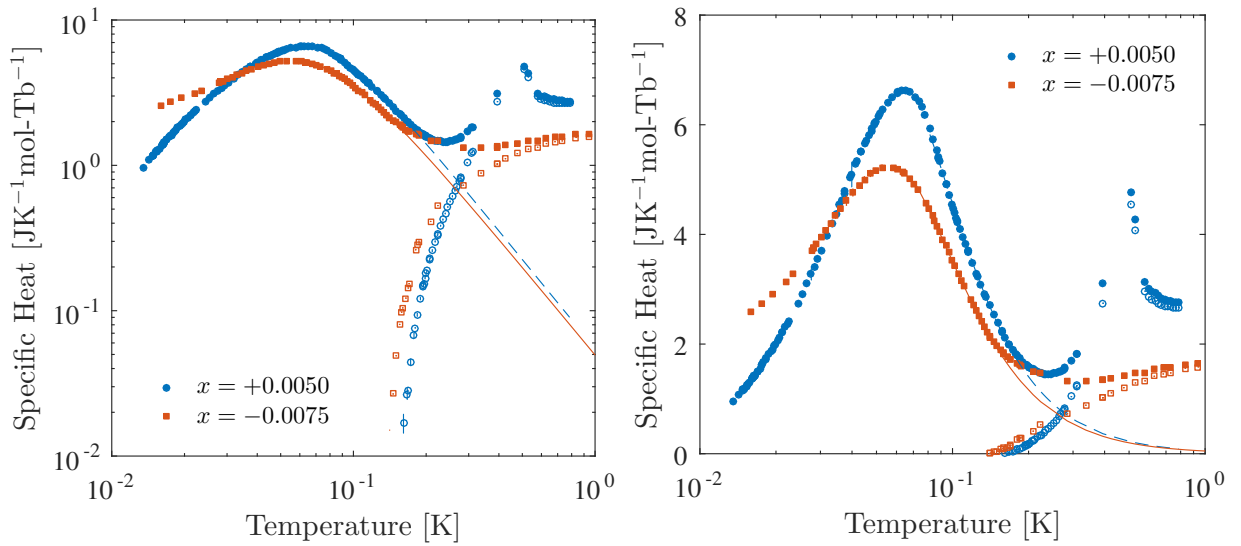
Figure 9.1: Specific heat of stuffed ($x = +0.005$), and under-stuffed ($x = -0.0075$) $Tb_{2+x}Ti_{2-x}O_{7+y}$ plotted with logarithmic, and linear axes to emphasize the low temperature behaviour. The high temperature side of the nuclear specific heat anomaly was fit to equation 9.1 (solid lines), and subtracted from each sample (hollow markers).

The apparent variations in the nuclear specific heat of both compounds below ~ 200 mK provides a strong indication that the hyperfine interactions are different for each compound. This is not surprising, considering that the dipolar and quadrupolar order is known to vary among these materials. There is also the possibility of an underlying transition in one of the materials. The magnetic moments of the Tb atoms are not fully ordered, which makes it difficult to apply the standard hyperfine theory. An attempt was made to fit the observed nuclear anomaly using the standard approach that was applied to $Yb_2Ti_2O_7$ in section 8.1.1;

where magnetic moments on the rare-earth atoms are fully saturated, and the electric field gradient has axial symmetry. This model did not produce satisfactory results for either sample of $Tb_2Ti_2O_7$. Based on the poor quality of those fits on the low temperature side of the nuclear anomaly, a simple hyperfine model cannot capture the nuclear behaviour. It is possible that the electronic quadrupole moment of the non-Kramers Tb^{3+} moment gives rise to a significant hyperfine interaction with its nuclear quadrupole moment.

In section 3.1, it was demonstrated that the specific heat obtained for the splitting of a spin$-I$ nucleus can be expanded in inverse powers of T, where the first three coefficients are given by equations 3.13. Within this approximation, the high temperature tail of the nuclear anomaly has the form

$$C_{\text{Sch}} = c_2 T^{-2} + c_3 T^{-3} + c_4 T^{-4} + \dots \tag{9.1}$$

This procedure may be valid within a limited temperature range if the hyperfine interactions are not changing significantly with temperature. The resulting nuclear fits shown in figure 9.1 describe the data very well in the fitted range $0.08 < T < 0.17$ (stuffed) and $0.07 < T < 0.15$ (understuffed). After subtracting this term, the residual specific heat exhibits a sharp drop characteristic of a gap in the energy spectrum.

Naturally occurring terbium contains only one stable isotope (^{159}Tb) with nuclear spin$-\frac{3}{2}$, and quadrupole moment 1.432 b. The maximum entropy that can be extracted from a nuclear specific anomaly is therefore equal to $R\ln(2I+1) = R\ln 4 \approx 11.53$ JK^{-1}mol^{-1}. The total entropy for each sample was obtained from the integral of cT^{-1} in figure 9.2, where the high temperature tail was extrapolated using the fitted curves. The resulting entropy associated with the stuffed sample is ≈ 11.0 JK^{-1}mol^{-1}, while for the understuffed sample it is 9.7 JK^{-1}mol^{-1}. Both of these values are less than expected, indicating that measurements need to be extended to lower temperatures in order to obtain the full nuclear entropy. The value obtained for the stuffed sample is very close to $R\ln 4$, indicating that there may be an additional entropy contribution that is not accounted for by splitting of ^{159}Tb nuclear spins alone, such as a transition at very low temperature.
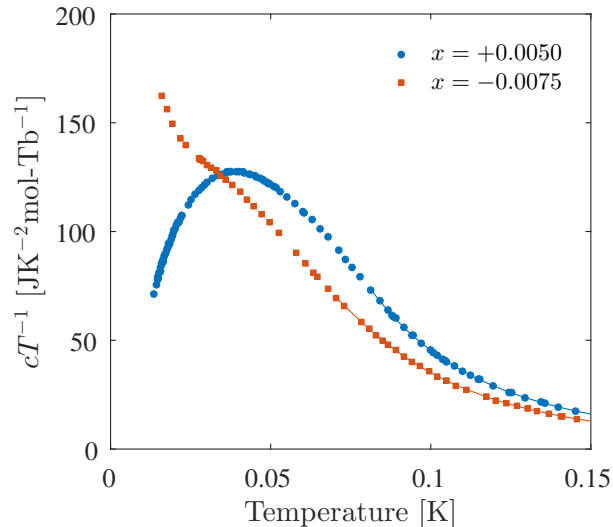
Figure 9.2: Specific heat divided by temperature of stuffed ($x = 0.005$), and under-stuffed ($x = -0.0075$) $Tb_{2+x}Ti_{2-x}O_{7+y}$. The total entropy of the nuclear peak $s = \int cT^{-1}dT$ should equal $R\ln(2I+1)$ for a spin$-I$ nucleus.

9.3 Discussion

Discrepancies between the standard hyperfine theory and experimental data could be due to several reasons. The ground state of $Tb_2Ti_2O_7$ has been described as a spin liquid with persistent dynamics, with a saturated magnetic moment $\langle J_z \rangle$ is less than the $\approx 5\mu_B$ expected for a fully saturated ground doublet.[90, 172] There is no strong indication from neutron scattering measurements of a temperature dependence to this parameter below 0.5 K,[36] suggesting that the magnetic hyperfine constant should not be affected. The electronic quadrupolar moment in $Tb_2Ti_2O_7$ may produce a contribution to the electric field gradient at the nucleus, not accounted for with the simple hyperfine model in section 8.1.1. However, this type of analysis is beyond the scope of the current work and certainly requires more rigorous investigation. Perhaps it is sufficient to use a generalized hyperfine Hamiltonian which captures the symmetry of the ordered quadrupolar moments.

The situation here in $Tb_2Ti_2O_7$ might also resemble the theoretical model discussed in reference [13], where electronic spin fluctuations persist in the low temperature regime of nuclear coupling. This produces an effective hyperfine temperature that appears out of equilibrium, with a nuclear Schottky anomaly that is shifted in temperature or amplitude.

In order to demonstrate these effects, Bertin *et al.* considered a model of nuclear spins subject to fluctuating electronic spins. The nuclear component was modeled as a two-level spin$-\frac{1}{2}$ system driven by a randomly time dependent hyperfine field. This type of model has the ability to modify the temperature dependence of the nuclear specific heat.

The generalized high temperature expansion in equation 9.1 captures the behaviour of a nuclear anomaly regardless of the spacing of nuclear energy levels. This should be a valid assumption for a system with partial or fully ordered multipole moments. Performing the analysis under these assumptions, the resulting subtraction for both samples indicates a rapid drop in specific heat, suggestive of gapped modes. This is in contrast to the expectation of cubic T^3 behaviour expected for a U(1) quantum spin liquid state, and therefore it is unlikely that such a phase exists in either of these samples within the measured temperature range.

Chapter 10

Summary

Specific Heat of Dy$_2$Ti$_2$O$_7$

Spin-ice is a theoretical model that has the same statistical properties of hydrogen atoms in water ice. One of the consequences of this analogy is the same intrinsic randomness below the freezing temperature. The geometrical structure of these ice models results in a highly degenerate system of energetically equivalent configurations equal to Pauling's residual entropy for water ice. Dy$_2$Ti$_2$O$_7$ and Ho$_2$Ti$_2$O$_7$ are the archetypes of spin-ice that are adequately described with the classical dipolar spin-ice model for a wide temperature range. While their behaviour above ~ 1 K is well understood, properties in the Coulomb phase are convoluted by the emergence of fractionalized excitations very similar to deconfined magnetic monopoles. These emergent quasiparticles inevitably have a strong influence on the low temperature properties of spin-ice that are not completely understood.

Specific heat measurements were performed on the archetypal spin-ice Dy$_2$Ti$_2$O$_7$ between 340 mK and 1 K with a unique approach; ensuring that the material is in thermal equilibrium throughout the entire measurement. Extremely slow attributes are apparent below $\sim$0.6 K where the magnetic spin relaxation time observed with ac susceptibility measurements diverges exponentially. Calorimetry was implemented with a thermal relaxation method to ensure the system equilibrates adiabatically on timescales of the magnetic system. In order to detect small changes in temperature associated with the release of heat from the system, it was essential to couple the sample to the cryostat with a weak thermal conductor. This weak link acts as an impedance to heat flow, which sets the rate at which the sample can equilibrate with the cryostat. It also acts as a heat sensor, where the temperature gradient across the link is proportional to the rate of heat flow. These measurements enforce that Dy$_2$Ti$_2$O$_7$ is characterized by slow dynamics in accordance with

the timescales determined by magnetic relaxation measurements, and the total entropy extracted from the system upon freezing is lower than expected for Pauling's entropy. This observation may imply that the material undergoes magnetic order on extremely slow timescales. According to our work, the thermal relaxation time can reach $\gtrsim 10^4$ seconds below ~ 0.3 K. The results presented in section 7.3 provide a strong argument that the variations in specific heat previously observed for these materials (figure 6.7) were likely due to equilibration issues.

Henelius *et al.,* have demonstrated that introducing additional parameters into the dipolar spin ice model associated with substitution defects (stuffing), is qualitatively consistent with the behaviour observed in our measurements, however, the required levels of disorder are on the order of 1%. The current status of many other projects in the literature that investigate this work are still relatively inconclusive, and the low-energy state of $Dy_2Ti_2O_7$ remains yet to be understood completely.

Magnetic Susceptibility of $Dy_2Ti_2O_7$

Magnetic susceptometry is a tool that probes intrinsic dynamics of a material, or the ability for magnetic moments to freely rotate within a lattice. A gentle magnetic field ≈ 5 mOe is applied to avoid driving resonant transitions when examining the kinetics. In chapter 7, results spanning 0.5 K to 1 K, and 1 mHz to 1 kHz, were presented for two samples of $Dy_2Ti_2O_7$ that were cut from a single crystal. In an attempt at reducing oxygen vacancies, one of these samples was annealed in oxygen at high temperature. This work was part of a larger collaboration that investigated the effect of oxygen vacancies and their effect on monopole dynamics in oxygen-deficient pyrochlores.[40].

In sections 4.4 and 7.3, the validity of experimental results were analyzed with various approaches. This was particularly important because errors associated with demagnetization effects can influence the observed susceptibility. The arguments presented were aimed at quantifying the magnitude of errors associated with these effects, and the complications that arise in measurements were scrutinized. From this analysis, susceptibility measurements demonstrate that oxygen deficiency has significant effects on low temperature magnetic dynamics. In particular,

1. Temperature dependence of the magnetic relaxation time $\tau(T)$ has qualitative similarities for both samples, but the annealed material exhibited slower dynamics corresponding to a larger energy cost to flip spins.

2. The widening of $\chi''(\omega)$ with T observed for the annealed sample suggests a broader distribution of relaxation timescales compared to the as-grown sample.

3. The dynamic spin correlation function $C(t)$ exhibits features consistent with a stretched exponential, followed by power-law (algebraic) behavior at longtime scales. It appears that annealing may eliminate this algebraic behavior, with the caveat that this function is very sensitive to the analytic form use to fit $\chi''(\omega)$ in equation 7.3. Although the Havriliak-Negami relaxation model in equation 7.2 provides a very good fit to the experimental data, it fails to capture this subtle effect that eliminates the algebraic behavior.

4. In the low frequency limit, the dc susceptibility $\chi''(\omega)$ appears insensitive to oxygen deficiency, stuffing, or other impurities that produce the observed sample variation. This suggests that the equilibrium ground state properties are less sensitive to these defects.

The important conclusions from this work should be emphasized. First, annealing the sample in oxygen lowers the exponential stretching factor β observed in the magnetic relaxation curves. This was surprising because the absence of random defects is typically associated with an exponential ($\beta = 1$). The presence of defects might destroy correlations that are otherwise responsible for slow dynamics.

The algebraic longtime tail in the dynamic spin correlation function, obtained using the fluctuation-dissipation theorem, is also very sensitive to subtle features in the low-frequency tail of the susceptibility $\chi''(\omega)$. Upon annealing, these subtle features are not captured by the standard Havriliak-Negami relaxation model, but require more generalized phenomenology that accounts for the asymmetry of the $\chi''(\omega)$ spectrum.

This study identifies the major qualitative features in the low temperatures susceptibility that differ as a result of oxygen annealing. It has been found that some features, including the barrier to relaxation, the longtime algebraic correlations, and the exponential decay stretching factor, can vary significantly with very low levels of defects. The characteristics of an ideal material are not yet understood, nor are many of the mechanisms that give rise to their intriguing behaviour, and these are certainly topics for future work.

Specific Heat of $Yb_2Ti_2O_7$

The Yb^{3+} ion in $Yb_2Ti_2O_7$ has significant planar anisotropy in comparison to the classical Ising-like spin-ices. Ice correlations are manifested as a Schottky-like anomaly in specific heat near 2 K, followed by a sharp feature at a critical temperature $T_c \approx 0.27$ K. While the nature of this transition was controversial for some time, there is now abundant evidence that $Yb_2Ti_2O_7$ enters a splayed-ferromagnet phase below T_c. This critical temperature has also revealed significant sample dependence that is correlated with substitutional defects due to stuffing. Despite exhibiting evidence of ferromagnetic long-range order, some experiments observe features associated with strong fluctuations that are reminiscent of a spin liquid. These characteristics may originate from higher order multipolar moments that go beyond the conventional description of magnetic dipoles.

In chapter 8, measurements were performed on two samples of $Yb_2Ti_2O_7$ between 15 mK and 660 mK using the quasi-adiabatic heat pulse method described in section 3.4. Measurements of specific heat in this temperature range are dominated by nuclear hyperfine contributions, arising from the interaction of nuclear spin with the surrounding electronic degrees of freedom. One of the samples containing natural abundances of Yb isotopes demonstrates excellent agreement with theoretical hyperfine models. After subtracting these nuclear contributions, the underlying specific heat exhibits unconventional quartic behaviour $c \propto T^4$ that does not have a conventional explanation. Another sample was prepared with $\approx 99\%$ ^{174}Yb isotopes to reduce the effect of hyperfine interactions. The measured specific heat of this sample was complicated by additional terms likely originating from impurities in the TiO_2 growth material ($\sim 0.6\%$ Fe). Careful analysis suggests these are described by an almost linear term $c \propto T^{1.1\pm0.1}$, on top of the quartic behaviour T^4 that was present in the natural isotopic sample. The magnitude of these terms were not accountable to the known levels of metallic impurities, and therefore this fitting procedure was performed on a phenomenological basis. While definitive conclusions should not be obtained from the isotopically enriched sample, they demonstrate the effect of impurities on the low energy state.

The quartic $c \propto T^4$ specific heat observed in the natural sample is evidence of unconventional excitations that persist below the critical temperature, to at least 55 mK. This rules out the possibility of purely cubic specific heat $c \propto T^3$ in our samples, which would be consistent with the linear energy-momentum dispersion relation of photons emerging from a $U(1)$ quantum spin liquid phase. However, another possibility is that the observed specific heat may be qualitatively consistent with a linear dispersion relation that acquires a small gap Δ where $\omega_{\boldsymbol{k}} = \sqrt{v|\boldsymbol{k}|^2 + \Delta^2}$, similar to a pseudo-Goldstone mode. The existence of such a mode was predicted in $Er_2Ti_2O_7$, a close relative of $Yb_2Ti_2O_7$. This

would give rise to a cubic temperature dependence that gives way to an exponential drop in specific heat. Using this phenomenological approach, the natural sample exhibits an upper bound on the gap of ~ 0.36 K. The isotopic sample had consistency with a gap of ~ 0.16 K, but this analysis was not as rigorous as for the natural sample. Within the context of the pseudospin$-\frac{1}{2}$ exchange model, both these compounds are positioned near competing phases in the ground-state phase diagram. As demonstrated for $Er_2Ti_2O_7$, quantum fluctuations play a role in the ground state selection for these materials through the mechanism of order by quantum disorder. We speculate that a similar mechanism may be at play in $Yb_2Ti_2O_7$ due to the reasonable agreement with the pseudo-Goldstone mode dispersion relations. Another scenario consistent with purely quartic specific heat, is fractional dispersion that scales as $\omega \propto k^{3/4}$. While uncommon in condensed matter physics, there are theoretical examples of fractional dispersion relations in the literature.

The measurements performed in this study also prompted a thorough evaluation of thermometer calibrations down to 14 mK that is described with detail in chapter 5. The accuracy and precision of thermometry can present challenges near the base temperature of any millikelvin-range cryostat because parasitic heat flow can offset the measured temperature from its actual value. Ensuring that these effects are negligible requires a significant effort in the design, assembly, and verification of the cryostat performance in accordance with various observations. Verification is especially important in the limit where the cooling power of the fridge is very low because thermal gradients can be significant. In an effort to minimize temperature offsets due to self-heating, resistance thermometers used for calorimetery were calibrated in-situ for each sample by mechanically shorting the thermal link between the calorimeter and cryostat. The layout of electrical leads on the cryostat was assembled very carefully to ensure that temperature gradients are minimized for each particular application. The calibration down to 14 mK was verified with paramagnetic cerium magnesium nitrate (CMN), and radioactive ^{60}Co nuclear gamma ray orientation as calibration references, using the methods described in section 5. This calibration process also revealed that a commercial germanium resistance (GRT) thermometer was significantly miscalibrated below 100 mK, despite a certificate of calibration down to 50 mK.

Specific Heat of $Tb_2Ti_2O_7$

The most recent project described in this thesis pertains to the compound $Tb_2Ti_2O_7$. Specific heat was measured between 15 mK and 1 K for two samples with stoichiometry $Tb_{2+x}Ti_{2-x}O_{7+y}$ where +0.0050 (stuffed), and $x = -0.0075$ (understuffed) respectively indicating an excess, and shortage of Tb. The sharp feature observed at a critical temperature $T_c = 0.5$ K for the stuffed sample is completely absent in the under-stuffed compound. Below the critical temperature, a variety of other experiments indicate that the magnetic component of the Tb^{3+} ion does not develop long-range dipolar spin order and is believed to have correlations associated with a quantum spin-liquid state. The Tb^{3+} crystal field ground doublet in this compound has a relatively small gap $\Delta \sim 18$ K separating it from the first excited state doublet, which among other facts, motivates the application of a quantum spin-ice Hamiltonian. While the nature of this transition has eluded researchers for several decades, recent experimental and theoretical evidence has emerged to support electric quadrupole ordering of the non-Kramers Tb^{3+} ions.

Akin to $Yb_2Ti_2O_7$, nuclear hyperfine interactions below ~ 200 mK conceal the underlying electronic specific heat. Furthermore, there are significant differences between the measured nuclear specific heat of the stuffed, and under-stuffed materials, indicating that hyperfine interactions are different between these samples. This is an indication that either the effective magnetic field produced by Tb^{3+} ions, or the quadrupolar interaction, depends on the level of stuffing. Attempting to fit the nuclear specific heat with the standard approach (described generally in section 3.1, and in section 8.1.1 for $Yb_2Ti_2O_7$) does not agree with the experimental data. The observed specific heat for both samples does not have the shape of a Schottky-like anomaly that is expected for standard splitting of the hyperfine Hamiltonian. This could imply that the nuclear hyperfine coupling parameters are not static, but changing with temperature, which is also consistent with a fluctuating magnetic or quadrupolar moment. Another possibility is that nuclear quadrupole moments couple to the electric quadrupole moments of the Tb^{3+} ion itself and perturb the standard hyperfine Hamiltonian.

Fitting the high temperature end of the nuclear term with the standard expansion in inverse powers of temperature as $c_2T^{-2} + c_3T^{-3} + c_4T^{-4} + \dots$ yields reasonable agreement with the data. Subtracting this contribution from each sample reveals a rapid drop in specific heat, implying the presence of a gapped excitation at low energy. This refutes the possibility of a $U(1)$ quantum spin liquid in the particular samples studied, where such a system would exhibit $c \propto T^3$ at low temperatures. More theoretical and experimental work is certainly required in order to completely understand the elusive nature of this compound.

References

[1] A. P. Ramirez. Strongly Geometrically Frustrated Magnets. Annual Review of Materials Science, 24(1):453–480, 1994.

[2] W. F. Giauque and Muriel F. Ashley. Molecular Rotation in Ice at 10 K. Free Energy of Formation and Entropy of Water. Physical Review, 43(1):81–82, January 1933.

[3] Linus Pauling. The Structure and Entropy of Ice and of Other Crystals with Some Randomness of Atomic Arrangement. Journal of the American Chemical Society, 57(12):2680–2684, December 1935.

[4] W. F. Giauque and J. W. Stout. The Entropy of Water and the Third Law of Thermodynamics. The Heat Capacity of Ice from 15 to 273 K. Journal of the American Chemical Society, 58(7):1144–1150, July 1936.

[5] M. J. Harris, S. T. Bramwell, D. F. McMorrow, T. Zeiske, and K. W. Godfrey. Geometrical Frustration in the Ferromagnetic Pyrochlore $Ho_2Ti_2O_7$. Physical Review Letters, 79(13):2554–2557, September 1997.

[6] A. P. Ramirez, A. Hayashi, R. J. Cava, R. Siddharthan, and B. S. Shastry. Zero-point entropy in 'spin ice'. Nature, 399(6734):333–335, May 1999.

[7] Claudine Lacroix, Philippe Mendels, and Frdric Mila. Introduction to Frustrated Magnetism: Materials, Experiments, Theory. Springer Science & Business Media, January 2011.

[8] P. W. Anderson. Ordering and Antiferromagnetism in Ferrites. Physical Review, 102(4):1008–1013, May 1956.

[9] Byron C. den Hertog and Michel J. P. Gingras. Dipolar Interactions and Origin of Spin Ice in Ising Pyrochlore Magnets. Physical Review Letters, 84(15):3430–3433, April 2000.

[10] R. Siddharthan, B. S. Shastry, A. P. Ramirez, A. Hayashi, R. J. Cava, and S. Rosenkranz. Ising Pyrochlore Magnets: Low-Temperature Properties, "Ice Rules," and Beyond. <u>Physical Review Letters</u>, 83(9):1854–1857, August 1999.

[11] R. Siddharthan, B. S. Shastry, and A. P. Ramirez. Spin ordering and partial ordering in holmium titanate and related systems. <u>Physical Review B</u>, 63(18):184412, April 2001.

[12] Roger G. Melko, Byron C. den Hertog, and Michel J. P. Gingras. Long-Range Order at Low Temperatures in Dipolar Spin Ice. <u>Physical Review Letters</u>, 87(6):067203, July 2001.

[13] E. Bertin, P. Bonville, J.-P. Bouchaud, J. A. Hodges, J. P. Sanchez, and P. Vulliet. Effective hyperfine temperature in frustrated $Gd_2Sn_2O_7$: two level model and 155-Gd M$'$ossbauer measurements. <u>The European Physical Journal B - Condensed Matter and Complex Systems</u>, 27(3):347–354, June 2002.

[14] G. Ehlers, A. L. Cornelius, M. Orendc, M. Kajnakov, T. Fennell, S. T. Bramwell, and J. S. Gardner. Dynamical crossover in 'hot' spin ice. <u>Journal of Physics: Condensed Matter</u>, 15(2):L9, 2003.

[15] K. Matsuhira, Y. Hinatsu, and T. Sakakibara. Novel dynamical magnetic properties in the spin ice compound $Dy_2Ti_2O_7$. <u>Journal of Physics: Condensed Matter</u>, 13(31):L737, 2001.

[16] J. Snyder, J. S. Slusky, R. J. Cava, and P. Schiffer. How 'spin ice' freezes. <u>Nature</u>, 413(6851):48–51, September 2001.

[17] G. Ehlers, A. L. Cornelius, T. Fennell, M. Koza, S. T. Bramwell, and J. S. Gardner. Evidence for two distinct spin relaxation mechanisms in 'hot' spin ice $Ho_2Ti_2O_7$. <u>Journal of Physics: Condensed Matter</u>, 16(11):S635, 2004.

[18] John P. Sutter, Satoshi Tsutsui, Ryuji Higashinaka, Yoshiteru Maeno, Olaf Leupold, and Alfred Q. R. Baron. Relaxation in the spin ice $Dy_2Ti_2O_7$ studied using nuclear forward scattering. <u>Physical Review B</u>, 75(14):140402, April 2007.

[19] J. Snyder, B. G. Ueland, J. S. Slusky, H. Karunadasa, R. J. Cava, Ari Mizel, and P. Schiffer. Quantum-Classical Reentrant Relaxation Crossover in $Dy_2Ti_2O_7$ Spin Ice. <u>Physical Review Letters</u>, 91(10):107201, September 2003.

[20] Nicolas Vernier and Guy Bellessa. Tunnelling of large magnetic moments in a single crystal. Journal of Magnetism and Magnetic Materials, 177-181:962–963, January 1998.

[21] L. Thomas, F. Lionti, R. Ballou, D. Gatteschi, R. Sessoli, and B. Barbara. Macroscopic quantum tunnelling of magnetization in a single crystal of nanomagnets. Nature, 383(6596):145–147, September 1996.

[22] J. Brooke, T. F. Rosenbaum, and G. Aeppli. Tunable quantum tunnelling of magnetic domain walls. Nature, 413(6856):610–613, October 2001.

[23] Kazuyuki Matsuhira, Carley Paulsen, Elsa Lhotel, Chihiro Sekine, Zenji Hiroi, and Seishi Takagi. Spin Dynamics at Very Low Temperature in Spin Ice $Dy_2Ti_2O_7$. Journal of the Physical Society of Japan, 80(12):123711, December 2011.

[24] L. R. Yaraskavitch. An experimental investigation of the spin dynamics of dipolar spin ice. PhD thesis, University of Waterloo, 2012.

[25] H. M. Revell, L. R. Yaraskavitch, J. D. Mason, K. A. Ross, H. M. L. Noad, H. A. Dabkowska, B. D. Gaulin, P. Henelius, and J. B. Kycia. Evidence of impurity and boundary effects on magnetic monopole dynamics in spin ice. Nature Physics, 9(1):34–37, January 2013.

[26] H. M. Revell. The low temperature magnetic relaxation of $Dy_2Ti_2O_7$. PhD thesis, University of Waterloo, 2012.

[27] C. Castelnovo, R. Moessner, and S. L. Sondhi. Magnetic monopoles in spin ice. Nature, 451(7174):42, January 2008.

[28] L. D. C. Jaubert and P. C. W. Holdsworth. Signature of magnetic monopole and Dirac string dynamics in spin ice. Nature Physics, 5(4):258–261, April 2009.

[29] G. C. Lau, B. D. Muegge, T. M. McQueen, E. L. Duncan, and R. J. Cava. Stuffed rare earth pyrochlore solid solutions. Journal of Solid State Chemistry, 179(10):3126–3135, October 2006.

[30] G. C. Lau, T. M. McQueen, Q. Huang, H. W. Zandbergen, and R. J. Cava. Long- and short-range order in stuffed titanate pyrochlores. Journal of Solid State Chemistry, 181(1):45–50, January 2008.

[31] H. D. Zhou, C. R. Wiebe, Y. J. Jo, L. Balicas, Y. Qiu, J. R. D. Copley, G. Ehlers, P. Fouquet, and J. S. Gardner. The origin of persistent spin dynamics and residual entropy in the stuffed spin ice $Ho_{2.3}Ti_{1.7}O_{7-\delta}$. Journal of Physics: Condensed Matter, 19(34):342201, 2007.

[32] G. Ehlers, J. S. Gardner, Y. Qiu, P. Fouquet, C. R. Wiebe, L. Balicas, and H. D. Zhou. Dynamic spin correlations in stuffed spin ice $Ho_{2+x}Ti_{2-x}O_{7-\delta}$. Physical Review B, 77(5):052404, February 2008.

[33] R. G. Palmer, D. L. Stein, E. Abrahams, and P. W. Anderson. Models of Hierarchically Constrained Dynamics for Glassy Relaxation. Physical Review Letters, 53(10):958–961, September 1984.

[34] J. S. Gardner, G. Ehlers, P. Fouquet, B. Farago, and J. R. Stewart. Slow and static spin correlations in $Dy_{2+x}Ti_{2-x}O_{7-\delta}$. Journal of Physics: Condensed Matter, 23(16):164220, 2011.

[35] Lin, Taoran. A study of the effect of perturbations in spin ice systems: site dilution, weak exchange, quantum and finite-size effects. PhD Thesis, UWSpace, 2014.

[36] T. Taniguchi, H. Kadowaki, H. Takatsu, B. Fk, J. Ollivier, T. Yamazaki, T. J. Sato, H. Yoshizawa, Y. Shimura, T. Sakakibara, T. Hong, K. Goto, L. R. Yaraskavitch, and J. B. Kycia. Long-range order and spin-liquid states of polycrystalline $Tb_{2+x}Ti_{2-x}O_{7+y}$. Physical Review B, 87(6):060408, February 2013.

[37] M. Wakita, T. Taniguchi, H. Edamoto, H. Takatsu, and H. Kadowaki. Quantum spin liquid and electric quadrupolar states of single crystal $Tb_{2+x}Ti_{2-x}O_{7+y}$. Journal of Physics: Conference Series, 683(1):012023, 2016.

[38] K. E. Arpino, B. A. Trump, A. O. Scheie, T. M. McQueen, and S. M. Koohpayeh. Impact of stoichiometry of $Yb_2Ti_2O_7$ on its physical properties. Physical Review B, 95(9):094407, March 2017.

[39] K. A. Ross, Th. Proffen, H. A. Dabkowska, J. A. Quilliam, L. R. Yaraskavitch, J. B. Kycia, and B. D. Gaulin. Lightly stuffed pyrochlore structure of single-crystalline $Yb_2Ti_2O_7$ grown by the optical floating zone technique. Physical Review B, 86(17):174424, November 2012.

[40] G. Sala, M. J. Gutmann, D. Prabhakaran, D. Pomaranski, C. Mitchelitis, J. B. Kycia, D. G. Porter, C. Castelnovo, and J. P. Goff. Vacancy defects and monopole dynamics in oxygen-deficient pyrochlores. Nature Materials, 13(5):488–493, May 2014.

[41] Lucile Savary and Leon Balents. Quantum spin liquids: a review. Reports on Progress in Physics, 80(1):016502, 2017.

[42] L. D. Landau. On the theory of phase transitions. Zh. Eksp. Teor. Fiz., 7:19–32, 1937.

[43] V. Kalmeyer and R. B. Laughlin. Equivalence of the resonating-valence-bond and fractional quantum Hall states. Physical Review Letters, 59(18):2095–2098, November 1987.

[44] X. G. Wen, Frank Wilczek, and A. Zee. Chiral spin states and superconductivity. Physical Review B, 39(16):11413–11423, June 1989.

[45] X. G. Wen. Vacuum degeneracy of chiral spin states in compactified space. Physical Review B, 40(10):7387–7390, October 1989.

[46] Edward Witten. Quantum field theory and the Jones polynomial. Communications in Mathematical Physics, 121(3):351–399, September 1989.

[47] P. W. Anderson. Resonating valence bonds: A new kind of insulator? Materials Research Bulletin, 8(2):153–160, February 1973.

[48] L. Pauling. A Resonating-Valence-Bond Theory of Metals and Intermetallic Compounds. Proceedings of the Royal Society of London. Series A, Mathematical and Physical Sciences, 196(1046):343–362, 1949.

[49] Chanchal K. Majumdar and Dipan K. Ghosh. On NextNearestNeighbor Interaction in Linear Chain. I. Journal of Mathematical Physics, 10(8):1388–1398, August 1969.

[50] Michael Hermele, Matthew P. A. Fisher, and Leon Balents. Pyrochlore photons: The $U(1)$ spin liquid in a $S = \frac{1}{2}$ three-dimensional frustrated magnet. Physical Review B, 69(6):064404, February 2004.

[51] Owen Benton, Olga Sikora, and Nic Shannon. Seeing the light: Experimental signatures of emergent electromagnetism in a quantum spin ice. Physical Review B, 86(7):075154, August 2012.

[52] J. G. Rau. Microscopic aspects of insulating rare-earth pyrochlore magnets- International Workshop on Quantum Spin Ice, June 2017.

[53] Shigeki Onoda. Effective quantum pseudospin-1/2 model for Yb pyrochlore oxides. Journal of Physics: Conference Series, 320(1):012065, 2011.

[54] Kate A. Ross, Lucile Savary, Bruce D. Gaulin, and Leon Balents. Quantum Excitations in Quantum Spin Ice. Physical Review X, 1(2):021002, October 2011.

[55] Shigeki Onoda and Yoichi Tanaka. Quantum fluctuations in the effective pseudospin-$\frac{1}{2}$ model for magnetic pyrochlore oxides. Physical Review B, 83(9):094411, March 2011.

[56] SungBin Lee, Shigeki Onoda, and Leon Balents. Generic quantum spin ice. Physical Review B, 86(10):104412, September 2012.

[57] Lucile Savary and Leon Balents. Coulombic Quantum Liquids in Spin-$\frac{1}{2}$ Pyrochlores. Physical Review Letters, 108(3):037202, January 2012.

[58] K. A. Ross, J. P. C. Ruff, C. P. Adams, J. S. Gardner, H. A. Dabkowska, Y. Qiu, J. R. D. Copley, and B. D. Gaulin. Two-Dimensional Kagome Correlations and Field Induced Order in the Ferromagnetic XY Pyrochlore $Yb_2Ti_2O_7$. Physical Review Letters, 103(22):227202, November 2009.

[59] J. Gaudet, D. D. Maharaj, G. Sala, E. Kermarrec, K. A. Ross, H. A. Dabkowska, A. I. Kolesnikov, G. E. Granroth, and B. D. Gaulin. Neutron spectroscopic study of crystalline electric field excitations in stoichiometric and lightly stuffed $Yb_2Ti_2O_7$. Physical Review B, 92(13):134420, October 2015.

[60] J. A. Hodges, P. Bonville, A. Forget, M. Rams, K. Krlas, and G. Dhalenne. The crystal field and exchange interactions in $Yb_2Ti_2O_7$. Journal of Physics: Condensed Matter, 13(41):9301, 2001.

[61] B. Z. Malkin, A. R. Zakirov, M. N. Popova, S. A. Klimin, E. P. Chukalina, E. Antic-Fidancev, Ph. Goldner, P. Aschehoug, and G. Dhalenne. Optical spectroscopy of $Yb_2Ti_2O_7$ and $Y_2Ti_2O_7$: Yb^{3+} and crystal-field parameters in rare-earth titanate pyrochlores. Physical Review B, 70(7), August 2004.

[62] S. A. Klimin, M. N. Popova, E. P. Chukalina, B. Z. Malkin, A. R. Zakirov, E. Antic-Fidancev, Ph Goldner, P. Aschehoug, and G. Dhalenne. Stark structure of the Yb^{3+} ion levels in $(Yb_xY_{1-x})_2Ti_2O_7$ and the crystal field in rare-earth titanates with a pyrochlore structure. Physics of the Solid State, 47(8):1425–1430, August 2005.

[63] Yukio Yasui, Minoru Soda, Satoshi Iikubo, Masafumi Ito, Masatoshi Sato, Nobuko Hamaguchi, Taku Matsushita, Nobuo Wada, Tetsuya Takeuchi, Naofumi Aso, and Kazuhisa Kakurai. Ferromagnetic Transition of Pyrochlore Compound $Yb_2Ti_2O_7$. Journal of the Physical Society of Japan, 72(11):3014–3015, November 2003.

[64] H. B. Cao, A. Gukasov, I. Mirebeau, and P. Bonville. Anisotropic exchange in frustrated pyrochlore $Yb_2Ti_2O_7$. Journal of Physics: Condensed Matter, 21(49):492202, 2009.

[65] J. D. Thompson, P. A. McClarty, and M. J. P. Gingras. Local susceptibility of the $Yb_2Ti_2O_7$ rare earth pyrochlore computed from a Hamiltonian with anisotropic exchange. Journal of Physics: Condensed Matter, 23(16):164219, 2011.

[66] Jordan D. Thompson, Paul A. McClarty, Henrik M. Rnnow, Louis P. Regnault, Andreas Sorge, and Michel J. P. Gingras. Rods of Neutron Scattering Intensity in $Yb_2Ti_2O_7$: Compelling Evidence for Significant Anisotropic Exchange in a Magnetic Pyrochlore Oxide. Physical Review Letters, 106(18):187202, May 2011.

[67] R. Applegate, N. R. Hayre, R. R. P. Singh, T. Lin, A. G. R. Day, and M. J. P. Gingras. Vindication of $Yb_2Ti_2O_7$ as a Model Exchange Quantum Spin Ice. Physical Review Letters, 109(9):097205, August 2012.

[68] Lieh-Jeng Chang, Shigeki Onoda, Yixi Su, Ying-Jer Kao, Ku-Ding Tsuei, Yukio Yasui, Kazuhisa Kakurai, and Martin Richard Lees. Higgs transition from a magnetic Coulomb liquid to a ferromagnet in $Yb_2Ti_2O_7$. Nature Communications, 3:992, August 2012.

[69] Lieh-Jeng Chang, Martin R. Lees, Isao Watanabe, Adrian D. Hillier, Yukio Yasui, and Shigeki Onoda. Static magnetic moments revealed by muon spin relaxation and thermodynamic measurements in the quantum spin ice $Yb_2Ti_2O_7$. Physical Review B, 89(18):184416, May 2014.

[70] J. A. Hodges, P. Bonville, A. Forget, A. Yaouanc, P. Dalmas de Rotier, G. Andr, M. Rams, K. Krlas, C. Ritter, P. C. M. Gubbens, C. T. Kaiser, P. J. C. King, and C. Baines. First-Order Transition in the Spin Dynamics of Geometrically Frustrated $Yb_2Ti_2O_7$. Physical Review Letters, 88(7):077204, February 2002.

[71] J. S. Gardner, G. Ehlers, N. Rosov, R. W. Erwin, and C. Petrovic. Spin-spin correlations in $Yb_2Ti_2O_7$: A polarized neutron scattering study. Physical Review B, 70(18):180404, November 2004.

[72] A. Yaouanc, P. Dalmas de Rotier, L. Keller, B. Roessli, and A. Forget. A novel type of splayed ferromagnetic order observed in $Yb_2Ti_2O_7$. Journal of Physics: Condensed Matter, 28(42):426002, 2016.

[73] R. M. DOrtenzio, H. A. Dabkowska, S. R. Dunsiger, B. D. Gaulin, M. J. P. Gingras, T. Goko, J. B. Kycia, L. Liu, T. Medina, T. J. Munsie, D. Pomaranski, K. A. Ross, Y. J. Uemura, T. J. Williams, and G. M. Luke. Unconventional magnetic ground state in $Yb_2Ti_2O_7$. Physical Review B, 88(13):134428, October 2013.

[74] E. Lhotel, S. R. Giblin, M. R. Lees, G. Balakrishnan, L. J. Chang, and Y. Yasui. First-order magnetic transition in $Yb_2Ti_2O_7$. Physical Review B, 89(22):224419, June 2014.

[75] N. R. Hayre, K. A. Ross, R. Applegate, T. Lin, R. R. P. Singh, B. D. Gaulin, and M. J. P. Gingras. Thermodynamic properties of $Yb_2Ti_2O_7$ pyrochlore as a function of temperature and magnetic field: Validation of a quantum spin ice exchange Hamiltonian. Physical Review B, 87(18):184423, May 2013.

[76] Hitesh J. Changlani. Quantum versus classical effects at zero and finite temperature in the quantum pyrochlore $Yb_2Ti_2O_7$. arXiv:1710.02234 [cond-mat], October 2017.

[77] H. W. J. Bl'ote, R. F. Wielinga, and W. J. Huiskamp. Heat-capacity measurements on rare-earth double oxides $R_2M_2O_7$. Physica, 43(4):549–568, September 1969.

[78] J.D. Thompson, P.A. McClarty, D. Prabhakaran, I. Cabrera, T. Guidi, and R. Coldea. Quasiparticle Breakdown and Spin Hamiltonian of the Frustrated Quantum Pyrochlore $Yb_2Ti_2O_7$ in a Magnetic Field. Physical Review Letters, 119(5):057203, August 2017.

[79] L.D.C. Jaubert, Owen Benton, Jeffrey G. Rau, J. Oitmaa, R.R.P. Singh, Nic Shannon, and Michel J.P. Gingras. Are Multiphase Competition and Order by Disorder the Keys to Understanding $Yb_2Ti_2O_7$? Physical Review Letters, 115(26):267208, December 2015.

[80] Han Yan, Owen Benton, Ludovic Jaubert, and Nic Shannon. Theory of multiple-phase competition in pyrochlore magnets with anisotropic exchange with application to $Yb_2Ti_2O_7$, $Er_2Ti_2O_7$, and $Er_2Sn_2O_7$. Physical Review B, 95(9):094422, March 2017.

[81] J. Gaudet, K. A. Ross, E. Kermarrec, N. P. Butch, G. Ehlers, H. A. Dabkowska, and B. D. Gaulin. Gapless quantum excitations from an icelike splayed ferromagnetic ground state in stoichiometric $Yb_2Ti_2O_7$. Physical Review B, 93(6):064406, February 2016.

[82] A. M. Hallas, J. Gaudet, N. P. Butch, M. Tachibana, R. S. Freitas, G. M. Luke, C. R. Wiebe, and B. D. Gaulin. Universal dynamic magnetism in Yb pyrochlores with disparate ground states. Physical Review B, 93(10):100403, March 2016.

[83] J. Robert, E. Lhotel, G. Remenyi, S. Sahling, I. Mirebeau, C. Decorse, B. Canals, and S. Petit. Spin dynamics in the presence of competing ferromagnetic and antiferromagnetic correlations in $Yb_2Ti_2O_7$. Physical Review B, 92(6):064425, August 2015.

[84] P. Bonville, J. A. Hodges, E. Bertin, J.-Ph Bouchaud, P. Dalmas de Rotier, L.-P. Regnault, H. M. Rnnow, J.-P. Sanchez, S. Sosin, and A. Yaouanc. Transitions and Spin Dynamics at Very Low Temperature in the Pyrochlores $Yb_2Ti_2O_7$ and $Gd_2Sn_2O_7$. Hyperfine Interactions, 156-157(1-4):103–111, December 2004.

[85] H. Cao, A. Gukasov, I. Mirebeau, P. Bonville, C. Decorse, and G. Dhalenne. Ising versus XY Anisotropy in Frustrated $R_2Ti_2O_7$Compounds as "Seen" by Polarized Neutrons. Physical Review Letters, 103(5):056402, July 2009.

[86] Lucile Savary, Kate A. Ross, Bruce D. Gaulin, Jacob P. C. Ruff, and Leon Balents. Order by Quantum Disorder in $Er_2Ti_2O_7$. Physical Review Letters, 109(16):167201, October 2012.

[87] Solene Guitteny, Sylvain Petit, Elsa Lhotel, Julien Robert, Pierre Bonville, Anne Forget, and Isabelle Mirebeau. Palmer-Chalker correlations in the XY pyrochlore antiferromagnet $Er_2Sn_2O_7$. Physical Review B, 88(13), October 2013.

[88] J. S. Gardner, S. R. Dunsiger, B. D. Gaulin, M. J. P. Gingras, J. E. Greedan, R. F. Kiefl, M. D. Lumsden, W. A. MacFarlane, N. P. Raju, J. E. Sonier, I. Swainson, and Z. Tun. Cooperative Paramagnetism in the Geometrically Frustrated Pyrochlore Antiferromagnet $Tb_2Ti_2O_7$. Physical Review Letters, 82(5):1012–1015, February 1999.

[89] J. S. Gardner, A. Keren, G. Ehlers, C. Stock, Eva Segal, J. M. Roper, B. Fk, M. B. Stone, P. R. Hammar, D. H. Reich, and B. D. Gaulin. Dynamic frustrated magnetism in $Tb_2Ti_2O_7$ at 50 mK. Physical Review B, 68(18):180401, November 2003.

[90] M. J. P. Gingras, B. C. den Hertog, M. Faucher, J. S. Gardner, S. R. Dunsiger, L. J. Chang, B. D. Gaulin, N. P. Raju, and J. E. Greedan. Thermodynamic and single-ion properties of Tb^{3+} within the collective paramagnetic-spin liquid state of the frustrated pyrochlore antiferromagnet $Tb_2Ti_2O_7$. Physical Review B, 62(10):6496–6511, September 2000.

[91] A. J. Princep, H. C. Walker, D. T. Adroja, D. Prabhakaran, and A. T. Boothroyd. Crystal field states of Tb^{3+} in the pyrochlore spin liquid $Tb_2Ti_2O_7$ from neutron spectroscopy. Physical Review B, 91(22):224430, June 2015.

[92] J. Zhang, K. Fritsch, Z. Hao, B. V. Bagheri, M. J. P. Gingras, G. E. Granroth, P. Jiramongkolchai, R. J. Cava, and B. D. Gaulin. Neutron spectroscopic study of crystal field excitations in $Tb_2Ti_2O_7$ and $Tb_2Sn_2O_7$. Physical Review B, 89(13):134410, April 2014.

[93] Hamid R. Molavian, Michel J. P. Gingras, and Benjamin Canals. Dynamically Induced Frustration as a Route to a Quantum Spin Ice State in $Tb_2Ti_2O_7$ via Virtual Crystal Field Excitations and Quantum Many-Body Effects. Physical Review Letters, 98(15):157204, April 2007.

[94] Hiroshi Takatsu, Hiroaki Kadowaki, Taku J. Sato, Jeffrey W. Lynn, Yoshikazu Tabata, Teruo Yamazaki, and Kazuyuki Matsuhira. Quantum spin fluctuations in the spin-liquid state of $Tb_2Ti_2O_7$. Journal of Physics: Condensed Matter, 24(5):052201, 2012.

[95] Nobuko Hamaguchi, Taku Matsushita, Nobuo Wada, Yukio Yasui, and Masatoshi Sato. Low-temperature phases of the pyrochlore compound $Tb_2Ti_2O_7$. Physical Review B, 69(13):132413, April 2004.

[96] H. Takatsu, S. Onoda, S. Kittaka, A. Kasahara, Y. Kono, T. Sakakibara, Y. Kato, B. Fk, J. Ollivier, J.W. Lynn, T. Taniguchi, M. Wakita, and H. Kadowaki. Quadrupole Order in the Frustrated Pyrochlore $Tb_{2+x}Ti_{2-x}O_{7+y}$. Physical Review Letters, 116(21):217201, May 2016.

[97] A. Yaouanc, P. Dalmas de Rotier, Y. Chapuis, C. Marin, S. Vanishri, D. Aoki, B. Fk, L.-P. Regnault, C. Buisson, A. Amato, C. Baines, and A. D. Hillier. Exotic transition in the three-dimensional spin-liquid candidate $Tb_2Ti_2O_7$. Physical Review B, 84(18):184403, November 2011.

[98] Jens Jensen and Allan R. Mackintosh. Rare Earth Magnetism Structures and Excitations. Clarendon Press Oxford, 1991.

[99] Arthur J. Freeman and Richard B. Frankel. Hyperfine interactions. Academic Press, 1967.

[100] K. W. H. Stevens. Matrix Elements and Operator Equivalents Connected with the Magnetic Properties of Rare Earth Ions. Proceedings of the Physical Society. Section A, 65(3):209, 1952.

[101] Eva Pavarini, Frithjof Anders, Erik Koch, and Mark (Eds) Jarrell. Correlated electrons. Technical Report PreJuSER-136393, Forschungszentrum Jülich GmbH, 2012.

[102] T. Kasuya. Exchange interactions in rare earth compounds. Journal of Alloys and Compounds, 192(1):11–16, February 1993.

[103] Jeffrey G. Rau and Michel J. P. Gingras. Magnitude of quantum effects in classical spin ices. Physical Review B, 92(14):144417, October 2015.

[104] Paul F. Sullivan and G. Seidel. Steady-State, ac-Temperature Calorimetry. Physical Review, 173(3):679–685, September 1968.

[105] R. Bachmann, F. J. DiSalvo, T. H. Geballe, R. L. Greene, R. E. Howard, C. N. King, H. C. Kirsch, K. N. Lee, R. E. Schwall, H.U. Thomas, and R. B. Zubeck. Heat Capacity Measurements on Small Samples at Low Temperatures. Review of Scientific Instruments, 43(2):205–214, February 1972.

[106] H. Tsujii, B. Andraka, K. A. Muttalib, and Y. Takano. Distributed τ_2 effect in relaxation calorimetry. Physica B: Condensed Matter, 329(Part 2):1552–1553, May 2003.

[107] J. A. Quilliam. Specifc Heat of the Dilute, Dipolar-Coupled, Ising Magnet LiHo$_x$Y$_{1-x}$F$_4$. PhD thesis, University of Waterloo, 2006.

[108] R B Goldfarb. Panel Discussion on Units in Magnetism. Magnetic and Electrical Separation, 6:105–116, 1995.

[109] Peter J. W Debye. Polar molecules. The Chemical Catalog Company, Inc., New York, 1929.

[110] Kenneth S. Cole and Robert H. Cole. Dispersion and Absorption in Dielectrics I. Alternating Current Characteristics. The Journal of Chemical Physics, 9(4):341–351, April 1941.

[111] D. W. Davidson and R. H. Cole. Dielectric Relaxation in Glycerine. The Journal of Chemical Physics, 18(10):1417–1417, October 1950.

[112] D. W. Davidson and R. H. Cole. Dielectric Relaxation in Glycerol, Propylene Glycol, and nPropanol. The Journal of Chemical Physics, 19(12):1484–1490, December 1951.

[113] S. Havriliak and S. Negami. A complex plane representation of dielectric and mechanical relaxation processes in some polymers. Polymer, 8:161–210, January 1967.

[114] J. H. Calderwood. A physical hypothesis for Cole-Davidson behavior. IEEE Transactions on Dielectrics and Electrical Insulation, 10(6):1006–1011, December 2003.

[115] S. T. Bramwell, S. R. Giblin, S. Calder, R. Aldus, D. Prabhakaran, and T. Fennell. Measurement of the charge and current of magnetic monopoles in spin ice. Nature, 461(7266):956, October 2009.

[116] Dietmar Drung and Michael Mück. SQUID Electronics. In The SQUID Handbook, pages 127–170. Wiley-Blackwell, 2005.

[117] D. X. Chen, E. Pardo, and A. Sanchez. Demagnetizing factors for rectangular prisms. IEEE Transactions on Magnetics, 41(6):2077–2088, June 2005.

[118] M. Twengström, L. Bovo, M. J. P. Gingras, S. T. Bramwell, and P. Henelius. Microscopic aspects of magnetic lattice demagnetizing factors. Physical Review Materials, 1(4):044406, September 2017.

[119] Ethan R. Kassner, Azar B. Eyvazov, Benjamin Pichler, Timothy J. S. Munsie, Hanna A. Dabkowska, Graeme M. Luke, and J. C. Samus Davis. Supercooled spin liquid state in the frustrated pyrochlore $Dy_2Ti_2O_7$. Proceedings of the National Academy of Sciences, 112(28):8549–8554, July 2015.

[120] Azar B. Eyvazov, Ritika Dusad, Timothy J. S. Munsie, Hanna A. Dabkowska, Graeme M. Luke, Ethan R. Kassner, J. C. Samus Davis, and Anna Eyal. Common Glass-Forming Spin-Liquid State in the Pyrochlore Magnets $Dy_2Ti_2O_7$ and $Ho_2Ti_2O_7$. arXiv:1707.09014 [cond-mat], July 2017.

[121] Amikam Aharoni. Demagnetizing factors for rectangular ferromagnetic prisms. Journal of Applied Physics, 83(6):3432–3434, March 1998.

[122] John Clarke, Wolfgang M. Goubau, and Mark B. Ketchen. Tunnel junction dc SQUID: Fabrication, operation, and performance. Journal of Low Temperature Physics, 25(1-2):99–144, October 1976.

[123] S. Sch'one, M. Mück, G. Thummes, and C. Heiden. Investigation of the response of superconducting quantum interference devices to temperature variation. Review of Scientific Instruments, 68(1):85–88, January 1997.

[124] S. Sendelbach, D. Hover, A. Kittel, M. Mück, John M. Martinis, and R. McDermott. Magnetism in SQUIDs at Millikelvin Temperatures. Physical Review Letters, 100(22):227006, June 2008.

[125] J. A. Quilliam. Disorder, Geometric Frustration and the Dipolar Interaction in Rare Earth Magnets. PhD thesis, University of Waterloo, 2010.

[126] L. R. Yaraskavitch, H. M. Revell, S. Meng, K. A. Ross, H. M. L. Noad, H. A. Dabkowska, B. D. Gaulin, and J. B. Kycia. Spin dynamics in the frozen state of the dipolar spin ice material $Dy_2Ti_2O_7$. Physical Review B, 85(2):020410, January 2012.

[127] Vinay Ambegaokar and Alexis Baratoff. Tunneling Between Superconductors. Physical Review Letters, 10(11):486–489, June 1963.

[128] W. Schoepe, K. Uhlig, and K. Neumaier. Carbon and germanium resistors in the variable-range hopping regime for thermometry below 1 K. Cryogenics, 29(4):467–468, April 1989.

[129] R. W. Willekers, F. Mathu, H. C. Meijer, and H. Postma. Thick film thermometers with predictable R-T characteristics and very low magnetoresistance below 1 K. Cryogenics, 30(4):351–355, April 1990.

[130] M. Affronte, M. Campani, B. Morten, M. Prudenziati, and O. Laborde. Magnetoresistance of RuO_2-Based Thick Film Resistors. Journal of Low Temperature Physics, 112(5-6):355–371, September 1998.

[131] N. F. Mott. Conduction in non-crystalline materials. The Philosophical Magazine: A Journal of Theoretical Experimental and Applied Physics, 19(160):835–852, April 1969.

[132] Vinay Ambegaokar, B. I. Halperin, and J. S. Langer. Hopping Conductivity in Disordered Systems. Physical Review B, 4(8):2612–2620, October 1971.

[133] B.I. Shklovskii and A.L. Efros. Electronic Properties of Doped Semiconductors. Springer-Verlag, 1984.

[134] Ping Sheng and J. Klafter. Hopping conductivity in granular disordered systems. Physical Review B, 27(4):2583–2586, February 1983.

[135] M. W. Meisel, G. R. Stewart, and E. D. Adams. Thick film chip resistors as millikelvin thermometers. Cryogenics, 29(12):1168–1169, December 1989.

[136] K. Uhlig. Magnetoresistance of thick-film chip resistors at millikelvin temperatures. Cryogenics, 35(8):525–528, August 1995.

[137] John David Jackson. Classical Electrodynamics. Wiley, New York, 3rd edition, August 1998.

[138] H. Marshak. Nuclear Orientation Thermometry. National Institute of Standards and Technology, 1983.

[139] H. A. Tolhoek and J. A. M. Cox. Angular distribution and polarization of gamma radiation emitted by oriented nuclei. Physica, 19(1):101–119, January 1953.

[140] K.S. Krane. Solid-angle correction factors for coaxial Ge(Li) detectors. Nuclear Instruments and Methods, 98(2):205–210, January 1972.

[141] Robert L. Heath. Scintillation Spectrometry Gamma-ray Spectrum Catalogue. Phillips petroleum Company Atomoc energy division, 1957.

[142] D. Pomaranski, L. R. Yaraskavitch, S. Meng, K. A. Ross, H. M. L. Noad, H. A. Dabkowska, B. D. Gaulin, and J. B. Kycia. Absence of Pauling's residual entropy in thermally equilibrated $Dy_2Ti_2O_7$. Nature Physics, 9(6):353–356, June 2013.

[143] B. Klemke, M. Meissner, P. Strehlow, K. Kiefer, S. A. Grigera, and D. A. Tennant. Thermal Relaxation and Heat Transport in the Spin Ice Material $Dy_2Ti_2O_7$. Journal of Low Temperature Physics, 163(5-6):345–369, June 2011.

[144] P. A. McClarty, O. Sikora, R. Moessner, K. Penc, F. Pollmann, and N. Shannon. Chain-based order and quantum spin liquids in dipolar spin ice. Physical Review B, 92(9):094418, September 2015.

[145] P. Henelius, T. Lin, M. Enjalran, Z. Hao, J. G. Rau, J. Altosaar, F. Flicker, T. Yavors'kii, and M. J. P. Gingras. Refrustration and competing orders in the prototypical $Dy_2Ti_2O_7$ spin ice material. Physical Review B, 93(2), January 2016.

[146] S. W. Kycia. Personal communication.

[147] S.R. Giblin, M. Twengstŕom, L. Bovo, M. Ruminy, M. Bartkowiak, P. Manuel, J.C. Andresen, D. Prabhakaran, G. Balakrishnan, E. Pomjakushina, C. Paulsen, E. Lhotel, L. Keller, M. Frontzek, S.C. Capelli, O. Zaharko, P.A. McClarty, S.T. Bramwell,

P. Henelius, and T. Fennell. Pauling Entropy, Metastability, and Equilibrium in $Dy_2Ti_2O_7$ Spin Ice. Physical Review Letters, 121(6), August 2018.

[148] D. Prabhakaran and A. T. Boothroyd. Crystal growth of spin-ice pyrochlores by the floating-zone method. Journal of Crystal Growth, 318(1):1053–1056, March 2011.

[149] Zh. V. Eremeeva, V. S. Panov, L. V. Myakisheva, A. V. Lizunov, A. A. Nepapushev, D. A. Sidorenko, and S. Vorotilo. Structure and properties of mechanochemically synthesized dysprosium titanate Dy_2TiO_5. Journal of Nuclear Materials, 495:38–48, November 2017.

[150] J. Snyder, B. G. Ueland, J. S. Slusky, H. Karunadasa, R. J. Cava, and P. Schiffer. Low-temperature spin freezing in the $Dy_2Ti_2O_7$ spin ice. Physical Review B, 69(6):064414, February 2004.

[151] Z. Nussinov, C. D. Batista, B. Normand, and S. A. Trugman. High-dimensional fractionalization and spinon deconfinement in pyrochlore antiferromagnets. Physical Review B, 75(9):094411, March 2007.

[152] C. I. Mitchelitis. Modification of a dilution refrigerator for in-field SQUID magnetometry of $Dy_2Ti_2O_7$. PhD thesis, University of Waterloo, 2015.

[153] R. Kubo. The fluctuation-dissipation theorem. Reports on Progress in Physics, 29(1):255, 1966.

[154] J. H Calderwood. The skewed arc representation for the frequency dependence of complex permittivity. Journal of Molecular Liquids, 114(1):59–62, September 2004.

[155] K. A. Ross, L. R. Yaraskavitch, M. Laver, J. S. Gardner, J. A. Quilliam, S. Meng, J. B. Kycia, D. K. Singh, Th. Proffen, H. A. Dabkowska, and B. D. Gaulin. Dimensional evolution of spin correlations in the magnetic pyrochlore $Yb_2Ti_2O_7$. Physical Review B, 84(17):174442, November 2011.

[156] B. Bleaney. Hyperfine Interactions in RareEarth Metals. Journal of Applied Physics, 34(4):1024–1031, April 1963.

[157] Hodges, J. A., Bonville, P., Forget, A., and Andr, G. First-order transition in frustrated $Yb_2Ti_2O_7$ without long-range order. 79:1373–1380, 2001.

[158] Gladys H. Fuller. Nuclear Spins and Moments. Journal of Physical and Chemical Reference Data, 5(4):835–1092, October 1976.

[159] Q.J. Li, L.M. Xu, C. Fan, F.B. Zhang, Y.Y. Lv, B. Ni, Z.Y. Zhao, and X.F. Sun. Single crystal growth of the pyrochlores $R_2Ti_2O_7$ (R=rare earth) by the optical floating-zone method. Journal of Crystal Growth, 377:96–100, August 2013.

[160] Haruki Watanabe and Hitoshi Murayama. Nambu-Goldstone bosons with fractional-power dispersion relations. Physical Review D, 89(10):101701, May 2014.

[161] Jeffrey G. Rau, Paul A. McClarty, and Roderich Moessner. Pseudo-Goldstone gaps and order-by-quantum-disorder in frustrated magnets. arXiv:1805.00947 [cond-mat], May 2018. arXiv: 1805.00947.

[162] Tom Brauner. Spontaneous Symmetry Breaking and NambuGoldstone Bosons in Quantum Many-Body Systems. Symmetry, 2(2):609–657, April 2010.

[163] Haruki Watanabe and Hitoshi Murayama. Unified Description of Nambu-Goldstone Bosons without Lorentz Invariance. Physical Review Letters, 108(25):251602, June 2012.

[164] J. P. C. Ruff, B. D. Gaulin, J. P. Castellan, K. C. Rule, J. P. Clancy, J. Rodriguez, and H. A. Dabkowska. Structural Fluctuations in the Spin-Liquid State of $Tb_2Ti_2O_7$. Physical Review Letters, 99(23):237202, December 2007.

[165] Pierre Bonville, Isabelle Mirebeau, Arsne Gukasov, Sylvain Petit, and Julien Robert. Tetragonal distortion yielding a two-singlet spin liquid in pyrochlore $Tb_2Ti_2O_7$. Physical Review B, 84(18):184409, November 2011.

[166] Sylvain Petit, Pierre Bonville, Julien Robert, Claudia Decorse, and Isabelle Mirebeau. Spin liquid correlations, anisotropic exchange, and symmetry breaking in $Tb_2Ti_2O_7$. Physical Review B, 86(17):174403, November 2012.

[167] B. D. Gaulin, J. S. Gardner, P. A. McClarty, and M. J. P. Gingras. Lack of evidence for a singlet crystal-field ground state in the magnetic pyrochlore $Tb_2Ti_2O_7$. Physical Review B, 84(14):140402, October 2011.

[168] E. Kermarrec, D. D. Maharaj, J. Gaudet, K. Fritsch, D. Pomaranski, J. B. Kycia, Y. Qiu, J. R. D. Copley, M. M. P. Couchman, A. O. R. Morningstar, H. A. Dabkowska, and B. D. Gaulin. Gapped and gapless short-range-ordered magnetic states with $(\frac{1}{2}, \frac{1}{2}, \frac{1}{2})$ wave vectors in the pyrochlore magnet $Tb_{2+x}Ti_{2-x}O_{7-\delta}$. Physical Review B, 92(24):245114, December 2015.

[169] H. Kadowaki, H. Takatsu, T. Taniguchi, B. Fk, and J. Ollivier. Composite Spin and Quadrupole Wave in the Ordered Phase of $Tb_{2+x}Ti_{2-x}O_{7+y}$. SPIN, 05(02):1540003, June 2015.

[170] Hiroaki Kadowaki, Mika Wakita, Bj'orn Fk, Jacques Ollivier, Seiko Ohira-Kawamura, Kenji Nakajima, Hiroshi Takatsu, and Mototake Tamai. Continuum Excitation and Pseudospin Wave in Quantum Spin-Liquid and Quadrupole Ordered States of $Tb_{2+x}Ti_{2x}O_{7+y}$. Journal of the Physical Society of Japan, 87(6):064704, May 2018.

[171] Q. J. Li, Z. Y. Zhao, C. Fan, F. B. Zhang, H. D. Zhou, X. Zhao, and X. F. Sun. Phonon-glass-like behavior of magnetic origin in single-crystal $Tb_2Ti_2O_7$. Physical Review B, 87(21):214408, June 2013.

[172] I. Mirebeau, P. Bonville, and M. Hennion. Magnetic excitations in $Tb_2Sn_2O_7$ and $Tb_2Ti_2O_7$ as measured by inelastic neutron scattering. Physical Review B, 76(18):184436, November 2007.

[173] G. R. Stewart, Z. Fisk, J. O. Willis, and J. L. Smith. Possibility of Coexistence of Bulk Superconductivity and Spin Fluctuations in UPt_3. Physical Review Letters, 52(8):679–682, February 1984.

[174] J. A. Sauls. The order parameter for the superconducting phases of UPt_3. Advances in Physics, 43(1):113–141, February 1994.

[175] J. D. Strand, D. J. Van Harlingen, J. B. Kycia, and W. P. Halperin. Evidence for Complex Superconducting Order Parameter Symmetry in the Low-Temperature Phase of UPt_3 from Josephson Interferometry. Physical Review Letters, 103(19):197002, November 2009.

[176] J. D. Strand, D. J. Bahr, D. J. Van Harlingen, J. P. Davis, W. J. Gannon, and W. P. Halperin. The Transition Between Real and Complex Superconducting Order Parameter Phases in UPt_3. Science, 328(5984):1368–1369, June 2010.

[177] E. R. Schemm, W. J. Gannon, C. M. Wishne, W. P. Halperin, and A. Kapitulnik. Observation of broken time-reversal symmetry in the heavy-fermion superconductor UPt_3. Science, 345(6193):190–193, July 2014.

[178] W. J. Gannon, W. P. Halperin, C. Rastovski, K. J. Schlesinger, J. Hlevyack, M. R. Eskildsen, A. B. Vorontsov, J Gavilano, U. Gasser, and G. Nagy. Nodal gap structure

and order parameter symmetry of the unconventional superconductor UPt$_3$. New Journal of Physics, 17(2):023041, 2015.

[179] Robert Joynt and Louis Taillefer. The superconducting phases of UPt$_3$. Reviews of Modern Physics, 74(1):235–294, March 2002.

[180] Jan Bronislaw Kycia. Growth and characterization of high quality UPt$_3$ single crystals and high resolution NMR study of superfluid He-3-B. Ph.D., Northwestern University, United States – Illinois, 1997.

[181] J. B. Kycia, J. I. Hong, M. J. Graf, J. A. Sauls, D. N. Seidman, and W. P. Halperin. Suppression of superconductivity in UPt$_3$ single crystals. Physical Review B, 58(2):R603–R606, July 1998.

[182] Jung-Il Hong. Structure-property relationships for a heavy fermion superconductor, UPt$_3$. Ph.D., Northwestern University, United States – Illinois, 1999.

[183] T. Vorenkamp, M. C. Aronson, Z. Koziol, K. Bakker, J. J. M. Franse, and J. L. Smith. Substitution studies and the nature of superconductivity in UPt$_3$. Physical Review B, 48(9):6373–6384, September 1993.

[184] R. J. Keizer. Evolution of Magnetism and its Interplay with Superconductivity in Heavy-Fermion U(Pt,Pd)$_3$. PhD thesis, Amsterdam Universiteit, 1999.

[185] K. Fritsch, E. Kermarrec, K. A. Ross, Y. Qiu, J. R. D. Copley, D. Pomaranski, J. B. Kycia, H. A. Dabkowska, and B. D. Gaulin. Temperature and magnetic field dependence of spin-ice correlations in the pyrochlore magnet Tb$_2$Ti$_2$O$_7$. Physical Review B, 90(1):014429, July 2014.

[186] K. Fritsch, K. A. Ross, Y. Qiu, J. R. D. Copley, T. Guidi, R. I. Bewley, H. A. Dabkowska, and B. D. Gaulin. Antiferromagnetic spin ice correlations at $(\frac{1}{2}, \frac{1}{2}, \frac{1}{2})$ in the ground state of the pyrochlore magnet Tb$_2$Ti$_2$O$_7$. Physical Review B, 87(9):094410, March 2013.

[187] Robert D'Ortenzio. Ground State of the Quantum Spin Ice Yb$_2$Ti$_2$O$_7$. thesis, October 2013.

[188] R. Coldea, D. A. Tennant, E. M. Wheeler, E. Wawrzynska, D. Prabhakaran, M. Telling, K. Habicht, P. Smeibidl, and K. Kiefer. Quantum Criticality in an Ising Chain: Experimental Evidence for Emergent E8 Symmetry. Science, 327(5962):177–180, January 2010.

[189] A. B. Zamolodchikov. Integrals of motion and s-matrix of the scaled t = t_c ising model with magnetic field. International Journal of Modern Physics A, 04(16):4235–4248, October 1989.

[190] David Borthwick and Skip Garibaldi. Did a 1-Dimensional Magnet Detect a 248-Dimensional Lie Algebra? 58(8):12, 2011.

[191] Timothy J. S. Munsie. Studies of the Low Temperature Behaviour of $CoNb_2O_6$. thesis, April 2012.

[192] Timothy John Sagan Munsie. Synthesis and Characterization of Constrained Magnetism in Niobates. Thesis, November 2017.

[193] Takeshi Hanawa, Kohtaro Shinkawa, Masayasu Ishikawa, Kazuo Miyatani, Kazuhiro Saito, and Kay Kohn. Anisotropic Specific Heat of $CoNb_2O_6$ in Magnetic Fields. Journal of the Physical Society of Japan, 63(7):2706–2715, July 1994.

[194] C. V. Heer and R. A. Erickson. Hyperfine Coupling Specific Heat in Cobalt Metal. Physical Review, 108(3):896–898, November 1957.

[195] Frank Pobell. Matter and Methods at Low Temperatures. Springer-Verlag, Berlin Heidelberg, 3 edition, 2007.

[196] Graziella Scandurra, Gianluca Cannata, and Carmine Ciofi. Differential ultra low noise amplifier for low frequency noise measurements. AIP Advances, 1(2):022144, 2011.

[197] Paul Horowitz and Winfield Hill. The Art of Electronics. Cambridge University Press, New York, NY, 3 edition edition, March 2015.

APPENDICES

Appendix A

Uranium Platinum UPt$_3$

UPt$_3$ is a heavy fermion compound that is believed to exhibit unconventional supercon-ductivity. While it has been studied for nearly three decades since the discovery of bulk superconductivity below ~ 0.5 K, the pairing symmetry of the order parameter is still under debate because of the existence of two distinct superconducting phases with critical tem-peratures occurring near $T_c^+ = 0.56$ K, and $T_c^- = 0.5$ K, suggestive of a multi-component order parameter.[173] These correspond to transitions into a $A-$, and $B-$phases, respec-tively with a multiple component $f-$wave symmetry order parameter that resembles the canonical unconventional superfluid ^{3}He. The leading theoretical proposition by Sauls is the prediction of E_{2u} symmetry for the order parameter, and is backed by significant ex-perimental evidence. [174, 175, 176, 177, 178] Within this theoretical framework, a small magnetic moment $\mu \sim 0.02\mu_B$ per U atom that develops around 5 K provides the source of a symmetry breaking field. For a more thorough review of the vast theoretical and experimental work relevant to UPt$_3$, please refer to reference [179].

Results presented here were performed on crystals prepared over two decades ago for the thesis of J. B. Kycia.[180, 181]. These samples prepared at Northwestern University have the highest residual resistivity ratios (RRR) we are aware of prior to the present time. The quality of these samples depends strongly on annealing temperature, where the lowest quality samples annealed at 1250 ºC have $RRR_c = 420$, and the highest quality samples annealed at 800 ºC have $RRR_c = 1490$. Measurements performed by Hong *et al.* with transmission electron microscopy (TEM) demonstrated that the primary defect responsible for controlling the T_c in the cleanest of these samples are most likely stacking faults.[182] Specific heat measurements were performed between 0.3 and 0.6 K on samples annealed at 800 ºC, 970 ºC, and 1250 º using the quasi-adiabatic heat pulse method. The

results shown in figure A.1 indicate that the width and position of both superconducting transitions T_c^+ and T_c^- are most ideal when low annealing temperatures are used.

In the normal state above ~ 0.55 K, the large effective mass of conduction electrons produces a large linear electronic specific heat coefficient $C_e = \gamma T$, while in in the superconducting state $C_s = \gamma_0 T + BT^2$.[183] Specific heat of the superconducting state below ~ 0.45 K is fitted for each sample to obtain a unique value of γ_0. This fit was used as a boundary to compute the entropy below the superconducting transition T_c^-. Above T_c^-, the integral of cT^{-1} should be equal to half the entropy released during the superconducting transition $S = \int cT^{-1}$. These are indicated by the shaded regions on either side of T_c-, where the area of each region is adjusted to be exactly equal. This condition is used to determine the position of T_c^-, and similarly for T_c^+.
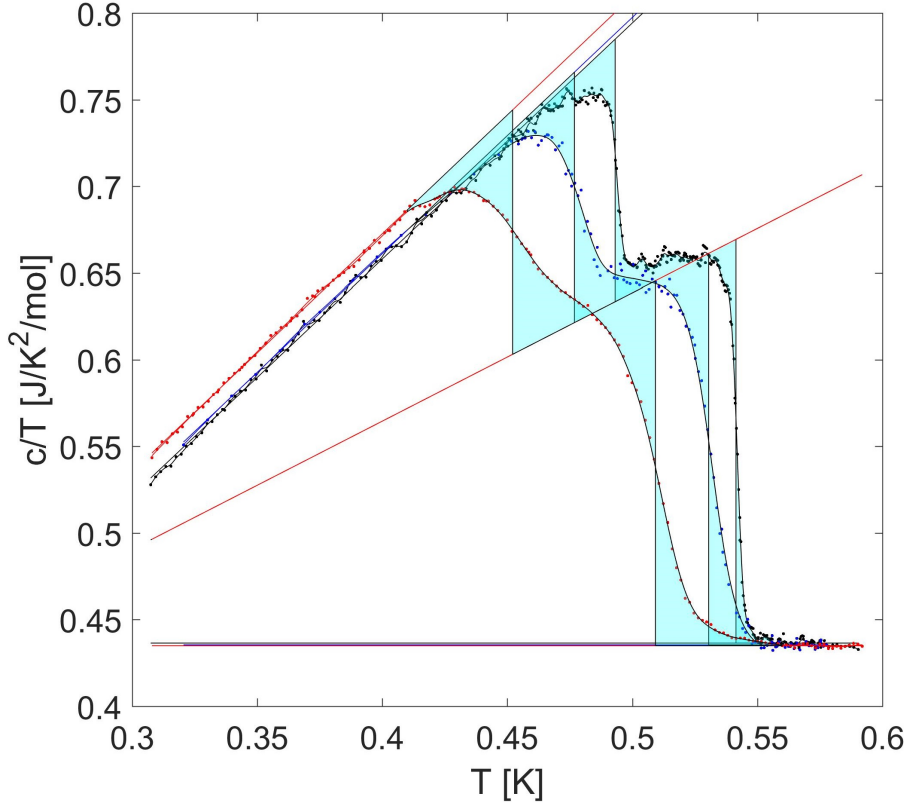

Figure A.1: Specifc heat of UPt$_3$ for three different samples annealed at 1250 °C (lowest T_c's) with $RRR_c = 420$, 970°C with $RRR_c = 720$, and 800 °C with $RRR_c = 1490$ (highest T_c's). The equal entropy condition discussed in the text is indicated by filled areas.
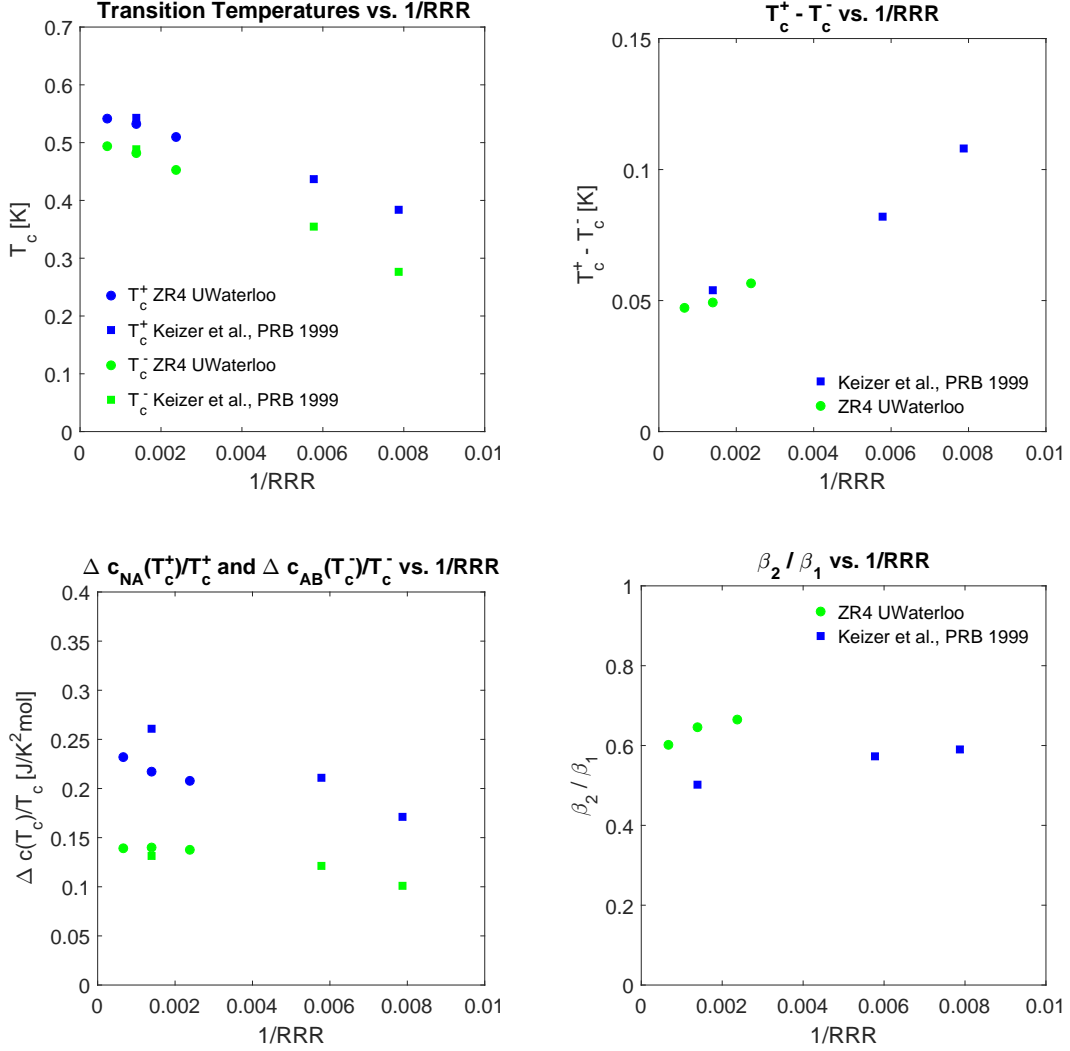
Figure A.2: Analysis of idealized parameters extracted from the specific heat of UPt$_3$. (Top Left): The evolution of critical temperatures T_c^- and T_c^+ with inverse residual resistivity ratio RRR^{-1} is shown along with data from Keiser *et al.,* for comparison.[184] (Top Right): The difference $T_c^+ - T_c^-$ versus RRR^{-1} converges to a finite value for the high quality samples. (Lower Left): Step in specific heat divided by temperature $\Delta_{NA}c(T_c^+)/T_c^+$ at $/T_c^+$, and T_c^- versus RRR^{-1}. (Lower Right): The ratio β_1/β_2 versus RRR^{-1} should converge to 0.5 in the weak coupling limit.[184]

Appendix B

Terbium Titanate $Tb_2Ti_2O_7$

Temperature and magnetic field dependence of spin-ice correlations in the pyrochlore magnet $Tb_2Ti_2O_7$

This project was part of a combined study of diffuse magnetic neutron scattering measurements, and specific heat on a high quality single crystal of $Tb_2Ti_2O_7$ that was published in reference [185]. The neutron measurements were performed by K. Fritsch *et al.,* at the NIST Center for Neutron Research, and the samples were prepared at McMaster University. Specific heat measurements were done at the University of Waterloo. This study was an extension of some earlier work published by Fritsch *et al.,* which found evidence for antiferromagnetic spin-ice correlations at $\left(\frac{1}{2}\frac{1}{2}\frac{1}{2}\right)$ positions in reciprocal space. As indicated by the title, the present work investigated the temperature and magnetic field dependence of this scattering feature.

The main result of this study was the first observation of diffuse magnetic scattering at $\left(\frac{1}{2}, \frac{1}{2}, \frac{1}{2}\right)$ positions in reciprocal space that develops strongly below ≈ 275 mK. This magnetic Bragg peak indicates the opening of a spin gap ≈ 0.06 to 0.08 meV, which is very fragile, and destroyed by the application of a small magnetic field > 0.075 T. The specific heat measurements performed between 800 mK and 200 mK reveal a sharp transition near 450 mK, which could not be associated with any features in the neutron scattering measurements. Another subsequent study on the same crystal by Kermarrec *et al.,* performed high resolution x-ray scattering measurements and determined that it has a nominal off-stoichiometry of the form $Tb_{2+x}Ti_{2x}O_{7+\delta}$ with $x \approx +0.0042$.

Additional Details for Specific Heat

Measurements were performed between 100 mK and 800 mK on a 33.8 mg piece of the single crystal used for neutron scattering. The thermal relaxation method discussed in section 3.3 was used with the typical calorimeter setup described in section 3.6, using a platinum tungsten wire for the dominant thermal link. The measured temperature dependence of this thermal link, and the resulting specific heat is in figure B.1.
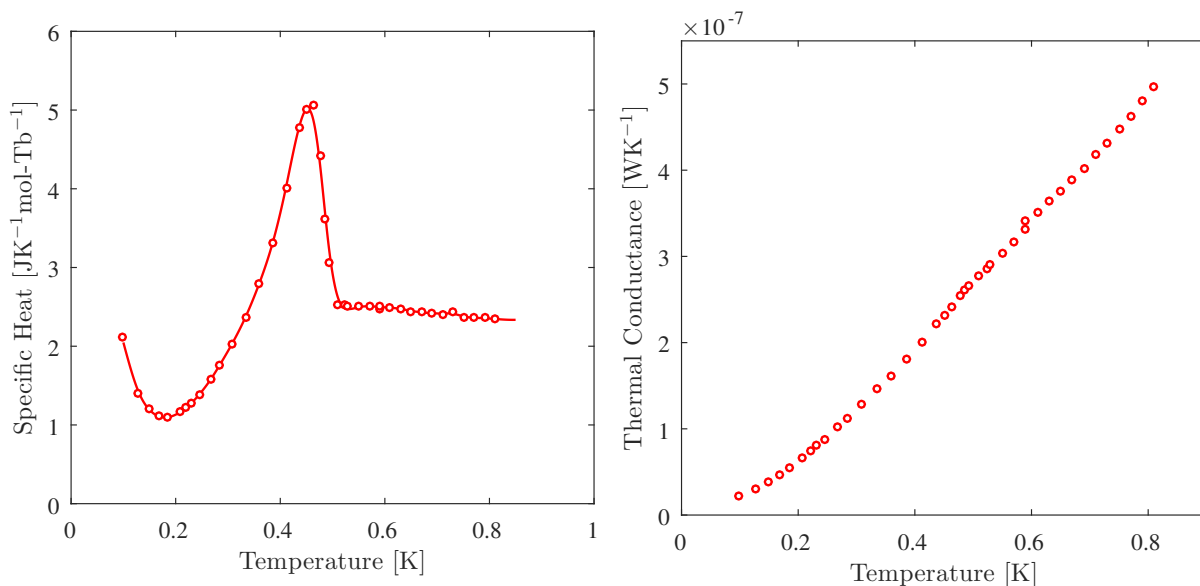

Figure B.1: Left: Specific heat of single crystal $Tb_2Ti_2O_7$ that appeared in Fritsch *et al.*, in reference [186], with several new low temperature points capturing the onset of the nuclear anomaly. Right: Thermal conductance of the platinum tungsten weak link.

Gapped and gapless short-range-ordered magnetic states with $\left(\frac{1}{2}, \frac{1}{2}, \frac{1}{2}\right)$ wave vectors in the pyrochlore magnet $\text{Tb}_{2+x}\text{Ti}_{2x}\text{O}_{7+\delta}$

In this collaboration,[168] three single cystals of $\text{Tb}_{2+x}\text{Ti}_{2x}\text{O}_{7+\delta}$ with $x = -0.001, +0.0042$, and $+0.0147$ were studied with time-of-flight neutron scattering, and specific heat measurements. The intermediate sample with $x = +0.0042$ was the same crystal from Fritsch *et al.*, investigated in the preceding section.[185] Stuffing levels x, were determined from high-resolution x-ray scattering measurements.
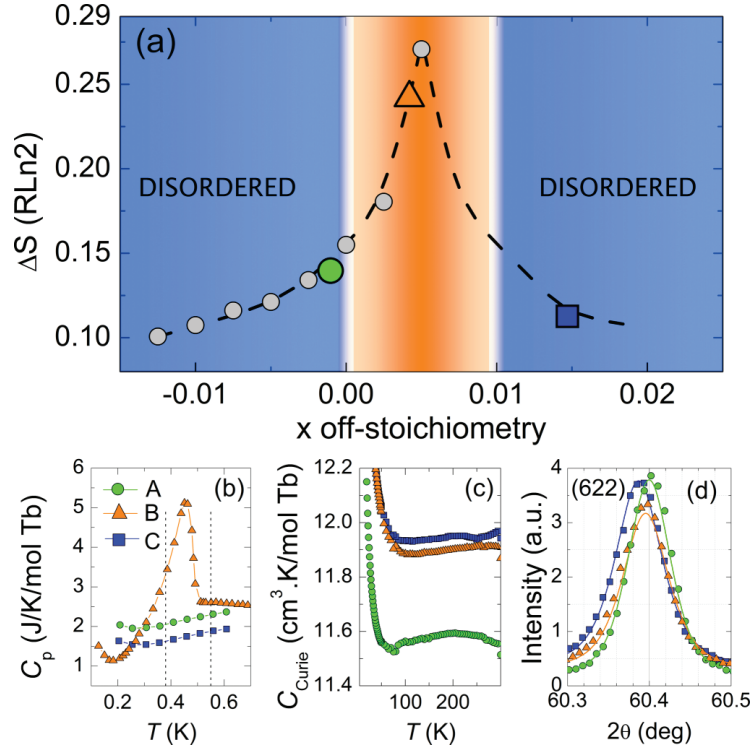

Figure B.2: Specific heat of off-stoichiometric $\text{Tb}_{2+x}\text{Ti}_{2x}\text{O}_{7+\delta}$ single crystals as it appeared in Kermarrec *et al.* Figure reproduced from reference [168] with permission.

The two new samples did not exhibit any interesting features in the specific heat, as shown in figure B.2. Furthermore, they did not develop the $\left(\frac{1}{2}, \frac{1}{2}, \frac{1}{2}\right)$ quasi-Bragg peaks below ~ 275 mK associated with short-range anitferromagnetic moments in zero-field (nominal, 0.01 T); unless they were cooled in a magnetic field of $\mu_0 H = 0.2$ T along the $[1\bar{1}0]$

direction. This state persists in both samples after the removal of the field. Therefore, it was concluded that the $\left(\frac{1}{2}, \frac{1}{2}, \frac{1}{2}\right)$ quasi-Bragg peaks are robust features of $Tb_2Ti_2O_7$ (insensitive to precise stoichiometry). This work supports the conclusion that the sharp transition observed with specific heat measurements near 0.5 K is not associated with magnetic dipole order, but likely originates from higher order multipole (quadrupole, octupole, etc.) moments. It also poses the question: Why are magnetic dipole degrees of freedom less sensitive to disorder (stuffing) than the multipolar order associated with T_c?

Additional Details for Specific Heat

Both $x = +0.0147$, and $x = -0.0010$ samples had an identical mass of 122.4 mg. The thermal relaxation method was implemented with a platinum tungsten weak link. The temperature dependence of weak link thermal conductance for both samples is shown in figure B.3.
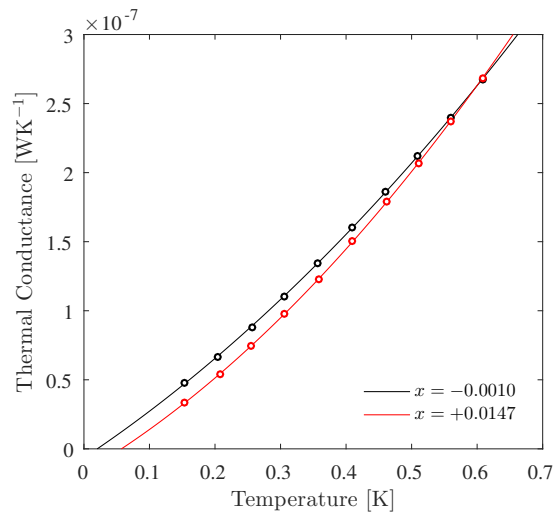

Figure B.3: Thermal conductance of weak link versus temperature for both samples of $Tb_{2+x}Ti_{2x}O_{7+\delta}$, fit to a second order polynomial.

Appendix C

Ytterbium Titanate $Yb_2Ti_2O_7$

Unconventional magnetic ground state in $Yb_2Ti_2O_7$

This project was a larger collaboration that was published in reference [73], and is described with great detail in the master's thesis of R. M. D'Ortenzio.[187] Two samples $Yb_2Ti_2O_7$ were prepared by collaborators at McMaster University in the forms of a single crystal, and a polycrystal powder from the same batch of starting material. These samples were studied with positive muon spin relaxation/rotation (μSR) at TRIUMF at the University of British Columbia, and low temperature specific heat measurements were performed at the University of Waterloo.

The muon spin relaxation showed very little temperature dependence for both samples. Longitudinal field (LF) μSR indicated that spin dynamics are almost identical at 1 K and 16 mK, in contraditction to measurements in reference [68] which presented evidence of dominant ferromagnetic order. Transverse field (TF) μSR was also performed on both samples with a field of 50 mT along [110], which identified the presence of several distinct frequencies associated with the local spin susceptibility of lattice sites nearby O^{2-} ions, where the positive muon likely resides. The highest of these frequencies has no temperature dependence, and is associated with muons landing in the silver sample holder. The lower frequencies exhibit a Curie-Weiss temperature of $T_{CW}^{\mu} = -1.3 \pm 0.5$ K, from fits in the range 400 mK $< T < 3.5$ K. This behaviour exhibits an abrupt disruption correlated with the transition temperatures identified by specific heat measurements, shown in figure C.1.
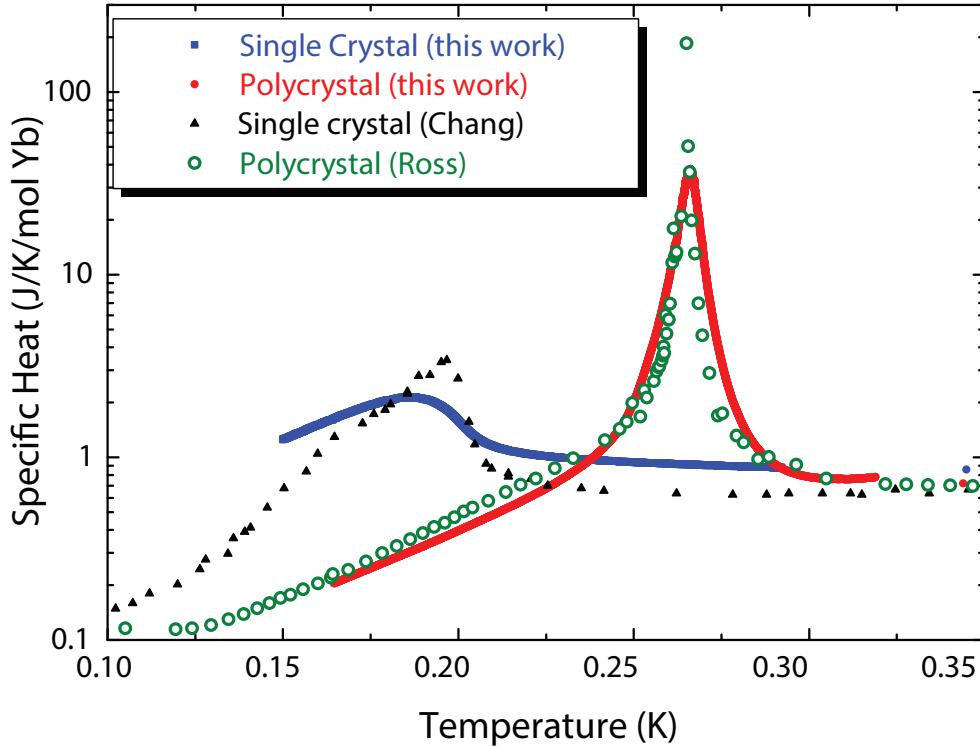
Figure C.1: Specific heat of single and polycrystal $Yb_2Ti_2O_7$ as it appeared in D'Ortenzio *et al.* Figure reproduced from reference [73] with permission.

The lack of temperature dependence observed with LF measurements is a common theme among many ordered frustrated pyrochlores that has not been completely resolved, and goes beyond the scope of this discussion. Although this study leaves the nature of the low temperature state unresolved, it likely points to a phase transition that goes beyond the conventional description of magnetic dipoles (M1), and possibly an exotic quantum spin liquid (QSL) or valence bond solid (VBS) type of ordering.

Additional Details for Specific Heat

Specific heat measurements were performed using the slope method, whereby both samples were cooled from 1 K to 60 mK as shown in figure C.2. The heat capacity is proportional to the slope of the cooing curve, which reflects the rate of energy leaving the material through the platinum tungsten weak link K, formally given by equation 3.25 in section 3.5. The temperature dependence of the thermal conductance $K = P/\Delta T$ of the weak link also

shown, was obtained from relaxation measurements, that were also used to calibrate the absolute value of specific heat. The samples had masses 45.5 mg, and 48.0 mg respectively for the single crystal, and powder.
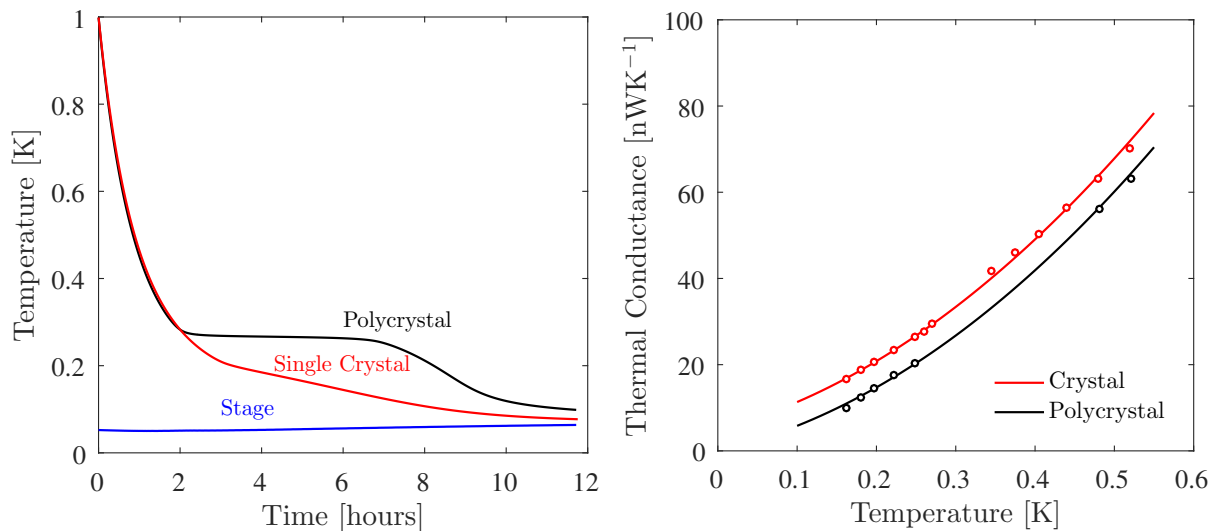

Figure C.2: Left: Slope method cooling curves for two samples of $Yb_2Ti_2O_7$. The plateau indicates a massive release of latent heat at the critical temperature. Right: Thermal conductance of weak link versus temperature for both samples of $Yb_2Ti_2O_7$, fit to a second order polynomial and subsequently used in equation 3.25.

Appendix D

Cobalt Niobate CoNb$_2$O$_6$

Cobalt Niobate has recently seen activity because its low energy magnetic excitations might be described by the **E$_8$** symmetry group, which is a 248-dimensional linear algebraic group. Applications of **E$_8$** are familiar in theoretical models of string theory and supergravity, but in a recent neutron scattering measurement, Coldea *et al.,*[188] detected spin excitation consistent with a spectrum of eight particles that were predicted to exist for the transverse field Ising model by Zamolodchikov in 1989.[189] Borthwick and Garibaldi have written an accessible introduction to this subject.[190] The project described here was part of a collaboration initiated at McMaster University, where the samples were prepared and characterized with x-ray diffraction, magnetometry, heat capacity and μSR measurements. These are described in the masters, and doctoral theis of T. J. S. Munsie.[191, 192]

Specific Heat Details

Zero-field ($< 10^{-3}$ G) Specific heat measurements below 2 K were performed at the University of Waterloo using the relaxation method described in section 3.3. While performing these measurements, a significant increase in the thermal relaxation time of the material was noticed, with properties very similar to the extremely slow behaviour discovered for Dy$_2$Ti$_2$O$_7$ in Chapter 6. The thermal conductance of the manganin weak link $K(T)$, is shown in figure D.2, next to a comparison of the measured thermal relaxation time with the intrinsic time constant of the weak link $\tau = C/K$. The features in this figure indicate that the material behaves very slowly below ~ 800 mK. The resulting specific heat is shown in figure D.1, where there are significant difference in these results compared with published measurements below 1 K.[193]

The observed low temperature behaviour $\propto T^{-2}$, is characteristic of a nuclear anomaly, which is most likely caused by the hyperfine interaction of ^{59}Co, which has nuclear spin $I = 7/2$. The data below 0.7 K was fit to the function $c(T) = AT^{-2}$ where $A/R = 17.2$ mK. This is consistent with the value reported from specific heat measurements on cobalt metal $A/R = 17.5$ mK.[194]

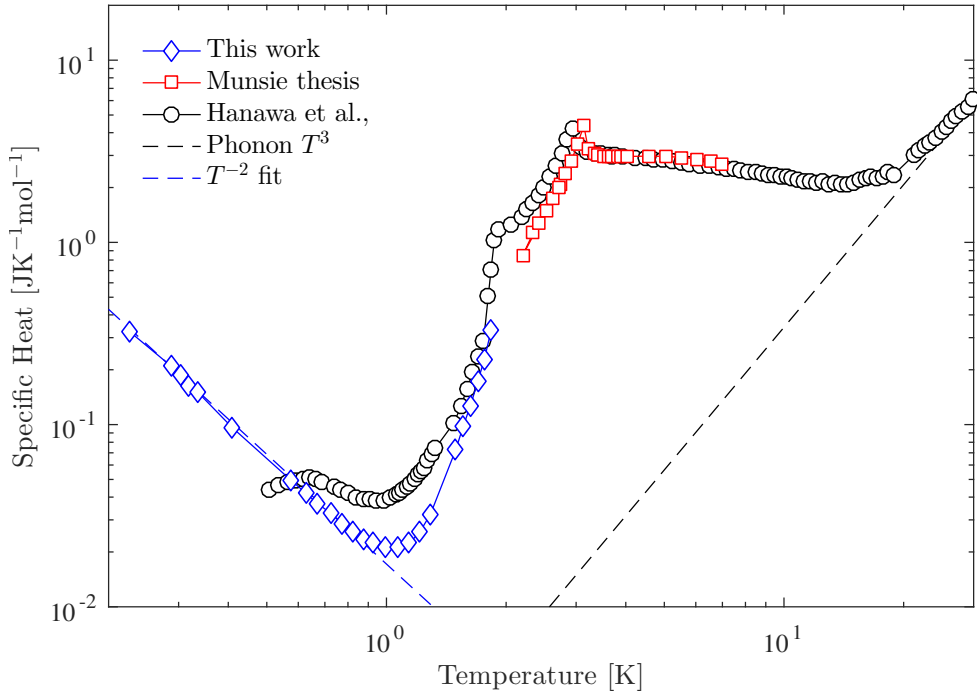Figure D.1: This work: Specific heat of $CoNb_2O_6$ below 2 K was obtained with the slow thermal equilibration method, which indicates a large upturn in specific heat below 0.5 K $\propto T^{-2}$. High temperature data for the same crystal was measured by T. J. S Munsie in reference [192]. The measured phonon contribution from $ZnNb_2O_6$ was also obtained from Hanawa $et\ al.,$ and is negligible below 3 K.[193]
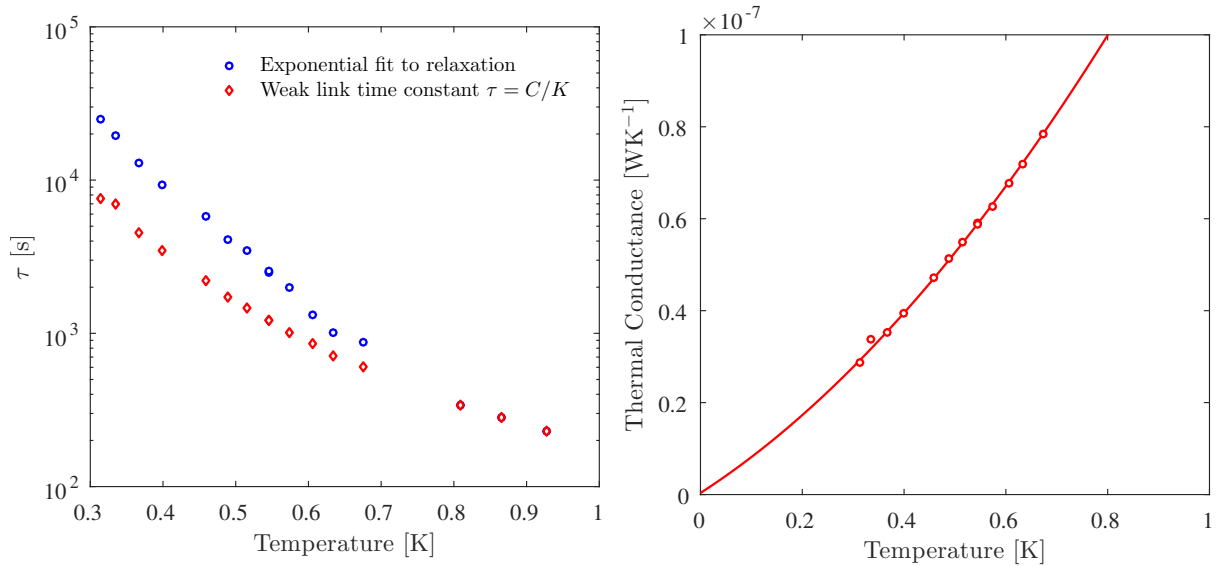
Figure D.2: Comparison of the weak link time constant $\tau = C/K$ with the measured thermal equilibration time of $CoNb_2O_6$ below from 0.3 K to 1 K shows a significant slowing down of the latter below 0.8 K. Right: Thermal conductance of the weak link fit to a second order polynomial.

Appendix E

Cryogenic Refrigeration

Before discussing the details of a dilution refrigerator, it is helpful to review some general properties of helium, which comes in two stable isotopes: ^{4}He and ^{3}He. The utility of helium as a refrigerant is determined by its latent heat of evaporation L, and its vapour pressure P_v. The latent heat of evaporation at a particular pressure is determined by the strength of forces binding the atoms together in the liquid state. Because the electronic structure of helium consists of a closed $s-$shell, the binding between atoms can only arise from weak van der Waals interactions. Furthermore, the relatively large quantum mechanical zero-point energy prevents the formation of a solid phase, even at zero temperature (except at high pressures, ~ 25 atm for ^{4}He). This finite energy

$$E_0 = \frac{h^2}{8ma^2}, \tag{E.1}$$

where a is a measure of the radius of a sphere occupied by the atoms, results in a zero-point vibration amplitude that is larger for ^{3}He than for ^{4}He, because of its reduced mass m.[195] This attribute also results in reduced latent heat of evaporation in ^{3}He. Generally, the cooling power for an evaporating liquid such as helium is given by

$$\dot{Q} = \dot{n}(H_{\text{liq}} - H_{\text{vap}}) = \dot{n}L, \tag{E.2}$$

where $\dot{n}$ is the rate of mass flow evaporating form the liquid to vapour phase, and L is the latent heat of evaporation.[195] If the vapour phase is maintained at a constant pressure by vacuum pump, then the rate of mass flow will be proportional to the vapor pressure, given approximately by $P_v \propto e^{-L/RT}$. It then follows that the cooling power also decreases rapidly at low temperature

$$\dot{Q} \propto e^{-1/T}. \tag{E.3}$$

The maximum cooling power of any such liquid is limited when the rate of evaporation is balanced by the external heat load to the liquid. In practice, this limit is about 1.3 K for ^{4}He, and 0.3 K for ^{3}He.

The principle of operation for a ^{3}He-^{4}He dilution refrigerator is very different than for an evaporation cryostat. It relies on the finite solubility of ^{3}He in ^{4}He that occurs when a mixture of these two isotopes are cooled below 0.867 K, as shown in the phase diagram in figure E.1. The cooling power of a dilution refrigerator comes from the change in enthalpy of mixing when ^{3}He atoms move from *concentrated* ^{3}He to a *dilute* phase containing mostly ^{4}He. In order to understand the origin of this finite solubility, we must consider a few important differences between the two isotopes. Because of its reduced mass, the ^{3}He isotope experiences larger zero-point fluctuations than ^{4}He (equation E.1), and the binding energy is weaker because the atoms are more spaced out. Thus, when a ^{3}He atom is transferred from the concentrated to dilute phase, the increase in binding energy is energetically favourable.

In opposition to this energy gain, the Fermi character of ^{3}He atoms results in a successive filling of energy states up to the Fermi energy $E_{\mathrm{F}} = k_{\mathrm{B}} T_{\mathrm{F}}$. Because of their larger effective radius, the average distance between closely packed atoms in pure ^{3}He is larger than it would be when surrounded by ^{4}He atoms. Since the electronic structure of both isotopes is identical, they both experience the same Van der Waals attraction. However, the ^{3}He atom surrounded by ^{4}He results in a lowering of this attractive energy relative to the pure ^{3}He phase where the atoms cannot pack so tightly. Therefore, it is energetically favorable for ^{3}He to mix with ^{4}He. ^{4}He is an isotope with nuclear spin-0, and undergoes Bose condensation to a superfluid below 2.177 K. ^{3}He on the other hand, is an isotope with nuclear spin$-\frac{1}{2}$, and therefore obeys Fermionic statistics.

The phase diagram for the mixtures of liquid ^{3}He-^{4}He, in figure E.1 indicates the presence of a region where phase separation occurs between the two nuclear isotopes. The critical point of this phase separation occurs at ~ 0.867 K. Below this temperature is a region (two-phase region), where the allowed concentration of Fermi liquid ^{3}He in superfluid ^{4}He is limited to a finite concentration, indicated by the phase separation line. In the limit $T \to 0$, this phase of ^{4}He can support a finite concentration limited to 6.6% ^{3}He.
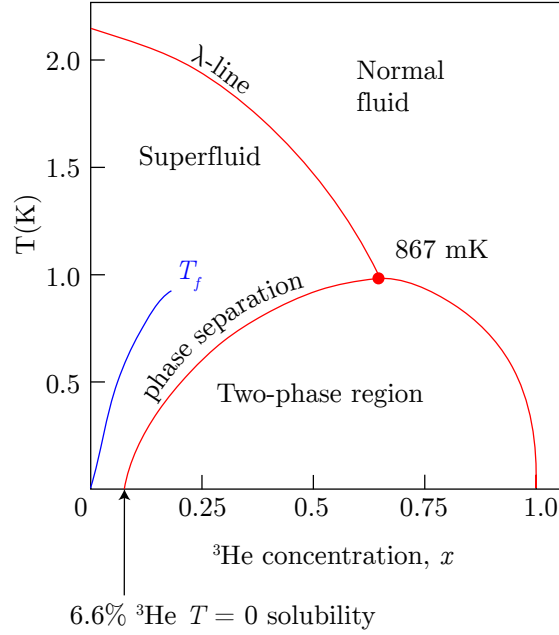
Figure E.1: Illustrated phase diagram of liquid ^{3}He-^{4}He below 2 K. Adopted from [195].

The cooling power of this dilution process comes from the difference in enthalpy of ^{3}He in the dilute and concentrated phases

$$\dot{Q} = \dot{n}_3 \left[H_d(T) - H_c(T) \right], \tag{E.4}$$

where a positive change in enthalpy ΔH, is endothermic. Energy is absorbed from the surroundings as the energetic ^{3}He atoms are pumped away into the concentrated phase. In thermal equilibrium, the chemical potential of both concentrated and dilute phases are equal[195]

$$
\begin{aligned}
\mu_{3,c}(x_c, T) &= \mu_{3,d}(x_c, T) \\
H_3 - T S_3 &= H_{3,d} - T S_{3,d} \\
\left(H_3(0) + 11T^2 \right) - T \int_0^T \frac{C_3}{T'} dT' &= H_{3,d}(T) - T \int_0^T \frac{C_{3,d}}{T'} dT' \\
H_{3,d}(T) &= H_3(0) + 95T^2 \text{ [J mol-He}^{-3}].
\end{aligned}
\tag{E.5}
$$

Hence, the cooling power for a circulation rate $\dot{n}_3$ [mol s^{-1}] is

$$
\begin{aligned}
\dot{Q}(T) &= \dot{n}_3 \left[H_d(T) - H_c(T) \right] \\
\dot{Q}(T) &= 84 \dot{n}_3 T^2 \text{ [W]}.
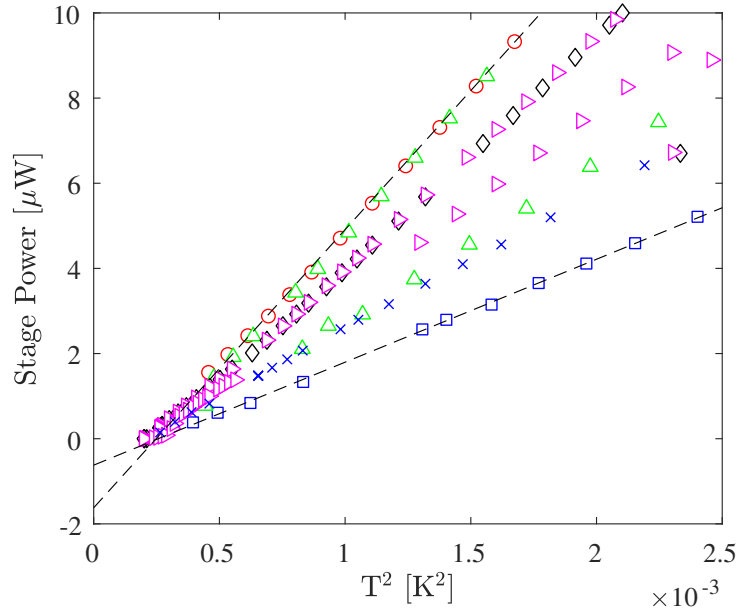\end{aligned}
\tag{E.6}
$$

Figure E.2: Measured heater power applied to the mixing chamber (S.H.E. Corporation Model DRP-36) for various circulation rates. Stepper curves correspond to a higher circulation rate. Extrapolating the intercept ($\sim$0.6 to 1.6 μW) provides the intrinsic heat load on the mixing chamber at base temperature. The cooling power of the dilution refrigerator follows the expected power law, $\dot{Q} \propto T^2$.

The measured cooling power for our dilution refrigerator (S.H.E. Corporation Model DRP-36) is plotted for various circulation rates in figure E.2 as a function of T^2. The base temperature was limited to $\sim$ 14 mK. The steeper curves correspond to a higher circulation rate, which was adjusted by changing the level of heat applied to the still. The extrapolated intercept on the left axis corresponds to the intrinsic heat load on the mixing chamber, which typically ranges from 0.6 μW to 1.6 μW. This indicates that the intrinsic heat load of the fridge is affected by the increased return heat load from the additional helium circulating.

Conc. ³He pre-cooled
from 1 K pot

Dilute ³He
from still

Main flow impedance
(Z ≈ 10⁻¹²cm⁻³) raises vapour
pressure of incoming ³He

Pinhole (<1mm) suppresses
superfluid creep

Coiled heat exchangers
cool incoming ³He

>90% ³He

Still

<1% ³He

Secondary impedance
prevents ³He from
re-evaporating

Continuous counterflow heat exchanger
concentrated ³He passes through
the inner concentric capillary

Discrete heat exchangers
filled with sintered Cu powder

Bypass channel lowers
flow impedance and
reduces viscous heating

outgoing

incoming

Thermal grounding tabs

A fridge with no
discrete heat exchangers
can get to ≈30 mK

Graphite supports

Phase boundary
between dilute and
concentrated ³He

conc. ³He

dilute ³He

Mixing chamber

3"

Figure E.3: General features of the S.H.E. Corporation Model DRP-36 ³He-⁴He dilution fridge. Figure adopted from reference [125].

196

Appendix F

Low $1/f-$Noise Differential Amplifier

This section summarizes the important points of a project that involved the construction and improvement of a differential voltage amplifier designed to work with very small signals at very low frequency.

Ultra-low noise measurements at ultra-low frequency can be useful for a range of applications from ac-heat capacity and susceptibility, to gravitational wave detection, to building vibration measurements. Many of the best amplifiers available on the market are limited in this regard, and they are typically designed for use above ~ 1 Hz. They are also limited by intrinsic $1/f-$noise (pink noise, or flicker noise) that arises in almost every condensed matter system.

The amplifier design shown in figure F.1 was described by Scandurra *et al.,* in reference [196], where optimal values of the components are summarized. This simple design is based on the standard differential FET configuraiton, but the key component is the IF3601 JFET, which has an amazing e_n=0.3 nv/$\sqrt{\text{Hz}}$.[1] A standard transistor Q_1 and R_{SS} biases each JFET J_L, and J_R with about 4.5 mA of current, and the gain of the first stage is determined by the ratio $R_2/R_1 = 100$ (40dB). Two instrumentation amplifiers IA1, and IA2 (Burr-Brown INA131) source current to the JFETs as their input gate voltage is modulated. The series element $R_C C_C$ is a for pole-zero compensation, in order to stabilize the amplifier and prevent feedback oscillations. A second stage amplifier can also be used to raise the voltage gain by another 40 dB.

---

[1]e_n = Equivalent short circuit input voltage noise. Praised by Horowitz and Hill: runners-up in the the low-noise comparison are the LSK170B and BF862, with considerably lower capacitance than IF3601.[197]
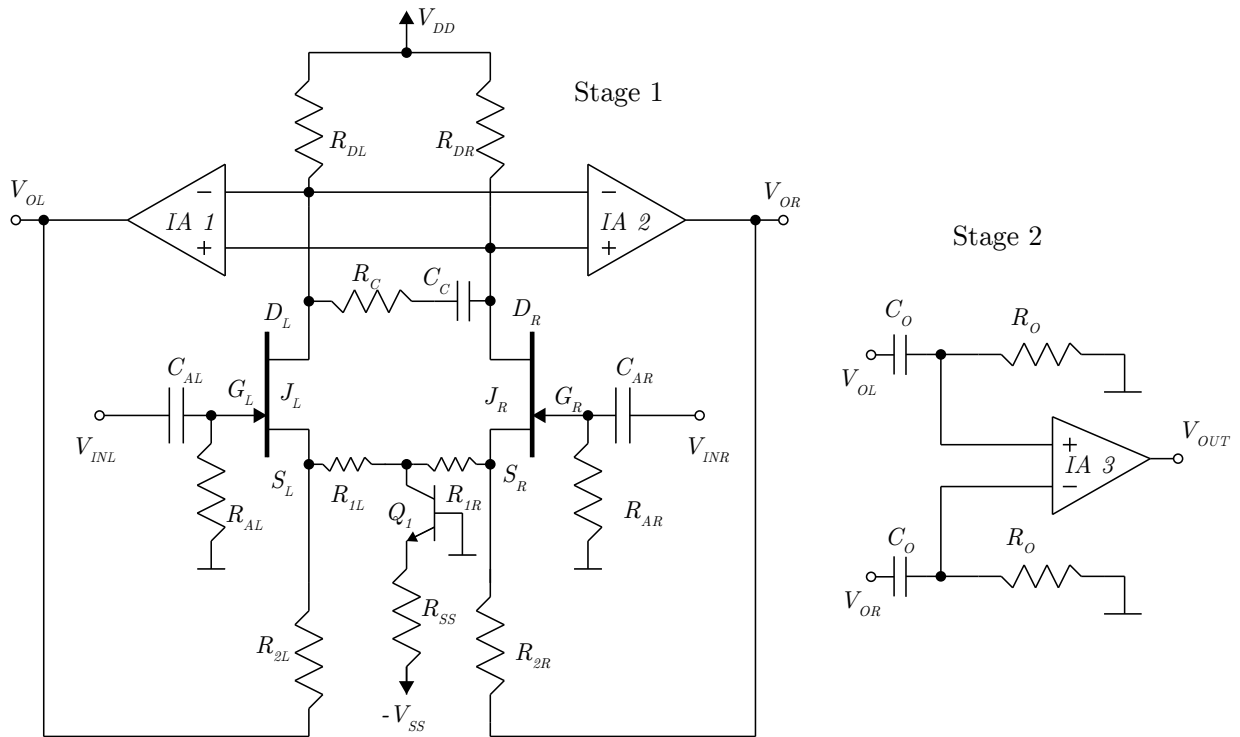
Figure F.1: Schematic diagram of the two stage differential amplifier. Figure adapted from reference [196].

The amplifier is powered by ± 18 V,[2]. An aluminum Hammond enclosure was used to shied from rf noise, and low-noise twinax cables were used to transmit signals. The measured equivalent input voltage noise spectrum measured for several different configurations is shown in figure F.2. It performs even better than stated in the original paper (0.9 nV/$\sqrt{\text{Hz}}$ instead of 1.2 nV/$\sqrt{\text{Hz}}$ at 10 Hz), and this was improved further by matching the pair of IF3601's based on similar transconductance. To do this, we purchased a bag of 200 IF3601's directly from Interfect Corp., that were obtained from a single wafer. The distribution of gate-to-source V_{GS}, voltages for each JFET was then measured with the circuit shown in figure F.3. The circuit was also modified to work with multiple JFETs in parallel at each input, which lowers the noise by a factor of $1/\sqrt{N}$ for N JFETs in parallel. This may involve modifying the circuit to provide double the bias current to the pair. It may also help to PID control the entire circuit board, or to cool the IF3601's with liquid nitrogen to lower their intrinsic noise. Both of these ideas require more testing.

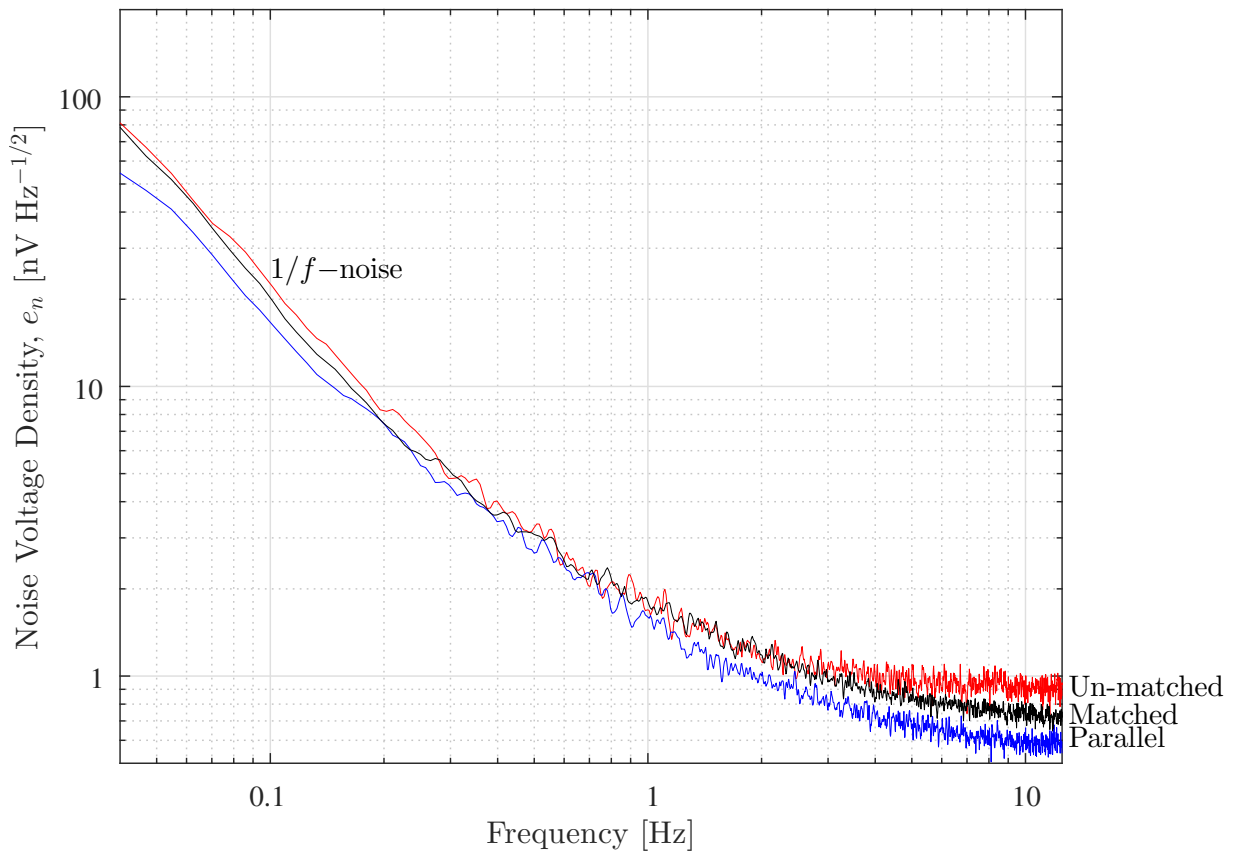[2]LM regulated from ± 24 V battery cells shorted to ground with capacitors

Figure F.2: Measured noise voltage density versus frequency for three different configurations of the circuit in figure F.1 (both inputs shorted to ground). The un-matched pair of IF3601's had the highest (but still great) noise of $\sim0.9\mathrm{nV}/\sqrt{\mathrm{Hz}}$ at 10 Hz. Closely matching a pair with the method in figure F.3, lowered the noise to ~0.8 nV/$\sqrt{\mathrm{Hz}}$ at 10 Hz. Using two matched JFETs in parallel at each input (for a total of 4) lowered this even further to $\sim0.6\mathrm{nV}/\sqrt{\mathrm{Hz}}$ at 10 Hz.
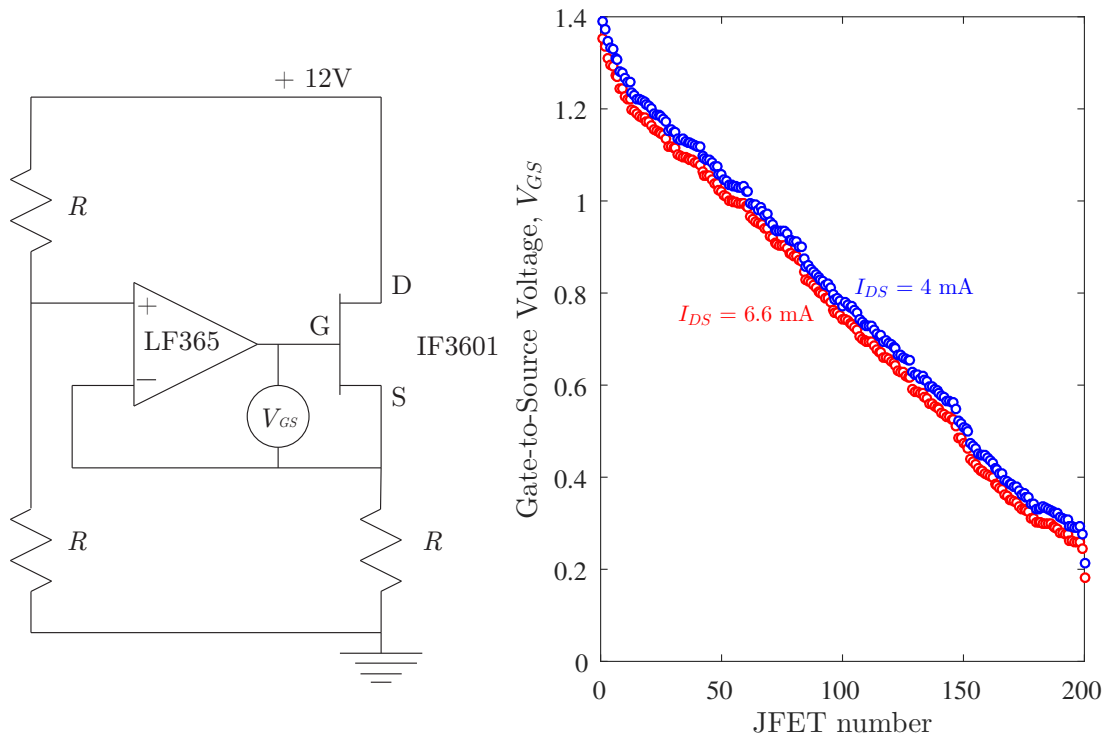
Figure F.3: Circuit used to measure, and match the gate-to-source voltage of 200 IF3601's that were obtained from a single wafer. An LF356 op-amp was configured to bias each JFET with $I_{DS} = 4$ mA and 6.6 mA of current.